SEARCH FOR VECTOR-LIKE QUARKS USING TRILEPTON AND SAME-SIGN DILEPTON EVENTS IN 20.3 fb^{-1} OF PROTON-PROTON COLLISIONS AT $\sqrt{s} = 8$ TeV WITH THE ATLAS DETECTOR

by

Fionnbarr O'Grady

A Dissertation Submitted to the Faculty of the

DEPARTMENT OF PHYSICS

In Partial Fulfillment of the Requirements

For the Degree of

DOCTOR OF PHILOSOPHY

In the Graduate College

THE UNIVERSITY OF ARIZONA

2015

The University of Arizona
Graduate College

As members of the Dissertation Committee, we certify that we have read the dissertation prepared by Fionnbarr O'Grady entitled Search for Vector-Like Quarks Using Trilepton and Same-Sign Dilepton Events in 20.3 fb^{-1} of Proton-Proton Collisions at $\sqrt{s} = 8$ TeV with the ATLAS Detector and recommend that it be accepted as fulfilling the dissertation requirement for the Degree of Doctor of Philosophy.

________________________________ Date: July 07, 2015

Kenneth Johns

________________________________ Date: July 07, 2015

Erich Varnes

________________________________ Date: July 07, 2015

Michael Shupe

________________________________ Date: July 07, 2015

Doug Toussaint

________________________________ Date: July 07, 2015

Koen Visscher

________________________________ Date: July 07, 2015

Final approval and acceptance of this dissertation is contingent upon the candidate's submission of the final copies of the dissertation to the Graduate College.

I hereby certify that I have read this dissertation prepared under my direction and recommend that it be accepted as fulfilling the dissertation requirement.

________________________________ Date: July 07, 2015

Dissertation Director: Kenneth Johns

Statement By Author

Acknowledgements

TABLE OF CONTENTS

TABLE OF CONTENTS – *Continued*

TABLE OF CONTENTS – *Continued*

LIST OF FIGURES

LIST OF FIGURES – *Continued*

LIST OF FIGURES – *Continued*

LIST OF FIGURES – *Continued*

LIST OF FIGURES – *Continued*

LIST OF FIGURES – *Continued*

LIST OF TABLES

Abstract

A search is presented for vector-like quarks using 20.3 fb^{-1} of proton-proton collisions at a center-of-mass energy of $\sqrt{s} = 8$ TeV collected with the ATLAS detector in 2012 at the CERN Large Hadron Collider. Vector-like quarks are predicted to exist in many theories beyond the Standard Model of particle physics that attempt to resolve the hierarchy problem. Events are selected containing jets including at least one b-jet, sizable missing transverse momentum, large scalar sum of the jet and lepton transverse momenta, and either three leptons or two leptons with the same electric charge. Standard Model processes rarely produce this final state and production of vector-like quarks would lead to an enhanced rate of such events. The data are interpreted in the context of a variety of models including pair production of vector-like quarks T and B, which have the same electric charge as the corresponding Standard Model quarks and can appear in either SU(2) weak isospin singlets, doublets or triplets. In addition single and pair production of the vector-like quark $T_{5/3}$, which appears in an SU(2) weak isospin doublet or triplet and has electric charge 5/3, is considered. A moderate excess of data above the SM background expectation is observed with a significance of less than two standard deviations. The data are used to set limits at 95% Confidence Level (CL) on the new heavy quark mass for the various VLQ models considered using the CL_S method. The vector-like quarks T and B in the singlet model are excluded at 95% CL below a mass of 0.59 TeV and 0.62 TeV respectively. The $T_{5/3}$ is excluded at 95% CL below a mass of 0.74 TeV when only pair production is considered and below 0.75 TeV when both pair and single production are considered.

CHAPTER 1

Introduction

The Standard Model (SM) of particle physics describes the fundamental building blocks of matter and the interactions among them. It has been fantastically successful in explaining a wide variety of phenomena and has been used to calculate physical quantities in agreement with experimental measurements to extraordinary precision. An example of the success of the theory is the calculation of the fine structure constant α which determines the strength of the force of electromagnetism. The value of α calculated from theory is consistent with experimental values to a precision of better than one part in a billion (10^{-9}) [1]. This makes the Standard Model one of the most accurate physical theories constructed to date.

Despite the success of the SM there are a number of important questions it leaves unanswered. Among these are the nature of dark matter, the origin of the force of gravity and a natural explanation of the hierarchy of the fundamental forces of nature. These missing elements mean that the SM is not a complete theory of the universe but rather an approximation that is valid for a limited, albeit very large, range of energies. Many theories have been advanced that seek to resolve one or more of the problems afflicting the SM. These theories often predict the existence of new particles that have not been observed in experiment. This dissertation describes a search for a class of particles known as vector-like quarks, carried out using 20.3 fb^{-1} of proton-proton collision data collected with the ATLAS detector at the CERN Large Hadron Collider (LHC) in 2012. These particles arise in theories that attempt to explain the observed hierarchy of the strengths of the fundamental forces without the need for fine tuning.

Historically particle physics began with J.J. Thompson's study of cathode rays, which in 1897 led to the discovery of the first subatomic particle known as the electron. [2] Since then the field has grown a great deal and has had a tremendous impact on our understanding of nature, making significant contributions to many areas of physics including atomic theory, optics and cosmology. It has also played a major role in the development of many important technologies such as electricity, nuclear power, medical diagnosis and treatment of disease.

In the SM the universe consists of particles divided into two classes, fermions and bosons. By definition fermions have half-integer spin while bosons have integer spin. Fermions include the particles that make up matter such as the up and down quarks contained in protons and neutrons inside nuclei as well as the familiar electron that binds to those nuclei to form atoms. Bosons include particles such as the photon and gluon which are responsible for mediating the fundamental forces of nature. Whenever two particles attract or repel one another a boson, such as a photon, is exchanged between them to communicate the force. There are three generations of fermions with the lightest and most stable of them occurring in the first generation. The electron and up and down quarks mentioned above, which are the constituents of everyday matter, occur in the first generation. The second and third generation particles mirror the first generation except that their masses increase from the first to the third generation. As a consequence of their larger masses these particles are unstable and decay very soon after creation. As an example the second generation cousin of the electron, known as the muon, is ~ 200 times as massive and lives on average for $\sim 10^{-6}$ second [3].

The bosons in the SM account for three of the four fundamental forces of nature: electromagnetism, and the strong and weak nuclear forces. Electromagnetism is by far the most ubiquitous and familiar of these, underlying many of the phenomena that we experience in the macroscopic world ranging from the molecular forces that hold matter together to the light reaching us from distant galaxies. The nuclear forces, as their names suggest, are limited to subatomic distance scales and thus play a more subtle yet vital role in physics. The strong force is responsible for holding protons together in nuclei against their mutual electric repulsion while the weak force allows for radioactive decay and the *pp* chain reaction that drives hydrogen burning at the center of stars. The conspicuous absence of gravity from the Standard Model remains one of its shortcomings. Attempts to incorporate gravity into a theory with the other three forces have all failed. Fortunately gravity is so weak compared to the other three forces that it can be safely ignored when studying particle interactions at the subatomic scale.

The final remaining piece of the Standard Model was verified in 2012 with the discovery of the long sought Higgs Boson by the ATLAS and CMS collaborations [4, 5]. This discovery lead to the awarding of the 2013 Nobel Prize in physics to Peter Higgs and Francois Englert for the theoretical prediction of the particle [6, 7]. The Higgs boson is a remnant of the Englert-Brout-Higgs (EBH) mechanism that describes how all the massive SM particles attained their mass through a process known as spontaneous symmetry breaking. The Standard Model is an extremely powerful theory that has unified many physical phenomena that at first blush seem disparate and unrelated. It is in this sense that it can be considered a truly fundamental theory of nature.

Despite the high precision and broad scope of the Standard Model it is not a perfect theory. There are a number of aspects of the Standard Model that are unsatisfactory both aesthetically and in terms of tension between its predictions and experimental observations. The first is that it does not include gravity. A complete theory of the universe must explain all of the fundamental forces including gravity. Another problem is that it cannot account for the observed matter antimatter imbalance in the universe. Interactions involving matter and antimatter are approximately symmetric in the Standard Model [1]. It follows that they should be produced in roughly the same proportions. However the universe seems to be almost completely composed of matter and very little antimatter. The existence of dark matter also poses a serious problem. Approximately 26.8% [8] of the universe is composed of matter that doesn't emit or absorb light and is only detected through its gravitational effects. In comparison only about 5% of the universe is accounted for by the visible matter made up of known SM particles. Within the framework of a particle theory there must be a neutral particle with sufficient mass to account

[1] Although this is not an absolute principle there are very few known violations

for dark matter. There is no such particle in the Standard Model. Finally the hierarchy problem refers to the dramatic difference between the electroweak symmetry breaking scale ($\sim 10^2$ GeV) where the three SM forces dominate and the Planck scale ($\sim 10^{19}$ GeV) where gravity becomes important as well. This difference is tied to the mass of the recently discovered Higgs boson that seems unusually small given its large quantum corrections. Delicate cancellations between these quantum corrections and the bare mass of the Higgs, an example of fine tuning, are needed to explain the observed mass of 125 GeV [4, 5]. For all these reasons the current theory is regarded as an approximation to a more fundamental theory of everything that would resolve these issues naturally. As such, particle physicists are constantly pushing the limits of the Standard Model in order to find violations to it that would point to new physics beyond the Standard Model (BSM).

1.1 Experimental Particle Physics

Of the large number of elementary particles in the Standard Model most are unstable and are observed only in very high energy environments. In order to study these particles, and to search for new particles that may exist beyond the Standard Model, particle accelerators are used to produce high energy collisions of stable particles such as protons or electrons. In these collisions heavier, more exotic particles are produced and detected. Particle accelerators are the main experimental tool used to test the Standard Model and indeed a number of SM particles were in fact discovered using particle accelerators [9–11].

The Large Hadron Collider (LHC), located at CERN (European Center for Nuclear Research) outside Geneva on the French-Swiss border is the largest and highest energy particle accelerator ever constructed. It was designed to collide proton-proton pairs at an unprecedented center of mass energy of $\sqrt{s} = 14$ TeV and during its first run, from 2009 to 2013, reached a record breaking energy of 8 TeV. There are six detectors located along the perimeter of the LHC where the proton beams intersect and collisions take place. The two general purpose detectors, ATLAS (A Toroidal

LHC ApparatuS) and CMS (Compact Muon Solenoid) are dedicated to the search for a broad range of new physics signals. Both were used in the discovery of the Higgs Boson in 2012. These experiments have allowed physicists to scrutinize the Standard Model like never before and to test a variety of new theories which are extensions to the Standard Model that attempt to resolve one or more of the problems associated with it.

The goal of collider experiments like ATLAS and CMS is to test the validity of the Standard Model and to search for evidence of new physics. The collision data are analyzed for signs of new particles that have been predicted to exist, either in the Standard Model or beyond, but have not been observed. This presents a challenge since most of these particles decay very soon after being created. This means experimentalists must look for events with a final state based on a particular decay mode of the particle. The final state refers to the measurements made in the detector after the collision takes place.

The situation is complicated further by the fact that there are a large number of SM particles that can produce the same final state. The new particle which is the subject of the search is known as the signal while the SM particles that can mimic it are known as the background. For any given event with a particular final state it is impossible to say exactly what produced it. All physicists can do is look at the total number of such events, and their kinematic properties, and compare them to the background only and signal+background hypotheses. In this way they can see which hypothesis is more consistent with the data and ultimately make a statement about the probability that the signal exists.

Very sophisticated techniques are used to discrimate between signal-like and background-like events and to reduce the background by refining the region of phase space explored in the search. These techniques exploit the characteristics of signal and background events which are known from theory. If an excess of events is observed above the background expectation this is interpreted either as a fluctuation or evidence of new physics depending on the significance of the excess. Excesses of two standard deviations or less are consistent with an upward fluctuation of the background and often go away when more data are collected. An excess of five standard deviations or more is interpreted as discovery of a new particle. An intermediate excess between two and five standard deviations is promising but inconclusive and requires more data to resolve. Exclusion limits are set at 95% confidence level (CL) on the mass of the particle which is not known a priori. As more data are collected if no excess is seen the mass limits increase and the particle is eventually ruled out completely when the limit exceeds the range of acceptable masses estimated from the theory.

This dissertation focuses on the search for a new class of particles known as vector-like quarks, using 20.3 fb^{-1} of data collected at the LHC with the ATLAS detector. These particles arise in a number of BSM theories that attempt to resolve the hierarchy problem. [12–30] They are identical to the SM quarks except that they are non-chiral and do not derive their mass from the EBH mechanism. The term 'vector-like' quark refers to the coupling of these quarks to the W bosons that constitute the charged current of the weak force. Their coupling is a vector current in contrast to the vector minus axial vector (V-A) current of SM quarks. Their non-chirality means that both their left and right handed components interact identically via the weak force, in contrast to the SM fermions. The origin of their mass is important as it means that they are not ruled out in the case that the new boson discovered at the LHC in 2012 is a manifestation of a minimal Higgs sector. Sequential fourth generation quarks that get their mass from the EBH mechanism, as the SM quarks do, would greatly enhance the Higgs production cross-section and thus are excluded provided there is no extended Higgs sector (i.e. multiple Higgs bosons). For this reason the existence of vector-like quarks is not constrained by the Higgs sector and there is strong theoretical motivation for a direct search. The existence of vector-like quarks would help to explain the tremendous difference in the strength of the SM forces and gravity and would remove the necessity for fine tuning to account for the mass of the Higgs boson.

The remainder of this dissertation is organized as follows. A detailed description of the SM and vector-like quarks is given in Chapter 2 followed by a description of the LHC and ATLAS in Chapter 3. Chapter 4 describes the data and Monte Carlo simulations used in the analysis. Chapter 5 and Chapter 6 describe the reconstruction of events and the selection applied to them to define the signal region. This is followed by a description of the background estimation and validation in Chapter 7 and a description of systematic uncertainties in Chapter 8. The results of the analysis are reported and discussed in the context of various models of vector-like quarks in Chapter 9. Chapter 10 gives a summary of the analysis and its results.

CHAPTER 2

Theory

The Standard Model (SM) of particle physics is the currently accepted theory of elementary particles and their interactions. It is formulated as a relativistic Quantum Field Theory (QFT) in which fundamental particles have associated fields and the forces between them arise from symmetry transformations that leave the field equations invariant. Despite the success of the SM, it is not a candidate for an ultimate theory of the universe as it has a number of unresolved problems. In particular it cannot account for the enormous difference between the electroweak energy scale ($\sim 10^2$ GeV) typical of the SM forces and the Planck energy scale ($\sim 10^{19}$ GeV) where all gravity becomes strong. This is referred to as the hierarchy problem. This dissertation describes a search for a class of particles known as vector-like quarks (VLQ) that exist in a number of QFTs that are extensions of the SM which attempt to resolve the hierarchy problem in a natural way.

2.1 Quantum Field Theory

QFT refers not to a single theory but rather a class of theories that share a common mathematical framework. It is a generalization of Quantum Mechanics that describes particles as the excitations of fields, which are continuous functions of space and time. The dynamics of these fields and their excitations (particles) are governed by the underlying symmetries of the theory. A relativistic QFT is one that is consistent with Special Relativity.

A proper description of particle physics must incorporate the principles of both Quantum Mechanics and Special Relativity. An important feature of QFT is that it is possible to unify both of these fields of physics in a single theoretical framework. Special Relativity was initially developed in the context of Classical Mechanics which describes the motion of macroscopic objects. However Quantum Mechanics, which describes the behavior of small scale systems such as atoms and molecules, does not include relativity. The velocities of particles in low energy systems such as these are small enough that relativity can be safely ignored. In order to describe the behavior of high energy particles ($v/c \sim 1$) both Quantum Mechanics and Special Relativity are essential. Early attempts to combine them failed for a variety of reasons. In particular the mass-energy equivalence of Special Relativity ($E = mc^2$) means that particles can be created or annihilated so that particle number is not conserved. This is incompatible with the probabilistic interpretation of Quantum Mechanics. Also Quantum Mechanics relies on the idea of action at a distance in which the influence of a force is communicated instantaneously through space. This violates special relativity, which states that nothing may travel faster than the speed of light. Relativistic QFT overcomes these difficulties by providing a mechanism for the creation and annihilation of particles and by introducing force-mediating particles that propagate at speeds that do not exceed the speed of light.

QFT makes use of the Lagrangian formalism originally developed in Classical Mechanics and later generalized to the description of fields. The particles in a theory and the interactions between them are specified by a quantity called the Lagrangian (L), which is a function of the particle fields. Symmetries in the theory are expressed mathematically as transformations of the fields under which the Lagrangian is invariant. According to Noether's theorem [31], differentiable symmetries of the action ($\int Ldt$) lead to conservation laws. This is a generalization of the classical principle that physical transformations of a system that leave the action unchanged lead to conserved quantities of motion.

In classical systems these space-time symmetries lead to conservation of energy, momentum and angular momentum. In QFT, in addition to space-time symmetries there are internal symmetries that account for the conservation of intrinsic properties of particles such as electric charge. An important class of internal symmetries represented by local gauge transformations give rise to the fundamental interactions in QFT. A gauge transformation shifts the phase of a field everywhere by a arbitrary value known as the gauge. When the value is a constant, independent of space-time coordinates, it is referred to as a global gauge transformation. In a local gauge transformation the value is a function of space and time.

Each local gauge transformation is associated with a boson, or group of bosons, that mediate one of the forces in the theory.

The transformations in QFT are described by a field of abstract algebra known as group theory. Each transformation belongs to a group that is defined by a generator or group of generators, which correspond to a physical property of the particles in the theory such as electric charge. The transformations and their generators are typically represented as matrices while the fields on which they act are represented as multi-component objects such as vectors or Dirac spinors. Applying a generator matrix to a field returns the value of the physical quantity it represents. Applying the transformation matrix defined by that generator rotates the field in the space of allowed values for the physical quantity. A transformation can have a number of different matrix representations. A group is designated by the simplest matrix representation, known as the fundamental representation, for the transformations it describes. Each force in the SM results from a particular group of local gauge transformations under which the Lagrangian is invariant, known as a gauge group. The conserved quantity for each gauge group is the physical quantity associated with the generator of the group. The number of gauge bosons needed to mediate the force is equal to the number of generators of the group. This also equals N^2-1, where N is the dimension of the fundamental representation of the gauge group. The details of the gauge groups that give rise to the SM forces are given in Section 2.2

Before imposing local gauge symmetries the field equations for a theory, which derive from the Lagrangian, have exact solutions. These solutions are plane waves representing free particles propagating through space. Adding a local gauge symmetry to a theory requires introducing an additional field which appears in an extra term in the Lagrangian called the interaction term. The dimensionless coefficient of this term, known as the coupling constant, determines the strength of the interaction. The excitations of the new field are the mediators of the force that results from the local gauge symmetry. The new Lagrangian with the interaction term no longer has exact solutions. In particular, the plane waves representing free particles are no longer solutions since the particles now interact with one another via exchange of the mediator particle.

An illustrative example is QED which describes the force of electromagnetism. Before imposing local gauge symmetry the theory consists of electrons and their antiparticles (positrons) that do not interact at all. In order to satisfy local gauge symmetry a new field is added for the photon. The electrons and positrons in the theory now interact with each other by exchanging photons. This is the origin of the electric forces between charged particles familiar from classical electromagnetism.

In a theory with interactions, processes are possible that bring some group of initial state particles to a group of final state particles. An example is the scattering of oppositely charged particles known as Bhabha scattering. The Bhabha scattering of an electron and a positron is represented symbolically as $e^+e^- \to e^+e^-$. Initially there is an electron and a positron, then there is an interaction and finally there is an electron and positron again. Another example is the decay of an unstable particle to some group of final state particles. The most well known example is the beta decay of unstable atomic nuclei. This process involves the decay of the quarks in the nucleus and is represented symbolically as $d \to ue^-\bar{\nu}_e$. A down quark disappears and an up quark, an electron and an electron antineutrino are emitted. In the SM Bhabha scattering takes place via the force of electromagnetism while beta decay takes place via the weak nuclear force.

Two important physical quantities in high energy particle physics are cross-sections, which represent the probability a particular process will take place, and the lifetimes (or equivalently the decay rates) of unstable particles. The primary tool for calculating these quantities is perturbation theory. In this approach the interaction term is expanded in powers of the coupling constant and the leading terms in the expansion are taken as an approximation. In order for this to be valid the coupling constant must be far less than one so that higher order terms in the expansion contribute very little. This is true in a wide variety of cases. The noted exception is in low energy Quantum Chromodynamics (see Section 2.2.5).

The terms in a perturbative expansion can be associated with Feynman diagrams that represent different ways the process can occur. In a Feynman diagram one dimension represents time. [2] The other dimension doesn't represent anything physical. Lines with an arrow pointing forward in time represent particles while those with an arrow pointing backward in time represent antiparticles. Each particle and antiparticle line has an energy and momentum associated with it. The sum of the energy and momentum into and out of each vertex is zero. The enforces the conversation of energy and momentum for the entire process. The lines that extend out of the diagram represent real particles with well defined mass that can be detected experimentally. The lines which are internal to the diagram represent virtual particles that have no well defined mass and cannot be detected experimentally. Virtual particles merely facilitate the interaction of real particles.

In QED, Feynman diagrams are constructed from the primitive vertex shown in Fig. 2.1. [3] The Feynman diagrams in Fig. 2.2 show different ways Bhabha scattering of electrons and positrons can take place by exchanging a photon. The higher order terms in the expansion correspond to diagrams with more vertices such as those shown in Fig. 2.3. There are infinitely many diagrams that contribute to a given process. All of them affect the value of the cross section, however higher order diagrams with more vertices contribute less and can be ignored. Depending on the desired level of precision a calculation is done to a certain order. Leading-order (LO) calculations consider only the diagrams with the fewest vertices. Next-to-leading order (NLO) calculations consider diagrams with the fewest vertices and those with the next to lowest number of vertices.

Each of the diagrams in Fig. 2.3 contain closed loops of virtual particles. The energy and momentum of the particles in these loops are not fixed and so must be integrated over the full range of allowed values in evaluating the contribution of the

[2]In this dissertation the horizontal dimension represents time with the positive flow of time taken from left to right.

[3]Feynman diagrams for the strong and weak nuclear interactions are constructed in a similar way using the primary vertices for those interactions.

loop diagram. If the integrals are taken to infinity they diverge. A process known as renormalization is used to cut off the integral at an upper bound so it remains finite and to ensure that the final result is independent of the cut off. A theory for which this is possible is renormalizable. The SM is a renormalizable theory.

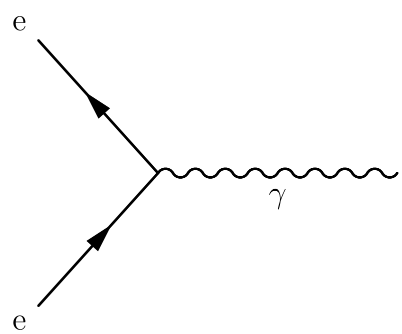

Figure 2.1: Primitive vertex for constructing Feynman diagrams in QED.

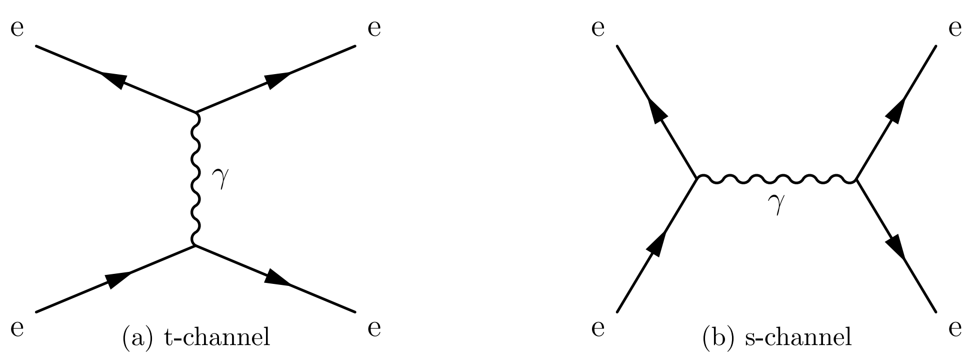

(a) t-channel

(b) s-channel

Figure 2.2: Leading order (LO) Feynman diagrams for Bhabha scattering of an electron and a positron $e^+e^- \to e^+e^-$.

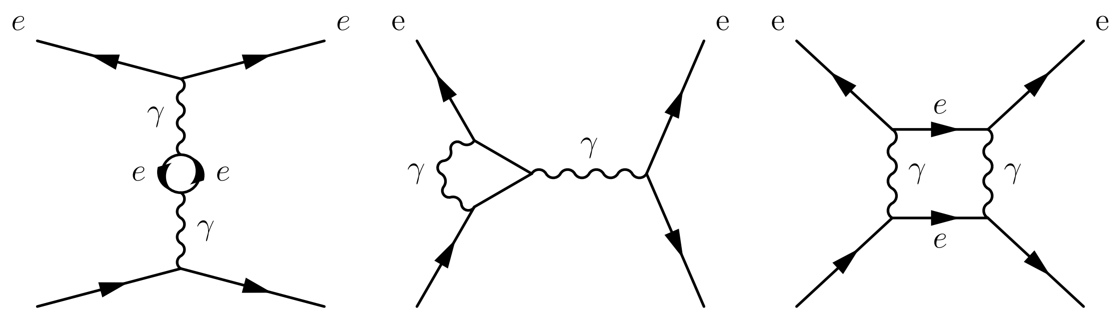

(a) virtual fermion loop (b) extra virtual photon (c) box diagram

Figure 2.3: Examples of next-to-leading order (NLO) Feynman diagrams for Bhabha scattering of an electron and a positron $e^+e^- \to e^+e^-$. This is not the complete set of NLO diagrams.

2.2 The Standard Model

The Standard Model of particle physics is a relativistic QFT that describes all of the known particles observed in the universe and three of the four fundamental forces of nature. Historically the first QFT of particles was Quantum Electrodynamics (QED) which describes the force of electromagnetism [32]. Since then other QFTs have been developed to explain the other forces of nature. Electroweak theory explains both electromagnetism and the weak nuclear force together in a unified theory. Quantum Chromodynamics (QCD) explains the strong nuclear force. There is no QFT of gravity. The SM is the most complete QFT formulated to date. It combines Electroweak theory and QCD and thus incorporates three of the four fundamental forces of nature.

The SM consists of 61 particles divided into 48 fermions and 13 bosons. Tables 2.1 and 2.2 summarize some of their important properties. Three of the fermions (electrons, up quarks and down quarks) make up the observable matter in the universe. With the exception of neutrinos the remaining fermions are unstable and only exist briefly in nature. They are created in high energy processes and quickly decay. The bosons include the force carrying particles that mediate interactions, and the Higgs boson which is the origin of mass in the SM (see Section 2.2.3).

The SM fermions are divided into two groups: leptons and quarks. They are organized into three generations with two leptons and two quarks in each generation. The particles in each generation have properties similar to their corresponding particles in the other generations. An important exception is mass, which increases from the first to the third generation [4]. There are three charged leptons known as the electron, muon and tau lepton. For each charged lepton there is a corresponding neutrino in the same generation that has an electric charge of zero.

There are six flavors of quarks and for each flavor there are three possible colors (red, green and blue). Each unique combination of flavor and color represents a distinct quark. Color is often denoted with a subscript, for example, the three top quarks of different color are denoted t_r, t_g and t_b. For every fermion in Table 2.1 there is a corresponding antiparticle that is not shown. An antiparticle is a symmetric copy of a particle which is identical except that it has opposite charge. [5] Here charge refers to any conserved quantity arising from local gauge symmetry. It includes electric charge as well as color charge (see Section 2.2.4). Antiparticles are denoted with a superscripted line over the letter representing the particle. For example the anti-top quark is represented as $\bar{t}$. [6]

In summary, quarks interact via all three SM forces: the electromagnetic force and the strong and weak forces. Charged leptons interact only via the electromagnetic and the weak force and neutrinos interact only by the weak force.

The bosons in the SM consist of 12 gauge bosons which are the mediators of the fundamental forces and the Higgs boson. The gauge bosons are the excitations of the gauge fields that arise in QFT when local gauge symmetries are included (see Section 2.1). The photon (γ) is the carrier of the electromagnetic force. The eight gluons (g) are the carriers of the strong nuclear force and the $W^{\pm}$ and Z bosons are the carriers of the weak nuclear force. The Higgs boson is a remnant of the EBH

[4] It is unclear if this is true for neutrinos as their exact masses are not known

[5] Other internal quantum numbers such as lepton number and baryon number also change sign for antiparticles

[6] Occasionally for charged leptons, particles and antiparticles are denoted with a superscript giving the sign of the charge of the particle. e.g. $e^+e^- \to e^+e^-$

Mechanism described in Section 2.2.3.

Generation	Particle	Symbol	Mass (MeV)	Charge (Q/e)	Spin
Leptons					
1	electron	e	0.511	-1	$\frac{1}{2}$
	electron-neutrino	ν_e	$< 2\times10^{-6}$	0	$\frac{1}{2}$
2	muon	μ	106	-1	$\frac{1}{2}$
	muon-neutrino	ν_μ	< 0.19	0	$\frac{1}{2}$
3	tau	τ	1777	-1	$\frac{1}{2}$
	tau-neutrino	ν_τ	< 18.2	0	$\frac{1}{2}$
Quarks					
1	up	u	1.7-3.3	$+\frac{2}{3}$	$\frac{1}{2}$
	down	d	4.1-5.8	$-\frac{1}{3}$	$\frac{1}{2}$
2	charm	c	$1.27^{+0.07}_{-0.09} \times 10^3$	$+\frac{2}{3}$	$\frac{1}{2}$
	strange	s	101^{+29}_{-21}	$-\frac{1}{3}$	$\frac{1}{2}$
3	top	t	$172.0 \pm 0.9 \pm 1.3 \times10^3$	$+\frac{2}{3}$	$\frac{1}{2}$
	bottom	b	$4.19^{+0.18}_{-0.06} \times 10^3$	$-\frac{1}{3}$	$\frac{1}{2}$

Table 2.1: Summary of fermions in the SM and some of their important properties [33]. The masses given in this table are expressed in natural units ($c = \hbar = 1$) in which energy, momentum and mass all share the same units (eV). The masses reported here are taken from the Particle Data Group (PDG) Review of Particle Physics. [33]. Charge is expressed in units of the fundamental charge (e). For each quark flavor shown there are three particles corresponding to the three colors: red, green and blue. For every fermion in the table there is a corresponding anti-fermion that is not shown.

Particle	Symbol	Mass (MeV)	Charge (Q/e)	Spin
photon	γ	0	0	1
gluons	$g_1 ... g_8$	0	0	1
$W^{\pm}$ bosons	$W^{\pm}$	$80.39 \pm 0.02 \times 10^3$	± 1	1
Z boson	Z	$91.188 \pm 0.002 \times 10^3$	0	1
Higgs boson	H	$125.09 \pm 0.21 \pm 0.11 \times 10^3$	0	0

Table 2.2: Summary of bosons in the SM and some of their important properties. There are eight gluons corresponding to the eight different combinations of color and anti-color (see Section 2.2.4). The Higgs boson mass is taken from the combined CMS-ATLAS results using 25 fb^{-1} of LHC data collected in 2011-2012 [34]. The masses reported for the other particles are taken from the Particle Data Group (PDG) Review of Particle Physics. [33] The masses given in this table are expressed in natural units ($c = \hbar = 1$) in which energy, momentum and mass all share the same units (eV).

2.2.1 QED

The part of the SM that describes the force of electromagnetism, known as Quantum Electrodynamics (QED), is based on the local gauge symmetry group $U(1)_Q$. This is the group of local gauge transformations whose fundamental representation is the set of 1×1 unitary matrices (complex numbers). The generator of this group of transformations is the operator Q which returns the electric charge of a particle field. Thus electric charge is the physical quantity that is conserved in QED according to Noether's theorem. The gauge field included in order to enforce this $U(1)_Q$ gauge symmetry is the electromagnetic field A^μ, for which the photon is the excitation [7]. All charged particles interact via exchange of photons.

2.2.2 Electroweak Theory

A QFT of the weak force on its own is not possible since it cannot account for the non-zero masses of the $W^{\pm}$ and Z bosons. In order to incorporate the weak force into the SM a single unified theory combining electromagnetism and the weak

[7] a μ superscript denotes a four-vector which has four components (μ = 0,1,2,3,)

force is needed. This theory, known as Elecroweak theory or Glashow-Weinberg-Salam (GWS) theory, is based on the gauge group $U(1)_Y \times SU(2)_L$. $U(1)_Y$ is the same gauge group as in QED except that the generator is associated with a different physical quantity known as weak hypercharge (Y). $SU(2)_L$ is the gauge group whose fundamental representation is the set of 2×2 unitary matrices with determinant one. The generators of this gauge group are the three components of weak isospin (T_1, T_2, T_3). $U(1)_Y \times SU(2)_L$ is the group of transformations formed from the tensor product of the transformations in the groups $U(1)_Y$ and $SU(2)_L$.

The chirality of a particle is a fundamental physical quantity related to the way it transforms under the parity operation which returns the mirror image of a particle. Chirality itself is rather abstract but it is closely related to another physical quantity called helicity which has a clear physical interpretation. Helicity is defined by the orientation of a particle's spin in relation to its direction of motion. A particle with its spin oriented in the same direction as its velocity is right-handed. A particle with its spin oriented opposite its velocity is left handed. For massive particles this is not an intrinsic property as it is not Lorentz invariant. The helicity of a particle is dependent on the frame of reference in which it is measured. For massless particles helicity is Lorentz invariant. In this case helicity and chirality are the same (i.e. a particle with left handed helicity also has left handed chirality). The L subscript in $SU(2)_L$ means that the transformations in this group apply only to left-handed particles (and right-handed antiparticles) [8]. This makes Electroweak Theory a chiral theory in which left-handed and right-handed particles interact differently.

In Electroweak theory left-handed fermions are grouped into pairs known as $SU(2)_L$ doublets. They are represented as two component vectors in weak isospin space where the first component has $T_3 = 1/2$ and the second has $T_3 = -1/2$. This is analogous to a spin 1/2 system in quantum mechanics where a particle is described by a two component ket vector in spin space with the first component representing the spin up state and the second representing the spin down state. An important difference is that each weak isospin state corresponds to a distinct particle. Within

[8] Here left handed and right handed refer to chirality

each generation the left-handed neutrino and charged lepton form a doublet and the two left-handed quarks form a doublet. This structure is repeated in all three generations.

$$\begin{pmatrix} \nu_e \\ e \end{pmatrix}_L \begin{pmatrix} \nu_\mu \\ \mu \end{pmatrix}_L \begin{pmatrix} \nu_\tau \\ \tau \end{pmatrix}_L \begin{pmatrix} u \\ d \end{pmatrix}_L \begin{pmatrix} c \\ s \end{pmatrix}_L \begin{pmatrix} t \\ b \end{pmatrix}_L \tag{2.1}$$

Right-handed fermions are $SU(2)_L$ singlets meaning that they transform trivially under an $SU(2)_L$ gauge transformation. For antiparticles the chiralities are reversed so that right-handed antiparticles are doublets and left-handed antiparticles are singlets.

Local gauge symmetry under $U(1)_Y \times SU(2)_L$ leads to four gauge fields denoted B^μ, W_1^μ, W_2^μ and W_3^μ. B^μ arises from the $U(1)_Y$ symmetry and the W_i^μ fields arise from the $SU(2)_L$ symmetry. W_1^μ and W_2^μ mix to produce the W_+^μ and W_-^μ gauge fields which are responsible for the $W^\pm$ bosons. W_3^μ and B^μ mix to produce the A^μ and Z^μ gauge fields that are responsible for the photon and the Z boson respectively. The mixing of the fields can be expressed as

$$W^\pm = (W_1 \mp W_2)/\sqrt{2}$$

$$Z = W_3 \cos\theta_W - B \sin\theta_W$$

$$\gamma = W_3 \cos\theta_W + B \sin\theta_W$$

where θ_W is the weak mixing angle also known as the Weinberg angle. The fact that only left-handed particles (and right-handed antiparticles) transform under the $SU(2)_L$ gauge group means that only left-handed particles (and right-handed antiparticles) interact by exchange of $W^\pm$ bosons (charged weak current) while both left-handed and right-handed particles interact interact via exchange of Z bosons (neutral weak current) and photons. Charged current interactions couple the fermions in each of the $SU(2)_L$ doublets described above. A fermion can change flavor within its $SU(2)_L$ doublet by giving off a $W^\pm$ boson. This is an important feature of Electroweak theory as it accounts for the flavor changing processes in nature such as nuclear beta decay ($d \rightarrow uW^-$).

Although flavor changing interactions are mostly confined within a generation they can change flavor across generations as well. The bottom row of fermions in the $SU(2)_L$ doublets in Eq. 2.1 are actually not the physical fermions observed in nature (the mass eigenstates) but rather weak isospin eigenstates which are linear combinations of the mass eigenstates. For quarks these two sets of eigenstates are related by the Cabibbo-Kobayashi-Maskawa (CKM) matrix. The CKM matrix is approximately equal to the identity matrix ($\mathbb{I}$) meaning that the mass eigenstates and weak isospin eigenstates are approximately equal. However the CKM matrix does have small non-zero off diagonal elements meaning that generation mixing is possible for charged weak current interactions of quarks. Since the off-diagonal elements are small compared to the diagonal elements, charged weak current interactions that change flavor across generations are rare compared to those that change flavor within a generation. Without generation mixing of quarks Electroweak theory could not explain the decay of the bottom quark. The bottom quark cannot decay within its generation since the top quark is too massive, making the process $b \rightarrow tW^-$ kinematically forbidden. The fact that it does decay means that generation mixing of quarks must be a part of the theory of weak interactions.

A gauge theory based on $U(1)_Y \times SU(2)_L$ symmetry that includes only fermion fields and the boson fields that arise from local gauge invariance cannot be a valid theory of the weak force. All the particles in such a theory are massless. Giving them mass directly in the Lagrangian destroys local gauge invariance. The gauge bosons are massless just as they are in QED, however the short range of the weak force means that the particles that mediate it ($W^{\pm}$ and Z bosons) must be massive. The massless fermions are a consequence of the chiral nature of the theory. This is unacceptable because it is well known from experiment that the SM fermions have mass. For these reasons the theory must be modified to allow for massive particles. These problems are resolved by an elegant mechanism that makes use of the idea of spontaneous symmetry breaking (SSB) known as the Englert-Brout-Higgs (EBH) mechanism.

2.2.3 The Englert-Brout-Higgs Mechanism

In order to construct a theory of the weak interactions with massive particles a scalar field Φ is added to the gauge theory described in the previous section. Φ is an $SU(2)_L$ doublet

$$\begin{pmatrix} \phi^+ \\ \phi^0 \end{pmatrix}$$

where ϕ^+ and ϕ^0 are complex fields with charge 1 and 0 respectively. A potential energy term for this new field given by

$$V(\Phi) = \mu^2\Phi^\dagger\Phi + \lambda(\Phi^\dagger\Phi)^2$$

where $\mu<0$ and $\lambda>0$, is added to the Lagrangian. This is the most general potential term that can be added while preserving the $SU(2)_L$ invariance and renormalizability of the theory. With this $V(\Phi)$ there is a non-vanishing expectation value for the field $\langle\Phi\rangle_0$ in the ground state (the physical vacuum). Moreover the vacuum expectation value (vev) of Φ is not unique but can take on an infinite number of values corresponding to a circle in two dimensional weak isospin space defined by

$$\mid \Phi \mid^2 = \Phi^\dagger\Phi = \phi^{1*}\phi^1 + \phi^{0*}\phi^0 = \nu/\sqrt{2}$$

where $\nu = \sqrt{-\mu^2/\mid\lambda\mid}$ is the minimum of V($\Phi^\dagger\Phi$). Selecting a particular value for the vev breaks the $SU(2)_L$ gauge invariance of the theory. By convention it is chosen to be

$$\langle\Phi\rangle_0 = \begin{pmatrix} 0 \\ \nu/\sqrt{2} \end{pmatrix}$$

In order to do calculations in perturbation theory it is necessary to redefine Φ in terms of fields that have zero vev. This is done with the following expression

$$\Phi(x) = exp\left(\frac{i\xi(x)\cdot\tau}{2\nu}\right)\left(\begin{array}{c} 0 \\ \frac{\nu+H(x)}{\sqrt{2}} \end{array}\right) \tag{2.2}$$

where $\xi_1(x)$, $\xi_2(x)$, $\xi_3(x)$ and $H(x)$ are real fields with zero vev. These real fields replace the real and imaginary components of ϕ^1 and ϕ^0 in expressing the four degrees of freedom of Φ. The Lagrangian written in terms of these real fields is no longer invariant under $U(1)_Y\times SU(2)_L$ transformations thus the symmetry has been spontaneously broken.

Goldstone's theorem states that whenever a continuous symmetry is spontaneously broken a massless scalar particle appears in the theory for each degree of freedom of the broken symmetry group. These are represented by the $\xi_i(x)$ fields in Eq. 2.2. When the broken symmetry is represented by a gauge transformation it is possible to remove these Goldstone bosons and in the process endow mass to the gauge bosons corresponding to the broken symmetry. By applying a gauge transformation with gauge $\xi(x)/\nu$ the $\xi_i(x)$ fields disappear from the Lagrangian and mass terms appear for the $W^\pm$ and Z bosons. The remaining scalar field $H(x)$ also gains a mass term as well as interaction terms with the $W^\pm$ and Z bosons. In order to give mass to the fermions in the theory a Yukawa term, coupling the fermion fields to Φ, is added to the Lagrangian for each fermion. When SSB happens these Yukawa terms lead to mass terms for the fermions and interaction terms between them and $H(x)$. No mass term or interaction terms appear for the photon field A^μ.

The EBH mechanism uses spontaneous symmetry breaking of a locally gauge invariant theory to produce a theory of electromagnetic and weak interactions in which the fermions and the carriers of the weak force are massive while the carrier of the electromagnetic force is massless. The massive scalar field $H(x)$ is a remnant of this process known as the Higgs boson. The fermions and the $W^\pm$ and Z bosons that couple to the Higgs boson effectively acquire mass while the photon, and the gluons to be discussed in the next section, that do not couple to it remain massless.

2.2.4 Quantum Chromodynamics

The QFT that describes the strong interactions is known as Quantum Chromodynamics (QCD). It is a gauge theory based on the symmetry group $SU(3)_C$. The C subscript stands for color charge, which is the generator of the group and the conserved quantity that arises due to Noether's theorem. The fundamental representation of this group is the set of 3×3 unitary matrices with determinant one. All quarks in the SM have color and are grouped into $SU(3)_C$ triplets. An $SU(3)_C$ triplet is a three component vector in color space consisting of three quarks of the same flavor but each of a different color. For the top quark the triplet is written

$$t = \begin{pmatrix} t_r \\ t_g \\ t_b \end{pmatrix}$$

where the indices stand for red, green and blue, the three values that color charge can take. Antiquarks exist in triplets where each component has anti-color ($\bar{r}$, $\bar{g}$, $\bar{b}$). There are eight gauge fields that are introduced to enforce $SU(3)_C$ symmetry. They correspond to the eight gluons that are the mediators of the strong force. Quarks and anti-quarks interact by exchanging gluons. In these interactions color may change but flavor does not. When a quark changes color the gluon that is given off carries away one unit of color and one unit of anti-color in order to conserve color charge. Since gluons have color they can also interact via exchange of gluons (self interactions).

Like the weak force, the strong force is a short range interaction. It is negligible on distance scales greater than $\sim 10^{-10}$ m which is the approximate size of a nucleus. The short range of the weak force is explained by the mass of the $W^{\pm}$ and Z bosons. In contrast electromagnetism has an infinite range because its carrier particle (the photon) is massless. In QCD the carrier particles (gluons) are also massless but despite this the strong force does not have infinite range. This is explained by a unique property of the strong force known as color confinement.

The coupling constants that determine the strength of each force are actually not constant but depend on the distance scale involved in the interaction. In the language of field theory they are referred to as running constants. This is true for all three SM forces however the dependence of the coupling constants on distance scale is different for each. In QED the coupling constant for electromagnetism decreases at larger distance scales. This is due to the polarization of the vacuum surrounding a charged particle. Virtual particle-antiparticle pairs are created out of the vacuum and then annihilate. The short lived particle-antiparticle pairs become polarized in the presence of the field of the charged particle. As a result the effective charge of the particle decreases due to a shielding effect similar to the way a charge particle in a dielectric material is shielded by the polarization of the medium. The coupling, which is proportional to the charge also decreases with distance.

In QCD color charge is also shielded by vacuum polarization due to virtual quark anti-quark pairs, however there is also an effect due to virtual gluon pairs. [9] The gluon pairs have the opposite effect as the quark anti-quark pairs, causing the color charge to increase with distance. Ultimately the contribution of the gluon pairs is stronger so the overall effect is that color charge and thus the strong coupling constant increases with distance. Although the coupling constant is itself dimensionless, its value depends on the energy scale of the interaction and this dependence leads to a characteristic energy scale for QCD known as Λ_{QCD}. This is the energy scale at which the strong coupling constant is approximately one and thus the limit above which perturbative QCD is no longer valid. Λ_{QCD} is $\sim$ 200 MeV [35]. In natural units energy corresponds to inverse distance. Intuitively more energetic collisions allow particles to reach shorter distances of separation. The distance scale that corresponds to Λ_{QCD} is $\sim$ a fermi (1 fm $= 10^{-15}$ m). On distance scales less than $\sim$ 1 fm the coupling constant is small enough that quarks and gluons interact very

[9] Virtual pairs of photons also appear out of the vacuum but do not contribute to vacuum polarization in QED since they are not charged.

little. This is known as asymptotic freedom. Above ~ 1 fm it increases very sharply with distance.

An important physical consequence of asymptotic freedom is that at small distance scales, or equivalently in high energy collisions, the coupling constant is small enough that perturbation theory can be applied to calculations in QCD. At larger distance scales, or lower energies, the coupling is greater than one so that higher order Feynman diagrams contribute more in calculations. This means lower order diagrams cannot suffice as approximations. However in high energy collisions of hadrons such as the proton-proton collisions at the LHC the interaction of partons via the strong force is weak enough that perturbative methods can be applied. In Electroweak theory perturbative methods can be applied on any energy scale since the couplings are always less than one. However the strength of the strong force made it unclear early in the development of QCD whether the perturbative approach would be valid. Asymptotic freedom guarantees that this approach is valid in the high energy regime, which is relevant for collider experiments such as ATLAS.

An important physical consequence of the sharp rise in the strong coupling constant around Λ_{QCD} is that quarks and gluons do not exist in isolation. They only occur in nature in bound states known as hadrons. Within these bound states, quarks and gluons, referred to collectively as partons, behave effectively as free particles. If a parton reaches a separation of ~ 1 fm from the other partons it will feel a tremendous force preventing it from breaking free from the hadron. Partons always combine in a unique way such that the hadrons they form are colorless. This is known as color confinement. There are two categories of hadrons known as baryons and mesons. Baryons consist of either three quarks (or anti-quarks) where each quark (anti-quark) has a different color (anti-color) so that the whole baryon is color neutral. Mesons consist of quark and anti-quark pairs with opposite color (e.g. $r\bar{r}$). All hadrons are color neutral.

Color confinement makes the study of QCD interactions far more complicated. Since bare quarks and gluons do not exist in nature the only option is to collide hadrons and interpret the results in terms of collisions of the partons which make them up. This is far more difficult than studying collisions of leptons (e.g. in an electron-positron collider such as LEP [10]) because it is not known exactly which partons collide nor what their collision energy is in a given hadronic collision. Hadrons are described by parton distribution functions (PDFs) that give the probability for each parton species they contain to have a given fraction of their overall momentum. Calculations of cross-sections in QCD make use of the factorization theorem which relates the cross-sections of parton-parton interactions to the measurable cross-sections of hadronic interactions using PDFs. The parton-parton cross-sections are calculable with perturbation theory provided the collisions are in the high energy regime defined by $Q^2 > \Lambda_{QCD}$, where Q^2 is the momentum transfer in the collision. PDFs are determined primarily from the results of deep inelastic scattering (DIS) experiments where probe particles (typically charged leptons such as electrons) are collided with hadrons [36].

When pairs of partons are produced in hadronic collisions they exist as free particles only very briefly. Once they reach $\sim$ 1 fm separation they experience a tremendous force due to the dramatic increase in the strong coupling constant. When the energy of the partons is large enough this causes new pairs of partons to be created from the potential energy in the gluon field. This process continues until the energy of the original partons is reduced enough that it can no longer produce new pairs. At this point all the partons combine into hadrons which are colorless in a process known as hadronization. The end result is that collider experiments do not detect free partons but rather narrow cones of hadrons referred to as jets. The momentum of the jet is related to the momentum of the original parton that produced it.

2.2.5 The Standard Model and Beyond

Combining Electroweak theory with QCD, the SM is a QFT based on $U(1)_Y \times SU(2)_L \times SU(3)_C$ gauge symmetry that incorporates three of the four forces of nature: electromagnetism, and the strong and the weak nuclear forces. Although

[10] The CERN Large Electron Positron Collider, decommissioned in 2001

the SM has been extremely successful in describing a wide variety of physical phenomena to high precision, there are aspects of the theory that are unsatisfactory. For this reason the SM is believed to be an approximation to a more fundamental theory that would resolve these problems naturally. Theories that are extensions to the SM that attempt to resolve one or more of the problems affecting it are referred to as Beyond the Standard Model (BSM) theories. In a BSM theory the SM emerges as a low energy approximation.

The SM is aesthetically unpleasing because of the large number of free parameters. The values of these parameters are not predicted by the theory and so must be measured in experiment. There are 19 free parameters in the SM. These include the three coupling parameters g, g' and g_s. These degrees of freedom are often expressed as the fine structure constant α, the Weinberg mixing angle θ_W and the strong coupling constant α_s

$$\begin{aligned} \alpha &= \frac{e^2}{4\pi} = \frac{g^2 g'^2}{4\pi(g^2 + g'^2)} \\ \sin^2\theta_W &= \frac{g'^2}{(g^2 + g'^2)} \\ \alpha_s &= \frac{g_s^2}{4\pi} \end{aligned}$$

The remaining parameters are the nine fermion masses (assuming massless neutrinos [11]), the three mixing angles and the CP-violating phase of the CKM matrix, the vev of the Higgs potential, the Higgs mass and the QCD vacuum angle θ which appears in the CP-violating term in the QCD Lagrangian. The large number of parameters in the SM that must be put in by hand in order to have agreement between its predictions and experimental measurements is seen as a shortcoming of the theory.

The SM also fails to explain a number of features of the universe including the force of gravity, the existence of dark matter and the matter anti-matter imbalance.

[11] In the SM neutrinos are massless however the observation of neutrino oscillations means that they must have some non-zero, albeit small mass. Experimental upper limits on their mass are given in Table 2.1

Every attempt to formulate a QFT of gravity has failed. In every case the theory proved to be non-renormalizable meaning that calculations of physical quantities diverge to infinity. The principle of local gauge invariance of quantum fields has been used to explain three of the four forces of nature but so far it has not been able to account for gravity. In order to explain all the fundamental forces of nature in a single mathematical framework a QFT of gravity must be added to the SM. A large body of evidence in astrophysics, including the rotation curves of galaxies and galaxy clusters, show that $\sim 26.8\%$ of the matter and energy in the universe is composed of matter that neither emits nor radiates light. Excluding the energy component this corresponds to approximately 84.5% of the matter in the universe. [8]. In order to account for this the SM would need a stable neutral particle with sufficiently large mass. However the only stable neutral particles in the SM are the photon and the gluons, which are all massless, and the neutrinos which are not massive enough to explain the gravitational effects of dark matter. The dominance of matter over anti-matter in the universe is a problem because the SM is approximately symmetric with respect matter and anti-matter. The majority of physical processes are invariant to the charge conjugation transformation that replaces particles with anti-particles. This means that particles and anti-particles should be produced in roughly equal proportions in nature. There are some CP-violating processes in the SM but not enough to account for the observed difference in the amount of matter and antimatter in the universe. Each of these problems with the SM represent conflicts between its predictions and experimental observations.

One of the most interesting and least understood features of particle physics is the enormous difference in the strength of the fundamental forces. The forces are given in Table 2.3 along with an approximate measure of their strength [37]. Within the SM the strength of each force is set by the coupling constants which are free parameters. Therefore an understanding of why each force has the strength it does is missing. However this is essentially a restatement of the problem mentioned above of the large number of free parameters in the SM. Furthermore while there is significant variation in the strength of the SM forces this is dwarfed by the difference in their strength and the strength of the force of gravity. The weakest force in the SM (the weak nuclear force) is about 30 orders of magnitude stronger than the force of gravity. The electroweak energy scale typical of processes in Electroweak theory is $\sim 10^2$ GeV. The energy scale at which gravity would be approximately as strong as the SM forces, known as the Planck scale, is $\sim 10^{19}$ GeV. The unknown origin of this tremendous difference in scale is known as the hierarchy problem.

Force	Strength
strong	10
electromagnetic	10^{-2}
weak	10^{-13}
gravity	10^{-42}

Table 2.3: The values shown in this table are an arbitrary dimensionless measure of the strength of the fundamental forces. The actual strengths depend on the particles involved and the distance between them. The precise values are not important. Rather what matters is the order of magnitude of the difference between them. [37]

The problem is made worse if we consider the effect of quantum fluctuations. The mass of the $W^{\pm}$ and Z bosons and strength of the weak force are all determined by the value of the vacuum expectation value (vev) of the Higgs field $\langle\Phi\rangle_0$ (see Section 2.2.3). The measured value of the Higgs vev, which sets the Electroweak energy scale, is 246 GeV [38]. The expression for the Higgs vev in QFT involves a term known as the bare vev which is a free parameter and a correction term that derives from quantum fluctuations. The correction term is enormous. In order for the physical vev to match the value measured in experiment the bare vev must be very large in the opposite direction to balance the correction term. Thus not only is there an very large difference between these two fundamental energy scales but one of the parameters of the SM must be fine tuned in order to be consistent with it.

The hierarchy problem represents one of the more serious failures of the SM and many BSM theories have been developed to try to remove the necessity of fine tuning in a natural way. [12–30] Among these BSM theories are the little Higgs and composite Higgs theories. In addition to resolving the hierarchy problem these theories also predict the existence of vector-like quarks.

2.3 Vector-Like Quarks

Vector-like quarks (VLQ) are predicted in many theories beyond the SM that attempt to resolve or mitigate the hierarchy problem. They are distinct from SM quarks, and indeed all SM fermions, in that they are non-chiral. This means that the left-handed and right-handed components of VLQs transform identically under SU(2). In the SM, left-handed fermions appear in weak isospin doublets (isodoublets) with the other quark or lepton in their generation. These isodoublets are shown in Eq. 2.1. Right-handed SM fermions are isosinglets. As a consequence only left-handed fermions couple to $W^{\pm}$ bosons while both chiralities couple to the Z boson. In contrast to this, both left-handed and right-handed VLQs have the same structure in weak isospin space and thus both chiralities interact in the same way under the weak force. VLQs can occur as either isosinglets, isodoublets or isotriplets. In each case however the same $SU(2)_L$ structure describes the left-handed and right-handed components of each VLQ field.

The term 'vector-like' quark refers to the coupling of VLQs to the W boson. In the SM, quarks couple to the W boson with a vertex factor $\gamma_\mu(1 \pm \gamma_5)$ where the sign is determined by the chirality of the quark. $(1 - \gamma_5)$ and $(1 + \gamma_5)$ are the projection operators that make the W interact only with the left-handed or right-handed component respectively. This is known as a vector minus axial vector (V-A) or vector plus axial vector (V+A) coupling. Since both chiralities of VLQs interact with the W the vertex factor is the combination of both V-A and V+A. The axial vector pieces cancel leaving a simple vector current coupling.

An important property of VLQs which follows from their non-chiral nature is that their mass is not generated by the EBH mechanism and so is not connected to electroweak symmetry breaking. The chiral nature of the SM fermions is exactly what makes them massless in the unbroken $U(1)_Y \times SU(2)_L$ gauge theory before SSB. Inserting a mass term in the Lagrangian directly would destroy local gauge symmetry as such terms are not invariant under $SU(2)_L$ transformations. The non-chiral nature of VLQs mean that their mass terms are $SU(2)_L$ invariant and so can be included in the Lagrangian directly. This is particularly important as it means that the mass of VLQs is not constrained by the Higgs sector.

Chiral fourth generation quarks are also predicted in some BSM theories and searches have been carried out in ATLAS and CMS [39, 40]. In fact the analysis containing the VLQ search described in this dissertation also contains a search for a chiral fourth generation quark of charge -1/3 (b'). However the existence of such a quark is highly constrained by the recent discovery of the Higgs boson with a mass of 125 GeV. If this particle is the SM Higgs, a fourth generation of chiral fermions would greatly enhance the Higgs production cross-section. A chiral fourth generation with two additional heavy quarks would increase the effective ggH coupling by roughly a factor of three, and hence increase the production cross-section $\sigma_{gg\to H}$ by a factor of nine [41]. This is because of additional fermion loop diagrams for the new quarks in the gluon fusion $gg \to H$ which is the leading Higgs production mechanism at the LHC. The contributions from these additional diagrams would be large due the large mass of the fourth generation quarks. This conflicts with the cross-section measurements produced by ATLAS and CMS [4,42]. Therefore under the assumption of a minimal Higgs sector (the SM Higgs doublet only) fourth generation chiral fermions are ruled out [43–48]. If the new particle discovered at 125 GeV is a manifestation of a broader Higgs sector, as in the Two Higgs doublet models [49], fourth generation chiral quarks are allowed. For this reason searches for such particles are still carried out. However VLQ searches are more highly motivated since they are not constrained at all by the Higgs sector.

The allowed $SU(2)_L$ representations for VLQs and their conserved charges under the $U(1)_Y$, $SU(2)_L$ and $U(1)_Q$ gauge groups are summarized in Table 2.4. Depending on the model in which they occur they are either isosinglets, isodoublets or isotriplets. The electric charge of VLQs can either follow the pattern of the SM quarks (i.e. 2/3 for up-type quarks and -1/3 for down-type quarks) or take on more exotic values. T and B represent the vector-like top and bottom with electric charge

2/3 and -1/3 respectively. $T_{5/3}$ and $B_{-4/3}$ represent VLQs with electric charge of 5/3 and -4/3 respectively. In the case of isosinglets there are two vector-like quarks, T and B. When they appear as isodoublets two scenarios are possible. Either T and B exist together in an isodoublet, or each is part of a separate isodoublet with $T_{5/3}$ or $B_{-4/3}$. When they appear as isotriplets T and B are part of an isotriplet with either $T_{5/3}$ or $B_{-4/3}$.

	SM quarks	VLQ Singlets	VLQ doublets	VLQ triplets
	$\begin{bmatrix}u\\d\end{bmatrix}_L$ $\begin{bmatrix}c\\s\end{bmatrix}_L$ $\begin{bmatrix}t\\b\end{bmatrix}_L$	T B	$\begin{bmatrix}T_{5/3}\\T\end{bmatrix}$ $\begin{bmatrix}T\\B\end{bmatrix}$ $\begin{bmatrix}B\\B_{-4/3}\end{bmatrix}$	$\begin{bmatrix}T_{5/3}\\T\\B\end{bmatrix}$ $\begin{bmatrix}T\\B\\B_{-4/3}\end{bmatrix}$
$SU(2)_L$	(left) T_3 = 1/2, -1/2 (right) $T_3 = 0$	$T_3 = 0$	T_3 = 1/2, -1/2	T_3 = 1, 0, -1
$U(1)_Y$	(left) $Y = 1/3$ (right) Y = 4/3, -2/3	Y = 4/3, -2/3	Y = 7/3, 1/3, -5/3	Y = 4/3, -2/3
$U(1)_Q$	Q = 2/3, -1/3	Y = 2/3, -1/3	Y = 5/3, 2/3, -1/3	Y = 2/3, -1/3, -4/3

Table 2.4: Summary of the different $SU(2)_L$ representations for VLQs with their conserved charges under the $U(1)_Y$, $SU(2)_L$ and $U(1)_Q$ gauge symmetries. The far left column shows the corresponding values for the SM quarks. the third component of isospin (T_3) and weak hypercharge (Y) are related by $Q = T_3 + Y/2$.

BSM theories that contain VLQs include Yukawa terms that couple them to the Higgs boson. In addition, there are interaction terms that couple them to the $W^\pm$ and Z bosons. In the case of the VLQ isosinglet models, the $W^\pm$ terms don't arise from the kinetic term for the VLQ fields, as they do for SM fields, since their covariant derivative doesn't contain an $SU(2)_L$ term. However the mixing of the $SU(2)_L$ gauge eigenstates with the mass eigenstates (described in Section 2.2.2) now includes the VLQs, making the CKM matrix 3×4. When the gauge eigenstates are expanded in terms of the mass eigenstates interactions terms appear for $W^\pm$ that mix the singlet VLQs with SM quarks. For the isodoublet and isotriplet models these terms combine with the terms arising from the covariant derivative to give the full charged weak current interaction term. The allowed decay modes for VLQs are

$$\begin{aligned} &T \rightarrow W^{+}b, T \rightarrow Zt, T \rightarrow Ht, \\ &B \rightarrow W^{-}t, B \rightarrow Zb, B \rightarrow Hb, \\ &T_{5/3} \rightarrow W^{+}t, \\ &B_{-4/3} \rightarrow W^{-}b, \end{aligned} \tag{2.3}$$

In general VLQs couple to all SM quarks, however it has been shown [50] that the mixings are of order m/M for isosinglet and isotriplet VLQs and $(m/M)^2$ for isodoublet VLQs, where m and M are the masses of the SM and vector-like quarks respectively. Therefore, due to the significantly larger mass of the SM quarks in the third generation compared with the lower generations, it is expected that VLQs couple primarily to the third generation. For the analysis described in this dissertation only decays to third generation SM quarks are considered.

The probability that a VLQ will decay in a particular mode is given by the branching ratio (BR) for that decay mode. The BRs for each of these decay modes depend on the model considered and the VLQ mass. Plots showing the BRs for T and B in the singlet and doublet models are shown in Fig. 2.4 [51]. For the singlet model the BR for charged decay is about 0.5 while the BR for neutral decays through Z and H are each about 0.25. This is only approximate as the true BRs vary with mass. In the doublet model (T,B), for T the charged decay mode is not permitted while for B it is the only decay mode allowed. For the doublet model $(T_{5/3}, T)$ the BRs for T decay are the same as those for the doublet model (T,B) while the $T_{5/3}$ decays exclusively to $W^{\pm}t$. In the doublet model (B,$B_{-4/3}$) for B the charged decay is not permitted and the BRs to Z and H are each approximately 0.5. $B_{-4/3}$ decays exclusively to $W^{-}b$.

VLQs can be produced at the LHC both in pairs via QCD and singly via QCD and the weak force. Figure 2.7 shows the pair-production of VLQs via gluon fusion followed by the decay of each VLQ into a W, Z or H boson and a third generation SM quark. VLQ pairs can also be produced by quark anti-quark annihilation however

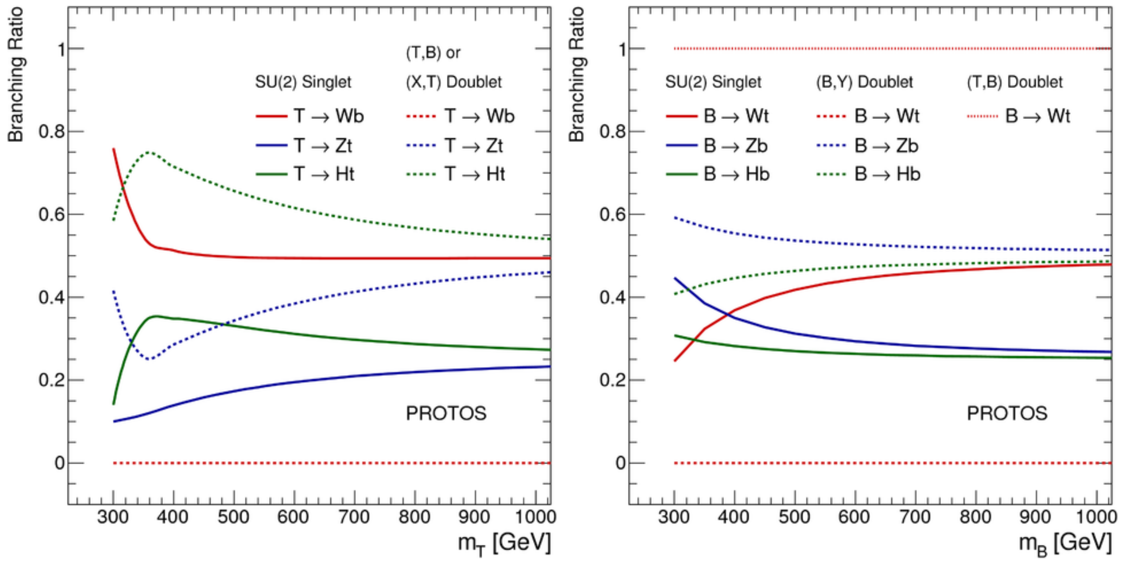

Figure 2.4: Branching ratios for decay of vector-like top (T) and vector-like bottom (B) for the singlet and doublet models [51]. For each model the three branching ratios add to one. In these plots X and Y represent $T_{5/3}$ and $B_{-4/3}$ respectively.

gluon fusion dominates at LHC energies This is because the parton distribution function is larger for gluons than anti-quarks in this regime. Figure 2.6 shows the Feynman diagram for single production of the vector-like quark $T_{5/3}$.

The cross-section for pair-production is independent of the VLQ model and depends only on mass. In fact, it is the same for pair-production of all new heavy quarks including fourth generation chiral quarks. This is because the differences between the various models of new heavy quarks are only related to the weak force and have no effect on how they interact with the strong force. In contrast to this, single production relies on the weak force so the cross-sections depend on the specific model considered. Figure 2.7 shows the cross-section versus mass for pair-production and single production for each of the VLQs discussed above. In the low mass range pair-production dominates simply because the strong coupling constant is greater than the weak coupling constant. At higher masses the kinematics cause the cross-section for pair-production to fall much faster than for single production. In hadronic collisions cross-sections generally fall with mass because it requires more energy to make a more massive particle. The probability of having a collision of partons with sufficient energy to produce a particle is less the more massive the particle. This effect is stronger for pair-production since there must be enough energy to produce two particles rather than one. For each VLQ there is a mass beyond which the effect of kinematics overcomes the stronger coupling constant so that single production becomes dominant.

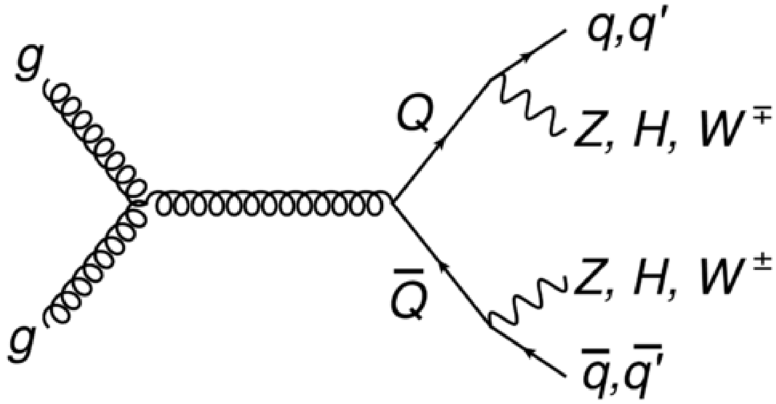

Figure 2.5: Feynman diagram showing the pair-production of vector-like quarks (VLQ) by gluon fusion and the range of different possibilites for their decay. Each VLQ decays first to a $W^{\pm}$, Z or H boson and a third SM quark. With the deay of these particles the system has an extremely rich variety of final states. [52]

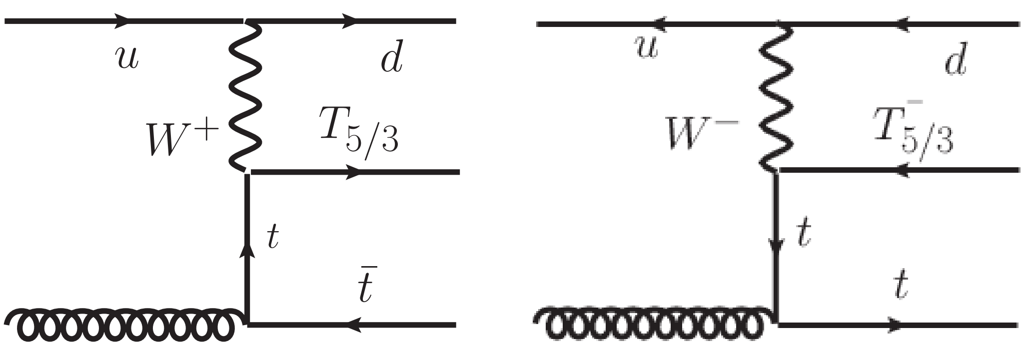

Figure 2.6: Feynman diagrams for single production of $T_{5/3}$

After the decay of the VLQs their decay products decay further, giving rise to a huge variety of different final states. These final states can contain multiple leptons, and a large number of jets, including many b-jets. A number of these final states are interesting because they have small SM background. In particular, events

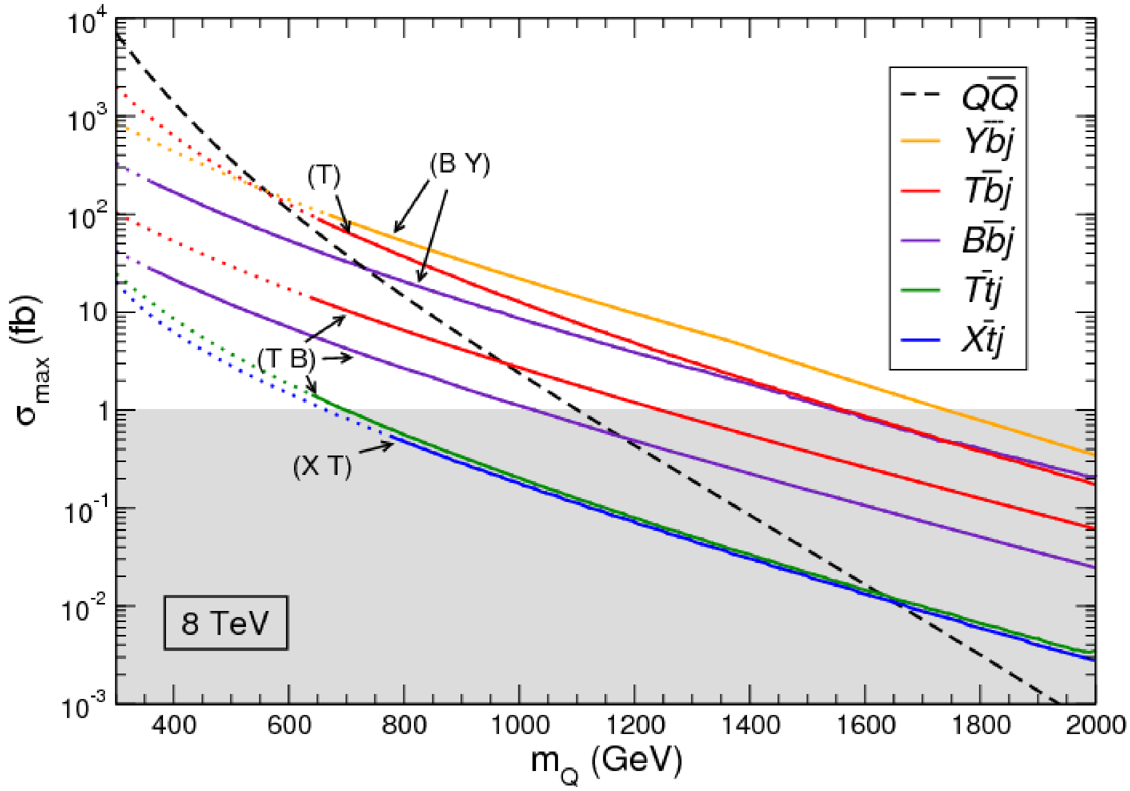

Figure 2.7: Cross-sections for pair-production and single production of vector-like quarks (VLQ) as a function of VLQ mass at $\sqrt{s} = 8$ TeV. The single production curves are shown for a variety of different VLQ models. X and Y represent the VLQs referred to as $T_{5/3}$ and $B_{-4/3}$ in the text. The dotted part of the line indicate the mass range already ruled out by direct searches. The shaded area corresponds to cross-sections below 1 fb, uninteresting for the integrated luminosity of ≈ 20 fb^{-1} collected in 2012 with the ATLAS detector . [53]

containing lepton pairs with the same electric charge are produced very rarely in the SM. The number of such events would be greatly enhanced by the existence of VLQs. Consider for example the pair-production of vector-like bottom quarks where each B decays to a W boson and a top quark. When the top quarks decay the event contains four W bosons and two b-jets ($B\bar{B} \to W^+W^-t\bar{t} \to W^+W^-W^+W^-b\bar{b}$). If either of the W bosons with the same sign decay leptonically the final state will contain a same-sign dilepton pair. Another final state that has very low SM background but a large potential contribution from VLQs is the trilepton final state. In the above example, if any three of the W bosons decayed leptonically the event would contain three leptons and two b-jets. With the exception of $T\bar{T} \rightarrow W^{+}bW^{-}\bar{b}$ all the decay modes shown in Eq. 2.3 can give rise to trilepton and same-sign dilepton events. These final states represent interesting signatures that are ideal for the search for VLQs since they are not produced often in the SM. For the search described in this dissertation $\mathrm{B}_{-4/3}$ is not considered since it cannot produce either of these final states. Single production is considered only for $\mathrm{T}_{5/3}$ since it is the only VLQ that can produce a same-sign dilepton pair when produced singly. An important parameter that affects the single production cross-section is the coupling constant λ between $\mathrm{T}_{5/3}$ and Wt. This coupling is related to the mixing parameter g^{*} used by the model [54, 55]: $\lambda = M_{T_{5/3}} g g^{*} / \, m_{W}\sqrt{2}$. Three scenarios for the $\mathrm{T}_{5/3}$ are considered in this analysis: pair-production only ($\lambda = 0$) and a combination of single and pair-production with two different values of the coupling ($\lambda = 0.5$ and 1.0).

CHAPTER 3

Experimental Apparatus

The Large Hadron Collider (LHC) is the most powerful particle accelerator ever built. It was designed to collide proton-proton pairs and heavy ion pairs (Pb-Pb) at high energies and luminosities. ATLAS (A Toroidal LHC Apparatus) is one of the six detectors located along its circumference used to study the collisions in order to perform high precision tests of the Standard Model and search for evidence of new rare physics. The high energy of the LHC combined with the incredible precision of ATLAS has allowed physicists to probe the Standard Model further than ever before. The LHC and ATLAS ran from 2009 to 2012 (Run 1) at progressively higher energies finally reaching the unprecedented energy of 8 TeV in 2012. The data collected during Run 1 was used, among other things, to discover the Higgs Boson, which was the last remaining piece of the Standard Model that had yet to be discovered. [4, 5] This phenomenal achievement of the ATLAS and CMS collaborations led to the awarding of the Nobel prize the following year to Peter Higgs and Francois Englert for the theoretical prediction of the particle nearly forty years earlier. [6, 7]

The search for vector-like quarks described in this thesis uses data collected at the LHC with ATLAS in 2012. The LHC was then shutdown from February 2012 till early 2015 for scheduled maintenance and upgrades, to prepare it for reaching its full design energy of 14 TeV. This scheduled shutdown period is referred to as Long Shutdown 1 (LS1) as it is the first in a series of three shutdowns planned over the life of the LHC. This chapter presents an overview of the LHC and ATLAS experiment. There is also a description of the data quality monitoring of part of the ATLAS muon spectrometer known as the Cathode Strip Chambers (CSCs).

3.1 Large Hadron Collider

The LHC [56, 57] is a circular synchrotron collider, 27 km in circumference and 100 meters underground. Located at CERN outside Geneva on the French-Swiss border it occupies the same tunnel used for the LEP (Large Electron-Positron Collider) which was decommissioned in 2001. It was designed to collide proton-proton pairs at a center-of-mass energy of 14 TeV and a luminosity of 10^{34} cm^{-2} s^{-1}. This collision energy and luminosity far exceed that of the Tevatron at the Fermi National Accelerator Laboratory which was the most powerful collider in the world prior to the construction of the LHC. The collision energy is seven times that of the Tevatron and the luminosity exceeds the peak luminosity of the Tevatron by two orders of magnitude. The Tevatron operated from 1983 to 2012 and made a number of important contributions to particle physics including the discovery of the top quark in 1995 [58]. The higher luminosity of the LHC means that it will produce far more collisions. The higher energy means that there is a higher probability of producing interesting events with signs of new physics. The combination of high energy and luminosity means that the LHC has tremendous potential both as a tool for precision measurement and discovery.

The layout of the LHC is shown in Fig. 3.1. It consists of eight arcs and eight straight sections called insertions. The insertions are used both for crossing the beams at the interaction points and other important utilities such as beam injection, cleaning and dumping. The center of each of the insertions are labeled point 1 through point 8 with ATLAS located at point 1. The eight regions between adjacent points are called sectors. The sectors are the primary working units of the LHC. Each sector is powered separately and the bending magnets in each sector are connected together in series and enclosed in the same continuous cryostat.

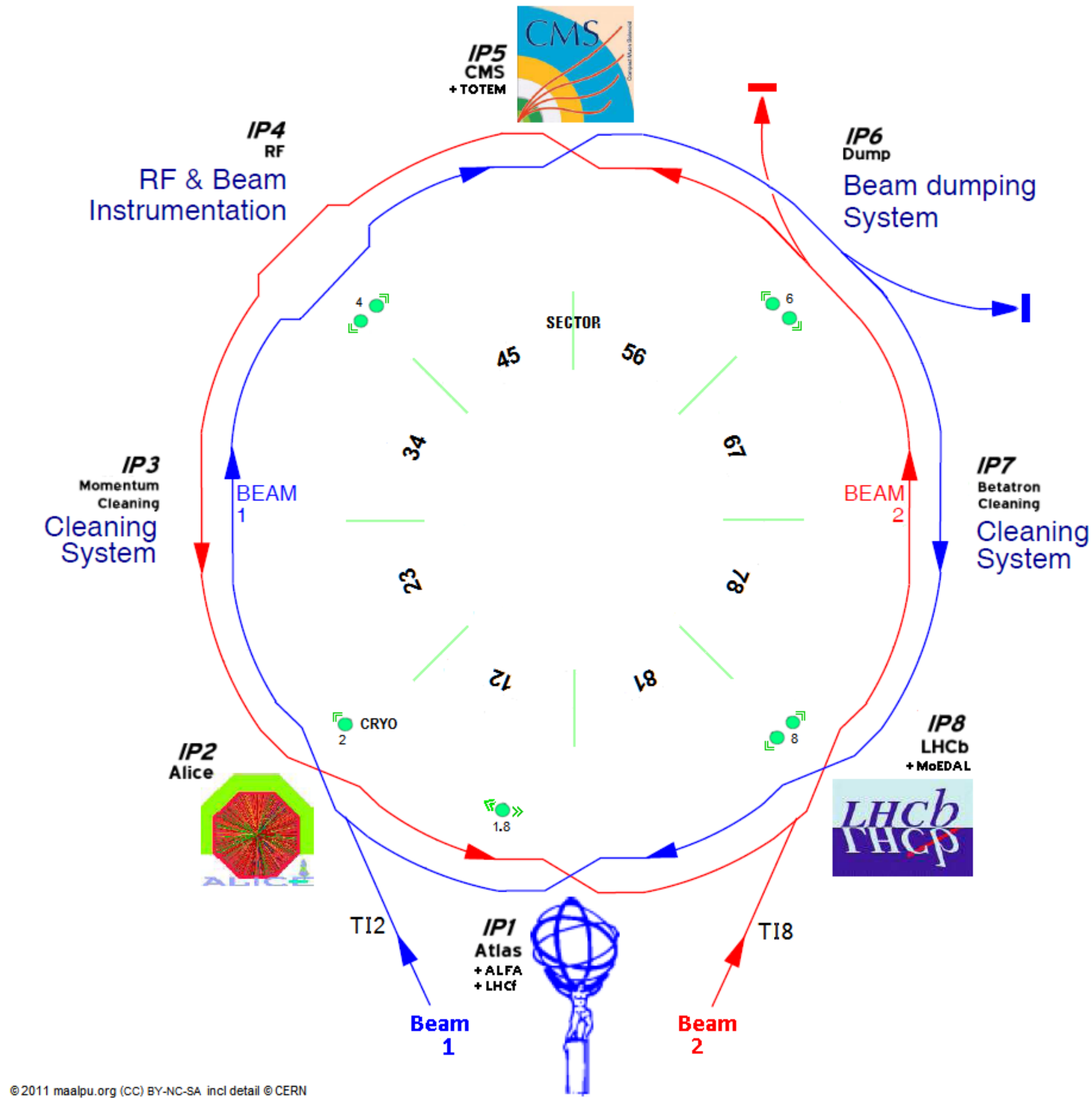

Figure 3.1: Layout of the LHC with four interaction points. [59]

There are six major experiments at the LHC. ATLAS and CMS (Compact Muon Solenoid) are the two general purpose detectors designed to collect data for a broad range of different analyses with very different final states. Both experiments are involved in a wide variety of searches including searches for supersymmetric particles, new heavy particles such as vector-like quarks and of course both contributed to the Higgs discovery. They are located at diametrically opposite sides of the LHC at point 1 and point 5 respectively. The remaining four experiments are specialized to study specific areas of particle physics. ALICE (A Large Ion Collider Experiment), located at point 2, is used to study collisions of heavy lead ions in order to investigate the nature of the quark-gluon plasma (QGP), which is believed to have existed in the early universe before temperatures cooled enough for hadrons to form. LHCb, located at point 8, is used to study heavy flavor hadrons, in particular hadrons containing b-quarks with the aim of measuring parameters of CP violation which could help explain the matter-antimatter asymmetry of the universe. LHCf is devoted to studying the particles scattered in the very forward direction at point 1. It consists of two detectors on either side of the interaction point at a distance of 140 m. Because of the large distance, LHCf can share point 1 with ATLAS which surrounds the interaction point at a much closer distance. Its goal is to measure the number and energy of pions produced in the collider which could help to explain the origin of ultra high energy cosmic rays. Finally TOTEM is dedicated to the measurement of the complete proton-proton cross-section at the LHC and shares point 5 with CMS.

A complex system known as the LHC injector chain [60] is used to produce the proton beams and accelerate them to an energy of 450 GeV before they enter the LHC. A schematic of the injector chain is shown in Fig. 3.2. The protons are first isolated from hydrogen gas using a duoplasmatron ion source. In the duoplasmatron source a cathode filament ejects electrons which pass through a vacuum chamber partially filled with hydrogen gas. The electrons break the hydrogen molecules H_2 into their constituent protons and electrons. The protons are then accelerated through a 90 KV potential difference to produce an ion beam. The beam is then sent to a radio frequency (RF) cavity where it is accelerated to 750 KeV and then passed to a linear accelerator (LINAC) known as LINAC2 where it is brought to 50 MeV. It then passes through a series of three synchrotrons known as the Proton Synchrotron Booster (PSB), the Proton Synchrotron (PS) and the Super Proton Synchrotron (SPS) where its energy is increased in steps to 1.4 GeV, 25 GeV and 450 GeV before it is injected into the LHC where it is accelerated to its final collision energy.

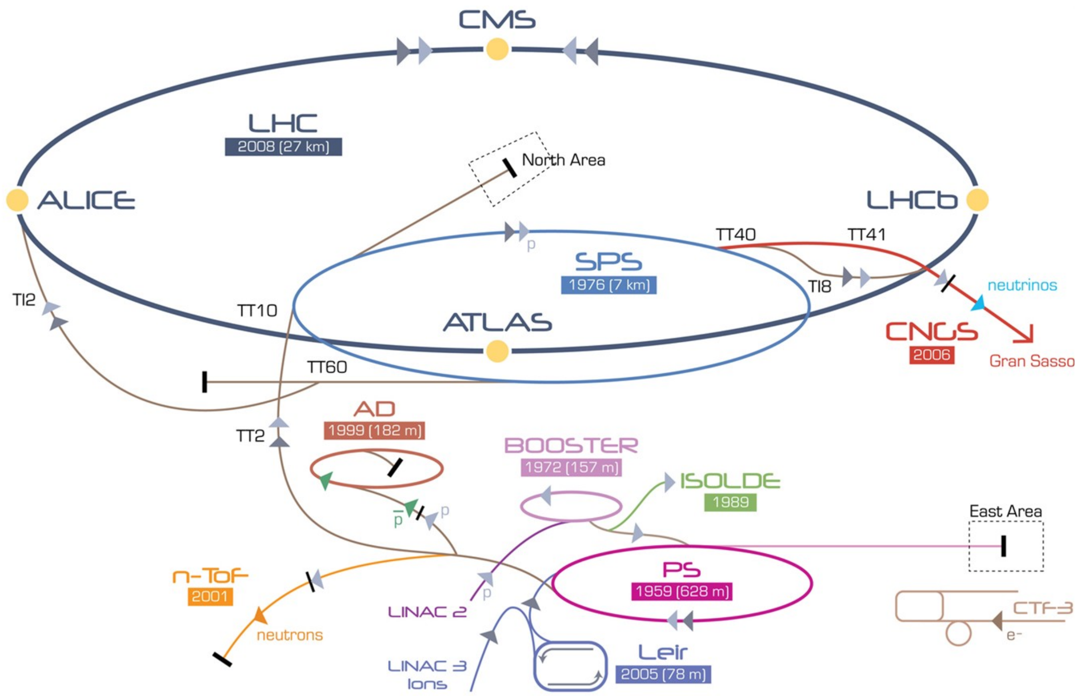

Figure 3.2: Schematic diagram of the LHC and LHC injector chain. [61]

One of the crucial design elements of the LHC is the use of superconducting magnets to bend the proton beams into their nearly circular paths and to focus them to a small cross-sectional area in order to maximize the probability of collisions at the interaction points. Higher beam energies require stronger fields to bend the beam within a fixed circumference. Thus very strong magnetic fields are needed to achieve the design energy of 14 TeV. The magnets use superconducting niobium-titanium (NbTi) cooled with superfluid liquid helium to 1.9 K and produce magnetic fields in the range 8-8.5 T. For reference the magnets used in the previous generation of colliders including the Tevatron and LEP did not exceed 5 T. There are approximately 6,700 magnets in the LHC. 1232 of these are dipole magnets located in the arc sections used for steering the beam. Figure 3.3 shows a three dimensional cut away view of the dipole magnets. The remainder are higher pole magnets such as quadrupole, sextupole, octupole, decapoles etc. They are located in the insertions and are used for focusing the beam and other purposes such as canceling horizontal

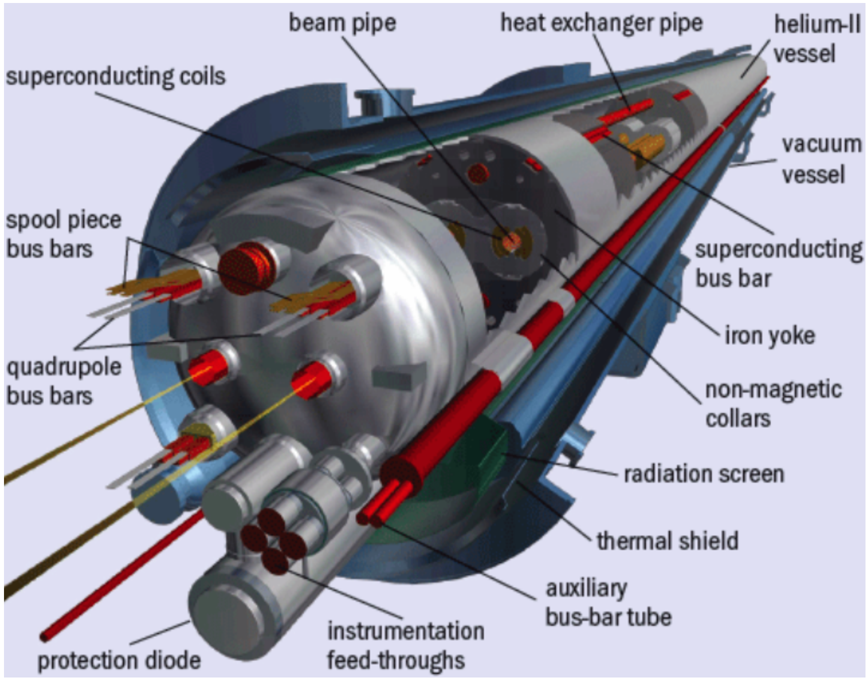

Figure 3.3: Cut away view of the LHC dipole magnets used for steering the proton beams. [62]

dispersion arising in the arc and deflecting the beam in order to dump it when data taking is finished.

RF cavities are used inside each of the synchrotrons in the chain as well as the LHC itself to accelerate the beam. An RF cavity is a metallic chamber containing a resonant electromagnetic field. An RF power supply is used to produce oscillating electromagnetic fields which form a standing wave inside the cavity. The size and shape of the cavity are designed to produce resonance at a particular frequency. The timing of the passage of the protons through the chamber and the oscillation of the field is critical. The ideally timed proton, with exactly the right energy, will see zero accelerating voltage when the LHC is at full energy. Protons with slightly different energies arriving earlier or later will be accelerated or decelerated so that they stay close to the energy of the ideal particle. In addition to accelerating the beam the RF cavities are also responsible for separating it into bunches of protons and squeezing the bunches to shorter lengths along the direction of the beamline. This increases the density of protons in each bunch and thus the probability of having collisions when the beams intersect. The RF cavities in the LHC are centered around point 4. There are two systems, one for each beam, each containing eight superconducting RF cavities operating at 4.5 K and 400 MHz. At the peak luminosity of 10^{34} cm^{-2} s^{-1}, there are 2808 bunches per direction in the LHC, and each bunch contains 10^{11} protons. The bunches are a few centimeters in length in the z-direction and 16 μm in radius in the transverse direction. Pairs of bunches cross at each of the four interaction points every 50 ns.

3.2 ATLAS Detector

The ATLAS (A Toroidal LHC Apparatus) detector is a cylindrical detector oriented with its symmetry axis along the beamline of the LHC and the interaction point of point 1 at its center [63–66]. It consists of a magnet system and three detector systems which are used to identify particles produced in collisions at the interaction point and measure their energy and momentum. The size and layout of the detector are shown in Fig. 3.4. The inner detector (ID) is closest to the beamline, followed by the calorimeter and then the muon spectrometer (MS). A superconducting solenoid magnet and three superconducting toroid magnets are used to produce magnetic fields to bend charge particles in the inner detector and muon spectrometer. The solenoid magnet is a cylinder centered on the beamline located between the inner detector and the calorimeter. The three superconducting toroid magnets surround the muon spectrometer in the barrel and end-cap regions. The inner detector measures the tracks of charged particles in the presence of the magnetic field of the solenoid. It's used both to identify particles based on their curvature in the magnetic field and to measure their momentum. The calorimeter is used to measure the energy of particles such as electrons, photons and hadrons. The muon spectrometer provides an additional measurement of the momentum of muons, which are not absorbed in the calorimeter, by reconstructing their tracks in the magnetic field of the toroid.

The geometry of ATLAS is described by a right handed coordinate system with

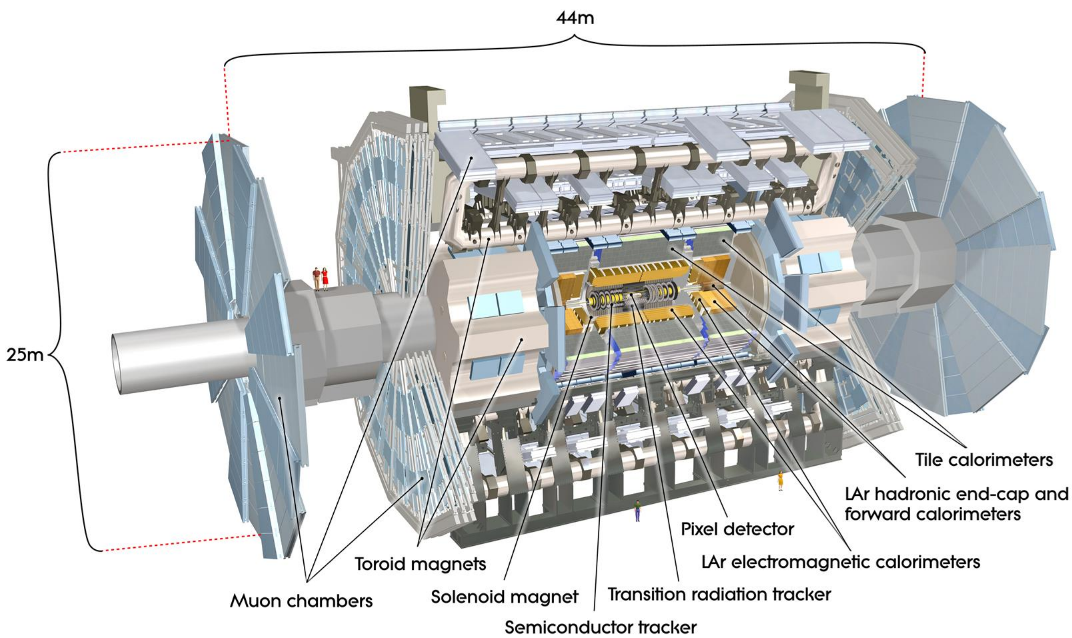

Figure 3.4: Cut-away view of the ATLAS detector. The detector is 25 m in height, 44 m long and weighs approximately 7000 tons. [67]

its origin at the interaction point. The z-axis is along the beamline with positive z pointing from point 1 to point 8. The x-axis points toward the center of the LHC ring and the y-axis points upward. Because of their azimuthal symmetry a cylindrical coordinate system is used to describe the trajectories of the final state particles. In this system the particle's momentum is expressed by giving its radial component, also known as its transverse component p_{T}, its azimuth ϕ and its pseudorapidity η. Here the pseudorapidity is given rather than the z-component which is typically given in a cylindrical coordinate system. The pseudorapidity is related to the polar angle by

$$\eta = -\ln[\tan(\theta/2)] \tag{3.1}$$

The pseudorapidity is zero in the transverse direction and diverges toward infinity in the forward direction (i.e. along the z-axis). It is used instead of the polar angle because differences in pseudorapidity ($\Delta\eta$) are Lorentz invariant and because it is convenient for plotting the angular distribution of particles produced in coillsions. Particle production is generally constant as a function of η while it tends to be sharply peaked close to zero as a function of the polar angle θ.

The performance goals of the different detector systems in ATLAS are shown in Fig. 3.1. For the inner detector and muon spectrometer the requirement is on the resolution of the transverse momentum σ_{p_T}/p_T which can be expressed as

$$\frac{\sigma_{p_{\mathrm{T}}}}{p_{\mathrm{T}}} = \frac{\sigma_s}{s} = \frac{p_{\mathrm{T}}\sigma_s}{L^2 B} \tag{3.2}$$

where s is the sagitta of the particle track, B is the magnetic field and L is the length of the arc of the track. Since both systems measure the p_{T} of particles by looking at the curvature of their tracks in a magnetic field the resolution is directly proportional to the p_{T} itself. More energetic particles with greater p_{T} are deflected less so the ability to measure track curvature is degraded. Despite the fact that the position resolution, and thus the resolution of the sagitta, is better for the inner detector and the magnetic field is stronger there the momentum resolution is better in the muon spectrometer because of the $1/L^2$ dependence. The muon spectrometer extends over a much larger distance than the inner detector. For the calorimeter the requirement is on energy resolution σ_E/E. The energy measured in each cell of the calorimeter is proportional to the amount of charge deposited there which is a stochastic process described by a Poisson probability distribution function. Therefore the resolution is given by

$$\frac{\sigma_E}{E} = \frac{\sigma_N}{N} = \frac{1}{\sqrt{N}} \sim \frac{1}{\sqrt{E}} \tag{3.3}$$

where N is the number of charge carriers produced by the particle as it passes through the cell. In contrast to the p_{T} resolution which is directly proportional to p_{T} the energy resolution is inversely proportional the square root of energy. This means that more energetic particles are measured better in the calorimeter but worse in the inner detector and muon spectrometer. The design requirements for the different detector systems in ATLAS are summarized in Table 3.1.

Detector component	Required resolution	η coverage	
		Measurement	Trigger
Inner tracking	$\sigma_{p_T}/p_T = 0.05\% p_T \oplus 1\%$	±2.5	
EM calorimetry	$\sigma_E/E = 10\%/\sqrt{E} \oplus 0.7\%$	±3.2	±2.5
Hadronic calorimetry (jets)			
barrel and end-cap	$\sigma_E/E = 50\%/\sqrt{E} \oplus 3\%$	±3.2	±3.2
forward	$\sigma_E/E = 100\%/\sqrt{E} \oplus 10\%$	$3.1 < \lvert\eta\rvert < 4.9$	$3.1 < \lvert\eta\rvert < 4.9$
Muon spectrometer	$\sigma_{p_T}/p_T = 10\%$ at $p_T = 1\ TeV$	±2.7	±2.4

Table 3.1: Performance goals for each detector system in ATLAS. E and p_{T} are expressed in GeV. [66]

3.2.1 Magnet System

The ATLAS detector includes a system of four large superconducting magnets used to bend the tracks of charged particles as they pass through the inner detector and muon spectrometer. This is done to measure the charge and momentum of particles from the direction they are deflected and the curvature of their tracks. The position of the magnets within the ATLAS detector is shown in Fig. 3.5 and some important parameters are listed in Table 3.2. All the magnets use superconducting Al-stabilized NbTi cooled with liquid helium to 4.5 K.

A co-axial solenoid magnet located between the inner detector and calorimeter is used to produce a 2T magnetic field in the z-direction. This produces a force on charged particles in the azimuthal direction leading to particle trajectories that curve around the central axis of the detector. The solenoid magnet uses a single coil. In order to minimize the amount of material in front of the calorimeter the solenoid was designed to be as thin as possible and is contained within the same vacuum vessel as the LAr calorimeter. This reduces the extent to which particles lose energy before reaching the calorimeter where they are absorbed and their energy is measured.

Three superconducting toroid magnets are used to bend charged particles passing through the muon spectrometer. Located in the barrel and the end-cap regions each toroid consists of eight coils oriented to produce a magnetic field in the azimuthal

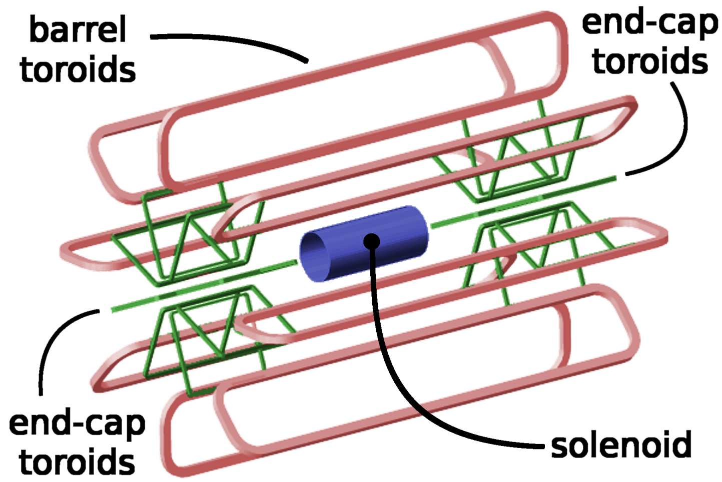

Figure 3.5: Superconducting solenoid and toroid magnets in ATLAS. [68]

direction pointing in a circle around the central axis of the detector. This field orientation produces forces on charged particles in the η direction. The toroid magnets produce a magnetic field of approximately 0.5 T and 1 T in the barrel and end-cap regions respectively. The end-cap toroid system is rotated by 22.5° in ϕ with respect to the barrel toroid system in order to provide radial overlap and to optimize the bending power ($\int Bd\ell$) at the interface between the two systems.

As part of the requirements placed on the resolution of the transverse momentum in the inner detector and muon spectrometer, outlined in Table 3.1, the field of the solenoid and toroid magnets must be known to high precision. For the solenoid the field is determined with in-situ mapping using dedicated instrumentation inside the ID cavity before the installation of the ID itself. The bending power of the solenoid field is required to have a fractional uncertainty less than 5×10^{-4}. For the toroid the field extends over a much larger region of space and varies significantly with position. This makes in-situ measurement of the B-field of the toroid impractical. Instead a combination of simulation and measurements made with $\sim$ 1840 B-field sensors in the muon spectrometer is used to reconstruct the B-field there. The uncertainty of the toroid field contributes to the degradation of the p_{T} resolution in the muon spectrometer. This uncertainty combined with the uncertainty of the position measurements of particles in the MS chambers and the uncertainty of the

Property	Feature	Unit	Solenoid	Barrel toroid	End-cap toroids
Size	Inner diameter	m	2.46	9.4	1.65
	Outer diameter	m	2.56	20.1	10.7
	Axial length	m	5.8	25.3	5.0
	Number of coils		1	8	2×8
Mass	Conductor	t	3.8	118	2×20.5
	Cold mass	t	5.4	370	2×140
	Total assembly	t	5.7	830	2 x 239
Coils	Turns per coil		1154	120	116
	Nominal current	kA	7.73	20.5	20.5
	Magnet stored energy	GJ	0.04	1.08	2 x 0.25
	Peak field in the windings	T	2.6	3.9	4.1
	Field range in the bore	T	0.9–2.0	0.2–2.5	0.2–3.5
Conductor	Overall size	mm^2	30 x 4.25	57 x 12	41 x 12
	Ratio Al:Cu:NbTi		15.6:0.9:1	28:1.3:1	19:1.3:1
	Number of strands (NbTi)		12	38–40	40
	Strand diameter (NbTi)	mm	1.22	1.3	1.3
	Critical current (at 5 T and 4.2 K)	kA	20.4	58	60
	Operating/critical-current ratio at 4.5 K	%	20	30	30
	Residual resistivity ratio (RRR) for Al		> 500	> 800	> 800
	Temperature margin	K	2.7	1.9	1.9
	Number of units × length	m	4×2290	$8 \times 4 \times 1730$	$2 \times 8 \times 2 \times 800$
	Total length (produced)	km	10	56	2 x 13
Heat load	At 4.5 K	W	130	990	330
	At 60–80 K	kW	0.5	7.4	1.7
	Liquid helium mass flow	g/s	7	410	280

Table 3.2: Important parameters of the ATLAS magnet systems [66].

positions of the chambers with respect to the magnet coils are required to degrade the p_{T} resolution by no more than 5%.

3.2.2 Inner Detector

The inner detector, as the name suggests, is the part of the ATLAS detector closest to the beamline [69,70]. It was designed to reconstruct the tracks of charged particles deflected by the magnetic field of the solenoid. The reconstructed tracks are then used to identify the particles and measure their p_{T}. Because of its proximity to the interaction point it must have very high granularity and be able to handle a high event rate and withstand high levels of radiation. The inner detector consists of three systems known as the semiconductor pixel tracker, the semiconductor tracker (SCT) and the transition radiation tracker (TRT). A diagram of the inner detector is shown in Fig. 3.6. The pixel tracker is closest to the interaction point followed by the SCT and then the TRT. Each system has multiple modules in both the barrel and end-cap regions. The position of charged particles as they pass through the inner detector is measured to a precision on the order of 10-100 μm depending on the part of the inner detector it passes through. This leads via Eq. 3.2 to excellent p_{T} resolution.

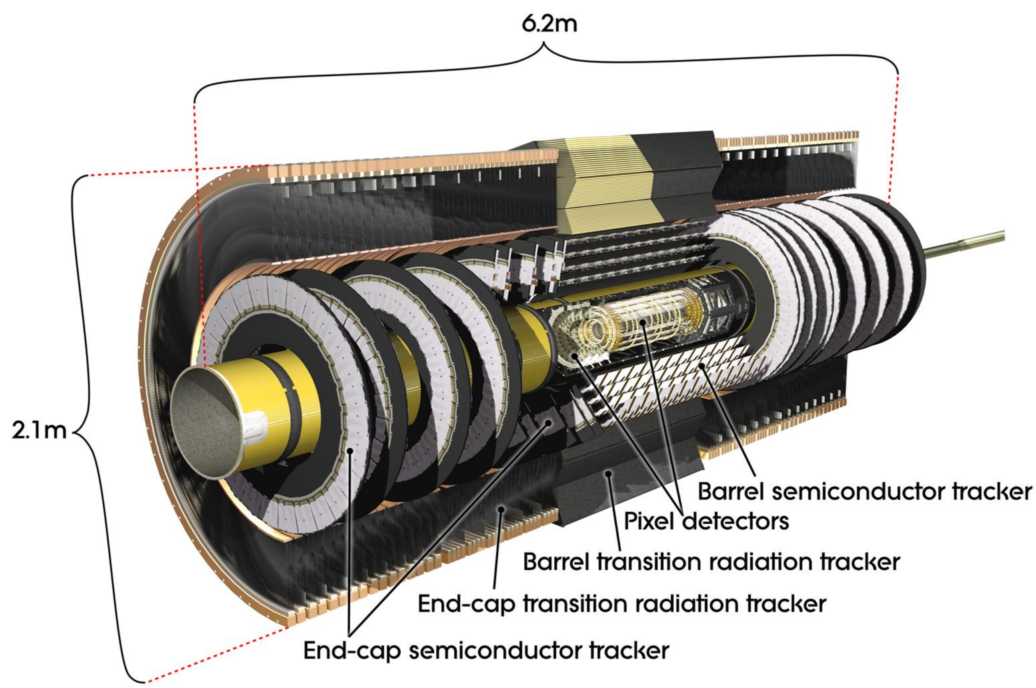

Figure 3.6: Three dimensional cut-away view of the inner detector (ID). [71]

The pixel tracker and the SCT are both based on semiconductor technology and consist of a large number of silicon sensors [72, 73]. The working principle in each is the same. Charged particles passing through the silicon sensors excite electrons from the valence to the conductance band giving rise to a measured current. Together the pixel tracker and the SCT provide a minimum of seven precision measurements along a particle's track. The pixel tracker consists of 1456 barrel modules and 288 end-cap modules. Each module contains 47323 pixels of nominal size 50 $\times$ 400 μm^2. This very fine segmentation leads to an excellent position resolution. The uncertainty of the position measurement in the bending plane is $\sim$ 12 μm. There are three barrel pixel layers at radial distances ranging from 50.5 to 122.5 mm and six end-cap disks at radial distances ranging from 88.8 to 149.6 mm. The inner-most barrel layer, known as the B-layer, is only 50.5 mm away from the beamline and is essential for identifying secondary vertices in particle tracks. This is particularly useful for identifying jets arising from b-quarks in the final state. The B-layer is made to be removable so it can be easily replaced since it is in such a high luminosity environment and thus susceptible to radiation damage.

The SCT consists of four barrel layers containing 2112 modules in the radial range 299 < R < 514 mm and nine disks in the end-cap regions each containing 1976 modules in the radial range 275 < R < 560 mm. All the models consist of a group of silicon micro-strips glued back to back with a 40 mrad stereo angle between them. The pitch of the strips is 80 μm, leading to a 23 μm point resolution per single side measurement in the coordinate perpendicular to the strip direction. The 40 mrad stereo angle provides transverse measurement capability and improves the measurement resolution to about 16 μm. The SCT is a very important part of the inner detector as it covers a much larger portion of the charged particle track than the pixel detector. This provides a greater arc length (L) which improves the resolution of the p_{T} measurement as shown in Eq. 3.2.

The TRT uses a different detection principle based on measuring ionized charge in an array of drift tubes [74]. It consists of a large number of drift tubes which are 4 mm in diameter aligned parallel with the beamline in the barrel region and radially in the end-cap regions. There are 52544 axial tubes in the barrel section and 122880 radial tubes in the end-caps. The axial tubes are 1.44 m long at radial distances of 554 mm to 1082 mm. The radial tubes are 370 mm long at radial distances of 617 mm to 1106 mm. The drift tubes are filled with $Xe/CO_2/O_2$ gas in the ratio 70%/27%/3% with anode wires at their center. Charged particles passing through the tubes ionize the gas producing a current in the anode. In addition to these standard tracking hits the TRT is also capable of identifying electrons by the characteristic transition radiation (TR) they give off when passing through materials of different index of refraction. Polypropylene foils installed in the space between the tubes cause electrons to emit x-ray TR photons which leads to further ionization in the drift tubes. Standard tracking hits deposit about 2 keV while a typical TR photon deposits $\sim$ 8 -10 keV [5]. This makes it possible to discriminate between electrons and heavier ionizing particles, such as pions, by looking at the number of hits above a certain energy threshold. Another advantage of the TRT is that it helps to minimize the material in the tracking volume as it introduces much less material per tracking point than the semiconductor trackers. Although the TRT has relatively low resolution per tracking point (130 μm) compared to the semiconductor detectors it is much larger and consequently has many more points per track ($\sim$ 36).

A summary of the important parameters of each of the ID systems is presented in Table 3.3. Performance studies have shown that the inner detector operates reasonably well at the design luminosity of 10^{34} cm^{-2} s^{-1}. With the exception of the B-layer in the pixel tracker the inner detector systems are designed to be radiation hard in order to function properly with minimal degradation over the course of the ten year design lifetime of the LHC. The B-layer will have to be replaced approximately every three years under the nominal luminosity. The pixel detector and SCT are maintained at -5 to -10° C in order to maintain adequate noise performance after radiation damage. In contrast the TRT is designed to operate at room temperature.

3.2.3 Calorimeter

The ATLAS calorimeter system is used to measure the energies of charged and neutral particles such as electrons, photons and pions. It is a sampling calorimeter consisting of layers of an absorber material that facilitate the growth of particle showers and an active material where energy is deposited and converted to a signal. A particle shower is a cascade of secondary particles produced when high-energy particles interact with atomic nuclei in dense matter. The shower grows until the energy of all the secondary particles falls below a certain threshold. Energy is deposited by these secondary particles in the active material via ionization or scintillation depending upon the part of the calorimeter.

Item		Radial extension (mm)	Length (mm)
Overall ID envelope		$0 < R < 1150$	$0 < \|z\| < 3512$
Beam-pipe		$29 < R < 36$	
Pixel	Overall envelope	$45.5 < R < 242$	$0 < \|z\| < 3092$
3 cylindrical layers	Sensitive barrel	$50.5 < R < 122.5$	$0 < \|z\| < 400.5$
2×3 disks	Sensitive end-cap	$88.8 < R < 149.6$	$495 < \|z\| < 650$
SCT	Overall envelope	$255 < R < 549$ (barrel)	$0 < \|z\| < 805$
		$251 < R < 610$ (end-cap)	$810 < \|z\| < 2797$
4 cylindrical layers	Sensitive barrel	$299 < R < 514$	$0 < \|z\| < 749$
2×9 disks	Sensitive end-cap	$275 < R < 560$	$839 < \|z\| < 2735$
TRT	Overall envelope	$554 < R < 1082$ (barrel)	$0 < \|z\| < 780$
		$617 < R < 1106$ (end-cap)	$827 < \|z\| < 2744$
73 straw planes	Sensitive barrel	$563 < R < 1066$	$0 < \|z\| < 712$
160 straw planes	Sensitive end-cap	$644 < R < 1004$	$848 < \|z\| < 2710$

Table 3.3: Important parameters of the ATLAS inner detector systems [66].

The calorimeter system in ATLAS consists of (EM) electromagnetic calorimeters [75], which are close the beamline just outside the inner detector, followed by hadronic calorimeters, which are farther from the beamline. Both the EM and hadronic calorimeters consist of barrel and end-cap sections. Additionally a forward calorimeter is included in the high pseudorapidity region which is used to measure both EM and hadronic showers. The EM calorimeters are designed for precision measurements of particles that interact primarily or exclusively via the electromagnetic force such as electrons and photons. The hadronic calorimeters are designed to measure the energy of hadrons that interact via the strong force such as protons, neutrons and pions. The EM calorimeters are closer to the interaction point and have finer granularity since EM showers are more compact and don't penetrate are far as hadronic showers. In contrast hadronic showers are much more diffuse and have greater penetration. Consequently EM showers are generally contained in the EM calorimeters while hadronic showers stretch across both the EM and hadronic calorimeters.

The mechanisms by which the EM and hadronic calorimeters produce showers and measure energy deposition differ. The EM calorimeter consists of layers of lead/stainless-steel and LAr which function as the absorber and active material respectively. Electrons and photons incident on the absorber layers initiate EM showers by bremsstrahlung radiation and electron-positron pair production in the presence of atomic nuclei. The electrons from the pair production also radiate through bremsstrahlung producing more photons which can pair produce further. The showering process continues until the energy of all photons falls below the pair production threshold ($\sim$ 1 MeV) and the energy of electrons falls to the point where energy loss through ionization begins to dominate over bremsstrahlung. The electrons in the shower deposit energy via ionization in the LAr layers. Liquid argon atoms are ionized producing electrons that drift toward a copper anode grid at the center of the LAr layers. The TileCal consist of layers of iron and plastic scintillating tiles made of doped polystyrene which function as the absorber and active material. The HEC consists of layers of copper and LAr. In each case hadrons interact with nuclei in the absorber layers via the strong force producing more hadrons. In the TileCal these hadrons then deposit energy by producing photons in the scintillator tiles which are collected by optical fibers and converted to an electrical current. In the HEC the energy deposition occurs by ionization as in the EM calorimeter. Due to the presence of particles such as neutral pions which decay electromagnetically ($\pi^0 \to \gamma\gamma$) all hadronic showers have an electromagnetic component. Due to energy lost in nuclear excitation and breakup in the absorber layers of the hadronic calorimeter, which is not recovered, the energy deposited is significantly less than that of the hadron that produced the shower. For this reason the energy measured must be recalibrated to the hadronic energy scale. This is an example of a non-compensating calorimeter where the ratio of energy deposited by an electromagnetic particle and a hadronic particle of the same incident energy is greater than one ($e/h > 1$).

The degree to which a particle shower penetrates a material is characterized by the radiation length (X_o), in the case of electrons and photons where electromagnetic interactions dominate, and the nuclear interaction length (λ) for hadrons which interact predominantly via the strong force. X_o is defined as the average distance over which an incident electron loses all but $1/e$ of its energy via bremsstrahlung radiation. λ is the mean distance travelled by a hadronic particle in a medium before undergoing an inelastic nuclear interaction. Both X_o and λ are properties of a material which depend on the atomic number (Z) and atomic mass (A) for the material. For a given material $\lambda > X_o$. The thickness of the EM calorimeter is $>$ 22 X_o in the barrel and $>$ 24 X_o in the end-caps. The full calorimeter is 11 λ thick at $\eta = 0$. This thickness provides good containment of EM and hadronic showers and minimizes punch-through to the muon spectrometer.

A diagram of the calorimeters in ATLAS is shown in Fig. 3.7. They are composed of a barrel, two end-caps and a forward calorimeter which covers the high η region. The inner barrel region contains the Liquid Argon (LAr) EM barrel (EMBA) housed in the same cryostat as the solenoid. Outside the EMBA is the Tile barrel and extended Tile barrel calorimeters (TileCal) [76]. The end-caps contain the LAr EM end-cap (EMEC) followed by the hadronic end-cap (HEC) calorimeters. The forward calorimeter (FCAL) consists of three modules on each side of the detector: the first, made of copper/LAr, is optimized for electromagnetic measurements, while the other two, made of tungsten/LAr, measure predominantly the energy of hadronic interactions. Important parameters of the calorimeter system are listed in Table 3.4

In all there are $\sim$ 180,000 calorimeter cells. The energy deposited in each cell for a particular event is combined to form clusters using topological clustering algorithms or fixed size projective towers in the $\eta \times \phi$ plane. A typical EM shower consists of a single cluster while a hadronic shower may contain multiple clusters. These objects are then used as the input to the reconstruction of physics objects such as electrons and jets to be discussed in Chapter 4.

	Barrel		End-cap	
EM calorimeter				
Number of layers and $\|\eta\|$ coverage				
Presampler	1	$\|\eta\| < 1.52$	1	$1.5 < \|\eta\| < 1.8$
Calorimeter	3	$\|\eta\| < 1.35$	2	$1.375 < \|\eta\| < 1.5$
	2	$1.35 < \|\eta\| < 1.475$	3	$1.5 < \|\eta\| < 2.5$
			2	$2.5 < \|\eta\| < 3.2$
Granularity $\Delta\eta \times \Delta\phi$ versus $\|\eta\|$				
Presampler	0.025×0.1	$\|\eta\| < 1.52$	0.025×0.1	$1.5 < \|\eta\| < 1.8$
Calorimeter 1st layer	$0.025/8 \times 0.1$	$\|\eta\| < 1.40$	0.050×0.1	$1.375 < \|\eta\| < 1.425$
	0.025×0.025	$1.40 < \|\eta\| < 1.475$	0.025×0.1	$1.425 < \|\eta\| < 1.5$
			$0.025/8 \times 0.1$	$1.5 < \|\eta\| < 1.8$
			$0.025/6 \times 0.1$	$1.8 < \|\eta\| < 2.0$
			$0.025/4 \times 0.1$	$2.0 < \|\eta\| < 2.4$
			0.025×0.1	$2.4 < \|\eta\| < 2.5$
			0.1×0.1	$2.5 < \|\eta\| < 3.2$
Calorimeter 2nd layer	0.025×0.025	$\|\eta\| < 1.40$	0.050×0.025	$1.375 < \|\eta\| < 1.425$
	0.075×0.025	$1.40 < \|\eta\| < 1.475$	0.025×0.025	$1.425 < \|\eta\| < 2.5$
			0.1×0.1	$2.5 < \|\eta\| < 3.2$
Calorimeter 3rd layer	0.050×0.025	$\|\eta\| < 1.35$	0.050×0.025	$1.5 < \|\eta\| < 2.5$
Number of readout channels				
Presampler	7808		1536 (both sides)	
LAr hadronic end-cap				
$\|\eta\|$ coverage			$1.5 < \|\eta\| < 3.2$	
Number of layers			4	
Granularity $\Delta\eta \times \Delta\phi$			0.1×0.1	$1.5 < \|\eta\| < 2.5$
			0.2×0.2	$2.5 < \|\eta\| < 3.2$
Readout channels			5632 (both sides)	
LAr forward calorimeter				
$\|\eta\|$ coverage			$3.1 < \|\eta\| < 4.9$	
Number of layers			3	
Granularity $\Delta x \times \Delta y$ (cm)			FCal1: 3.0×2.6	$3.15 < \|\eta\| < 4.30$
			FCal1: $\sim$ four times finer	$3.10 < \|\eta\| < 3.15$, $4.30 < \|\eta\| < 4.83$
			FCal2: 3.3×4.2	$3.24 < \|\eta\| < 4.50$
			FCal2: $\sim$ four times finer	$3.20 < \|\eta\| < 3.24$, $4.50 < \|\eta\| < 4.81$
			FCal3: 5.4×4.7	$3.32 < \|\eta\| < 4.60$
			FCal3: $\sim$ four times finer	$3.29 < \|\eta\| < 3.32$, $4.60 < \|\eta\| < 4.75$
Readout channels			3524 (both sides)	
Scintillator tile calorimeter				
	Barrel		Extended barrel	
$\|\eta\|$ coverage	$\|\eta\| < 1.0$		$0.8 < \|\eta\| < 1.7$	
Number of layers	3		3	
Granularity $\Delta\eta \times \Delta\phi$	0.1×0.1		0.1×0.1	
Last layer	0.2×0.1		0.2×0.1	
Readout channels	5760		4092 (both sides)	

Table 3.4: Main parameters of the ATLAS calorimeter system. [77]

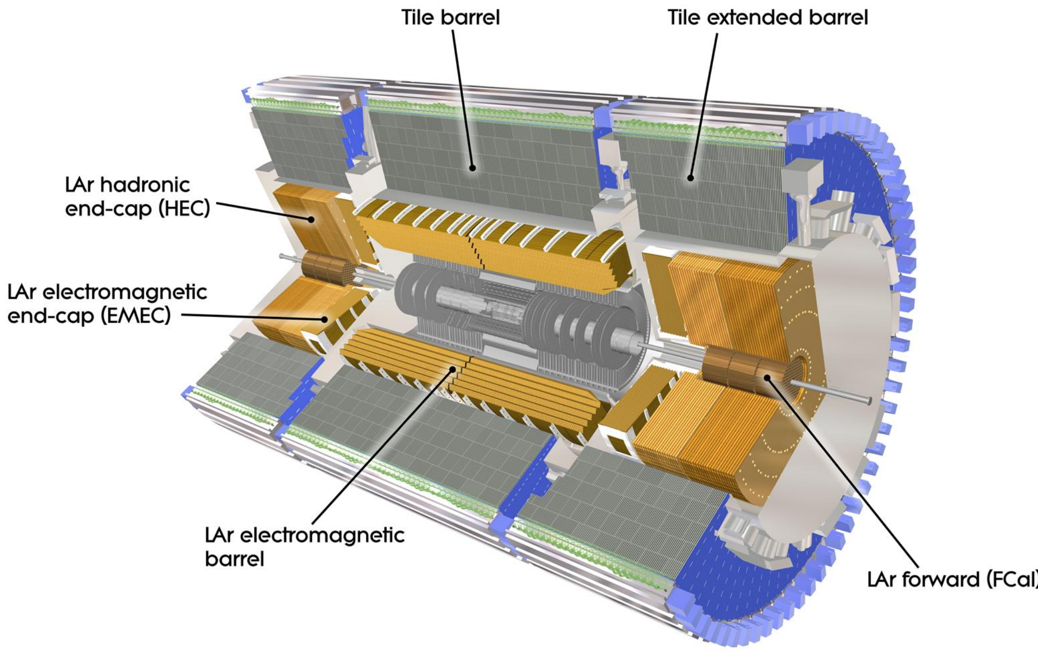

Figure 3.7: Three dimensional cut-away view of the EM and hadronic Calorimeters in ATLAS. [77]

3.2.4 Muon Spectrometer

Among the final state particles measured with the ATLAS detector, muons are unique in that they don't deposit significant energy in the calorimeter. Compared to electrons they emit very little bremsstrahlung radiation due to their much larger mass and so rarely produce EM showers. They don't interact via the strong force and thus don't produce hadronic showers either. This means they pass through the calorimeter losing very little energy. Simulation shows that the most probable value of the energy loss of 1 TeV muons in the calorimeter is ~ 3 GeV ($< 1\%$) [78]. Although muon p_{T} is measured in the inner detector the resolution is limited due to the small sagitta. This is particularly problematic for high p_{T} muons ($\gtrsim 100$ GeV) because the tracks of such particles are nearly straight making it difficult to measure the sagitta and degrading the p_{T} resolution (Eq. 3.2). To mitigate this, the muon spectrometer is added outside the calorimeter to provide another measurement of

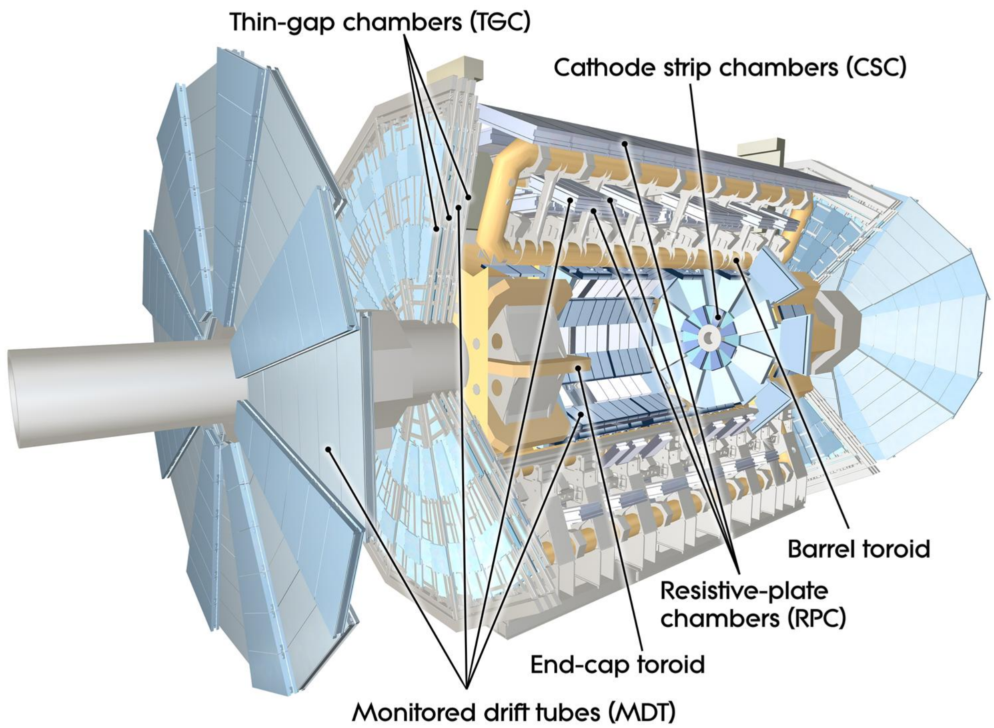

Figure 3.8: Three dimensional cut-away view of the ATLAS Muon Spectrometer. [77]

muon p_{T} [79–81]. The combination of the p_{T} measurements from each system and the intrinsically better resolution in the muon spectrometer improves the overall p_{T} resolution for muons significantly.

The muon spectrometer makes use of four different types of detector technologies including high precision tracking chambers for p_{T} measurement and fast response chambers for triggering events (the details of event triggering are discussed in Chapter 4). The Monitoring Drift Tubes (MDTs) and Cathode Strip Chambers (CSCs) are used for precision measurements of p_{T} while the Resistive Plate Chambers (RPCs) and Thin Gap Chambers (TGCs) provide the high timing resolution necessary for triggering. A cut-away view of the muon spectrometer, showing each of the different types of chambers that make it up, is shown in Fig. 3.8.

Figure 3.9 shows a cross-section of the muon spectrometer in the upper right quadrant of the y-z plane with the interaction point at the origin. In the barrel the chambers are arranged in three concentric cylindrical layers at radii of 5m, 7.5m and

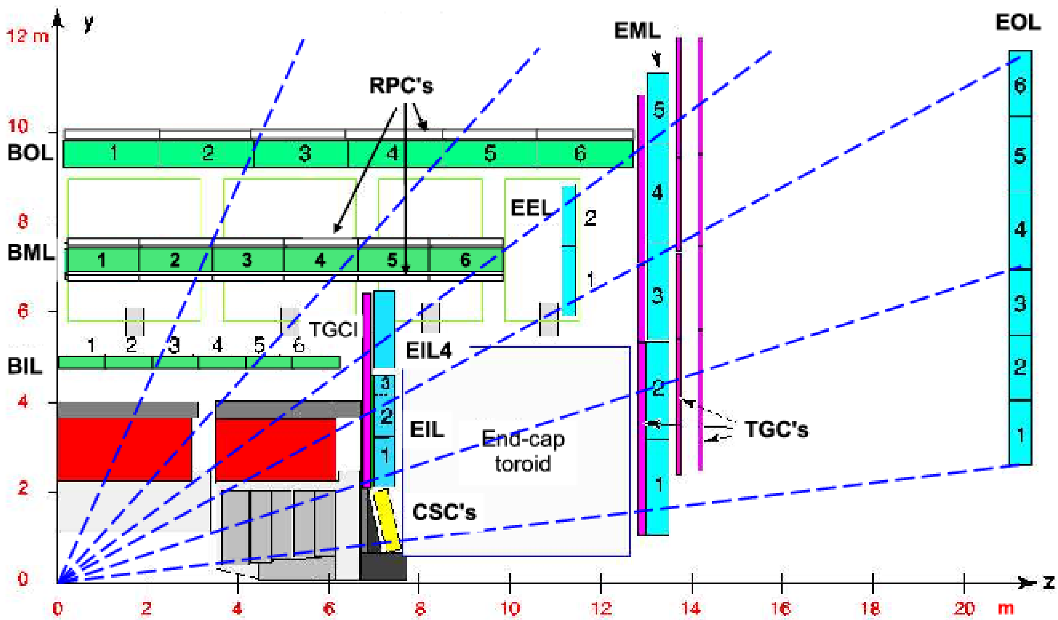

Figure 3.9: cross-sectional view of the ATLAS Muon Spectrometer in the upper right quadrant of the y-z plane. The interaction point is at the origin. [77]

10m. They are labeled the inner, middle and outer barrel chambers. The middle barrel layer is surrounded by the barrel toroid magnet. The end-cap chambers are located in four disks at distances of about 7.4m, 10.8m, 14m and 21.5m along the z-axis. They are labeled the inner, extra, middle and outer end-cap chambers. The CSCs, which cover the forward region, are located just below the inner end-cap chambers. The structures containing the end-cap muon chambers (excluding the extra chambers) are labeled, in ascending order of distance from the interaction point, the small wheel, big wheel and outer wheel where the small wheel contains both the inner end-cap chambers and the CSCs. The end-cap toroid magnetic is between the inner and middle end-cap chambers and just below the extra end-cap chamber. The CSCs and TGCs are entirely in the end-cap region while the RPCs are entirely in the barrel. The MDTs are the only chambers in both the end-cap and the barrel. With the exception of the TGCs the rest of the muon spectrometer has perfect azimuthal symmetry and can be divided into identical octants. Each octant

Monitored drift tubes	**MDT**
- Coverage	$\|\eta\| < 2.7$ (innermost layer: $\|\eta\| < 2.0$)
- Number of chambers	1088 (1150)
- Number of channels	339 000 (354 000)
- Function	Precision tracking
Cathode strip chambers	**CSC**
- Coverage	$2.0 < \|\eta\| < 2.7$
- Number of chambers	32
- Number of channels	31 000
- Function	Precision tracking
Resistive plate chambers	**RPC**
- Coverage	$\|\eta\| < 1.05$
- Number of chambers	544 (606)
- Number of channels	359 000 (373 000)
- Function	Triggering, second coordinate
Thin gap chambers	**TGC**
- Coverage	$1.05 < \|\eta\| < 2.7$ (2.4 for triggering)
- Number of chambers	3588
- Number of channels	318 000
- Function	Triggering, second coordinate

Table 3.5: Main parameters of the ATLAS muon system. [77]

contains pairs of large and small chambers that overlap slightly in order to prevent regions where muons can pass undetected between chambers. The larger chambers are farther from the interaction point.

The MDTs and CSCs are the chambers that provide precision tracking of muons. MDTs are included in every layer of chambers in both the barrel and the end-cap regions. They cover the psuedorapidity range $\mid \eta \mid < 2.7$ in every layer except the inner end-cap layer where they cover the range $\mid \eta \mid < 2.0$. The range $2.0 < \mid \eta \mid < 2.7$ of the inner end-cap layer is covered by the CSCs which have the high timing resolution necessary to handle the higher rate of charged particles in the forward direction. The MDTs consist of gas-filled aluminum tubes that function as drift chambers. Muons passing through the tubes liberate electrons that drift toward a central anode wire and produce a current. The time taken by the electrons to drift toward the anode in each of the tubes the muon passes through is used to reconstruct its track to high precision. The MDT chambers contain eight layers of tubes in the inner chambers and six in the outer chambers. The tubes are 30 mm in diameter with lengths ranging from 0.7 m to 6.30 m and run perpendicular to the beamline in the ϕ direction. The position resolution in a single layer of tubes is 80 μm. With multiple layers the resolution reduces to 30 (35) μm in chambers with eight (six) layers of tubes. The CSCs are multi-wire proportional chambers (MWPC) located on disks on each of the small wheels in the end-cap regions. Each disk is divided into 16 sectors, each containing four layers of gas filled chambers surrounded by cathode strips aligned in both the transverse and ϕ directions. Anode wires at the center of each chamber, running parallel to the transverse strips, collect electrons which induce positive charge on the strips. Charge is induced across multiple strips forming a cluster in each layer. The strips on either side of each chamber form a criss-cross pattern allowing measurement of both coordinates of the muon as it passes through the plane of the CSCs. The strips aligned in the ϕ direction, which measure the coordinate in the bending plane of the toroid magnet, are referred to as the precision strips since they have much finer segmentation and thus better position resolution. The pitch of the precision strips is 5.31 (5.56) mm while that of the transverse strips is 12.9 (21.0) mm for the large and small chambers respectively. Both the anode wire pitch and the anode to cathode distance is 2.54 cm. The distribution of charge collected in adjacent strips within a cluster is used to determine the position of the muon within the central strip. This yields a single layer precision of 60 μm in the bending plane of the magnet. Performing a fit across all four layers reduces this to 40 μm. In addition to good position resolution an important feature of the CSCs is their good time resolution. This is essential given the high muon flux in the forward direction. Maximum electron drift times in the CSCs are approximately 40 ns resulting in a timing resolution of about 7 ns per plane. Also the much smaller pitch of the CSC strips compared to the diameter of the MDT tubes means that the CSCs can resolve separate hits for muons that pass through very close to one another.

An essential design criterion of the muon system was the ability to trigger on muon tracks. The triggering capability of the muon spectrometer is handled by the TGCs and RPCs. The primary purpose of these chambers is to deliver track information, including p_{T}, to the level one trigger on the order of tens of nanoseconds after the passage of a particle and to match events to bunch-crossings which occur every 50 ns. The chambers are required to have sufficient time resolution to ensure 99% matching efficiency. In addition, these chambers also measure the second coordinate in the non-bending plane to complement the precision measurement of the MDTs. The RPCs are rectangular gas chambers located on the middle and outer barrel layers. Each RPC chamber contains a single gas gap and two readout strips, one parallel to the MDT tubes and the other perpendicular. The most important feature of the RPCs is their excellent timing performance with a resolution of 5 ns. The TGCs, located on the end-cap inner and middle layers, provide the triggering capability in the forward direction. They are MWPCs with a resolution of 4 ns.

Important parameters of each of the muon chambers are given in Table 3.5. In addition to the intrinsic position resolution of each chamber another source of uncertainty that must be accounted for is that associated with the alignment of the chambers with respect to each other as well as other components of ATLAS such as the toroid magnets. The MDT and CSC chambers were installed with a precision of 5 mm and 2 mrad with respect to their nominal positions. However their positions must be known to within 30 μm in order to meet the performance requirement on p_{T} resolution. This is crucial to the calculation of muon p_{T}. To accomplish this optical alignment systems are used to monitor the position of the muon chambers within ATLAS and estimate their uncertainty. This optical network is able to reliably detect relative changes in chamber position at the 20 μm level. Internal displacements of up to 10 mm can be corrected for in offline analysis. The combination of the position resolutions of each of the chambers and that of the optical alignment system are sufficient to meet the performance goal described in Table 3.1 of a 10% p_{T} resolution for a 1 TeV muon.

3.2.4.1 CSC Data Quality Monitoring

An important part of running the ATLAS experiment is monitoring the detector performance and ensuring the quality of data before it can be used for physics analysis. A system known as the Data Quality Monitoring Framework (DQMF) is used to identify potential problems in the detector that may arise during data taking [82,83]. The DQMF serves two functions. It provides a record of the data quality for each detector system in ATLAS. This record is used to produce GoodRunsLists (GRLs) that specify the runs, and the LumiBlocks within each run, that can be used in physics analyses (see Section 4.1). It also makes it possible to spot problems in real time as data is being collected. In some cases immediate action can be taken to resolve the problem and avoid a degradation in data quality.

The DQMF is divided into online and offline monitoring. The online DQMF runs a series of automatic monitoring algorithms on the raw data from the detector that returns data quality (DQ) flags. A green flag means that the detector is operating normally and that data quality is high. A yellow or red flag means that there may be a problem with part of the detector that could compromise the data. A red flag indicates a more severe problem. The output of the online DQMF is displayed in the ATLAS control room and monitored by experts during detector operation.

The offline DQMF monitors the detector using the full ATLAS reconstruction software, which is designed to reconstruct physics objects such as particles and jets for use in physics analyses. By using fully reconstructed data the offline monitoring has access to more information than the online monitoring and so can perform more precise tests. In addition it is used to monitor the ATLAS software which is updated over time to improve reconstruction. The disadvantage of the offline monitoring is that it cannot be used to spot problems quickly because the reconstruction takes time. In order to spot problems as they occur and potentially fix them the prevent the loss of data the online monitoring is needed. This section describes the online DQMF system used in 2012 to monitor the Cathode Strip Chambers (CSCs) in the forward region of the muon spectrometer. [12] This includes a number of modifications of the online DQMF introduced during the year to improve its performance.

The DQMF for CSCs includes five DQ algorithms that are applied separately in each of the 32 CSC sectors. These algorithms return DQ flags that then propagate upward to determine the overall flag for the CSCs. The DQMF is organized in four layers according to the following structure: CSC → end-cap → sector → DQAlgorithm. A single yellow/red flag at the DQAlgorithm level produces a yellow/red flag for the whole sector. At the sector level, at least 10% of the sectors (i.e. at least two of the 16 sectors per end-cap) must be yellow/red for the end-cap flag to be yellow/red. If either of the end-cap flags are yellow/red the overall flag for the CSCs is yellow/red. This structure can be seen in the graphical interface of the DQMF known as the Data Quality Monitoring Display (DQMD) shown in Fig. 3.10. The segmented rings represent the two end-caps of the CSC, which are divided into 16 sectors each. The flag for each sector is determined from the results of five DQAlgorithms known as IsROSEvent, RPUStatusBad, Landau Fit, Segment Efficiency, and Segment Occupancy. All five DQAlgrithms include a minimum statistics condition that requires that there be at least a thousand events (MinStat=1000). If there are fewer than a thousand events the algorithm returns a green flag. This is to avoid returning unnecessary red flags early in a run when statistics are low.

[12] For the remainder of this section DQMF refers specifically to the online DQMF

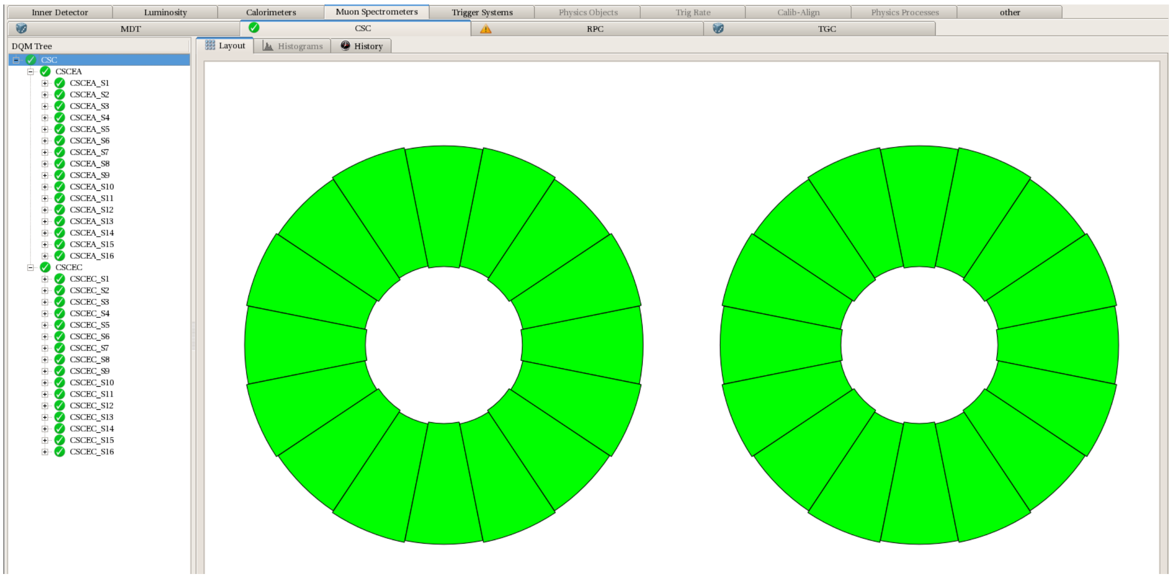

Figure 3.10: Image of the Data Quality Monitoring Display (DQMD) that shows the structure of the DQ flags for the CSC DQMF. In this image all flags are green.

The IsROSEvent and RPUStatusBad DQ flags measure the fraction of total events that have specific types of errors known as ROS and RPU errors. These are errors associated with the read out driver (ROD) electronics that read out the raw data from the CSCs. If there are an unusually large number of such events it can mean there is a problem with the ROD electronics. Fig. 3.11 shows the histogram used for these algorithms in the DQMD. These algorithms take the ratio of the ROS and RPUStatusBad bins over the first bin that contains the total number of events. If the ratio exceeds 0.01 a red flag is returned. Otherwise the flag is green.

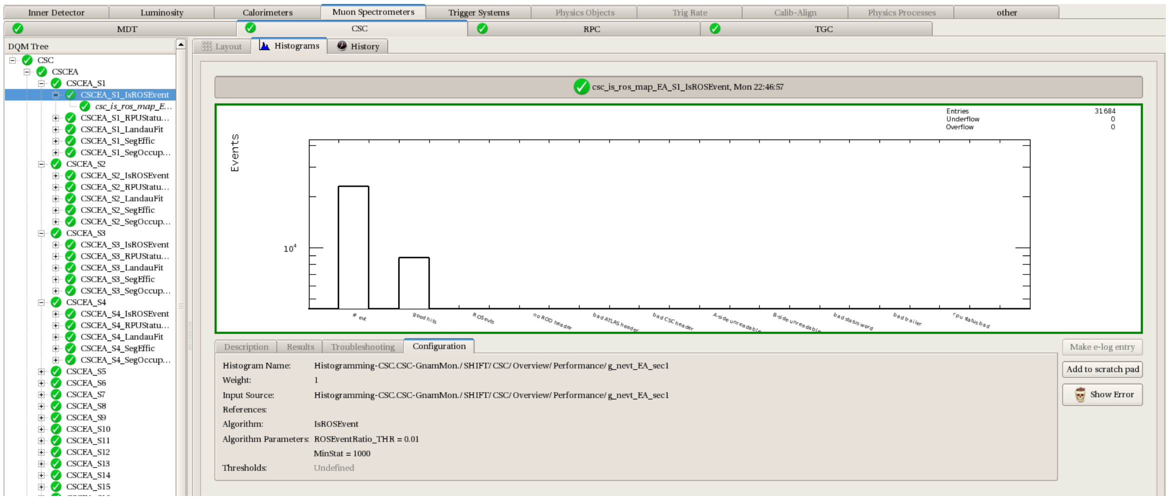

Figure 3.11: Image of the Data Quality Monitoring Display (DQMD) showing the isROSEvent DQAlgorithm. The bins on the x-axis represent different types of errors that can affect events. Important among these are ROS and RPUStatusBad events which this DQAlgorithm monitors.

The Landau Fit flag is based on the results of a Landau fit to the cluster charge distributions. The charge induced on the cathode stripes by the passage of a muon should follow a Landau distribution with most probable value (MPV) of 250 ADC counts (1 ADC count $\sim 10^3 e$). The algorithm returns a green flag if the fit MPV value differs from 250 ADC counts by less than 50%. It returns a yellow flag if the difference is between 50% and 70% and a red flag if it is greater than 70%. It also returns a red flag if the fit χ^2 value is greater than 30.

For this DQAlgorithm, only clusters on track segments with at least three clusters across the four CSC layers are considered. Clusters that are not on segments are typically caused by photon or neutron background in the detector rather than the passage of a muon. These clusters tend to have charge much lower than 250 ADC counts leading to a sharp peak near zero in the charge distributions. Excluding these clusters leads to much improved Landau fits. The Landau Fit flag is essential to check the gas gain of the CSC chambers. This includes both the gas pressure and the HV setting, as well as the distance between the cathode stripes and the annode wires. These parameters are typically very stable but it is still necessary to check the response of the chambers by ensuring that the charge clusters have the correct amplitude. Maintaining the correct value for the cluster charge amplitude is crucial to accurately determining the position of the muon in the central strip. A separate flag is returned for each layer of each sector in the CSCs. Figure 3.12 shows the Landau Fit algorithm in the DQMD.

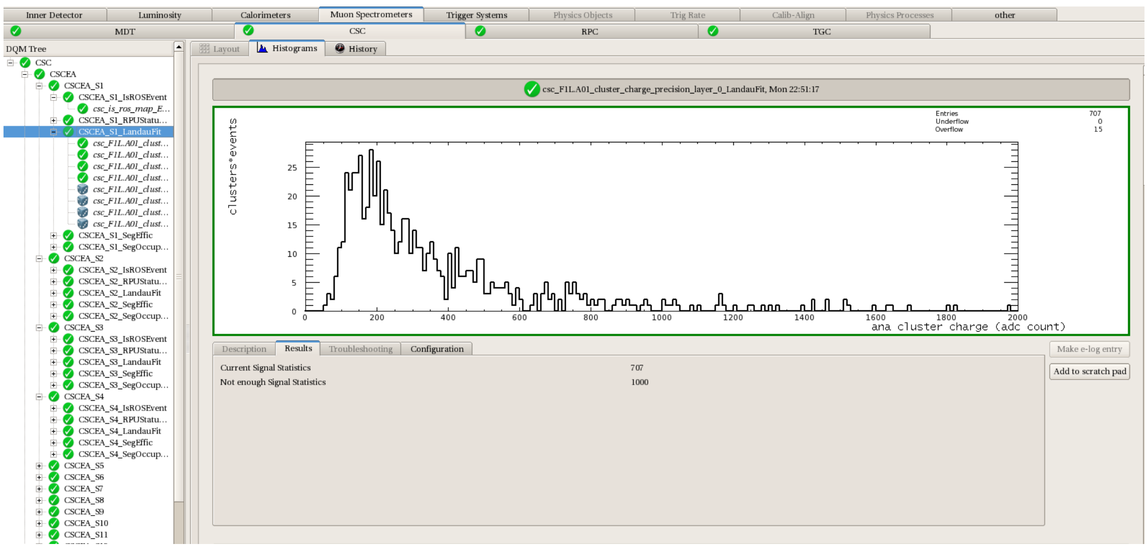

Figure 3.12: Image of the Data Quality Monitoring Display (DQMD) showing the Landau Fit DQAlgorithm. This histogram shows the distribution of cluster charge measured in ADC counts ($\sim 10^3 e$) for clusters on segments of at least three clusters across the four layers of the CSC.

The Segment Efficiency DQAlgorithm produces a flag based on how efficiently track segments are found across the four layers of the CSC. A segment consists of clusters in at least three of the four layers of the CSC that are close to one another in η and ϕ. The clusters must be within 5 strips of one another and the angle between the segment and the z-axis must be less than four degrees [13]. This is to reduce the number of segments arising from cosmic ray muons or muons produced away from the interaction point. Clusters in three of the four layers are required to allow for the possibility that one of the layers may malfunction. In 2012 there were five dead CSC layers that had lost high voltage (HV) due to broken wires. With this

[13] The CSCs are tilted with respect to the transverse direction (see Fig. 3.9 so the segment angle for a muon from the IP is typically very low

definition, segments could still be found in the sectors containing those dead layers (except sector 1 in end-cap C that had two dead layers). The fraction of segments that have clusters on all four layers is a measure of the efficiency of the segment finding. A muon should produce a cluster of charge in all four layers. However it is possible that three clusters from neutron or photon background could fall close to one another and form a segment. Segments such as these don't represent muons passing through the CSCs. The Segment Efficiency DQAlgorithm calculates the ratio of the number of segments with clusters on all four layers to the total number of segments for each sector and returns a red flag if it falls below 0.25. Separate flags are returned for each sector and for segments on transverse and precision layers. The algorithm always returns a green flag for the sectors containing the known dead layers where the segment efficiency is approximately zero. This algorithm is used to spot technical problems such as the appearance of new dead layers. If another layer loses HV because of a broken wire the segment efficiency in the sector containing that layer will drop dramatically leading to a red flag in the DQMF. Fig. 3.13 shows the segment efficiency histogram used for this algorithm. The sectors with dead layers are clearly visible.

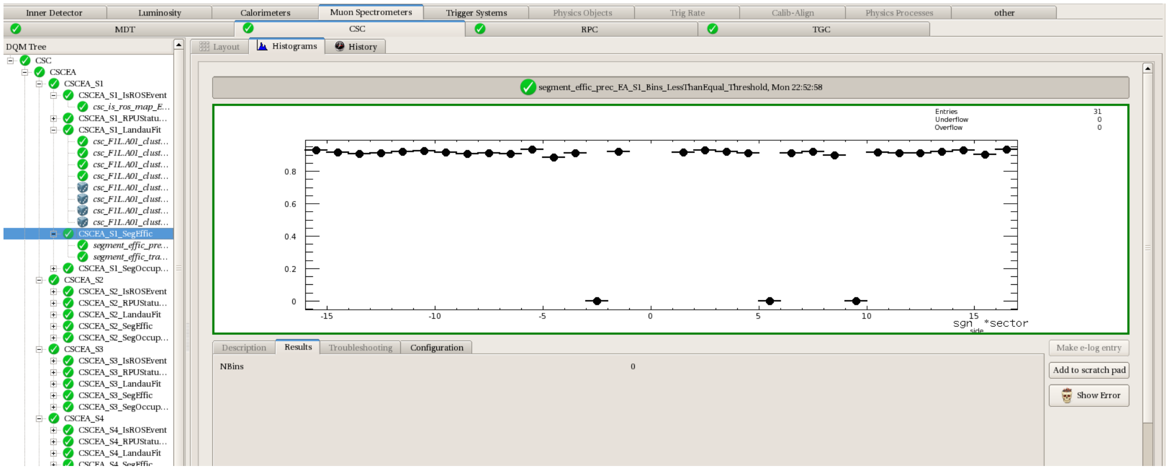

Figure 3.13: Image of the Data Quality Monitoring Display (DQMD) showing the Segment Efficiency DQAlgorithm. The x-axis indicates the sector number with positive numbers representing end-cap A and negative numbers indicating end-cap C. The y-axis represents the segment efficiency defined as the ratio of segments with clusters on all four layers over all segments. The efficiency is above 90% in all sectors except those with dead layers. At the time this image was taken there were five dead layers, two of which were in the same sector. Thus three sectors show segment efficiency near zero and sector C1 shows no efficiency at all since no segments are found there.

The Segment Occupancy DQAlgorithm counts the number of segments in each sector of the CSC and compares it to the average number across all sectors. A red flag is returned if the occupancy differs from the average by more than three standard deviations. Otherwise a green flag is returned. A separate average is calculated for the large and small sectors since large sectors have greater occupancy. The occupancy in each sector is compared to the appropriate average to determine the flag for that sector. Separate flags are returned for the occupancy of segments on precision and transverse layers. The algorithm accounts for the known dead layers by not returning red flags for those sectors. Like the Segment Efficiency DQAlgorithm, this DQAlgorithm is also designed to identify problems such as broken wires or faulty electrical connections that cause the loss of one or more layers in a given sector. The Segment Occupancy DQAlgorithm displayed in the DQMD is shown in Fig. 3.14. The sectors containing dead layers have very low segment occupancy compared with the average.

Figure 3.14: Image of the Data Quality Monitoring Display (DQMD) showing the Segment Occupancy DQAlgorithm. The x-axis indicates the sector number with positive numbers representing end-cap A and negative numbers indicating end-cap C. The y-axis shows the number of segments in each sector. At the time this image was taken there were five dead layers, two of which were in the same sector. Thus three sectors show low occupancy compared to the other sectors. Sector C1 shows zero occupancy since no segments are found there because two layers are dead.

A number of important developments were made during 2012 to make the DQMF more robust and improve its ability to spot potential problems. The structure described above, in which flags are returned for each individual sector and then propagate upward to the overall flag for the CSCs, was introduced. In the process new histograms were added to check the error fractions (ROS and RPUStatusBad events) in specific sectors rather than simply looking at the overall error fraction for the full CSCs. Also a flag merging algorithm was implemented so that the DQMF could successfully spot serious problems without returning unnecessary red flags for minor problems. This includes the requirement that 10% of the sectors on either end-cap must be yellow/red in order for the flag to propagate upward. In principle the CSCs can still function well if only one sector on either end-cap is experiencing problems. Under this merging algorithm the flag for that sector will indicate a problem that will draw the attention of experts in the control room. However the run, or the effected LumiBlocks within the run, will not be removed from the GRLs. If the whole CSC is red, a CSC expert will be consulted to decide if the run, or the effected LumiBlocks within it, can be included in the GRLs.

Another major improvement made to the DQMF during 2012 was the introduction of cluster charge histograms for clusters on segments. This was a significant improvement in particular for the Landau Fit DQAlgorithm. Without the requirement that clusters be on segments, the cluster charge distributions deviate significantly from the Landau shape. Figure 3.15 shows cluster charge distributions for all clusters and for clusters on segments. These plots are taken from Run 212172 recorded in 2012. These plots clearly show that restricting the algorithm to clusters on segments significantly improves the fit. This is primarily because the distributions of all clusters have a sharp spike near zero due to clusters from background interactions in the detector. After introducing the Landau fit algorithm a number of changes were made to the segment finding in order to improve the performance of the flag. These included reducing the distance between clusters on segments from 20 strips to 5 strips and tightening the cut on segment angle from $10°$ to $4°$. The Segment Occupancy and Segment Efficiency DQAlgorithms can only be used to check for broken connections that lead to the complete loss of a layer. Adding the Landau fit flag allows the DQMF to spot more subtle problems with the gas flow or the HV in the chambers.

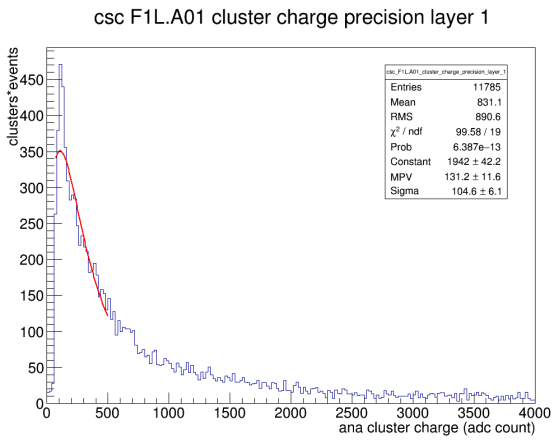

(a) all clusters

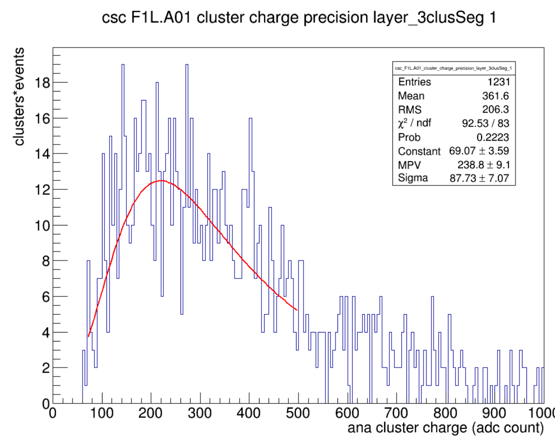

(b) clusters on segments

Figure 3.15: Cluster charge distributions for all clusters and for clusters on segments for run 212172 recorded in 2012. The distribution for clusters on segments has an MPV value much closer to the expected value of 250 ADC. Also the χ^2/ndf value is approximately one for the distribution of clusters on segments while it is approximately five for the distribution of all clusters.

Another major improvement made to the DQMF in 2012 was the introduction of the segment occupancy algorithm described above. Prior to this a basic algorithm was in place that simply checked that the segment occupancy histograms were not empty. The algorithm which replaced this is far more sophisticated and makes better use of the segment occupancy information. It allows the DQMF to determine the specific sector which is experiencing problems. This was very useful and helped to identify a new dead layer that lost HV in 2012.

Also in 2012 histograms were introduced to measure quantities such as error ratios (for ROS and RPUStatusBad events) and segment efficiencies as a function of LumiBlock during a run. The denominators of these quantities grow steadily as the run progresses. After a large amount of time passes the denominators become so large that the ratios are very small and are unlikely to exceed the threshold values specified by the DQAlgorithm. This means that they are unlikely to return red flags making the DQAlgorithms less sensitive to problems that arise late in a run. This problem is resolved by applying the same threshold test to the ratio calculated for the next to last LumiBlock rather than for the entire run. The next to last LumiBlock is used since the last LumiBlock is being filled while the DQAlgorithm is being applied. This prevents the denominator from increasing to the point that the ratio is kept below the threshold value and red flags are never returned. Figure 3.16 shows examples of these histograms taken from runs in 2012 for the RPUStatusBad error ratio and the segment efficiency. This upgrade was still in development at the end of 2012 and so was never implemented in the DQMF. The effort is ongoing to introduce these modifications to the isROSEvent, RPUStatusBad and Segment Efficiency DQAlgorithms for the next period of operation of the LHC starting in 2015.

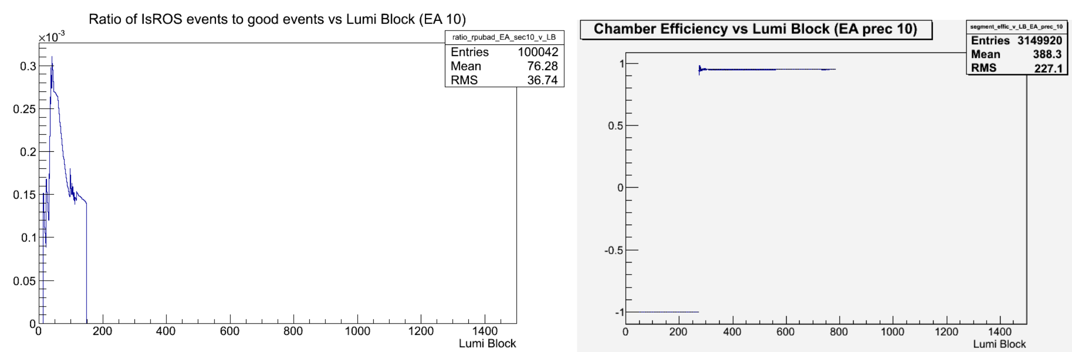

(a) error ratio v.s. LumiBlock

(b) segment efficiency v.s. LumiBlock

Figure 3.16: Histograms showing RPUStatusBad error ratio and segment efficiency v.s. LumiBlock for runs taken in 2012. The error ratio v.s. LumiBlock plot shows a sudden increase in the error ratio near the beginning of the run. The segment efficiency v.s. LumiBlock plot taken from run 208982 shows a constant value of ∼0.95 throughout the run. The modified DQAlgorithms that apply threshold tests to the next to last bin in these histograms were still under development at the end of 2012. They may be implemented for the next period of operation of the LHC starting in 2015.

3.2.5 ATLAS Trigger and Data Aquisition System

The extremely high design energy and luminosity of the LHC leads to a high rate of scattering events which exceeds the rate at which events can be recorded and stored for further analysis. To reduce the event rate and in the process select hard scattering events of interest a three tier trigger system known as the Trigger and Data Acquisition (TDAQ) system is implemented at ATLAS [84–88]. At 14 TeV the total collision cross-section is ~ 100 mb [64] (101.7 ± 2.9 mb [89] at 8 TeV). However ~ 27 mb of this corresponds to low energy elastic collisions ($pp \to pp$) where the final state protons pass directly down the beamline and are not seen in the detector. The remaining ~ 74 mb are inelastic events were the protons are broken up and the final state particles have a more substantial transverse momentum and thus fall into the acceptance of the detector. At the design luminosity of 10^{34} cm^{-2} s^{-1}this leads to an inelastic event rate of $\sim 10^{9}$ Hz . Since the proton beam in the LHC is not continuous but rather bunched, with bunches of protons crossing each other at each interaction point every 25 ns, and only one event can be recorded per bunch crossing the actual event rate is 40 MHz. This means the number of collision events per bunch crossing, known as pileup, is ~ 23. The typical size of an event in ATLAS is 1.6 MB [90]. The limitations of the computing hardware and software at ATLAS mean that events cannot be recorded at a rate $\gtrsim 200$ Hz [90]. The TDAQ system is designed as a filter used to find the most interesting hard scattering events that are useful for physics analysis while reducing the event rate from 40 MHz to ~ 200 Hz. It consists of three levels of triggers known as the Level 1 (L1) and Level 2 (L2) triggers and the Event Filter (EF). The L2 trigger and the Event Filter together are referred to as the High Level Trigger (HLT). A schematic of the three levels of the TDAQ system is shown in Fig. 3.17. Each level applies tighter selection criteria and decreases the event rate further.

The L1 trigger uses a subset of the information available from the detector in order to reach a decision of whether to reject the event or pass it to the HLT as quickly as possible. It uses information from specific muon chambers dedicated to triggering and information from the calorimeter with decreased granularity (i.e. not every calorimeter cell is used). No information from the inner detector is used at L1. Due to the limited processing time the L1 trigger is hardware based, implemented in electronics and firmware installed on the detector. The L1 trigger uses the Central Trigger Processor (CTP) to implement a menu of different triggers,

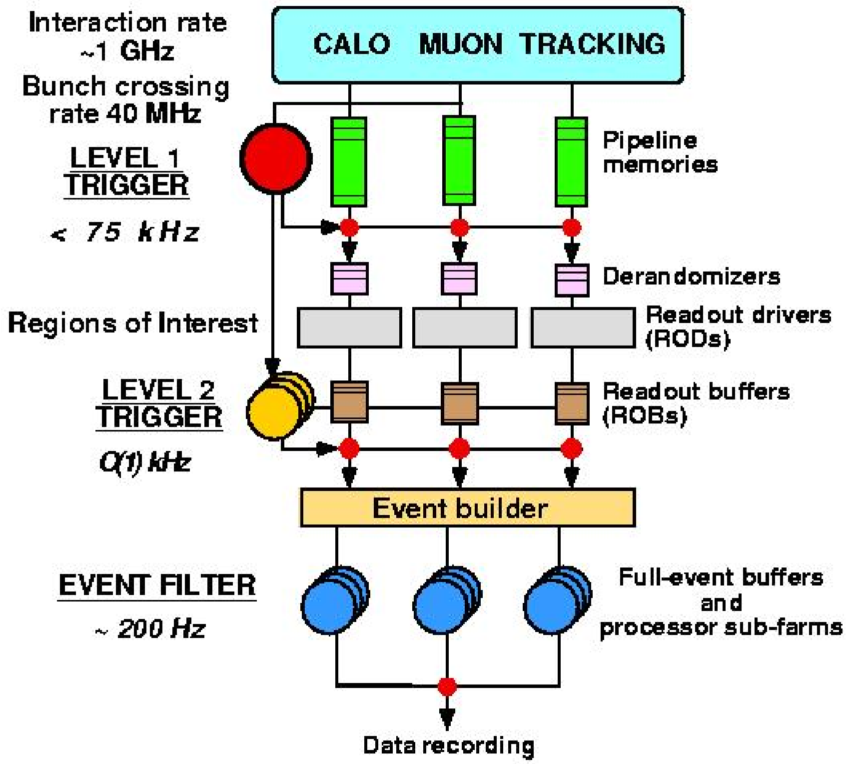

Figure 3.17: Schematic diagram of the ATLAS Trigger and Data Acquisition (TDAQ) system. [64]

defined by combinations of selection criteria and thresholds. It also assigns one or more regions of interest (ROIs), consisting of η and ϕ coordinates, to each event to identify regions of the detector with high activity for that event. While the CTP is processing the event on the basis of the subset of information used at L1 the full event information is stored in an array of custom electronics known as pipeline memories. Any event passing the L1 trigger is passed to the HLT together with its ROIs and information about which triggers it passed. The latency period of the L1 trigger is ~ 2.5 μs and it reduces the event rate to ~ 75 kHz.

The HLT uses the full information for each event, including information from the inner detector, as well as all calorimeter cells and muon chambers. Unlike the L1 trigger, which runs on custom electronics on the detector, it is software based and runs on a group of computer farms near the detector. The L2 trigger focuses on the

ROIs passed from L1 corresponding to only $\sim$ 1-2% of the full data for the event. It applies a trigger menu similar to that applied at L1 but with a tighter selection based on a certain signature such as a specific cluster shape in the calorimeter, a match between an ID track and a calorimeter cluster, a particular $E_{\mathrm{T}}^{\mathrm{miss}}$ threshold etc. The L2 trigger has a latency of $\sim$ 40 ms and reduces the event rate to O(1) kHz. The output of L2 is sent to the event builder which combines the information from the entire detector for each event. These whole events are then sent to the EF which applies algorithms, similar to those used in offline analysis, to each event's ROIs in order to make a final decision. It has a latency of $\sim$ 4 s and reduces the event rate to $\sim$ 200 Hz. The HLT reduces the event rate by a factor of $\sim 10^3$. Finally the events passing the EF are sorted into one of a series of data streams on the basis of the specific triggers they passed. The principle data streams are based on the presence of specific physics objects in the final state and include the e, μ, jet, γ, $E_{\mathrm{T}}^{\mathrm{miss}}/\tau$ and B-physics steams. Additionally a calibration and express stream are used for detector calibration and data quality monitoring respectively.

CHAPTER 4

Data and Monte Carlo Samples

4.1 Data Collection

This analysis uses proton-proton collision data collected in 2012, from April 4 through December 16, with the ATLAS detector at the CERN Large Hadron Collider (LHC) at a center of mass energy of 8 TeV. The data were collected with the Trigger and Data Acquisition (TDAQ) system described in detail in Section 3.2.5 using the electron and muon data streams. Each stream records events that pass any of the triggers on either the electron or muon trigger menu. The data are further skimmed by applying offline cuts on physics objects according to the recommendations of the Top Physics Working Group (TopCommonObjecats [91]). These criteria include the trigger requirement that considers only events that pass at least one of the following single electron and muon triggers:

- `EF_mu24i_tight` or `EF_mu36_tight` for the Muon stream,
- `EF_e24vhi_medium1` or `EF_e60_medium1` for the Egamma stream.

The number in the trigger name indicates the p_{T} threshold while "tight" and "medium1" indicates the lepton quality level (see Section 5.1). The "i" in the low p_{T} triggers indicates that these triggers include isolation requirements. This means that events containing either an isolated electron with $p_{\mathrm{T}} > 24$ GeV or an electron with $p_{\mathrm{T}} > 60$ GeV, regardless of its isolation, will pass the trigger cut with high efficiency (in the plateau region of the efficiency curves in Fig. 4.1 and 4.2). Similarly an event containing either an isolated muon with $p_{\mathrm{T}} > 24$ GeV or a muon with $p_{\mathrm{T}} > 36$ GeV regardless of its isolation will also pass the cut with high efficiency. The selection requires an inclusive OR of the four triggers so that any event matching at least one of the four triggers is recorded. The isolation requirement for low p_{T} muons is

$$\frac{p_{\mathrm{T}}^{cone20}}{p_{\mathrm{T}}^{\mu}} < 0.12$$

where p_{T}^{cone20} is the scalar sum of p_{T}, in a cone $\Delta R = 0.2$ around the muon track, of inner detector tracks having

$$p_{\mathrm{T}} > 1 \text{ GeV}$$

$$|z_0 - z_0^{\mu}| < 6mm$$

excluding the muon track itself. The isolation requirements for low p_{T} electrons are

$$\frac{p_{\mathrm{T}}^{cone20}}{p_{\mathrm{T}}^{e}} < 0.10$$

and a cut on the hadronic core isolation ($\leq$ 1 GeV) at L1. The hadronic core isolation refers to the energy deposited in the hadronic cell towers directly behind the cluster in the EM calorimeter. Both isolation cuts are applied at the Event Filter level (see Section 3.2.5). Stronger isolation requirements are applied to leptons in the offline analysis to reduce the contribution from instrumental background in the signal region. The above trigger level isolation requirements are included in the low p_{T} triggers in order to reduce the event rate to a level that can be recorded by the ATLAS software. This is unnecessary for the high p_{T} triggers since far fewer events pass the high p_{T} threshold. Another option for reducing the event rate of the low p_{T} triggers is to apply a pre-scale that arbitrarily accepts some percentage of events that pass the other requirements of the trigger. The isolation requirement has the advantage that it both reduces the event rate and selects events that are more interesting for physics analyses. The pre-scale does the former but not the latter. It is equivalent to discarding some percentage of the data before analysis which should be avoided if possible. The disadvantage of the isolation requirement is that it leads to complications in the data driven techniques used to model the fake/non-prompt lepton background where the isolation is relaxed for the loose lepton definition. This difficulty and the strategy for overcoming it are described in detail in Section 7.2.1. The full list of offline cuts applied to physics objects is detailed in Section 5.1

The trigger efficiencies are measured as a function of lepton η and E_{T} in both MC simulation and in data using a tag-and-probe technique with $Z \to ee$ and $Z \to \mu\mu$ events. The efficiency is defined as the percent of either true electrons(muons) in MC simulation or probe electrons(muons) in data that match at least one of the electron(muon) triggers. The efficiencies for the single electron triggers, as measured in data, are shown in Fig. 4.1. The efficiencies for the single muon triggers, measured in both MC simulation and data, are shown in Fig. 4.2.

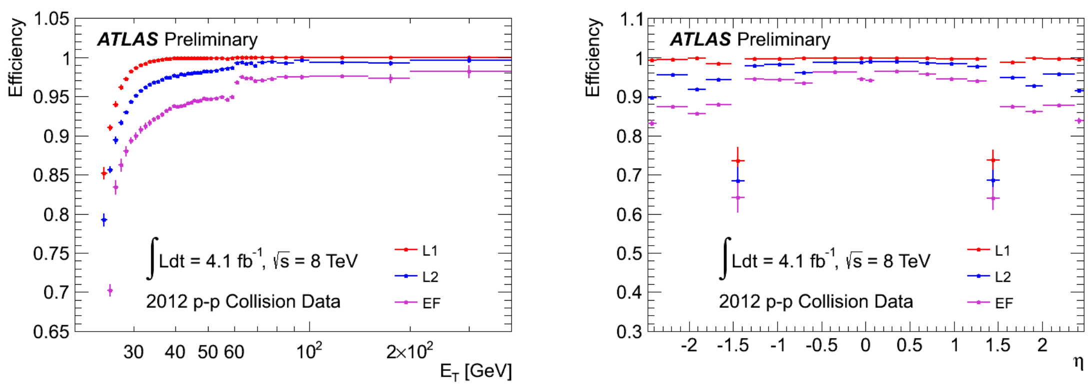

(a) Trigger efficiency v.s. E_{T}

(b) Trigger efficiency v.s. η

Figure 4.1: Electron trigger efficiencies for the logical OR of `EF_e24vhi_medium1` and `EF_e60_medium1` as a function of electron E_{T} and η. The efficiencies are shown for all three levels of the ATLAS TDAQ system: level 1 (L1), level 2 (L2) and the Event Filter (EF). sharp increases are seen at 24 GeV and 60 GeV which correspond to the low and high p_{T} thresholds. [92]

The ATLAS data for a given year are divided into periods, sub-periods, runs and luminosity blocks (LBs). The periods break up the full year of data according to the time of year it was recorded and are labelled with letters A-M. Each period is further divided into a number of sub-periods that are labelled with positive integers. The separation of events into periods and sub-periods is generally determined by changing conditions in the accelerator and/or the detector. Each sub-period contains a range of runs. The time duration of a run ranges from a few hours to

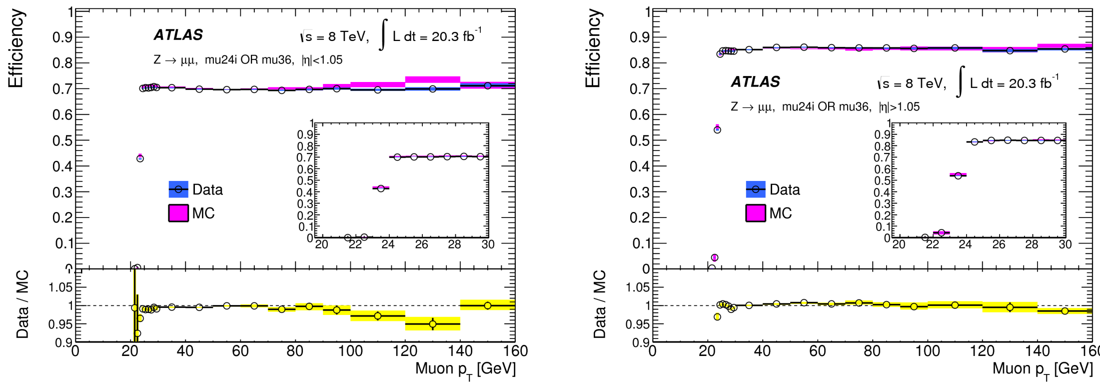

(a) Barrel region

(b) Endcap region

Figure 4.2: Muon trigger efficiencies for the logical OR of `EF_mu24i_tight` and `EF_mu36_tight` as a function of muon p_{T} in the barrel and endcap regions. [93]

$\sim$ 1 day. The breakdown of the 2012 data set into periods, sub-periods and runs is summarized in Table 4.1. There were a total of 308 runs in 2012 [94]. Within each run the events are further divided into LBs that are approximately one to two minutes in duration on average. They are defined such that the luminosity of the beam is roughly constant during each LB, however a LB transition is also issued whenever certain beam or detector conditions (e.g. trigger pre-scale settings) change. Another reason this is done is to segment the data as much as possible so that an entire run does not need to be discarded if problems arise that compromise data quality for only part of the run. In this case a limited number of LBs within the run will be effected. Data quality (DQ) algorithms are used to identify runs and the LBs within each that have high quality and thus can be used for physics analyses. These DQ algorithms are used to produce GRL (GoodRunsList) files that save this information for use by the analyzers. This analysis used the standard GRL for 2012 data recommended for all physics analyses using the full detector (data12_8TeV.periodAllYear_DetStatus-v61-pro14-02_DQDefects-00-01-00_PHYS_StandardGRL_All_Good.xml [95]). This GRL excludes the three runs from period M that used a bunch cross time of 25 ns rather than the 50 ns used for the rest of 2012.

Period	Sub-periods	Run Range	# Runs
A	A1-A8	200804-201556	29
B	B1-B14	202660-205113	72
C	C1-C9	206248-207397	34
D	D1-D8	207447-209025	48
E	E1-E5	209074-210308	29
G	G1-G5	211522-212272	18
H	H1-H6	212619-213359	22
I	I1-I3	213431-213819	14
J	J1-J8	213900-215091	29
L	L1-L3	215414-215643	10
M	M1	216399-216432	3

Table 4.1: ATLAS data taking periods and sub-periods for 2012 *pp* data. Taken from the COMA Data Period Documentation Interface. [94]

The luminosity of the colliding beams in ATLAS is measured with a variety of detectors that perform the measurement by counting the inelastic event rate at the interaction point. Multiple detectors and counting algorithms are used in order to compare results and better understand systematic errors. The ATLAS luminosity community choses one preferred detector and algorithm that it considers the most reliable. The luminosity measurement chosen as the ATLAS preferred for 2012 is that made by the Beam Condition Monitors (BCM). Further details on the luminosity measurement in ATLAS are given in Ref. [96]. The integrated luminosity of the data is determined from the GRL and the triggers used in the analysis with the LumiCalc tool [97]. The luminosity calculation is trigger dependent since different triggers have different dead times and some may be pre-scaled. Figures 4.3a and 4.3b show the peak luminosity per fill as well as the total cumulative integrated luminosity as a function of day in 2012. The peak luminosity in 2012 was 7.3×10^{33} cm^{-2} s^{-1}. The total integrated luminosity of the data used in this analysis is 20.3 fb$^{-1}\pm$ 2.8%. The estimation of the uncertainty on the integrated luminosity is described in Section 8.1.4.

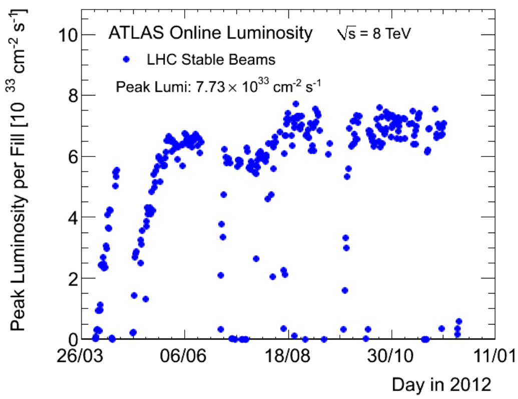

(a) Peak luminosity per fill

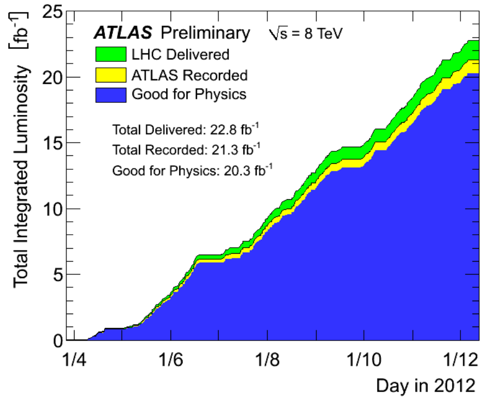

(b) Cumulative integrated luminosity

Figure 4.3: Peak luminosity per fill and integrated luminosity shown as a function of day in 2012. [98]

4.2 Monte Carlo Simulation

Monte Carlo (MC) simulations play an important role in particle physics analyses. They are used to model SM processes and predict their contribution to all of the phase space regions considered in the analysis. These include the signal region, control regions where the instrumental backgrounds (see Section 7.2) are evaluated and validation regions where the full background estimate is tested before looking at the data in the signal region. MC samples contain events that are generated from theoretical probability distribution functions of the physical observables in the final state of the pp collision such as the transverse momentum and the angular position of the final state particles. The samples are then sent through a detector simulation to simulate the response of the ATLAS detector to each event. At this point the simulation output is identical in format to the RAW data from the detector. They are then passed through the same reconstruction and identification algorithms (described in Section 5) as the data in order to produce reconstructed physics objects that can be compared directly to those in data. An important feature of MC simulations is that in addition to the reconstructed physics objects they also contain information about the simulated events prior to reconstruction known as truth information. The truth information includes all the particles in the event and their kinematic properties. In data we must infer the truth given the reconstructed objects but in MC simulation we have both since each event has been generated to simulate a particular process that might occur in nature. This makes them very valuable tools for measuring the efficiency of the reconstruction and identification algorithms.

The simulation of hadronic collisions takes place in multiple stages. The first is the hard scattering event, followed by parton showering, hadronization and the decay of final state particles. These stages are represented in Fig. 4.4. The simulation of the hard scattering event is carried out using perturbative QCD to calculate the differential cross-section for a SM process at a particular order of the relevant coupling constant (α or α_s depending on the nature of the process). The differential cross-section yields the probability distribution functions that are used to generate the events. This step is followed by the simulation of the parton shower and hadronization of colored objects in the final state that produces jets. These processes are described in more detail in Section 2.2.4. Many of the hadrons produced in this step are unstable and will decay within the detector. This in effect changes the final state and so must also be included in the simulation.

In addition to the hard scattering event there are a number of other processes that effect the final state of the collision that are referred to as the underlying event (UE) and initial and final state radiation (ISR/FSR). The UE includes beam-beam remnants and multiple parton interactions. Beam-beam remnants refers to the partons in the colliding proton-proton pair that don't participate in the hard scatter. These partons typically pass straight down the beamline however they can interact with the particles produced in the hard scatter and thus effect the final state. Multiple parton interactions (MPI) occur when more than one pair of partons within the colliding proton pair have hard or semi-hard collisions. ISR/FSR is the radiation of gluons by the initial and final state partons in the hard scatter. It is the QCD equivalent of bremsstrahlung radiation in QED where gluons are radiated instead of photons. The simulation of the UE and ISR/FSR is typically done in the

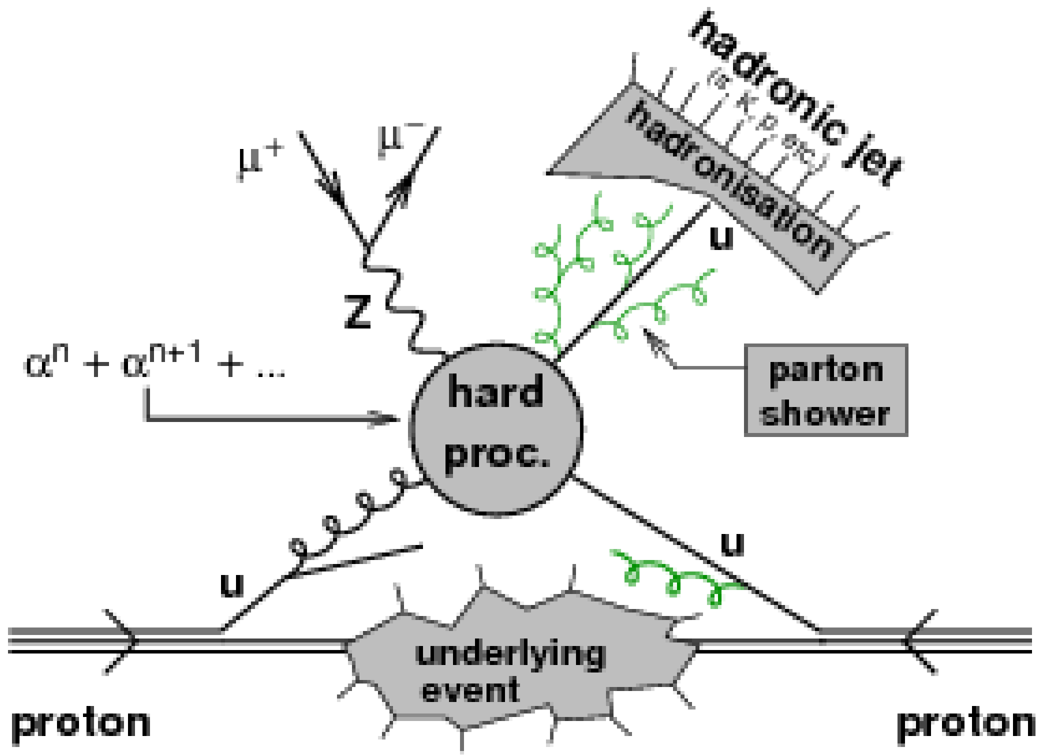

Figure 4.4: Diagram of a hard hadronic scattering event [99].

showering and hadronization steps.

Another important part of the MC simulation is the pile-up arising from extra proton-proton collisions in addition to that associated with the hard scatter of interest. Pile-up includes both *pp* collisions within the same bunch crossing as the hard scatter (in-time pile-up) as well as collisions from neighboring bunch crossings (out-of-time pile-up). The average number of pile-up events per bunch crossing in 2012 was 36.2 [100]. The majority of the collisions that make up pile-up are "soft" or low energy collisions. As such, pile-up is simulated by superimposing minimum bias (min-bias) events over the hard scattering event. Min-bias events are events selected with a loose trigger intended to select inelastic collisions with as little bias as possible. They are typically low energy events. The number of min-bias events added to each hard scatter event is taken from a Poisson probability distribution function with a mean set by the luminosity and the total min-bias cross-section.

Pile-up also includes the effects arising from beam-gas and beam-halo events.

A beam-gas event involves a collision between a proton in the beam and a residual gas particle in the beam pipe within the ATLAS cavern which leads to a measurable signal in the detector. An ultra high vacuum is maintained in the beam pipe to reduce the probability of these collisions and ensure a beam lifetime of $\sim$ 100 hours. The gas in the beam pipe is primarily made up of H_2, CH_4, CO and CO2 with densities of around 10^{13} molecules/m^3 per molecular species at the entrance of the ATLAS cavern. Despite this, collisions between protons in the beam and residual gas particles in the beam pipe is a non-negligible effect that must be included in the simulation.

The beam-halo refers to a low density ring of particles in the beam that surround the core of the bunch at large radial distances compared to the size of the core itself (16 μm). These particles come from a variety of sources including collisions of pairs of protons within a given bunch, collisions of protons with gas particles in the beam-pipe outside the ATLAS cavern and low energy inelastic collisions of protons in crossing bunches at the interaction point. In each of these cases the collisions can either knock protons out of the core of the bunch or produce new particles that are caught in the bending field of the superconducting magnets (see Section 3.1) and thus follow the bunch as it moves through the LHC beam pipe at large radial distances up to several meters (for reference the LHC beam pipe has a radius of 29 mm). The particles in the halo are predominantly charged hadrons such as protons and muons in order of decreasing flux. These particles can enter the ATLAS detector as the bunch approaches the interaction point and leave a measurable signal particularly in the end-cap regions. Further details of beam-gas and beam-halo events can be found in Ref. [101].

It is common to use different MC generators to simulate the different stages of the collision. Generators that simulate only the hard scattering of partons from the calculation of matrix elements in QFT are referred to as Matrix Element (ME) generators. ME generators calculate the cross-section for a given process using perturbative QCD to calculate the cross-section for parton interactions and the

QCD factorization theorem to relate these to the cross-section for pp collisions. A crucial element in applying the factorization theorem is the Parton Distribution Function (PDF) for the proton which describes the distribution of the fractional momentum for each parton species in the proton. Many ME generators are limited to leading order (LO) calculations where only leading order Feynman diagrams (e.g. no diagrams containing loops) are considered. These are referred to as LO or tree level ME generators. There are also generators capable of next-to-leading order (NLO) calculations, where higher order diagrams with more vertices, are included. These are referred to as NLO ME generators.

The events produced by ME generators don't represent actual physical events since they contain isolated partons that don't actually exist in the final state due to color confinement (see Section 2.2.4). Because of this, it is essential that ME generators are interfaced with generators capable of simulating the parton shower and hardonization as well as the UE and pile-up. Showering and Hadronization Generators (SHGs) evolve events produced with ME generators from parton level to the particles measured in the final state. The parton shower is simulated by allowing partons to radiate gluons (QCD bremsstrahlung) and allowing partons to split into pairs of other partons. The partons produced in the shower are then combined into color neutral hadrons following phenomenological hadronization models tuned to experimental data. As mentioned above the simulation of ISR/FSR and the UE is handled by the SHGs. ISR/FSR is included in the parton showering step and beam-beam remnants and multiple parton interactions are included in the hadronization step because their products may be color connected to products of the hard scatter. There are also general purpose MC generators that can be used to simulate the full collision including the hard scatter, parton shower and hadronization making it unnecessary to interface with a second generator.

The MC generators used in this analysis are MadGraph (MG) v5.1, Pythia v6.4 and v8.1, Sherpa v1.4 and Protos v2.2. Madgraph is an LO ME generator while Pythia, Sherpa and Protos are general purpose generators. Protos is specialized for heavy quark production and thus is used for the generation of the vector-like quark signals. When MG is used it is interfaced with PYTHIA for showering and hadronization. More information about each of these generators can be found in Ref. [102–106].

After the MC samples are generated they are sent through a simulation of the ATLAS detector based on the GEANT4 simulation toolkit [107,108]. The simulation accounts for the detector geometry, the layout of each subsystem, the materials each detector is made of, the principles of detection in each and up-to-date information about inactive cells and electrical components. It simulates the interaction of the final state particles in each MC event with the detector, including their bending due to the magnetic fields in ATLAS as well as EM and hadronic showering in the calorimeter. It then simulates the response of the detector producing for each final state particle a set of signals for each of the detector modules through which it passes. The simulation takes into account up-to-date information about the known response of the detector and calibration information from test beam data. The full simulation with GEANT4 is an extremely accurate simulation of ATLAS. A disadvantage of using GEANT4 is that it is very time consuming. In fact it is usually the most time consuming part of the simulation chain. To speed up the process a faster simulation known as AtlFastII [109] (AF2) is sometimes applied which consists of a GEANT simulation of the inner detector and muon spectrometer and a faster simulation of shower development in the calorimeter based on smearing the MC truth information with resolutions measured in the full simulation. A reduction of CPU time of a factor of three can be achieved with AtlFastII compared with the full GEANT4 simulation. In cases where both simulations are used the final yields from each are compared and found to be in agreement within the systematic uncertainty assigned to the efficiency estimate.

Tables 4.3, 4.4 and 4.2 list the MC simulations used for each of the signal and background samples in the analysis as well as the generators used to produce them, the parton distribution function (PDF), cross-section and the detector simulation. The various background processes are described in detail in Section 7.1.

ATLAS / SampleID	Process	Generator	PDF	Cross-section [pb]	K-factor	$\mathcal{L}$ dt [fb^{-1}]	Det. sim.
			$t\bar{t}$+boson(s)				
119353	$t\bar{t}W$	MG+Pyth.	CTEQ6L1	0.104	1.17	3284	G4
174830	$t\bar{t}W$j excl.	MG+Pyth.	CTEQ6L1	0.053	1.17	6404	G4
174831	$t\bar{t}W$jj incl.	MG+Pyth.	CTEQ6L1	0.041	1.17	8237	G4
119355	$t\bar{t}Z$	MG+Pyth.	CTEQ6L1	0.068	1.35	4377	G4
174832	$t\bar{t}Z$j excl.	MG+Pyth.	CTEQ6L1	0.045	1.35	6532	G4
174833	$t\bar{t}Z$jj incl.	MG+Pyth.	CTEQ6L1	0.040	1.35	7446	G4
158814	$t\bar{t}W^+W^-$	MG+Pyth.	MSTW2008	0.0022	1	91730	AF2
			$t\bar{t}H$				
161305	$H \to W^+W^-$	Pythia 8	CTEQ6L1	0.0195	1.43	7014	G4
169072	$H \to ZZ$	Pythia 8	CTEQ6L1	0.0023	1.45	29300	G4
161719	$H \to \tau^+\tau^- \to \ell h$	Pythia 8	CTEQ6L1	0.0029	1.30	8051	G4
			Diboson				
185393	$W^\pm W^\pm \to \ell\nu\ell\nu$ EWK	Sherpa	CT10	0.028	0.84	4332	G4
185394	$W^\pm W^\pm \to \ell\nu\ell\nu$ QCD	Sherpa	CT10	0.016	1.04	6007	G4
185396	$WZ \to \ell\ell\ell\nu$ EWK	Sherpa	CT10	0.082	0.89	6809	G4
185397	$WZ \to \ell\ell\ell\nu$ QCD	Sherpa	CT10	2.34	1.27	672	G4
147196	$ZZ \to \ell\ell\ell\ell$ EWK	Sherpa	CT10	0.0069	1	27120	G4
126894	$ZZ \to \ell\ell\ell\ell$ QCD	Sherpa	CT10	8.73	1.11	186	G4
			$W^\pm W^\pm$jj from DPI				
147281	DPI W+jet	Pythia 8	CTEQ6L1	0.0019	1	10310	G4
			WH				
161455	$H \to W^+W^- \to \ell\nu qq$	Pythia 8	CTEQ6L1	0.053	1.25	301	G4
161105	$H \to W^+W^- \to \ell\nu\ell\nu$	Pythia 8	CTEQ6L1	0.012	1.32	1213	G4
161646	$H \to \tau^+\tau^- \to \ell h$	Pythia 8	CTEQ6L1	0.018	1.18	24060	G4
			ZH				
161505	$H \to W^+W^- \to \ell\nu qq$	Pythia 8	CTEQ6L1	0.028	1.38	5623	G4
161155	$H \to W^+W^- \to \ell\nu\ell\nu$	Pythia 8	CTEQ6L1	0.0068	1.43	2058	G4
			Triboson				
167006	$WWW^* \to \ell\nu\ell\nu\ell\nu$	MG+Pyth.	CTEQ6L1	0.0051	1	9811	G4
167007	$ZWW^* \to \ell\ell\ell\nu\ell\nu$	MG+Pyth.	CTEQ6L1	0.0016	1	32160	G4
			tWZ				
179991	$Z \to \ell\ell$	MG+Pyth.	CTEQ6L1	0.0041	1	24211	G4
			tH				
189200	$H \to WW$	MG+Pyth.	CT10	0.00366	1	273596	G4
189203	$H \to ZZ$	MG+Pyth.	CT10	0.00981	1	1113855	G4
189204	$H \to \tau\tau$	MG+Pyth.	CT10	0.000449	1	465374	G4

Table 4.2: Monte Carlo samples used for the background estimation (ℓ means any kind of charged lepton). The sample identifier is the sample number in the ATLAS production. The K-factor is the rescaling factor between LO and NLO cross-sections. $\mathcal{L}$ is the integrated luminosity corresponding to each sample, in fb^{-1}. MG+Pyth. means MadGraph followed by Pythia. [110]

Table 4.3: Monte Carlo samples for the various vector-like quark signals. The sample identifier is the sample number in the ATLAS production. Note that the pair production cross section is the same for all heavy quarks (b', vector-like B, and vector-like T).

Sample	Mass (GeV)	Generator	PDF	Cross-section [pb]	Events	Detector simulation
Vector-like B pair production						
180308	350	Protos	MSTW2008LO	5.32	238000	AF2
180265	400	Protos	MSTW2008LO	2.39	249499	AF2, G4
180310	450	Protos	MSTW2008LO	1.15	250000	AF2
180312	500	Protos	MSTW2008LO	0.589	250000	AF2
180314	550	Protos	MSTW2008LO	0.315	249000	AF2
158937	600	Protos	MSTW2008LO	0.174	150000	AF2, G4
180316	650	Protos	MSTW2008LO	0.0996	248999	AF2
180318	700	Protos	MSTW2008LO	0.0583	499000	AF2
180320	750	Protos	MSTW2008LO	0.0349	249000	AF2
180267	800	Protos	MSTW2008LO	0.0212	250000	AF2, G4
180322	850	Protos	MSTW2008LO	0.0131	248000	AF2
Vector-like T pair production						
180307	350	Protos	MSTW2008LO	5.32	249999	AF2
180264	400	Protos	MSTW2008LO	2.39	250000	AF2, G4
180309	450	Protos	MSTW2008LO	1.15	250000	AF2
180311	500	Protos	MSTW2008LO	0.589	249500	AF2
180313	550	Protos	MSTW2008LO	0.315	250000	AF2
158936	600	Protos	MSTW2008LO	0.174	99999	AF2, G4
180315	650	Protos	MSTW2008LO	0.0996	250000	AF2
180317	700	Protos	MSTW2008LO	0.0583	497999	AF2
180319	750	Protos	MSTW2008LO	0.0349	250000	AF2
180266	800	Protos	MSTW2008LO	0.0212	249000	AF2, G4
180321	850	Protos	MSTW2008LO	0.0131	250000	AF2

Table 4.4: Monte Carlo samples for the $T_{5/3}$ signals. Note that the pair production cross section is the same for all heavy quarks (vector-like B, vector-like T, and $T_{5/3}$).

Sample	Mass (GeV)	Generator	PDF	Cross-section [pb]	Events	Detector simulation
Pair production						
188554	600	MG5+Pythia8	CTEQ6L1	0.174	100000	AF2
188555	650	MG5+Pythia8	CTEQ6L1	0.0996	99999	AF2
188556	700	MG5+Pythia8	CTEQ6L1	0.0583	100000	AF2
188557	750	MG5+Pythia8	CTEQ6L1	0.0349	100000	AF2
188558	800	MG5+Pythia8	CTEQ6L1	0.0212	100000	AF2
188559	850	MG5+Pythia8	CTEQ6L1	0.0131	100000	AF2
188560	900	MG5+Pythia8	CTEQ6L1	0.00819	100000	AF2
188561	950	MG5+Pythia8	CTEQ6L1	0.00517	99999	AF2
188562	1000	MG5+Pythia8	CTEQ6L1	0.00329	100000	AF2
Single production $\lambda = 1$						
188565	600	MG5+Pythia8	CTEQ6L1	0.0217	100000	AF2
188566	650	MG5+Pythia8	CTEQ6L1	0.0147	99999	AF2
188567	700	MG5+Pythia8	CTEQ6L1	0.0101	100000	AF2
188568	750	MG5+Pythia8	CTEQ6L1	0.0071	100000	AF2
188569	800	MG5+Pythia8	CTEQ6L1	0.005	100000	AF2
188570	850	MG5+Pythia8	CTEQ6L1	0.00364	99000	AF2
188571	900	MG5+Pythia8	CTEQ6L1	0.0026	100000	AF2
188572	950	MG5+Pythia8	CTEQ6L1	0.0019	100000	AF2
188573	1000	MG5+Pythia8	CTEQ6L1	0.0014	100000	AF2
Single production $\lambda = 0.5$						
188576	600	MG5+Pythia8	CTEQ6L1	0.0054	99999	AF2
188577	650	MG5+Pythia8	CTEQ6L1	0.0037	100000	AF2
188578	700	MG5+Pythia8	CTEQ6L1	0.00254	100000	AF2
188579	750	MG5+Pythia8	CTEQ6L1	0.00177	100000	AF2
188580	800	MG5+Pythia8	CTEQ6L1	0.00125	100000	AF2
188581	850	MG5+Pythia8	CTEQ6L1	0.0009	100000	AF2
188582	900	MG5+Pythia8	CTEQ6L1	0.00065	99999	AF2
188583	950	MG5+Pythia8	CTEQ6L1	0.00048	100000	AF2
188584	1000	MG5+Pythia8	CTEQ6L1	0.00035	100000	AF2

CHAPTER 5

Event Reconstruction and Object Identification

The data collected by the ATLAS detector consists of the digitized electrical response from a large number of readout channels. It is recorded as bitstream or raw data. In order to facilitate the analysis of the proton-proton collisions these readout signals are used to reconstruct a picture of what particles were produced in the final state and what their properties were. Event reconstruction is the process of using the raw data to build detector objects such as tracks, vertices and energy clusters and ultimately physics objects such as particles and jets. Object identification refers to the algorithms used to identify specific particle species such as electrons and muons according to criteria placed on the reconstructed final state objects. These algorithms are designed to optimize signal efficiency and background rejection and to provide the best possible measurements of physical quantities. They are developed and tested using data and Monte Carlo simulated samples. Object definitions vary depending on the analysis. Generally each analysis follows the definitions recommended by the Physics Analysis (PA) group to which it belongs within ATLAS. Each PA group is devoted to a specific area of research (e.g. Top, Higgs, SUSY). For this analysis the important physics objects that must be defined are jets, b-jets, electrons, muons and missing transverse momentum ($E_{\mathrm{T}}^{\mathrm{miss}}$).

5.1 Object Identification

The identification of electrons, muons and jets and the calculation of missing transverse momentum in this analysis generally follow the recommendations of the Top PA Group known as TopCommonObjects2012 [111]. Instances where the definitions used in this analysis deviate from these recommendations are noted. The variables used to describe these final state objects are the transverse momentum p_{T} measured in the inner detector and muon spectrometer (for muons), transverse energy E_{T} measured in the calorimeter, the azimuthal angle ϕ and the pseudorapidity η (defined in terms of the polar angle with respect to the z-axis in Eq. 3.1). In addition to these, other variables describe the event as a whole. These include the angular separation between different final state objects defined as $\Delta\mathrm{R} = \sqrt{\Delta\phi^2 + \Delta\eta^2}$ and the missing transverse momentum described in detail below. These variables are used in the selections that define each of these objects in the final state. Before applying object level selection criteria an event must meet some minimal requirements. Each event is required to have at least one vertex formed from at least five particle tracks with a $p_{\mathrm{T}} > 0.4$ GeV. In cases where more than one such vertex exists the primary vertex is defined as the vertex with the largest scalar sum of the p_{T} of the tracks associated with it.

5.1.1 Jets

Jets are reconstructed by combining energy clusters in the calorimeter according to the anti-k_t algorithm described in detail in Ref. [112–114]. The anti-k$_t$ algorithm represents an extension of a class of sequential recombination algorithms that build jets by recombining entities, such as particles (in the case of MC simulation) or calorimeter clusters, according to the distance parameters d$_{ij}$ and d$_{iB}$ defined as:

$$d_{ij} = min(k_{ti}^{2p}, k_{tj}^{2p})\frac{\Delta_{ij}^2}{R^2}$$
$$d_{iB} = k_{ti}^{2p}$$

d_{ij} is the distance parameter between entities i and j and d_{iB} is the distance parameter between entity i and the beam. $\Delta_{ij} = (y_i - y_j)^2 + (\phi_i - \phi_j)^2$ where y and ϕ are the rapidity and azimuth respectively. R is a constant which is set to 0.4 for the jest used in this analysis. The algorithm proceeds by identifying the smallest distance d_{ij} or d_{iB} for all i and j on the list of entities. If the smallest distance is a d_{ij}, entities i and j are recombined. If the smallest distance is a d_{iB}, it is labeled a jet and removed from the list. In addition to the radius parameter R the parameter p is included to govern the relative power of the energy scale versus the geometrical scale Δ_{ij}. Setting p = 0 defines the Cambridge/Aachen (CA) algorithm. This essentially removes the energy scale entirely and simply recombines entities based on their angular separation alone, starting from the entities that are closest together. Setting p = 1 defines the k_t algorithm which scales the distance parameters so that lower energy entities are recombined before higher energy entities. Setting p = -1 defines the anti-k_t algorithm which is used to reconstruct jets for this analysis.

The anti-k_t algorithm is designed to recombine high energy entities before low energy entities. This choice of the value of p exhibits some clear advantages over the values that define the CA and k_t algorithms. The main advantage is that the reconstructed jets are less sensitive to the presence of soft radiation in the event. This is desirable since soft radiation is subject to large random fluctuations on a jet-by-jet basis. The size, shape and location of the jets reconstructed by the anti-k_t algorithm are effected far less by variations in the amount of soft radiation. Figure 5.1 shows the distribution of the active area of jets in simulated dijet events for a number of jet finding algorithms. The distribution for the anti-k_t algorithm can be closely approximated with a δ-function around the value πR^2. The distributions for the other algorithms show a much broader spread of values reflecting their sensitivity to variations in the level of soft radiation in each event. In addition to this, anti-k_t jets tend to be roughly circular in shape in (y,ϕ) space. This is a consequence of the fact that the jet is initiated by recombining the hardest entities first. The location of the jet axis changes very little after the initial recombination since the entities recombined thereafter are comparatively low energy. In both the CA and k_t algorithms the jet axis wanders significantly in (y,ϕ) space as the jet is being built leading to an irregular shape. This can be seen in the Fig. 5.2 which shows a sample parton-level event generated with Herwig reconstructed with four different jet finding algorithms. The circular shape characteristic of anti-k_t jets is beneficial for a number of reasons. In particular it simplifies the implementation of jet grooming techniques designed to account for the effect of pile-up in jet reconstruction.

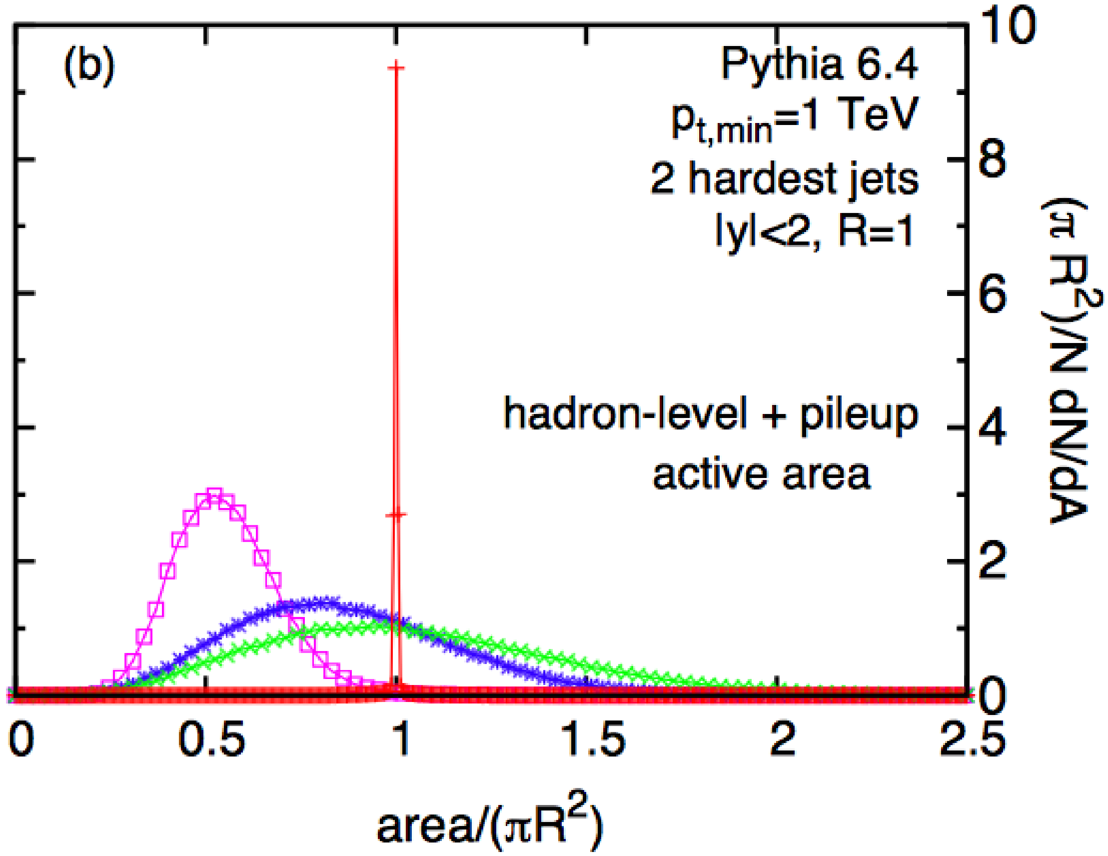

Figure 5.1: Distribution of active jet area in dijet events generated with PYTHIA6.4 with a minimum p_{T} of 1 TeV. Only the two hardest jets have been kept with a further requirement that $|\, y \,| \leq 2$. The distribution obtained with anti-k_t is compared with that obtained with a number of other algorithms. [112]

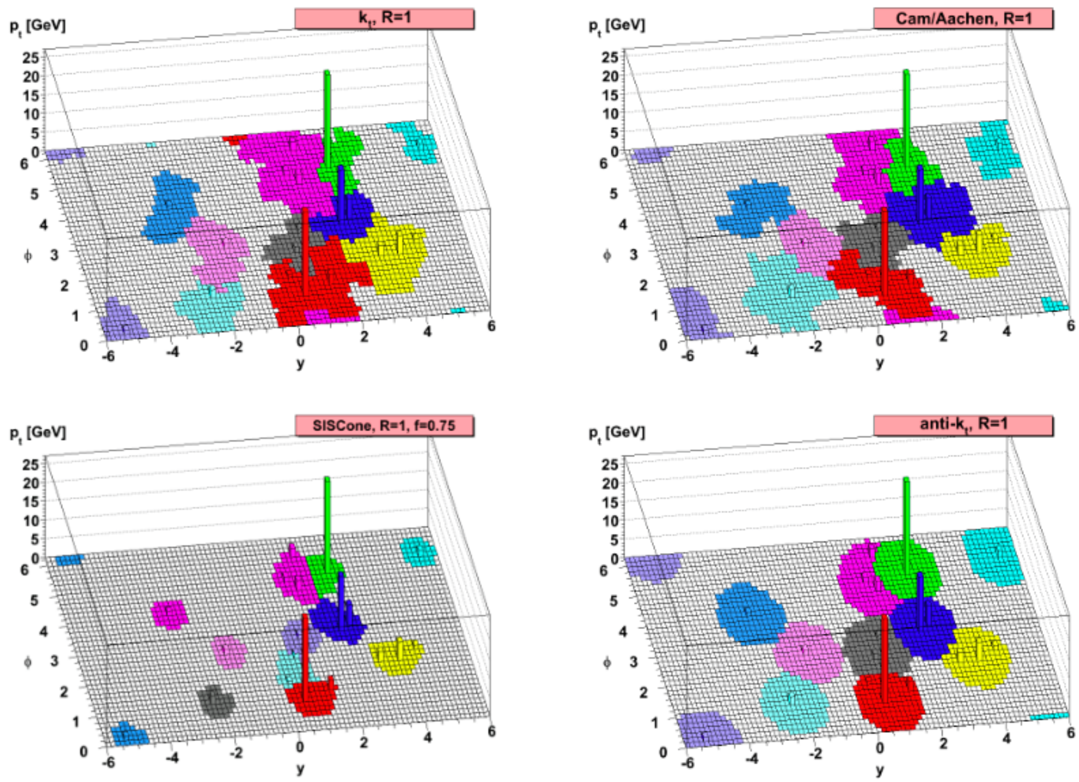

Figure 5.2: A sample parton level event generated with Herwig together with many soft random "ghosts", reconstructed with four different jet algorithms. The shape of the jets produced by the CA and k_t algorithms depends on the specific sets of ghosts used and changes when the ghosts are modified. [112]

Before combining calorimeter clusters to form jets the clusters are recalibrated using the local cell signal reweighting (LCW) method [115]. The clusters are originally calibrated at the EM scale, which correctly measures the energy deposited in the calorimeter by particles produced in electromagnetic showers. The LCW method recalibrates the energy of the clusters in order to better account for the response of the calorimeter to hadrons. This calibration aims at an improved resolution compared to the EM scale by partially correcting the signals from hadronic deposits and thus reduces fluctuations from the non-compensating nature of the ATLAS calorimeter. Dedicated corrections address effects of calorimeter non-compensation, signal losses due to noise threshold effects and energy loss in non-instrumented regions close to the cluster. The TopCommonObjets recommendation for 2012 was to use jets build from clusters calibrated at LCW scale. This is different from top analyses using 2011 data, where jets at the (EM) scale were used.

Jet quality selection criteria are used to distinguish between high p_{T} jets produced in proton-proton collisions and background jets arising from a variety of sources including beam-gas and beam-halo events (described in Section 4.1) and calorimeter noise. Four levels of jet quality known as *Looser*, *Loose*, *Medium* and *Tight* are defined by placing cuts on discriminating variables. Each successive jet quality level applies stricter cuts and thus has higher background rejection and lower efficiency for reconstruction of good jets. In order to distinguish between good jets and bad jets it is necessary to distinguish good energy deposits from noise. The pulse quality ($\mathcal{Q}_{cell}^{LAr}$) is a measure of how closely the pulse shape in a calorimeter cell matches the expectation from showering particles. Energy deposits arising from particles showering in the calorimeter cause a characteristic pulse in the calorimeter cells that can be used to distinguish ionization signals from noise. The pulse quality is defined as the quadratic difference between the actual and expected pulse shape summed across the five measurements that constitute the pulse. It is given by the expression

$$\mathcal{Q}_{cell} = \Sigma_{j=1}^{5}(s_j - Ag_j^{phys})^2$$

where s_j are the amplitudes of each measurement, A is the total measured amplitude of the pulse and g_j^{phys} is the normalized predicted ionization shape. The variables used to discriminate between good jets to be used for physics analysis and background jets are the following:

- f_{LAr}: fraction of energy in LAr calorimeter cells
- f_{HEC}: fraction of energy in HEC calorimeter cells
- $\langle \mathcal{Q} \rangle$: average pulse quality of calorimeter cells ($\mathcal{Q}_{cell}$) in the jet weighted by the square of the cell energy.
- f_Q^{LAr}: fraction of energy in LAr calorimeter cells with poor signal shape quality

($\mathcal{Q}_{cell}^{LAr}$> 4000)

- f_Q^{HEC}: fraction of energy in HEC calorimeter cells with poor signal shape quality ($\mathcal{Q}_{cell}^{HEC}$> 4000)

The specific cuts placed on these variables for each jet quality level are given in Table 5.1. These criteria were optimized by studying events enriched with good jets and background jets in both MC simulated samples and data collected in 2011 at a center-of-mass energy of 7 TeV [116]. Reconstruction efficiencies were measured for each jet quality selection using the tag-and-probe method with dijet events. These efficiencies are shown in Fig. 5.3 as a function jet p_{T} for eight different η ranges. The *Loose* jet quality selection is adopted for this analysis as recommended by TopCommonObjects2012 [111].

In addition to the cuts listed in Table 5.1 the jets used in this analysis must satisfy a number of other requirements. They must have p_{T}> 25 GeV and $\mid \eta \mid <$ 2.5. The jet energy is re-calibrated to the hadronic energy scale using η and p_{T} dependent corrections that are determined from collision and test beam data as well as simulations [115]. To mitigate the effect of pile-up (see Section 4.1) the jet-vertex-fraction (JVF) [117] is defined as the ratio of the scalar sum of the p_{T} of the tracks within the jet originating from the primary vertex to the scalar sum of the p_{T} of all tracks matched to the jet. For jets without associated tracks JVF = -1. Jets with p_{T}< 50 GeV, $\mid \eta \mid <$ 2.4 are required to have |JVF| > 0.5. Jets that have p_{T}> 50 GeV or $\mid \eta \mid >$ 2.4 have no requirement placed on JVF. In order to avoid reconstructing electrons as jets the latter are required to be separated from *Medium* electrons with an angular separation ΔR(e,jet) of at least 0.2. Jet candidates which fail this requirement are not reconstructed as jets and the calorimeter cluster is associated with the electron.

	Looser	Loose
HEC spikes	($f_{HEC} > 0.5$ and $\mid f_Q^{HEC} \mid > 0.5$ and $\langle Q \rangle > 0.8$) or $\mid E_{neg} \mid > 60$ GeV	Looser or ($f_{HEC} > 0.5$ and $\mid f_Q^{HEC} \mid > 0.5$)
Coherent EM noise	($f_{EM} > 0.95$ and $f_Q^{LAr} > 0.8$ and $\langle Q \rangle > 0.8$ and $\mid \eta \mid < 2.8$)	Looser or ($f_{EM} > 0.95$ and $f_Q^{LAr} > 0.8$ and $\mid \eta \mid < 2.8$)
Non-collision background	($f_{max} > 0.99$ and $\mid \eta \mid < 2$) or ($f_{EM} < 0.05$ and $f_{ch} < 0.05$ and $\mid \eta \mid < 2$) or ($f_{EM} < 0.05$ and $\mid \eta \mid \geq 2$)	Looser or $\mid t_{jet} \mid > 25$ ns

(a) central region

	Medium	Tight
HEC spikes	Loose or $f_{HEC} > 1 - \mid f_Q^{HEC} \mid$	Medium
Coherent EM noise	Loose or ($f_{EM} > 0.9$ and $f_Q^{LAr} > 0.8$ and $\mid \eta \mid < 2.8$)	Medium or $f_Q^{LAr} > 0.95$ or ($f_{EM} > 0.98$ and $f_Q^{LAr} > 0.05$)
Non-collision background	Loose or $\mid t_{jet} \mid > 10$ ns or ($f_{EM} < 0.05$ and $f_{ch} < 0.1$ and $\mid \eta \mid < 2$) or ($f_{EM} > 0.95$ and $f_{ch} < 0.05$ and $\mid \eta \mid < 2$)	Medium or ($f_{EM} < 0.1$ and $f_{ch} < 0.2$ and $\mid \eta \mid < 2.5$) or ($f_{EM} > 0.9$ and $f_{ch} < 0.1$ and $\mid \eta \mid < 2.5$) or ($f_{ch} < 0.01$ and $\mid \eta \mid < 2.5$) or ($f_{EM} < 0.1$ and $\mid \eta \mid \geq 2.5$)

(b) forward region

Table 5.1: Criteria used to identity fake jets for the *Looser*, *Loose*, *Medium* and *Tight* selections. HEC spikes and Coherent EM noise are two types of calorimeter noise, while Non-collision background refers to energy depositions due to beam-gas and beam-halo events. [116]

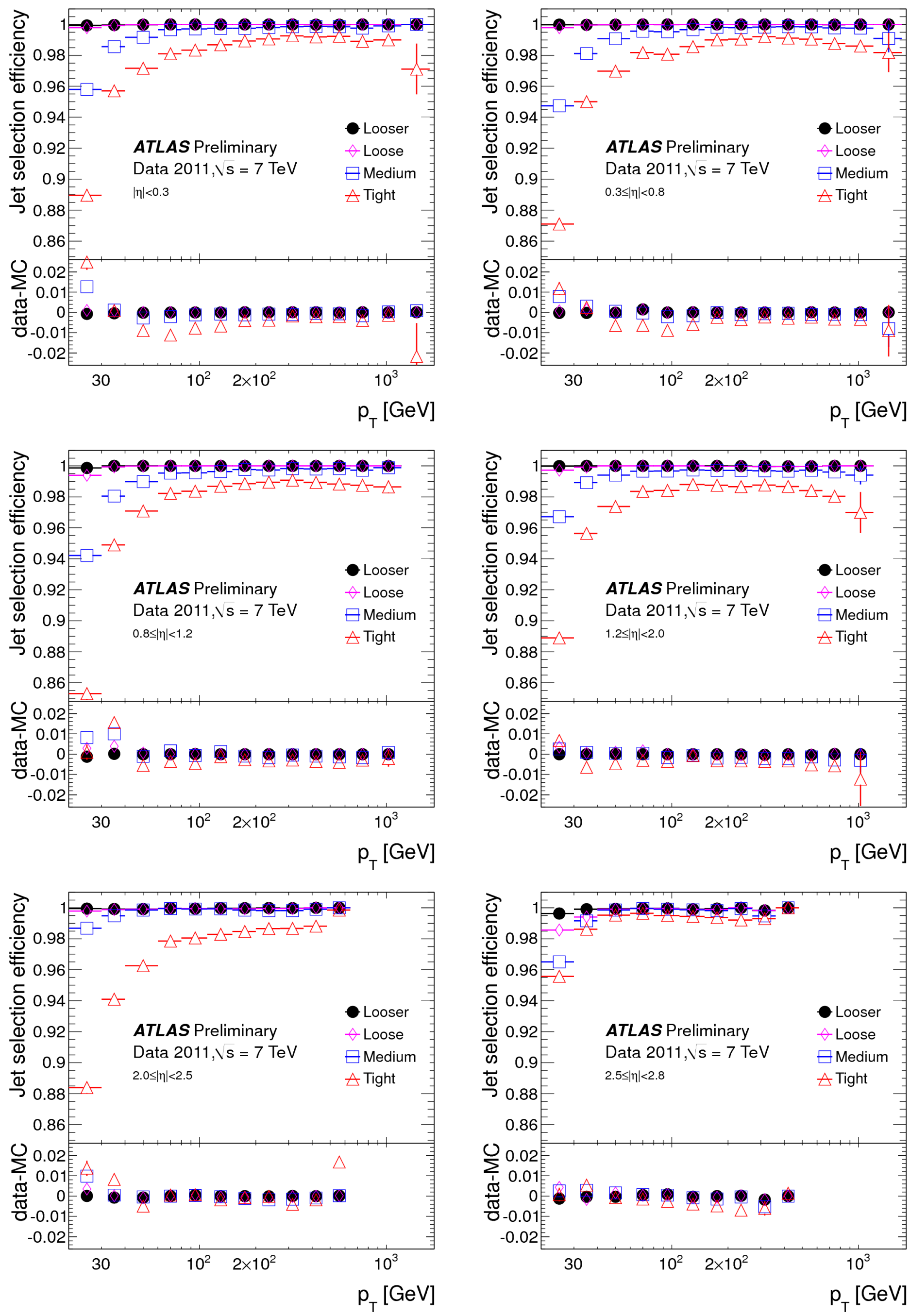

Figure 5.3: Jet reconstruction efficiencies for each of the four selection criteria (*Looser*, *Loose*, *Medium* and *Tight*) as a function of p_{T} for eight η bins, from $\mid \eta \mid <$ 0.3 (top-left) to $2.5 < \mid \eta \mid < 2.8$ (bottom-right). The efficiencies are extracted from both tag-and-probe measurements using dijet events in minbias data as well as dijet MC simulations. [116]

5.1.2 B-tagging

An important part of the selection criteria for this analysis is the identification of jets containing b-hadrons, known as b-jets. The techniques implemented in this analysis for identifying b-jets follow those recommended in TopCommonObjects [111]. B-jets are distinguished from light flavor jets in a number of ways. The main feature of b-jets that allow them to be distinguished from light flavor jets is the long lifetime of the b-hadron, which leads to tracks with large impact parameters and secondary vertices within the jet. In addition to this, b-hadrons have large mass and large branching ratio for leptonic decay compared with light flavor jets. Multivariate algorithms exploit these differences to tag jets which have high probability of containing a b-hadron. The b-tagging algorithm used in this analysis, known as MV1, is a neural network-based algorithm which combines the output of three separate tagging algorithms: IP3D, SV1 and JetFitterCombnNN. Each of these tagging algorithms is designed to discriminate between b-jets and light flavor jets by exploiting particular features of b-jets. IP3D uses the impact parameter of tracks in jets while SV1 looks for secondary vertices. JetFitterCombnNN uses similar variables as SV1 and additional variables such as flight length significances of the vertices. A full description of these individual tagging algorithms can be found in Ref. [118].

MV1 returns a value for each jet that characterizes the likelihood that it contains a b-hadron. Jets are then classified as b-jets if the MV1 value is greater than a threshold value chosen to correspond to a particular b-tagging efficiency. B-tagging efficiency is defined as the fraction of true b-jets which are identified as b-jets by the tagging algorithm. The c-jet mistag rate is the percent of jets containing c-quarks that are mistakenly identified as b-jets by the tagging algorithm. The light-jet rejection rate is the reciprocal of the light jet mistag rate, which is the fraction of true light flavor jets which are mistakenly identified as b-jets by the tagging algorithm. These quantities are measured using a $t\bar{t}$ MC simulated sample. Figure 5.4 shows the light-jet rejection plotted against b-tagging efficiency for the MV1 tagging algorithm. For each b-tagging algorithm and jet collection a set of operating points are defined based on the b-tagging efficiency. These operating points are summarized in Table 5.2. The operating point used in this analysis is that for the MV1 tagging algorithm and LCW - jets corresponding to a 70% b-tagging efficiency: 0.7892

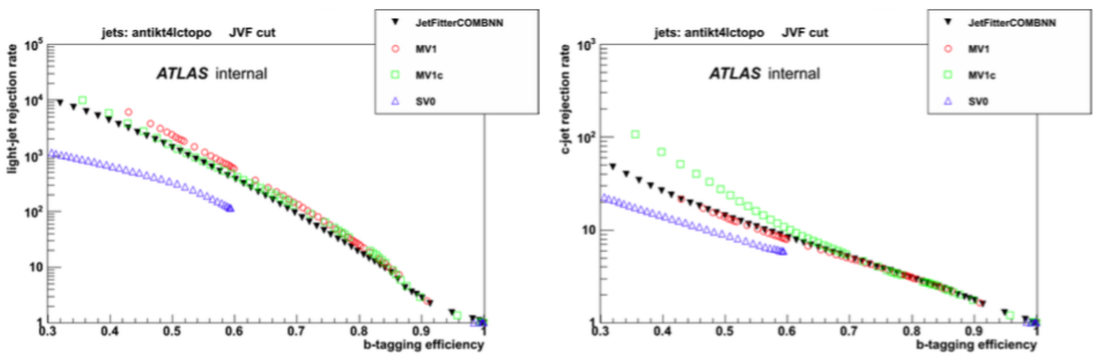

Figure 5.4: The rejection rate of light jets and c-jets for the individual tagging algorithms as a function of the tagger's efficiency. In addition to the rates for the MV1 algorithm the rates for SV0 and MV1c are also shown. The MV1c tagging algorithm is identical to MV1 except that it is trained to optimize rejection of c-jets. It can be clearly seen that it has better c-jet rejection in the region of low b-tagging efficiency. [111]

tagger	ϵ_b^{MC}[%]	weight	RF_{light}	RF_c	RF_τ	weight	RF_{light}	RF_c	RF_τ
		LC - jets				EM - jets			
MV1	80	0.3511	25.18	3.08	5.39	0.3900	27.13	3.09	5.64
MV1	70	0.7892	136.66	4.97	13.24	0.8119	150.00	4.99	14.07
MV1	60	0.9827	584.94	7.93	23.69	0.9867	651.81	7.98	25.21
MV1c	57	0.8641	621.02	13.28	49.42	0.8674	624.37	13.35	47.23
MV1c	50	0.9195	1472.63	25.60	119.29	0.9237	1388.28	26.22	120.33

Table 5.2: Operating points for b-tagging algorithms with LCW/EM-jet collection determined from $t\bar{t}$ MC simulation using a JVF > 0.5 cut for jets with $p_{\mathrm{T}} > 50$ GeV and $\mid \eta \mid < 2.4$. [111]

In order to apply the results of the MV1 algorithm in the analysis the b-tagging efficiency must be measured in data and compared with the value in MC simulation. Scale factors are calculated as the ratio of the b-tagging efficiency in data and MC simulation:

$$\kappa_{\epsilon_b}^{data/MC} = \frac{\epsilon_b^{data}}{\epsilon_b^{MC}}$$

Similar scale factors are calculated for the c-jet mistag rate and light jet rejection rates. These scale factors are then used to correct the MC to agree with data. This is done to account for the fact that the detector simulation applied to the MC samples does not perfectly simulate the detector response. The scale factors are parametrized as a function of η and p_{T} of the jet. A variety of techniques are implemented to measure the efficiencies in data. They are described in detail in Ref. [111]. To improve the precision of the b-tagging efficiency calibration, a combination of the results from each technique is produced to determine the best estimate for the scale factors. Table 5.3 summarizes the combination of techniques considered for each jet collection and tagging algorithm. The scale factors used in this analysis are calculated from a combination of the System8, tag-and-probe and kinematic selection techniques. The System8 technique measures the b-tagging efficiency by selecting events containing jets with associated muons. Because of semileptonic decay of b-hadrons this sample is naturally enriched in b-jets. Both the tag-and-probe and kinematic selection techniques measure the efficiency in a sample of $t\bar{t}$ events selected by requiring an $e\mu$ pair and at least one b-tagged jet. In the tag-and-probe technique the events are required to have only one additional jet, assumed to be b-jet since the sample is populated primarily by $t\bar{t}$ events, which is then used as the probe. In the kinematic selection technique an expression relates the total number of tagged jets to the b-tagging efficiency and mistag rates. The mistag rates are taken from simulation and the expression is solved for the b-tagging efficiency. Figure 5.5 shows b-tagging data-to-simulation scale factors for each of these techniques as well as the combination plotted against jet p_{T}. Figure 5.6 shows the c-tagging efficiencies and data-to-simulation scale factors plotted against jet p_{T}. Figure 5.7 shows the mistag rates and data-to-simulation scale factors plotted against jet p_{T} in the central and forward regions.

The uncertainties on these scale factors lead to a systematic uncertainty on the

MC event yields associated with b-tagging that is described in Section 8.1.3.

Jet collection	JVF cut	Taggers	System8	KinSel	Tag and Probe	PDF method
AntiKt4TopoEM	–	MV1, MV1c	X	X		
AntiKt4TopoEM	> 0.5	MV1	X			X
AntiKt4TopoEM	> 0.5	MV1c	X	X		
AntiKt4TopoLC	–	MV1, MV1c	X	X		
AntiKt4TopoLC	> 0.5	MV1, MV1c	X	(3-jet bin)	X	

Table 5.3: Calibration methods used to determine the data-to-simulation scale factors and their uncertainties for each jet collection. The jet collection relevant for this analysis is AntiKt4TopoLC with JVF cut shown in the final row. [111]

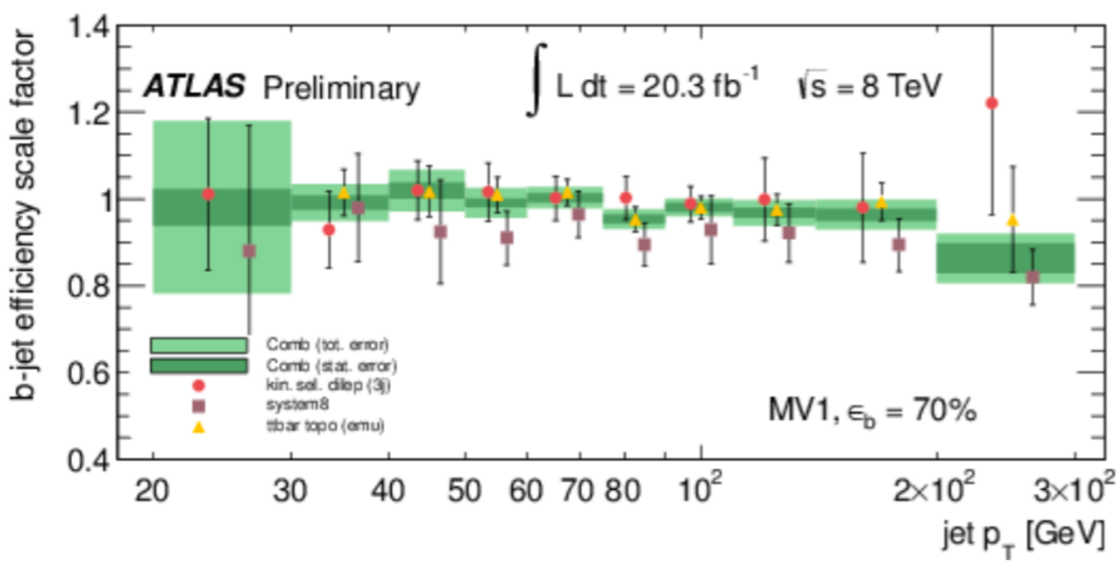

Figure 5.5: The b-tagging efficiency data-to-simulation scale factor for the MV1 tagging algorithm at 70% efficiency for LCW-jets. [111]

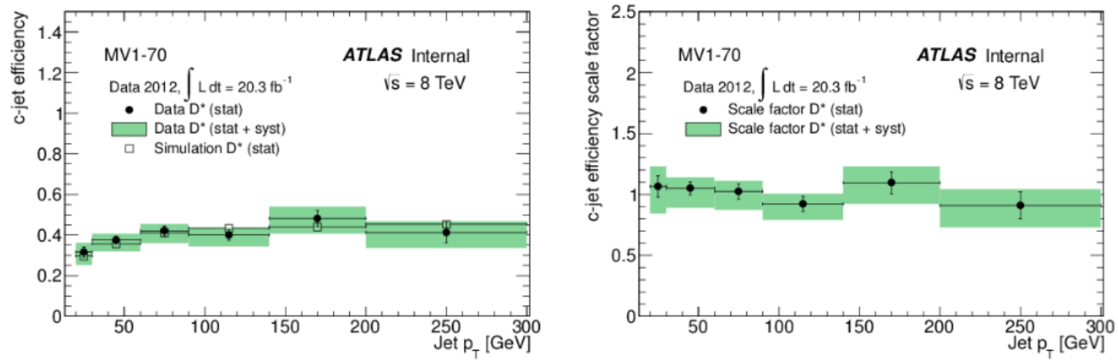

Figure 5.6: The c-jet mistag rate in data and simulation and the data-to-simulation scale factor for the MV1 tagging algorithm at 70% efficiency for LCW-jets. [111]

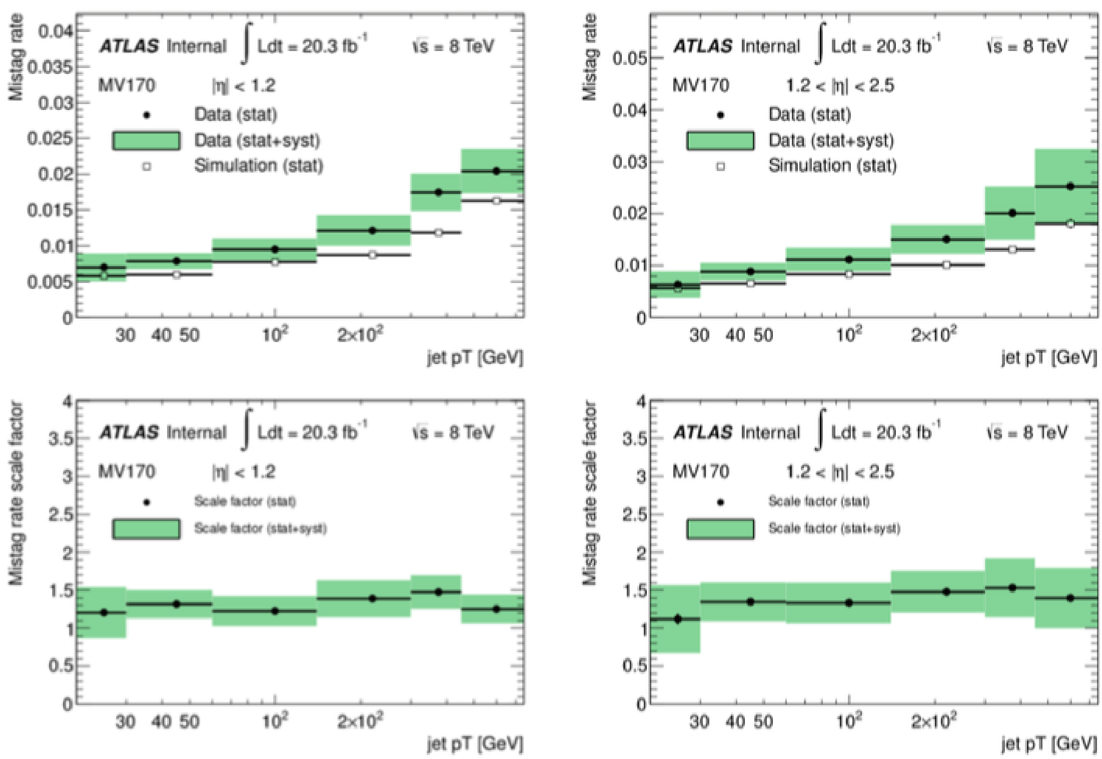

Figure 5.7: The mistag rate in data and simulation (top) and the data-to-simulation scale factor (bottom) for the MV1 tagging algorithm at 70% efficiency for LCW-jets with $|\eta| < 1.2$ (left) and jets with $1.2 < |\eta| < 2.5$. [111]

5.1.3 Electrons

Electrons are reconstructed from an energy cluster in the calorimeter with a good quality track pointing to it in the inner detector. The shape and size of the energy cluster must be consistent with that arising from an electromagnetic (EM) shower. Typically EM showers produce clusters that are smaller, more dense and don't penetrate as far into the calorimeter as compared with the hadronic clusters used to reconstruct jets. Electron candidates must pass the ATLAS electron quality cuts which include requirements on cluster shape and track quality [119]. The complete list of variables used in the definition of the three levels of electron quality known as *Loose*, *Medium* and *Tight* are shown in Table. 5.4. The identification efficiencies for each of these electron quality levels were measured using the tag-and-probe method on $Z \to$ ee data collected in 2012 and using $Z \to$ ee MC simulations. These efficiencies are shown in Fig. 5.9 for a variety of η and p_{T} bins. The electrons used in this analysis are required to be *Tight*. For some aspects of the analysis, such as the removal of jets that overlap electron candidates and the estimation of the fake/non-prompt lepton background described in Section 7.2, the looser *Medium* quality criteria is used.

In addition to these quality criteria, electrons must have $E_{\mathrm{T}}> 25$ GeV and $\mid \eta_{cluster} \mid < 2.47$, excluding the region ($1.37 < \mid \eta_{cluster} \mid < 1.52$) where the calorimeter is not well instrumented. The impact parameter of the electron track with respect to the primary vertex is required to be less than 2mm in the z direction and less than 1mm in the transverse direction. Isolation requirements are imposed following the "mini-isolation" scheme in which a cone radius is set depending on the p_{T} of the electron: ΔR = 10 GeV/ p_{T}. The summed p_{T} of all tracks within the cone other than the electron track must be less than $0.05 \times p_{\mathrm{T}}$ of the electron. This scheme is used in order to reduce unwanted rejection of boosted electrons from the decay of high p_{T} W/Z bosons in the final state of energetic events [120]. Higher p_{T} electrons have a smaller isolation cone and thus a weaker isolation cut. This isolation scheme is different from that recommended for electrons in TopCommonObjects2012 where fixed radius E_{T} and p_{T} cone isolation cuts are used instead. Electrons must also be well isolated from jets that pass the above jet selection criteria. Any electron that falls within a cone of radius 0.4 of a jet is removed from the event.

Electrons satisfying these criteria are referred to as tight. For the purposes of estimating the fake/non-prompt lepton background a loose electron is defined by relaxing or removing some of these criteria. To be clear, this is distinct from the *Loose* electron quality level mentioned above. The loose definition is equal to the tight with the isolation requirement removed and the electron ID criteria relaxed from *Tight* to *Medium*. However the requirement of a hit in the innermost layer of the pixel detector (included in *Tight* but not *Medium*) is retained in the loose definition in order to veto electrons from photon conversions. The full explanation of the fake/non-prompt lepton background estimation is given in Section 7.2. The definitions of loose and tight electrons are also important for the event selection described in Chapter 6.

Category	Description	Variable
	loose	
Acceptance	$\|\eta\| < 2.47$	
Hadronic leakage	In $\|\eta\| < 0.8$ and $\|\eta\| > 1.37$: ratio of E_T in the first layer of the hadronic calorimeter to E_T of the EM cluster	$R_{\mathrm{had},1}$
	In $0.8 < \|\eta\| < 1.37$: ratio of E_T in whole hadronic calorimeter to E_T of the EM cluster	R_{had}
Middle layer of the EM	Ratio of energies in 3×7 cells over 7×7 cells	R_η
	Lateral width of the shower	$w_{\eta 2}$
Front layer of the EM	Total shower width	w_{stot}
	Energy difference of the largest and second largest energy deposits in the cluster divided by their sum	E_{ratio}
Track quality and track–cluster matching	Number of hits in the pixel detector (> 0)	
	Number of hits in the silicon detectors (≥ 7)	
	$\|\Delta\eta\|$ between the cluster position in the first layer and the extrapolated track (< 0.015)	$\Delta\eta_1$
	***medium* (includes *loose* with tighter requirements on shower shapes)**	
Track quality and track–cluster matching	Number of hits in the b-layer > 0 for $\|\eta\| < 2.01$	
	Number of hits in the pixel detector > 1 for $\|\eta\| > 2.01$	
	Transverse impact parameter $\|d_0\| < 5$ mm	d_0
	Tighter $\|\Delta\eta_1\|$ cut (< 0.005)	
TRT	Loose cut on TRT high-threshold fraction	
	***tight* (includes *medium*)**	
Track quality and track–cluster matching	Tighter transverse impact parameter cut ($\|d_0\| < 1$ mm)	
	Asymmetric cut on $\Delta\phi$ between the cluster position in the middle layer and the extrapolated track	$\Delta\phi$
	Ratio of the cluster energy to the track momentum	E/p
TRT	Total number of hits in the TRT	
	Tighter cut on the TRT high-threshold fraction	
Conversions	Reject electron candidates matched to reconstructed photon conversions	

(a) central region

Category	Description	Variable
Acceptance	$2.5 < \|\eta\| < 4.9$	
Shower depth	Distance of the shower barycentre from the calorimeter front face measured along the shower axis	$\lambda_{\mathrm{centre}}$
Maximum cell energy	Fraction of cluster energy in the most energetic cell	f_{max}
Longitudinal second moment	Second moment of the distance of each cell to the shower centre in the longitudinal direction (λ_i)	$\langle\lambda^2\rangle$
Transverse second moment	Second moment of the distance of each cell to the shower centre in the transverse direction (r_i)	$\langle r^2\rangle$
Normalised lateral moment	w_2 and w_{max} are second moments of r_i for different weights per cell	$\frac{w_2}{w_2+w_{\mathrm{max}}}$
Normalised longitudinal moment	l_2 and l_{max} are the second moments of λ_i for different weights per cell	$\frac{l_2}{l_2+l_{\mathrm{max}}}$

(b) forward region

Table 5.4: Variables used in *Loose*, *Medium* and *Tight* electron identification criteria in the central ($|\eta| < 2.47$) and forward ($2.5 < |\eta| < 4.9$) regions in ATLAS [121]

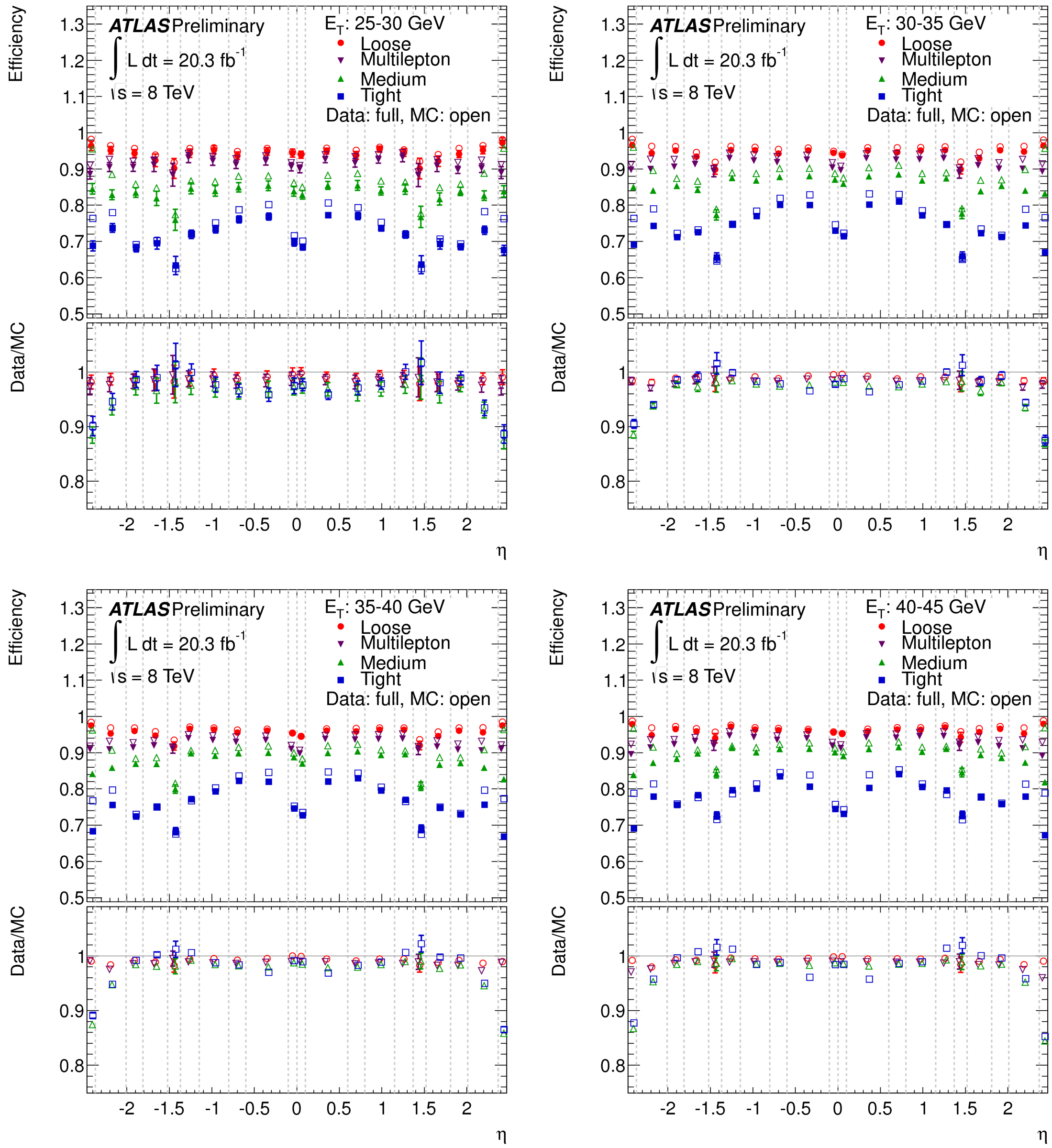

Figure 5.8: Electron identification efficiencies as a function of η for four $E_{\rm T}$ bins, from 20-25 GeV (top-left) to > 40-45 GeV (bottom-right). The efficiencies are extracted from both tag-and-probe measurements in $Z \rightarrow$ ee data collected in 2012 as well as with $Z \rightarrow$ ee MC simulations. The lower plots show the ratio of the efficiencies measured with data to those measured with MC simulations. [119]

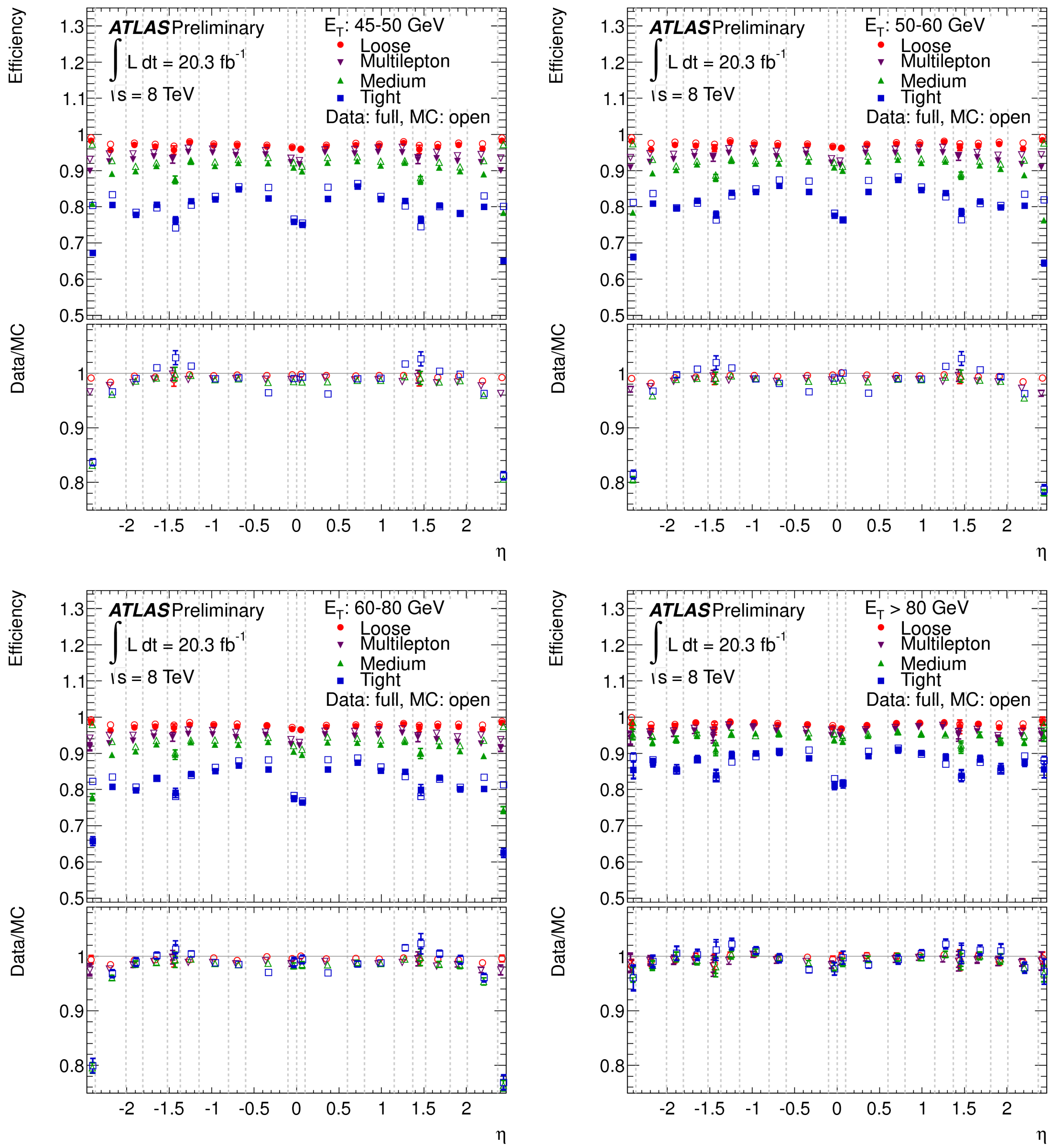

Figure 5.9: Electron identification efficiencies as a function of η for four E_{T} bins, from 45-50 GeV (top-left) to > 80 GeV (bottom-right). The efficiencies are extracted from both tag-and-probe measurements in $Z \to$ ee data collected in 2012 as well as with $Z \to$ ee MC simulations. The lower plots show the ratio of the efficiencies measured with data to those measured with MC simulations. [119]

5.1.4 Muons

Muons are reconstructed from a combination of tracks in the inner detector and the muon spectrometer and to a lesser extent energy deposits in the calorimeter. There are several different ways to reconstruct muons depending on the information that is available from each detector system. The different types of reconstructed muons are Stand-Alone (SA), Combined (CB), Segment-tagged (ST) and Calorimeter-tagged (CaloTag). SA muons are reconstructed entirely from tracks in the muon spectrometer. The parameters of the muon track at the interaction point are determined by extrapolating the track back to the point of closest approach to the beam-line. For CB muons, tracks are reconstructed independently in the inner detector and muon spectrometer and then combined. An ST muon consists of a track in the inner detector that when extrapolated to the muon spectrometer is associated with at least one local track segment in the MDT or CSC chambers. A CaloTag muon is a track in the inner detector that can be associated with an energy deposit in the calorimeter consistent with the passage of a minimum ionizing particle. CB muons are the most commonly used and have the highest muon purity. ST and CaloTag muons are primarily used in regions where the acceptance of the muon spectrometer is compromised due to structural elements and electronics. An example of this is in the very central region ($\eta \approx 0$) where the muon spectrometer is only partially equipped with chambers to allow for services for the inner detector and calorimeter.

The reconstruction efficiencies for each muon type were measured with the tag-and-probe technique using $Z \to \mu\mu$ and $J/\psi \to \mu\mu$ events in data collected in 2011-2012 at $\sqrt{s}$= 7-8 TeV. Complementary measurements were made using $Z \to \mu\mu$ MC simulated samples and found to be in agreement with those measured in data [122]. These efficiencies are shown Fig. 5.10. For this analysis, only CB muons are considered.

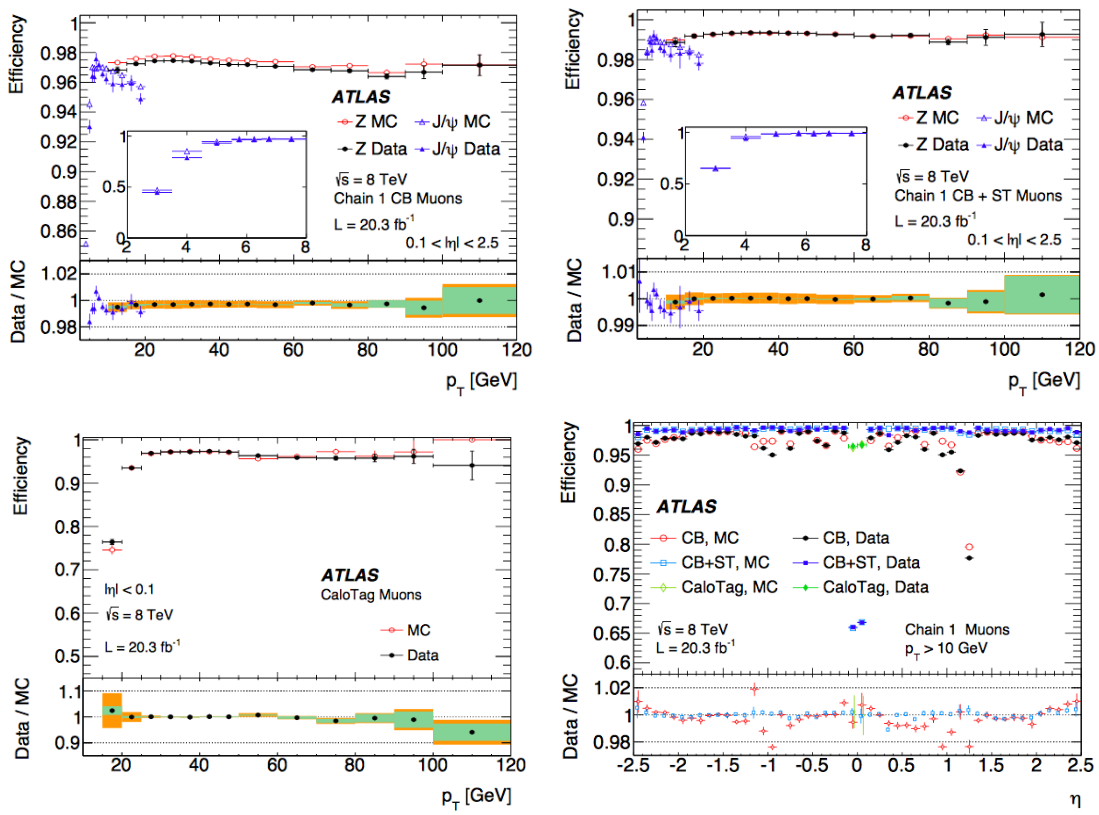

Figure 5.10: Reconstruction efficiencies for CB (top-left), CB+ST (top-right) and CaloTag (bottom-left) muons as a function of muon p_{T} for muons with $0.1 < \mid \eta \mid < 2.5$ for CB and CB+ST muons and $\mid \eta \mid < 0.1$ for CaloTag muons. The CB and CB+ST efficiencies are measured with both $Z \to \mu\mu$ and $J/\psi \to \mu\mu$ events in data where the $J/\psi \to \mu\mu$ events were used specifically for low p_{T} muons (shown in the insert). The CaloTag efficiencies are measured with $Z \to \mu\mu$ events only. The reconstruction efficiencies for each type of muon is shown as a function of η in the bottom-right. [122]

Once a CB muon has been reconstructed it must pass a series of additional cuts in order to be used in this analysis. The muon must have p_{T}> 25 GeV and $\mid \eta \mid < 2.5$. As for electrons muons are also required to originate from within 2mm of the primary vertex in z and be isolated according to the mini-isolation scheme. Unlike electrons mini-isolation is the isolation scheme recommended for muons by TopCommonObjects2012. Muons are also required to be isolated from jets. Any muon that falls within a cone of radius $\Delta\mathrm{R} = 0.04 + 10\ \mathrm{GeV}/p_{\mathrm{T}}$ of a jet is removed from the event. This muon-jet isolation requirement is different from that recommended by TopCommonObjects2012 where a fixed cone radius of ΔR = 0.4 is used. Using a variable cone radius that decreases with muon p_{T} allows for the reconstruction of a larger percentage of boosted muons from the decay of high energy particles in the final state. Another requirement added to this analysis that is not part of the TopCommonObjects2012 recommendations is a cut placed on the significance of the transverse impact parameter of the muon, defined as $\mid d0_{sig} \mid = \mid \frac{d0}{\sigma_{d0}} \mid$ where d0 is the projection of the impact parameter of the muon in the transverse direction. $\mid d0_{sig} \mid$ is required to be less than 3 in order to reduce the non-prompt muon background arising from secondary muons from the decay of final state particles. Events that contain two muon tracks with an angular separation in the transverse plane ($\Delta\phi$) greater than 3.1 such that they may have come from the passage of a cosmic muon through the interaction point are rejected. Events containing an electron and muon candidate that share a track in the inner detector are also rejected.

Muons satisfying these criteria are referred to as tight. As for electrons in certain aspects of the analysis such as the estimation of the fake/non-prompt lepton background a looser muon definition is used. The loose definition is obtained from the standard definition described here by removing the isolation requirement. The definition of loose and tight muons is important for the event selection described in Chapter 6.

5.1.5 Missing Transverse Momentum

Missing transverse momentum ($E_{\mathrm{T}}^{\mathrm{miss}}$) is defined as the momentum imbalance in the plane transverse to the beam axis. This imbalance represents the energy carried away by particles such as neutrinos that escape the detector without interacting. It is the negative of the vector sum of the p_{T} of all objects and energy deposits in the event. The calculation relies on the assumption that momentum is conserved in each collision. Since the momentum in the transverse direction is initially zero it must be zero in the final state. It follows that the transverse momenta of all final state particles should sum to zero. However not all final state objects leave a signal in the detector, so their transverse momenta are missing from the sum. The calculation of $E_{\mathrm{T}}^{\mathrm{miss}}$ includes contributions from energy deposits in the calorimeter and muons reconstructed in the muon spectrometer. More details on the calculation can be found in Ref. [123]. The calculation is validated by comparing distributions of $E_{\mathrm{T}}^{\mathrm{miss}}$ in data to the true $E_{\mathrm{T}}^{\mathrm{miss}}$ in MC simulations for $Z \to \ell\ell$ and $W \to \ell\nu$ events. The true $E_{\mathrm{T}}^{\mathrm{miss}}$ in MC samples is determined from the presence of neutrinos (for $W \to \ell\nu$ events), particles that are outside the η acceptance of the detector and instrumental effects such as punch-through or the failure of the detector to reconstruct low p_{T} objects.

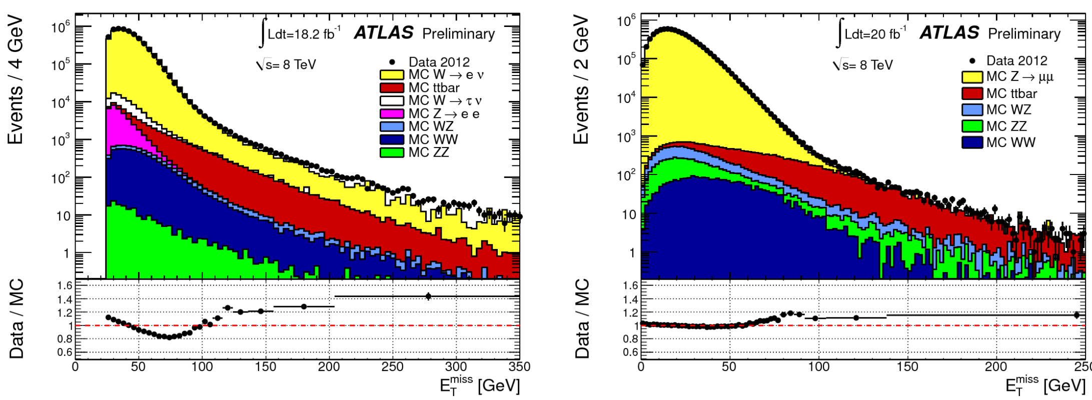

Figure 5.11: Distribution of $E_{\mathrm{T}}^{\mathrm{miss}}$ as measured in data samples of $W \to \mathrm{e}\nu$ (left) and $Z \to \mu\mu$ (right) events. The expectation of Monte Carlo simulation is superimposed and normalized to data after each MC sample is weighted to its corresponding cross-section. The lower part of the plots show the ratio of data over MC. [123]

CHAPTER 6

Event Selection

An extremely important feature of a particle physics search is the definition of the signal region. It is what defines the search and makes it distinct from other searches carried out with the same experiment. It is typically defined in order to maximum the expected limits [14] for a particular signal or a collection of signals that have a similar signature in the detector. This ensures a high likelihood of discovery if the signal exists, or strong exclusion if it does not. The signal region is already partly defined by the choice of trigger(s) and the object definitions discussed in Chapter 4 and Chapter 5 respectively. These trigger and object level selections are generally not unique to a particular analysis but rather are used by a range of analyses that share some common features of their final state. As such data sets with these selections applied are centrally produced by the ATLAS experiment. Subsequently a more analysis-specific event selection is applied to these data sets to further increase the significance for the signal(s) of interest.

6.1 Preselection

The basic preselection applied to all events is the following:

- the event must pass one of the single lepton triggers defined in Section 4.1
- the event must be in a run/LumiBlock on the Good Runs List (GRL)
- the event must contain at least one primary vertex with at least 5 tracks with $p_{\mathrm{T}} > 0.4$ GeV

[14] the exclusion limits one could expect to set in the absence of any signal (see Section 9.1)

- the event is rejected if any quality criteria are not fulfilled (no overlap between an electron and a muon, no bad jet, no LAr noise burst, no cosmic-like pair of muons, no Tile error or trip, not incomplete event),
- the event must contain at least two jets
- the event must have $E_{\mathrm{T}}^{\mathrm{miss}} > 40$ GeV

After this preselection, the events are separated into two different channels based on the highest p_{T} leptons in the event:

- if the three highest p_{T} leptons are tight, the event is a trilepton event,
- if there are only two tight leptons amongst the three highest p_{T} leptons in the event, it is a dilepton event.

6.1.1 Same-sign dilepton channel

In the same-sign dilepton channel, after the previous basic preselection, the specific preselection is:

- two of the three highest p_{T} leptons must be tight, if a third lepton is present, it should not be tight (otherwise it is a trilepton event, see below),
- these two leptons must have the same electric charge,
- if the two leptons are electrons ($e^{\pm}e^{\pm}$), a quarkonia/Z-veto is applied on the mass of the two leptons m_{ee}: $m_{ee} > 15$ GeV and $|m_{ee} - 91\ \text{GeV}| > 10$ GeV, [15]
- one of the two leptons must match the trigger.

With this preselection, the fake/non-prompt background can be determined by applying the 4×4 matrix method described in detail in Section 7.2.1.

[15] This is to reduce the background from electron charge misid and thus is not needed for eμ or $\mu\mu$ pairs

6.1.2 Trilepton channel

In the trilepton channel, after the basic preselection described previously, the preselection requirements are:

- the three highest p_{T} leptons must be tight,
- one of the three leptons must match the trigger.

With this preselection, the non-prompt/fake background can be determined by applying the 8×8 matrix method to the three leading leptons.

6.2 Optimization

Events containing vector-like quarks are characterized by a large number of jets, including a high fraction of b-jets, as well as a large amount of total transverse energy and missing transverse momentum compared with most SM processes. Consequently the most powerful variables for discriminating the VLQ signal from background events that pass the preselection are N_{jets}, N_{b-jets}, H_{T} and $E_{\mathrm{T}}^{\mathrm{miss}}$ where H_{T} is defined as the scalar sum of the transverse momentum of all jets and leptons in the event:

$$H_T = \sum_{jets} p_T + \sum_{leptons} p_T$$

Another signal with significant overlap in its final state topology to VLQ events is the production of four top quarks ($t\bar{t}t\bar{t}$). Four top quarks can be produced in proton-proton collisions via SM interactions. In addition there are a number of BSM theories that predict an enhanced rate of production of these events. The Feynman diagrams for these processes are shown in Fig. 6.1. Due to the similarity of their final state, these $t\bar{t}t\bar{t}$ signals are included in the same analysis as the VLQ search described in this dissertation. This means that in addition to the VLQ signal the data observed in the signal region were also interpreted in terms of these $t\bar{t}t\bar{t}$ models and used to produce exclusion limits at 95% CL. These limits are not included in this dissertation as they are not central to the search for VLQ. However some important aspects of the analysis, such as the optimization of the signal region, were carried out using these $t\bar{t}t\bar{t}$ signals and the results applied to the search for VLQ. Figure 6.2 shows the distribution of the variables listed above for each background as well as the $t\bar{t}t\bar{t}$ models for events passing the above preselection. In these plots all leptonic channels (ee, $\mu\mu$, eμ, eee, eeμ, e$\mu\mu$, $\mu\mu\mu$) are combined. The signal histograms are scaled such that their integral is equal to that of the combined background. This is done to make them clearly visible and does not effect their shape. The distributions show that these variables discriminate very well between the $t\bar{t}t\bar{t}$ signals and background.

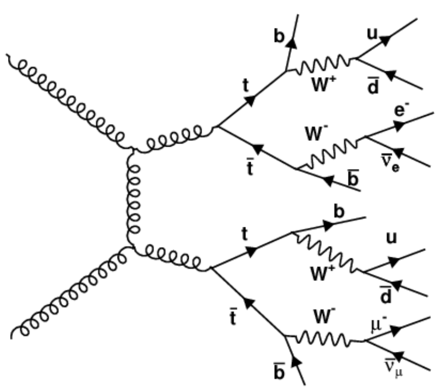

(a) Standard Model

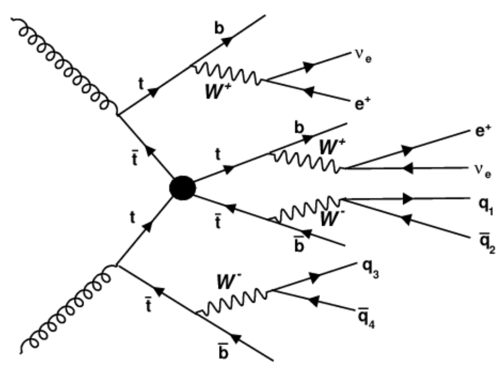

(b) Contact Interaction

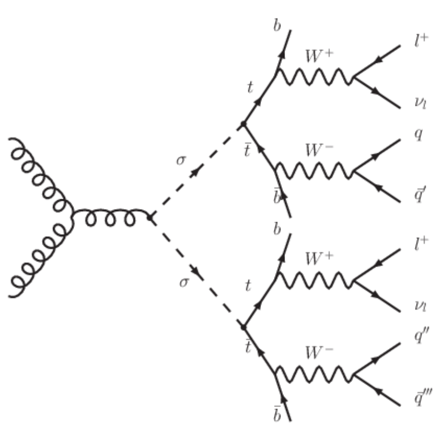

(c) Sgluon Pair Production

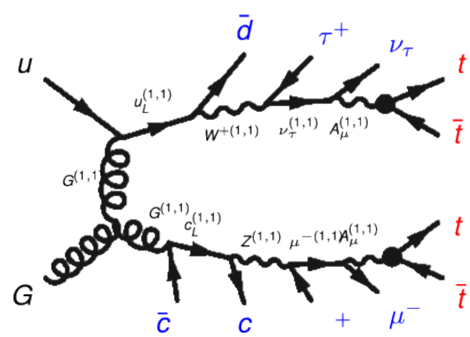

(d) 2UED RRP Model

Figure 6.1: Feynman diagrams representing production of $t\bar{t}t\bar{t}$ via four different models. [110]

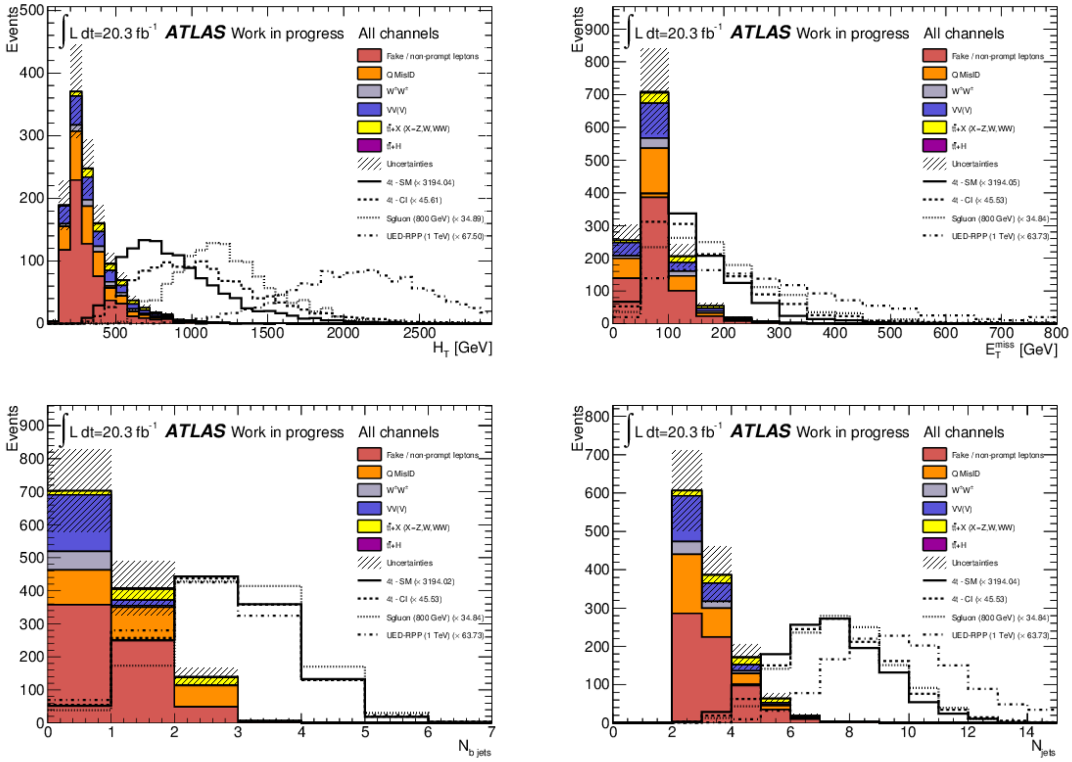

Figure 6.2: Discriminating variables for various $t\bar{t}t\bar{t}$ signals adding all leptonic channels. The signal histograms are scaled such that their integral is equal to that of the combined background. [110]

In the previous incarnation of this analysis carried out with a partial 2012 data set consisting of 14.3 fb^{-1} of proton-proton collisions [124] the event selection was implemented as a simple cut-and-count method. This means a single set of cuts were applied on these four discriminate variables and the yields were calculated separately for each lepton channel ee, eμ and $\mu\mu$ (there was no trilepton channel at this point). For the analysis carried out with the full 20.3 fb^{-1} collected in 2012 a different approach referred to as the categorization method was adopted. Under this approach multiple signal regions are defined by placing different combinations of cuts on these discriminate variables. The original plan for the categorization is outlined in Table 6.1. In this table, the cut values labeled $H_{T,1}$, $H_{T,2}$, $E_{\mathrm{T}}^{\mathrm{miss}}{}_1$ and $E_{\mathrm{T}}^{\mathrm{miss}}{}_2$, are unspecified. A dedicated optimization study was carried out on the $t\bar{t}t\bar{t}$

sgluon samples to determine their values. The strategy for the optimization study was to calculate expected limits for a large number of different combinations of cut values and to choose the optimal combination that leads both to the strongest mass limits and the strongest cross-section limits for low mass samples. The cross-section limits are normalized to the theoretical cross-section. They are expressed as the ratio

$$\mu = \frac{\sigma_{95\%CL}}{\sigma_{th}}$$

known as the signal strength. For the mass limits, the signal strength was calculated for four mass points and then used to find the mass at which the signal is expected to be excluded at 95% CL (the point where the signal strength falls below 1). The goal was to find the combination of cut values that produces the highest mass limit while keeping the signal strength as low as possible for low mass samples. These limits were calculated using most of the systematic uncertainties eventually included in the calculation of the final limits. These include the uncertainties on the cross-sections for the MC backgrounds, the fake/non-prompt lepton and charge misidentification background estimations and uncertainties on object definitions and scale factors. The remaining systematic uncertainties are small in comparison to these. The ranges of different values that were considered for each cut are shown in Table. 6.2.

Table 6.1: Summary of the analysis categories for the $t\bar{t}t\bar{t}$ signals

			Category name
$H_{T,1} \leq H_T \leq H_{T,2}$	$N_b = 2$		SR4t0
	$N_b \geq 3$		SR4t1
$H_T \geq H_{T,2}$	$N_b = 2$	${E_{\mathrm{T}}^{\mathrm{miss}}}_1 \leq E_{\mathrm{T}}^{\mathrm{miss}} \leq {E_{\mathrm{T}}^{\mathrm{miss}}}_2$	SR4t2
		$E_{\mathrm{T}}^{\mathrm{miss}} \geq {E_{\mathrm{T}}^{\mathrm{miss}}}_2$	SR4t3
	$N_b \geq 3$		SR4t4

The mass limits calculated for each combination are shown in Fig. 6.3 and the signal strengths for a 400 GeV mass point are shown in Fig. 6.4. From Fig. 6.3 it is clear that while the mass limit is unaffected by the value of $H_{T,1}$ it increases with $H_{T,2}$. It is expected that $H_{T,1}$ has no effect since most events coming from a sgluon

Table 6.2: Tested values of the categorisation parameters.

Variable	Lowest value [GeV]	Highest value [GeV]	Step [GeV]
$H_{\mathrm{T}1}$	350	600	50
$H_{\mathrm{T}2}$	500	900	50
$E_{\mathrm{T}}^{\mathrm{miss}}{}_1$	40	60	10
$E_{\mathrm{T}}^{\mathrm{miss}}{}_2$	90	120	10

mass $\approx$ 800 GeV [16] lie in the high H_{T} bin. Fig. 6.4 shows two effects. First for large $H_{T,2}$ ($>$ 600-700 GeV) decreasing $H_{T,1}$ below 400 actually makes the signal strength worse. This is explained by the fact that reducing $H_{T,1}$ causes more background to fall in the lower H_{T} bin while the high value of $H_{T,2}$ means that most of the 400 GeV sgluon signal falls there as well. As a consequence the difference between signal and background and therefore the signal significance decreases leading to a weaker signal strength. Second, increasing $H_{T,1}$ beyond 500 GeV also makes the signal strength worse. This is because increasing $H_{T,1}$ removes both signal and background events from the low H_{T} bin and for a 400 GeV mass sgluon it actually removes more signal that background making the signal strength worse.

From the results of the optimization study the cut values are chosen to be:

- $H_{\mathrm{T}1} = 400$ GeV
- $H_{\mathrm{T}2} = 700$ GeV
- $E_{\mathrm{T}}^{\mathrm{miss}}{}_1 = 40$ GeV
- $E_{\mathrm{T}}^{\mathrm{miss}}{}_2 = 100$ GeV

This choice leads to good expected mass limits and a low signal strength in the low-mass range. Comparing to the expected mass limits in the previous round of the analysis [124], there is an improvement of more than 120 GeV, corresponding to a 15% improvement. In addition, the cut-and-count selection applied in the previous analysis was applied (with object definitions updated to those described

[16] The observed mass limit in the previous incarnation of the analysis

in Section 5.1) to the full 2012 data to facilitate a direct comparison with the categorization selection. The cut-and-count method applies the following cuts:

- At least 2 b jets
- H_{T}> 650 GeV
- $E_{\mathrm{T}}^{\mathrm{miss}}$> 40 GeV

Expected limits on cross-section as a function of sgluon mass are shown in Fig. 6.5 for both the cut-and-count and the categorization selections. Applying the categorization selection improves the mass limit by ~ 50 GeV with respect to the cut-and-count selection. Furthermore the cross-section limit is improved by a factor of two for a 400 GeV sample and by $\sim 60\%$ for a 1 TeV sample.

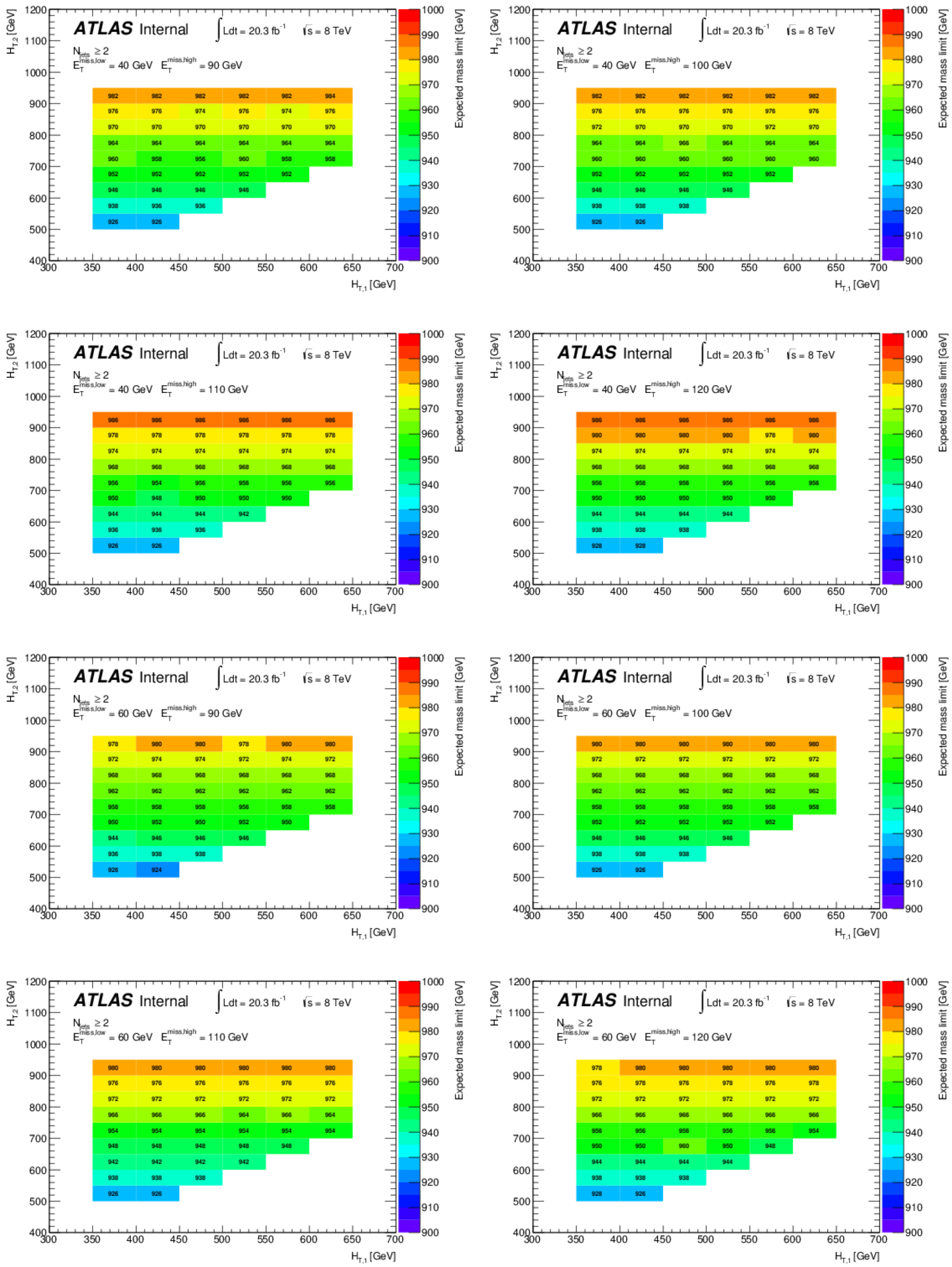

Figure 6.3: Expected mass limit on sgluon for various categorization parameters. The numbers written in the bins correspond to the value of the expected mass limit on sgluon for a given configuration. [110]

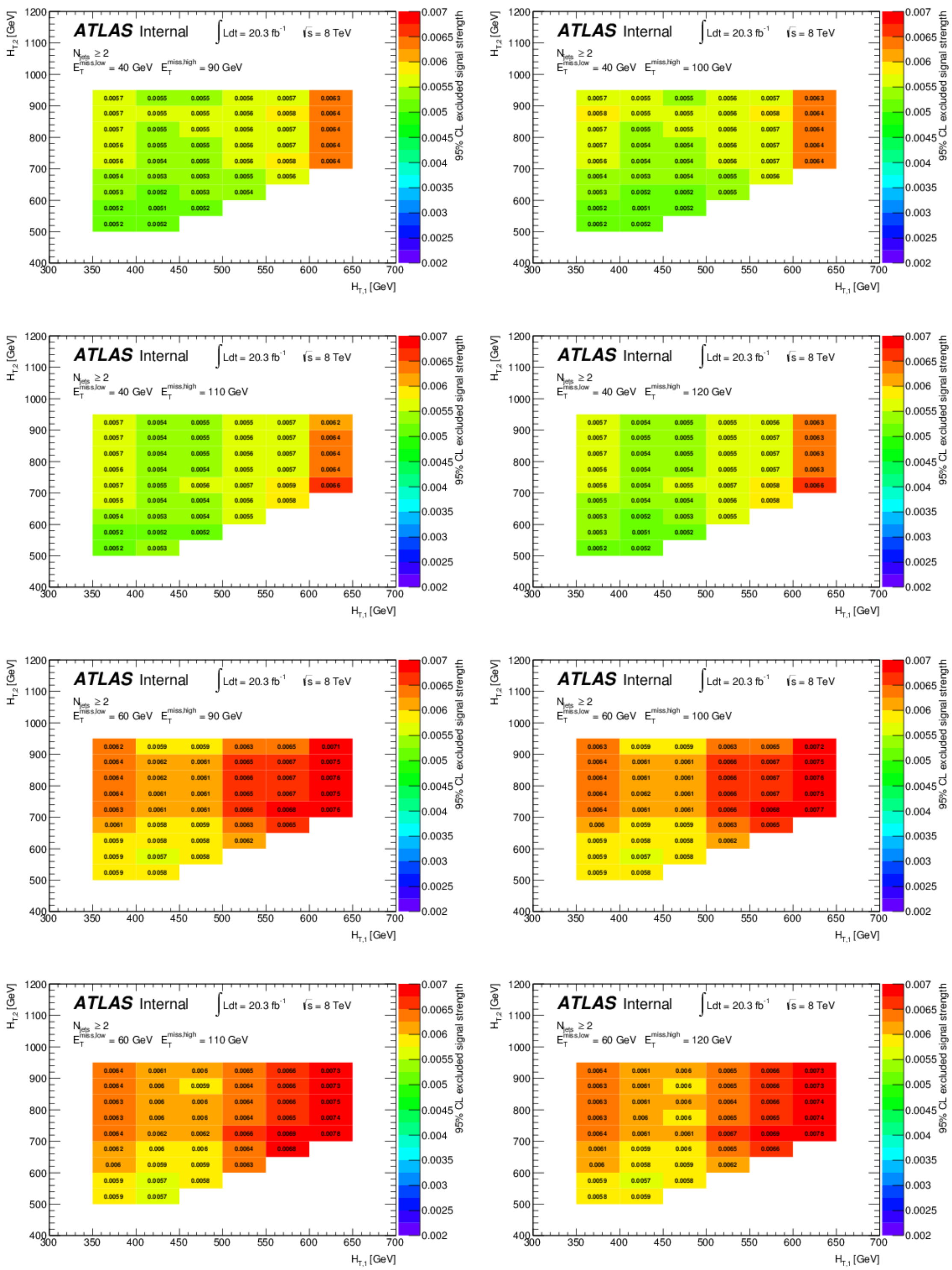

Figure 6.4: Expected limit on 400 GeV sgluon signal strength for various categorization parameters. The precise value of the expected limit on the signal strength is written in the plot. [110]

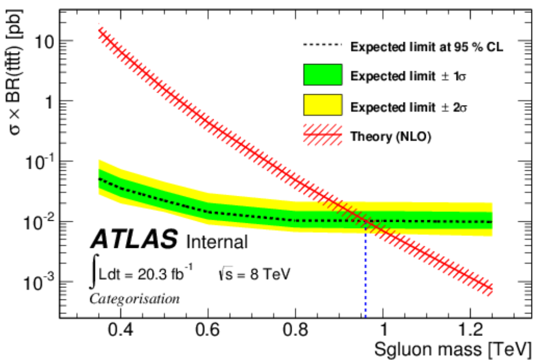

(a)

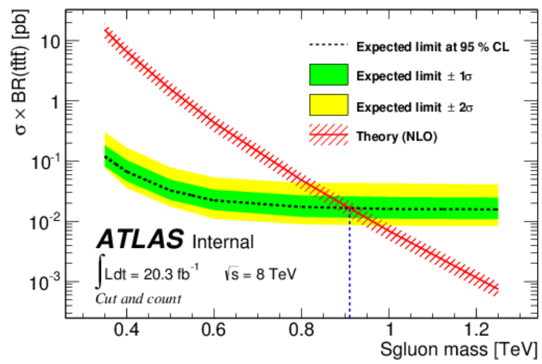

(b)

Figure 6.5: Expected limit for sgluon signal in two configurations. (a) using the categorization procedure, (b) using the cut-and-count method from the previous incarnation of the analysis. [110]

Although this optimization study was carried out using $t\bar{t}t\bar{t}$ signal samples, the results can be applied to the VLQ signals because of the similarity in their final states. Like $t\bar{t}t\bar{t}$ the VLQ signals also have large H_{T}, $E_{\mathrm{T}}^{\mathrm{miss}}$, jet and b-jet multiplicity compared to the SM background. This is shown in Fig. 6.6 for vector-like top and bottom quark signals with a mass of 800 GeV. As for the $t\bar{t}t\bar{t}$ plots the VLQ signal histograms are scaled such that their integral is equal to that of the combined background. However there are some differences between the $t\bar{t}t\bar{t}$ and VLQ final states that require modifying the categories defined for the $t\bar{t}t\bar{t}$ signals. One significant difference is that the VLQ final state contains a large number of events with a single b-tagged jet. To account for this, three extra categories for events including a single b-tagged jet are added to the categories defined in Table 6.1 for the $t\bar{t}t\bar{t}$ signals. The full list of categories which together define the signal region for the VLQ search described in this dissertation is given in Table 6.3. In the following they are referred to as SR categories.

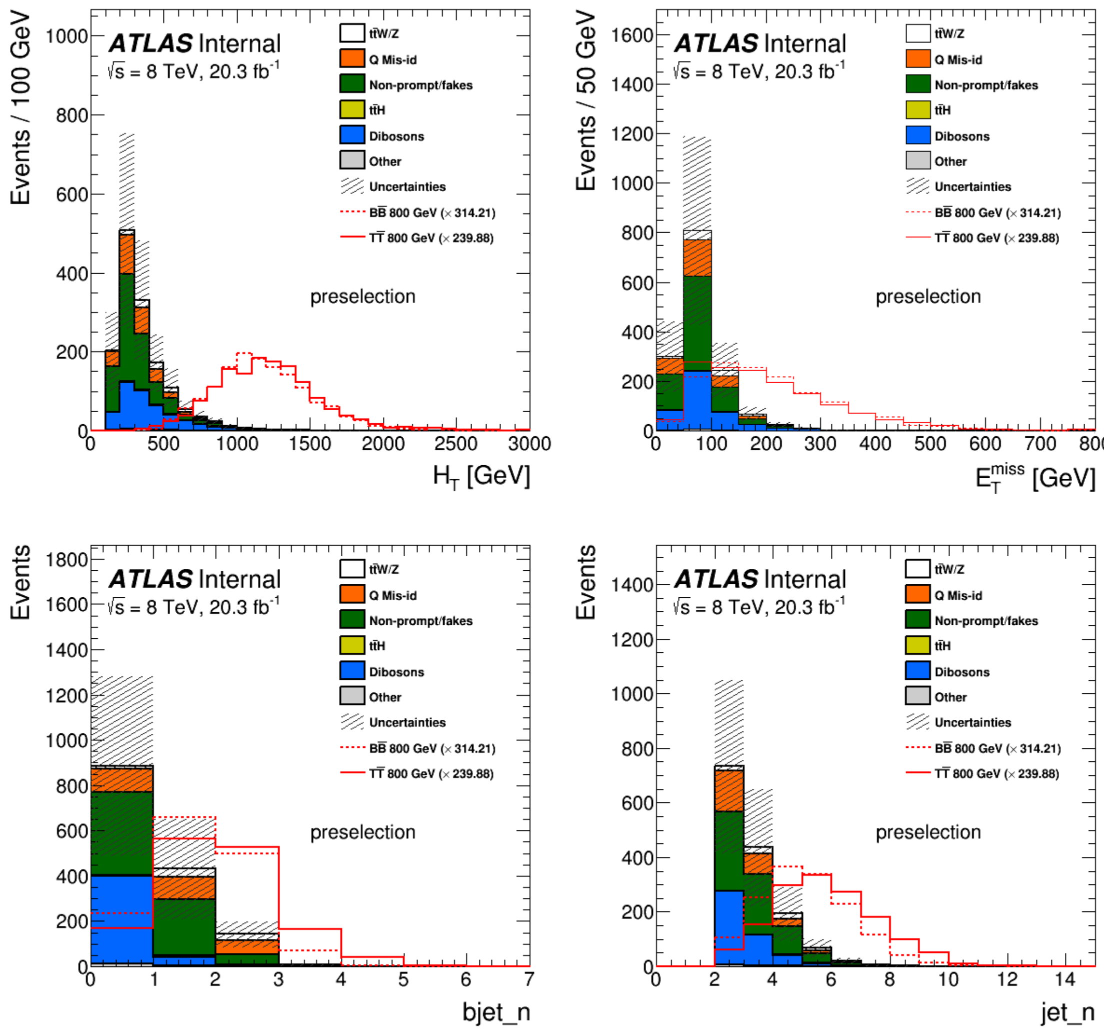

Figure 6.6: Discriminating variables for pair production of vector-like top and bottom quark signals with a mass of 800 GeV. These samples do not use the branching ratios defined for the singlet model discussed in Section 2.3 but rather use a flat 1/3-1/3-1/3 branching ratio for each of the three VLQ decay modes. The signal histograms are scaled such that their integral is equal to that of the combined background. All leptonic channels are combined.

Table 6.3: Summary of the analysis categories for VLQ signals for events with two same-sign leptons or three leptons. The correspondence between these categories and those used for the four tops analysis is indicated.

<table>
<tr><th colspan="3">Definition</th><th colspan="2">Name</th></tr>
<tr><td colspan="5">$e^{\pm}e^{\pm} + e^{\pm}\mu^{\pm} + \mu^{\pm}\mu^{\pm} + eee + ee\mu + e\mu\mu + \mu\mu\mu,\ N_j \geq 2$</td></tr>
<tr><td rowspan="3">$400 < H_T < 700$ GeV</td><td>$N_b = 1$</td><td rowspan="3">$E_{\mathrm{T}}^{\mathrm{miss}} > 40$ GeV</td><td>SRVLQ0</td><td></td></tr>
<tr><td>$N_b = 2$</td><td>SRVLQ1</td><td>SR4t0</td></tr>
<tr><td>$N_b \geq 3$</td><td>SRVLQ2</td><td>SR4t1</td></tr>
<tr><td rowspan="5">$H_T \geq 700$ GeV</td><td rowspan="2">$N_b = 1$</td><td>$40 < E_{\mathrm{T}}^{\mathrm{miss}} < 100$ GeV</td><td>SRVLQ3</td><td></td></tr>
<tr><td>$E_{\mathrm{T}}^{\mathrm{miss}} \geq 100$ GeV</td><td>SRVLQ4</td><td></td></tr>
<tr><td rowspan="2">$N_b = 2$</td><td>$40 < E_{\mathrm{T}}^{\mathrm{miss}} < 100$ GeV</td><td>SRVLQ5</td><td>SR4t2</td></tr>
<tr><td>$E_{\mathrm{T}}^{\mathrm{miss}} \geq 100$ GeV</td><td>SRVLQ6</td><td>SR4t3</td></tr>
<tr><td>$N_b \geq 3$</td><td>$E_{\mathrm{T}}^{\mathrm{miss}} > 40$ GeV</td><td>SRVLQ7</td><td>SR4t4</td></tr>
</table>

6.3 Expected Yields and Selection Efficiencies

The expected number of events that pass the selection for the SR categories SRVLQ0-7 defined in Table 6.3 are calculated for each signal and background process. These event yields are calculated with the following expression

$$N = \sigma \times \int \mathcal{L}dt \times \epsilon \tag{6.1}$$

where σ is the production cross-section for the process, $\int \mathcal{L}dt$ is the integrated luminosity of the data set and ϵ is the selection efficiency for the sample. The selection efficiency is defined as the ratio of the number of events in the MC sample that pass the selection to the total number of events in the MC sample. In some MC samples a generator filter can be applied that selects certiain events, such as events containing a lepton, at the generator level. In this case the selection efficiency is the ratio defined above multiplied by the generator filter efficiency. Table 6.4 shows the number of events for each of the background processes described in Chapter 7 as well as the total number of background events. These background yields are expressed along with their statistical and systematic uncertainties. Table 6.5 shows the number of signal events in each SR category for vector-like top and vector-like bottom. Tables 6.6 and 6.7 show the selection efficiencies for each VLQ sample in each SR category. Both the signal yields and selection efficiencies are given with their corresponding statistical uncertainty. For each flavor vector-like quark 11 masses are considered ranging from 350 GeV to 850 GeV in steps of 50 GeV [17]. Tables 6.8 through 6.11 give the yields and efficiencies for the $T_{5/3}$ samples for three values of the coupling constant λ.

The matrix method used to estimate the fake/non-prompt lepton background (see Section 7.2) is limited in that in relies on reasonably large statistics in the loose data sample. If statistics are too low for a particular region the matrix method can give unreliable and even unphysical results. For example the fakes yield for a low statistics region with an unusually large number of events containing tight leptons

[17] Table 6.5 shows signal yields for six of these eleven samples

can be negative. In fact we see this for the SR category SRVLQ6. An alternative to the standard matrix method, known as the likelihood matrix method[18], can be used to avoid this problem however it is difficult to incorporate lepton-by-lepton real and fake efficiencies in this approach. In the likelihood matrix method real and fake efficiencies are input for the leptons in an event and a probability density function (p.d.f.) is returned for the fakes yield. This explicitly avoids the possibility of having a negative yield since the p.d.f. is only defined for a yield greater than zero. In principle this could be done event by event and then the p.d.f.s for each event could be convoluted to produce a final p.d.f. for each SR category. The fake yield and its uncertainty are then taken from the most probable value (MPV) and standard deviation of the convoluted p.d.f. Although this is straightforward in principle the large number of loose events in each SR category make it difficult in practice. Another possibility is to use the likelihood matrix method to produce a single p.d.f. using average real and fake efficiencies for all events in the loose data sample. This has the disadvantage that it ignores the dependence of these efficiencies on event kinematics. As a compromise we apply the standard matrix method to determine the fakes yield but use a version of the likelihood matrix method to estimate the statistical uncertainty. Also, when the fakes yield is negative as in SRVLQ6 we set it to zero. This is justified since the negative yield produced by the standard matrix method in SRVLQ6 is small enough that it is consistent with zero given its uncertainty.

The standard prescription for estimating the statistical uncertainty of the fakes yield is to take the quadratic sum of the weights produced with the matrix method. This can underestimate the statistical uncertainty in low statistics regions where the yield is subject to larger fluctuations. To account for this an alternate statistical uncertainty is calculated using a version of the likelihood matrix method. For each SR category the average real efficiency is computed. The fake efficiency is then tuned such that the MPV of the p.d.f. produced with the likelihood matrix method

[18] A description of the technique is available at https://indico.cern.ch/event/112438/material/slides/0?contribId=1

using these efficiencies matches the yield produced with the standard matrix method where per-lepton efficiencies are used. p.d.f.s are computed in this way separately for trilepton and same-sign dilepton events for each SR category. The trilepton and same-sign dilepton p.d.f.s are convoluted to produce a single p.d.f for each SR category. The p.d.f.s are shown in Fig. 6.8. If this convoluted p.d.f. peaks away from zero the standard deviation is taken as the alternate statistical uncertainty. If it peaks near zero the standard deviation calculated with respect to zero is taken. In most SR categories the alternate uncertainty is larger than the standard uncertainty. However in order to be conservative and avoid reducing the uncertainty unnecessarily the larger of the two is taken as the statistical uncertainty.

	SRVLQ0	SRVLQ1/SR4t0	SRVLQ2/SR4t1
$t\bar{t}+W/Z$	16.2 ± 0.3 ± 7.0	12.6 ± 0.3 ± 5.4	1.24 ± 0.09 ± 0.53
$t\bar{t}+H$	2.5 ± 0.1 ± 0.3	1.8 ± 0.1 ± 0.2	0.26 ± 0.03 ± 0.05
Dibosons	11.2 ± 0.6 ± 2.8	0.95 ± 0.19 ± 0.25	0.07 ± 0.12 ± 0.05
Fake/Non-prompt	42.1 ± 5.4 ± 24.6	8.61 ± 2.34 ± 5.02	1.17 ± 0.82 ± 0.68
Q mis-Id	20.8 ± 0.7 ± 5.2	15.1 ± 0.6 ± 3.5	0.7 ± 0.11 ± 0.18
Other bkg.	1.76 ± 0.13 ± 0.17	0.75 ± 0.04 ± 0.1	0.1 ± 0.08 ± 0.03
Total bkg.	94.5 ± 5.4 ± 24.9	40.0 ± 2.4 ± 7.3	3.6 ± 0.9 ± 0.8

	SRVLQ3	SRVLQ4
$t\bar{t}+W/Z$	2.07 ± 0.11 ± 0.89	3.14 ± 0.13 ± 1.35
$t\bar{t}+H$	0.4 ± 0.04 ± 0.07	0.57 ± 0.05 ± 0.07
Dibosons	2.36 ± 0.29 ± 0.61	2.03 ± 0.25 ± 0.49
Fake/Non-prompt	3.09 ± 1.29 ± 1.80	4.24 ± 1.59 ± 2.47
Q mis-Id	1.72 ± 0.22 ± 0.63	1.45 ± 0.17 ± 0.52
Other bkg.	0.22 ± 0.08 ± 0.03	0.41 ± 0.10 ± 0.06
Total bkg.	9.87 ± 1.35 ± 2.10	11.9 ± 1.6 ± 2.8

	SRVLQ5/SR4t2	SRVLQ6/SR4t3	SRVLQ7/SR4t4
$t\bar{t}+W/Z$	1.87 ± 0.09 ± 0.8	2.46 ± 0.11 ± 1.06	0.57 ± 0.05 ± 0.25
$t\bar{t}+H$	0.31 ± 0.04 ± 0.05	0.44 ± 0.04 ± 0.006	0.08 ± 0.02 ± 0.2
Dibosons	0.33 ± 0.14 ± 0.10	0.04 ± 0.12 ± 0.03	0.00 ± 0.12 ± 0.00
Fake/Non-prompt	1.03 ± 0.97 ± 0.60	0.00 ± 1.02 ± 0.28	0.04 ± 0.83 ± 0.24
Q mis-Id	1.17 ± 0.16 ± 0.38	1.09 ± 0.14 ± 0.34	0.30 ± 0.09 ± 0.10
Other bkg.	0.16 ± 0.08 ± 0.02	0.23 ± 0.08 ± 0.05	0.14 ± 0.08 ± 0.08
Total bkg.	4.86 ± 1.00 ± 1.01	4.25 ± 1.05 ± 1.11	1.12 ± 0.85 ± 0.37

Table 6.4: Expected number of events with statistical (first) and systematic (second) uncertainties for the signal regions defined for VLQ production searches. [39]

Table 6.5: VLQ yields in the signal regions. Uncertainties are statistical only. [110]

Source	SRVLQ0	SRVLQ1	SRVLQ2	SRVLQ3
BBS (350 GeV)	205.56 ± 9.98	163.33 ± 8.66	15.00 ± 2.52	44.14 ± 4.61
BBS (450 GeV)	44.43 ± 2.45	37.59 ± 2.17	4.40 ± 0.75	19.98 ± 1.63
BBS (550 GeV)	10.26 ± 0.65	8.29 ± 0.61	0.46 ± 0.13	7.65 ± 0.57
BBS (650 GeV)	2.12 ± 0.19	1.27 ± 0.14	0.09 ± 0.03	2.42 ± 0.19
BBS (750 GeV)	0.42 ± 0.05	0.27 ± 0.04	0.02 ± 0.01	0.68 ± 0.06
BBS (850 GeV)	0.07 ± 0.01	0.06 ± 0.01	0.00 ± 0.00	0.29 ± 0.03
TTS (350 GeV)	147.93 ± 8.99	129.93 ± 8.24	39.19 ± 4.40	28.96 ± 4.09
TTS (450 GeV)	34.07 ± 1.95	28.67 ± 1.74	9.58 ± 0.98	15.13 ± 1.30
TTS (550 GeV)	6.24 ± 0.43	5.41 ± 0.40	1.25 ± 0.18	4.60 ± 0.37
TTS (650 GeV)	1.12 ± 0.10	0.89 ± 0.09	0.19 ± 0.04	1.72 ± 0.13
TTS (750 GeV)	0.24 ± 0.03	0.18 ± 0.02	0.03 ± 0.01	0.59 ± 0.05
TTS (850 GeV)	0.06 ± 0.01	0.04 ± 0.01	0.00 ± 0.00	0.19 ± 0.02

Source	SRVLQ4	SRVLQ5	SRVLQ6	SRVLQ7
BBS (350 GeV)	43.36 ± 4.64	34.79 ± 3.81	38.82 ± 4.19	9.92 ± 2.28
BBS (450 GeV)	30.42 ± 2.06	16.64 ± 1.36	21.11 ± 1.50	7.17 ± 0.93
BBS (550 GeV)	17.63 ± 0.91	8.04 ± 0.56	13.98 ± 0.74	2.84 ± 0.32
BBS (650 GeV)	7.77 ± 0.34	2.15 ± 0.16	7.33 ± 0.32	1.43 ± 0.15
BBS (750 GeV)	3.28 ± 0.14	0.74 ± 0.06	2.81 ± 0.12	0.47 ± 0.05
BBS (850 GeV)	1.48 ± 0.06	0.22 ± 0.02	1.15 ± 0.05	0.23 ± 0.02
TTS (350 GeV)	26.35 ± 3.67	34.66 ± 4.68	35.97 ± 4.36	21.25 ± 2.96
TTS (450 GeV)	24.38 ± 1.85	15.01 ± 1.25	19.83 ± 1.44	13.63 ± 1.10
TTS (550 GeV)	11.60 ± 0.62	5.95 ± 0.39	10.72 ± 0.55	6.54 ± 0.40
TTS (650 GeV)	5.52 ± 0.24	1.86 ± 0.13	4.85 ± 0.20	2.41 ± 0.13
TTS (750 GeV)	2.01 ± 0.09	0.54 ± 0.04	1.96 ± 0.08	0.92 ± 0.05
TTS (850 GeV)	0.97 ± 0.04	0.21 ± 0.01	0.82 ± 0.03	0.36 ± 0.02

Table 6.6: Event selection efficiencies (in percent), relative to the inclusive cross section for the vector-like B signal as a function of the generated B mass. Efficiencies are computed assuming the branching ratios from the singlet model. [110]

Process	SRVLQ0	SRVLQ1	SRVLQ2	SRVLQ3
BBS (350 GeV)	0.190 ± 0.007	0.151 ± 0.007	0.014 ± 0.002	0.041 ± 0.003
BBS (400 GeV)	0.215 ± 0.008	0.167 ± 0.007	0.019 ± 0.002	0.073 ± 0.005
BBS (450 GeV)	0.190 ± 0.007	0.161 ± 0.007	0.019 ± 0.002	0.086 ± 0.005
BBS (500 GeV)	0.184 ± 0.007	0.132 ± 0.006	0.015 ± 0.002	0.119 ± 0.006
BBS (550 GeV)	0.160 ± 0.007	0.130 ± 0.006	0.007 ± 0.001	0.120 ± 0.006
BBS (600 GeV)	0.131 ± 0.006	0.101 ± 0.005	0.008 ± 0.002	0.122 ± 0.006
BBS (650 GeV)	0.105 ± 0.006	0.063 ± 0.004	0.005 ± 0.001	0.119 ± 0.006
BBS (700 GeV)	0.080 ± 0.004	0.055 ± 0.003	0.006 ± 0.001	0.116 ± 0.004
BBS (750 GeV)	0.059 ± 0.004	0.038 ± 0.003	0.003 ± 0.001	0.095 ± 0.005
BBS (800 GeV)	0.044 ± 0.004	0.033 ± 0.003	0.003 ± 0.001	0.112 ± 0.006
BBS (850 GeV)	0.026 ± 0.003	0.023 ± 0.003	0.001 ± 0.001	0.110 ± 0.006

Process	SRVLQ4	SRVLQ5	SRVLQ6	SRVLQ7	Total
BBS (350 GeV)	0.040 ± 0.003	0.032 ± 0.003	0.036 ± 0.003	0.009 ± 0.002	0.514 ± 0.012
BBS (400 GeV)	0.076 ± 0.005	0.059 ± 0.004	0.060 ± 0.004	0.015 ± 0.002	0.683 ± 0.014
BBS (450 GeV)	0.130 ± 0.006	0.071 ± 0.005	0.090 ± 0.005	0.031 ± 0.003	0.779 ± 0.015
BBS (500 GeV)	0.194 ± 0.008	0.094 ± 0.005	0.181 ± 0.007	0.045 ± 0.004	0.963 ± 0.017
BBS (550 GeV)	0.276 ± 0.009	0.126 ± 0.006	0.219 ± 0.008	0.044 ± 0.004	1.082 ± 0.018
BBS (600 GeV)	0.361 ± 0.010	0.117 ± 0.006	0.322 ± 0.010	0.067 ± 0.004	1.229 ± 0.019
BBS (650 GeV)	0.383 ± 0.011	0.106 ± 0.006	0.361 ± 0.010	0.071 ± 0.005	1.212 ± 0.019
BBS (700 GeV)	0.450 ± 0.008	0.105 ± 0.004	0.389 ± 0.008	0.074 ± 0.003	1.275 ± 0.014
BBS (750 GeV)	0.463 ± 0.012	0.105 ± 0.006	0.397 ± 0.011	0.066 ± 0.005	1.226 ± 0.020
BBS (800 GeV)	0.527 ± 0.013	0.066 ± 0.005	0.431 ± 0.012	0.081 ± 0.005	1.297 ± 0.020
BBS (850 GeV)	0.556 ± 0.013	0.084 ± 0.005	0.433 ± 0.012	0.085 ± 0.005	1.319 ± 0.020

Table 6.7: Event selection efficiencies (in percent), relative to the inclusive cross section for the vector-like T signal as a function of the generated T mass. Efficiencies are computed assuming the branching ratios from the singlet model. [110]

Process	SRVLQ0	SRVLQ1	SRVLQ2	SRVLQ3
TTS (350 GeV)	0.137 ± 0.006	0.120 ± 0.006	0.036 ± 0.003	0.027 ± 0.003
TTS (400 GeV)	0.159 ± 0.007	0.161 ± 0.007	0.047 ± 0.004	0.040 ± 0.003
TTS (450 GeV)	0.146 ± 0.007	0.123 ± 0.006	0.041 ± 0.004	0.065 ± 0.004
TTS (500 GeV)	0.119 ± 0.006	0.109 ± 0.006	0.028 ± 0.003	0.083 ± 0.005
TTS (550 GeV)	0.098 ± 0.005	0.085 ± 0.005	0.020 ± 0.002	0.072 ± 0.005
TTS (600 GeV)	0.081 ± 0.005	0.064 ± 0.004	0.015 ± 0.002	0.095 ± 0.005
TTS (650 GeV)	0.055 ± 0.004	0.044 ± 0.004	0.009 ± 0.002	0.084 ± 0.005
TTS (700 GeV)	0.042 ± 0.003	0.028 ± 0.002	0.006 ± 0.001	0.091 ± 0.004
TTS (750 GeV)	0.034 ± 0.003	0.026 ± 0.003	0.004 ± 0.001	0.083 ± 0.005
TTS (800 GeV)	0.021 ± 0.003	0.019 ± 0.002	0.004 ± 0.001	0.082 ± 0.005
TTS (850 GeV)	0.023 ± 0.003	0.014 ± 0.002	0.001 ± 0.001	0.072 ± 0.005

Process	SRVLQ4	SRVLQ5	SRVLQ6	SRVLQ7	Total
TTS (350 GeV)	0.024 ± 0.003	0.032 ± 0.003	0.033 ± 0.003	0.020 ± 0.002	0.430 ± 0.011
TTS (400 GeV)	0.057 ± 0.004	0.044 ± 0.004	0.047 ± 0.004	0.037 ± 0.003	0.592 ± 0.013
TTS (450 GeV)	0.104 ± 0.006	0.064 ± 0.004	0.085 ± 0.005	0.058 ± 0.004	0.687 ± 0.014
TTS (500 GeV)	0.128 ± 0.006	0.077 ± 0.005	0.123 ± 0.006	0.075 ± 0.005	0.742 ± 0.015
TTS (550 GeV)	0.181 ± 0.007	0.093 ± 0.005	0.168 ± 0.007	0.102 ± 0.006	0.818 ± 0.016
TTS (600 GeV)	0.224 ± 0.008	0.115 ± 0.006	0.227 ± 0.008	0.128 ± 0.006	0.949 ± 0.017
TTS (650 GeV)	0.272 ± 0.009	0.092 ± 0.005	0.239 ± 0.009	0.119 ± 0.006	0.914 ± 0.017
TTS (700 GeV)	0.288 ± 0.007	0.092 ± 0.004	0.262 ± 0.006	0.134 ± 0.005	0.942 ± 0.012
TTS (750 GeV)	0.284 ± 0.010	0.077 ± 0.005	0.276 ± 0.009	0.131 ± 0.006	0.915 ± 0.017
TTS (800 GeV)	0.344 ± 0.011	0.081 ± 0.005	0.301 ± 0.010	0.131 ± 0.007	0.982 ± 0.018
TTS (850 GeV)	0.366 ± 0.011	0.078 ± 0.005	0.308 ± 0.010	0.136 ± 0.007	0.998 ± 0.018

Table 6.8: $T_{5/3}$ expected yields in the signal regions SRVLQ0-SRVLQ3 . Uncertainties are statistical only. [110]

Sample	SRVLQ0	SRVLQ1	SRVLQ2	SRVLQ3
600 $\lambda \ll 1$	17.435 ± 0.755	8.587 ± 0.497	1.009 ± 0.162	12.579 ± 0.667
600 $\lambda = 0.5$	18.091 ± 0.755	9.013 ± 0.497	1.042 ± 0.163	12.681 ± 0.667
600 $\lambda = 1$	20.378 ± 0.762	10.417 ± 0.502	1.171 ± 0.164	12.96 ± 0.668
650 $\lambda \ll 1$	7.788 ± 0.383	4.036 ± 0.255	0.346 ± 0.077	7.293 ± 0.38
650 $\lambda = 0.5$	8.289 ± 0.383	4.352 ± 0.256	0.367 ± 0.077	7.376 ± 0.38
650 $\lambda = 1$	9.743 ± 0.389	5.218 ± 0.26	0.435 ± 0.078	7.552 ± 0.381
700 $\lambda \ll 1$	3.336 ± 0.191	1.917 ± 0.138	0.115 ± 0.037	4.148 ± 0.221
700 $\lambda = 0.5$	3.646 ± 0.191	2.099 ± 0.139	0.134 ± 0.037	4.214 ± 0.221
700 $\lambda = 1$	4.607 ± 0.196	2.683 ± 0.142	0.178 ± 0.038	4.402 ± 0.222
750 $\lambda \ll 1$	1.727 ± 0.108	0.801 ± 0.067	0.09 ± 0.021	2.585 ± 0.135
750 $\lambda = 0.5$	1.932 ± 0.108	0.939 ± 0.068	0.101 ± 0.021	2.636 ± 0.135
750 $\lambda = 1$	2.603 ± 0.112	1.301 ± 0.071	0.122 ± 0.022	2.766 ± 0.136
800 $\lambda \ll 1$	0.844 ± 0.058	0.369 ± 0.035	0.04 ± 0.012	1.453 ± 0.078
800 $\lambda = 0.5$	0.99 ± 0.058	0.458 ± 0.036	0.047 ± 0.012	1.488 ± 0.078
800 $\lambda = 1$	1.221 ± 0.06	0.583 ± 0.037	0.056 ± 0.012	1.55 ± 0.078
850 $\lambda \ll 1$	0.363 ± 0.03	0.217 ± 0.022	0.02 ± 0.007	0.699 ± 0.042
850 $\lambda = 0.5$	0.463 ± 0.03	0.277 ± 0.022	0.026 ± 0.007	0.731 ± 0.042
850 $\lambda = 1$	0.766 ± 0.033	0.456 ± 0.024	0.036 ± 0.007	0.813 ± 0.043
900 $\lambda \ll 1$	0.202 ± 0.017	0.109 ± 0.012	0.004 ± 0.002	0.506 ± 0.028
900 $\lambda = 0.5$	0.267 ± 0.017	0.146 ± 0.012	0.007 ± 0.002	0.53 ± 0.029
900 $\lambda = 1$	0.466 ± 0.02	0.265 ± 0.014	0.015 ± 0.002	0.592 ± 0.029
950 $\lambda \ll 1$	0.1 ± 0.009	0.041 ± 0.005	0.005 ± 0.002	0.309 ± 0.017
950 $\lambda = 0.5$	0.147 ± 0.009	0.069 ± 0.006	0.007 ± 0.002	0.324 ± 0.017
950 $\lambda = 1$	0.295 ± 0.012	0.143 ± 0.007	0.013 ± 0.002	0.388 ± 0.018
1000 $\lambda \ll 1$	0.048 ± 0.005	0.022 ± 0.003	0.001 ± 0	0.166 ± 0.01
1000 $\lambda = 0.5$	0.078 ± 0.005	0.039 ± 0.003	0.002 ± 0	0.178 ± 0.01
1000 $\lambda = 1$	0.179 ± 0.007	0.1 ± 0.005	0.005 ± 0.001	0.215 ± 0.01

Table 6.9: $T_{5/3}$ expected yields in the signal regions SRVLQ4-SRVLQ7 . Uncertainties are statistical only. [110]

Sample	SRVLQ4	SRVLQ5	SRVLQ6	SRVLQ7
600 $\lambda \ll 1$	46.281 ± 1.273	8.984 ± 0.505	28.319 ± 0.902	6.725 ± 0.438
600 $\lambda = 0.5$	46.482 ± 1.273	9.067 ± 0.505	28.45 ± 0.902	6.754 ± 0.438
600 $\lambda = 1$	46.939 ± 1.274	9.259 ± 0.505	28.896 ± 0.903	6.856 ± 0.438
650 $\lambda \ll 1$	29.538 ± 0.764	5.294 ± 0.298	19.019 ± 0.558	3.402 ± 0.235
650 $\lambda = 0.5$	29.684 ± 0.764	5.348 ± 0.298	19.136 ± 0.558	3.423 ± 0.235
650 $\lambda = 1$	30.196 ± 0.765	5.535 ± 0.299	19.437 ± 0.559	3.481 ± 0.235
700 $\lambda \ll 1$	18.116 ± 0.454	2.82 ± 0.164	12.318 ± 0.345	2.341 ± 0.145
700 $\lambda = 0.5$	18.245 ± 0.455	2.863 ± 0.164	12.411 ± 0.345	2.356 ± 0.145
700 $\lambda = 1$	18.671 ± 0.456	3 ± 0.164	12.681 ± 0.346	2.409 ± 0.145
750 $\lambda \ll 1$	11.722 ± 0.285	1.672 ± 0.098	7.851 ± 0.214	1.422 ± 0.089
750 $\lambda = 0.5$	11.849 ± 0.285	1.71 ± 0.099	7.937 ± 0.214	1.437 ± 0.089
750 $\lambda = 1$	12.141 ± 0.286	1.815 ± 0.099	8.137 ± 0.215	1.477 ± 0.089
800 $\lambda \ll 1$	7.729 ± 0.181	1.043 ± 0.06	5.155 ± 0.134	0.966 ± 0.057
800 $\lambda = 0.5$	7.824 ± 0.181	1.071 ± 0.06	5.214 ± 0.134	0.977 ± 0.057
800 $\lambda = 1$	7.94 ± 0.181	1.111 ± 0.06	5.328 ± 0.134	0.996 ± 0.057
850 $\lambda \ll 1$	5.144 ± 0.115	0.518 ± 0.032	3.116 ± 0.082	0.607 ± 0.034
850 $\lambda = 0.5$	5.221 ± 0.115	0.538 ± 0.033	3.169 ± 0.082	0.615 ± 0.034
850 $\lambda = 1$	5.446 ± 0.116	0.6 ± 0.033	3.33 ± 0.082	0.643 ± 0.034
900 $\lambda \ll 1$	3.388 ± 0.074	0.341 ± 0.021	1.942 ± 0.051	0.366 ± 0.021
900 $\lambda = 0.5$	3.451 ± 0.074	0.356 ± 0.021	1.986 ± 0.051	0.371 ± 0.021
900 $\lambda = 1$	3.624 ± 0.075	0.397 ± 0.022	2.105 ± 0.051	0.393 ± 0.021
950 $\lambda \ll 1$	2.165 ± 0.047	0.199 ± 0.012	1.344 ± 0.033	0.197 ± 0.012
950 $\lambda = 0.5$	2.214 ± 0.047	0.209 ± 0.012	1.379 ± 0.033	0.201 ± 0.012
950 $\lambda = 1$	2.366 ± 0.048	0.238 ± 0.013	1.475 ± 0.034	0.213 ± 0.012
1000 $\lambda \ll 1$	1.426 ± 0.03	0.107 ± 0.007	0.862 ± 0.021	0.129 ± 0.008
1000 $\lambda = 0.5$	1.466 ± 0.03	0.115 ± 0.007	0.889 ± 0.021	0.132 ± 0.008
1000 $\lambda = 1$	1.599 ± 0.031	0.136 ± 0.008	0.971 ± 0.022	0.143 ± 0.008

Table 6.10: Event selection efficiencies (in percent), relative to the inclusive cross section for the $T_{5/3}$ signal in SRVLQ0-SRVLQ3 as a function of the generated mass. [110]

Sample	SRVLQ0	SRVLQ1	SRVLQ2	SRVLQ3
600 $\lambda \ll 1$	0.494 ± 0.021	0.243 ± 0.014	0.028 ± 0.004	0.356 ± 0.018
600 $\lambda = 0.5$	0.497 ± 0.02	0.248 ± 0.013	0.028 ± 0.004	0.348 ± 0.018
600 $\lambda = 1$	0.514 ± 0.019	0.263 ± 0.012	0.029 ± 0.004	0.327 ± 0.016
650 $\lambda \ll 1$	0.385 ± 0.018	0.199 ± 0.012	0.017 ± 0.003	0.361 ± 0.018
650 $\lambda = 0.5$	0.396 ± 0.018	0.208 ± 0.012	0.017 ± 0.003	0.352 ± 0.018
650 $\lambda = 1$	0.42 ± 0.016	0.225 ± 0.011	0.018 ± 0.003	0.326 ± 0.016
700 $\lambda \ll 1$	0.282 ± 0.016	0.162 ± 0.011	0.009 ± 0.003	0.35 ± 0.018
700 $\lambda = 0.5$	0.295 ± 0.015	0.17 ± 0.011	0.01 ± 0.003	0.341 ± 0.017
700 $\lambda = 1$	0.332 ± 0.014	0.193 ± 0.01	0.012 ± 0.002	0.317 ± 0.016
750 $\lambda \ll 1$	0.244 ± 0.015	0.113 ± 0.009	0.012 ± 0.003	0.365 ± 0.019
750 $\lambda = 0.5$	0.259 ± 0.014	0.126 ± 0.009	0.013 ± 0.002	0.354 ± 0.018
750 $\lambda = 1$	0.306 ± 0.013	0.153 ± 0.008	0.014 ± 0.002	0.325 ± 0.016
800 $\lambda \ll 1$	0.196 ± 0.013	0.085 ± 0.008	0.009 ± 0.002	0.338 ± 0.018
800 $\lambda = 0.5$	0.217 ± 0.012	0.1 ± 0.007	0.01 ± 0.002	0.327 ± 0.017
800 $\lambda = 1$	0.249 ± 0.012	0.118 ± 0.007	0.011 ± 0.002	0.316 ± 0.016
850 $\lambda \ll 1$	0.136 ± 0.011	0.082 ± 0.008	0.007 ± 0.002	0.263 ± 0.016
850 $\lambda = 0.5$	0.163 ± 0.01	0.097 ± 0.007	0.009 ± 0.002	0.258 ± 0.015
850 $\lambda = 1$	0.225 ± 0.009	0.134 ± 0.007	0.01 ± 0.002	0.239 ± 0.012
900 $\lambda \ll 1$	0.121 ± 0.01	0.065 ± 0.007	0.002 ± 0.001	0.305 ± 0.017
900 $\lambda = 0.5$	0.149 ± 0.009	0.081 ± 0.006	0.004 ± 0.001	0.295 ± 0.016
900 $\lambda = 1$	0.213 ± 0.009	0.121 ± 0.006	0.007 ± 0.001	0.27 ± 0.013
950 $\lambda \ll 1$	0.096 ± 0.009	0.039 ± 0.005	0.004 ± 0.002	0.295 ± 0.016
950 $\lambda = 0.5$	0.129 ± 0.008	0.06 ± 0.005	0.006 ± 0.002	0.283 ± 0.015
950 $\lambda = 1$	0.206 ± 0.008	0.1 ± 0.005	0.009 ± 0.002	0.27 ± 0.012
1000 $\lambda \ll 1$	0.072 ± 0.008	0.033 ± 0.005	0.001 ± 0.001	0.249 ± 0.015
1000 $\lambda = 0.5$	0.106 ± 0.007	0.053 ± 0.004	0.003 ± 0.001	0.242 ± 0.013
1000 $\lambda = 1$	0.188 ± 0.008	0.105 ± 0.005	0.005 ± 0.001	0.226 ± 0.011

Table 6.11: Event selection efficiencies (in percent), relative to the inclusive cross section for the $T_{5/3}$ signal in SRVLQ4-SRVLQ7 as a function of the generated mass. [110]

Sample	SRVLQ4	SRVLQ5	SRVLQ6	SRVLQ7
600 $\lambda \ll 1$	1.311 ± 0.036	0.254 ± 0.014	0.802 ± 0.025	0.19 ± 0.012
600 $\lambda = 0.5$	1.279 ± 0.035	0.249 ± 0.013	0.782 ± 0.024	0.185 ± 0.012
600 $\lambda = 1$	1.185 ± 0.032	0.233 ± 0.012	0.73 ± 0.022	0.173 ± 0.011
650 $\lambda \ll 1$	1.462 ± 0.037	0.262 ± 0.014	0.941 ± 0.027	0.168 ± 0.011
650 $\lambda = 0.5$	1.418 ± 0.036	0.255 ± 0.014	0.914 ± 0.026	0.163 ± 0.011
650 $\lambda = 1$	1.304 ± 0.033	0.239 ± 0.012	0.839 ± 0.024	0.15 ± 0.01
700 $\lambda \ll 1$	1.532 ± 0.038	0.238 ± 0.013	1.042 ± 0.029	0.198 ± 0.012
700 $\lambda = 0.5$	1.479 ± 0.036	0.232 ± 0.013	1.006 ± 0.028	0.191 ± 0.011
700 $\lambda = 1$	1.348 ± 0.032	0.216 ± 0.011	0.915 ± 0.025	0.173 ± 0.01
750 $\lambda \ll 1$	1.656 ± 0.04	0.236 ± 0.013	1.109 ± 0.03	0.2 ± 0.012
750 $\lambda = 0.5$	1.594 ± 0.038	0.23 ± 0.013	1.067 ± 0.028	0.193 ± 0.011
750 $\lambda = 1$	1.429 ± 0.033	0.213 ± 0.011	0.957 ± 0.025	0.173 ± 0.01
800 $\lambda \ll 1$	1.798 ± 0.042	0.242 ± 0.014	1.199 ± 0.031	0.224 ± 0.013
800 $\lambda = 0.5$	1.718 ± 0.039	0.235 ± 0.013	1.145 ± 0.029	0.214 ± 0.012
800 $\lambda = 1$	1.619 ± 0.037	0.226 ± 0.012	1.086 ± 0.027	0.203 ± 0.011
850 $\lambda \ll 1$	1.936 ± 0.043	0.195 ± 0.012	1.173 ± 0.03	0.228 ± 0.013
850 $\lambda = 0.5$	1.841 ± 0.04	0.189 ± 0.011	1.118 ± 0.028	0.217 ± 0.012
850 $\lambda = 1$	1.604 ± 0.034	0.177 ± 0.009	0.981 ± 0.024	0.189 ± 0.01
900 $\lambda \ll 1$	2.04 ± 0.045	0.205 ± 0.013	1.169 ± 0.03	0.22 ± 0.012
900 $\lambda = 0.5$	1.923 ± 0.041	0.198 ± 0.012	1.107 ± 0.028	0.207 ± 0.011
900 $\lambda = 1$	1.656 ± 0.034	0.181 ± 0.01	0.962 ± 0.023	0.179 ± 0.009
950 $\lambda \ll 1$	2.065 ± 0.045	0.189 ± 0.012	1.282 ± 0.032	0.188 ± 0.012
950 $\lambda = 0.5$	1.932 ± 0.041	0.183 ± 0.011	1.204 ± 0.029	0.176 ± 0.011
950 $\lambda = 1$	1.65 ± 0.033	0.166 ± 0.009	1.028 ± 0.023	0.148 ± 0.008
1000 $\lambda \ll 1$	2.139 ± 0.046	0.16 ± 0.011	1.293 ± 0.032	0.194 ± 0.012
1000 $\lambda = 0.5$	1.992 ± 0.041	0.156 ± 0.01	1.209 ± 0.029	0.18 ± 0.01
1000 $\lambda = 1$	1.681 ± 0.033	0.143 ± 0.008	1.021 ± 0.023	0.15 ± 0.008

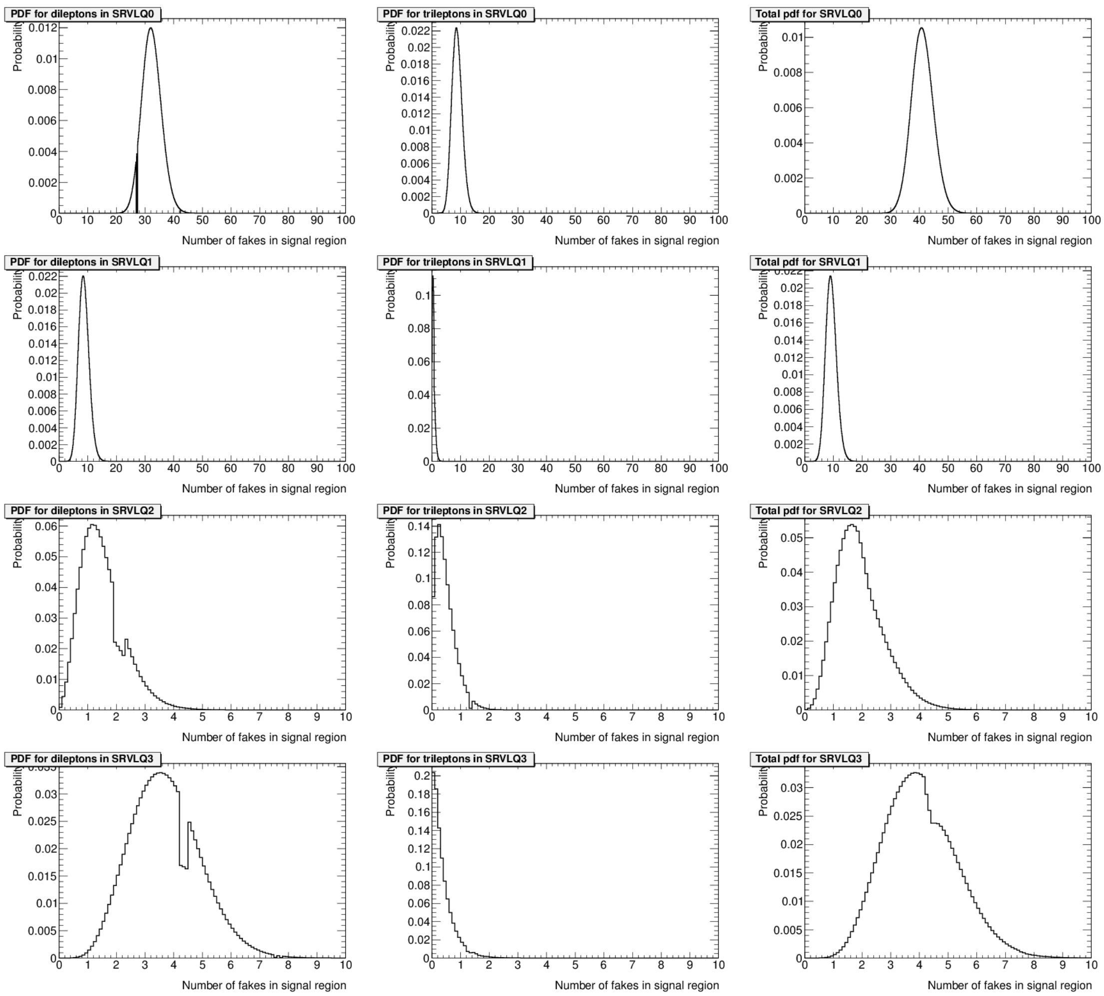

Figure 6.7: Probability density functions for the fake/non-prompt yield computed as described in the text, for signal regions SRVLQ0-SRVLQ3. The contribution from dilepton events is shown in the left-most plots, from trilepton events in the center plots, and the total in the right-hand plots. Discontinuities in some distributions arise from occasional non-convergence of the likelihood fit. These have a negligible impact on the statistical uncertainties used in the analysis. [110]

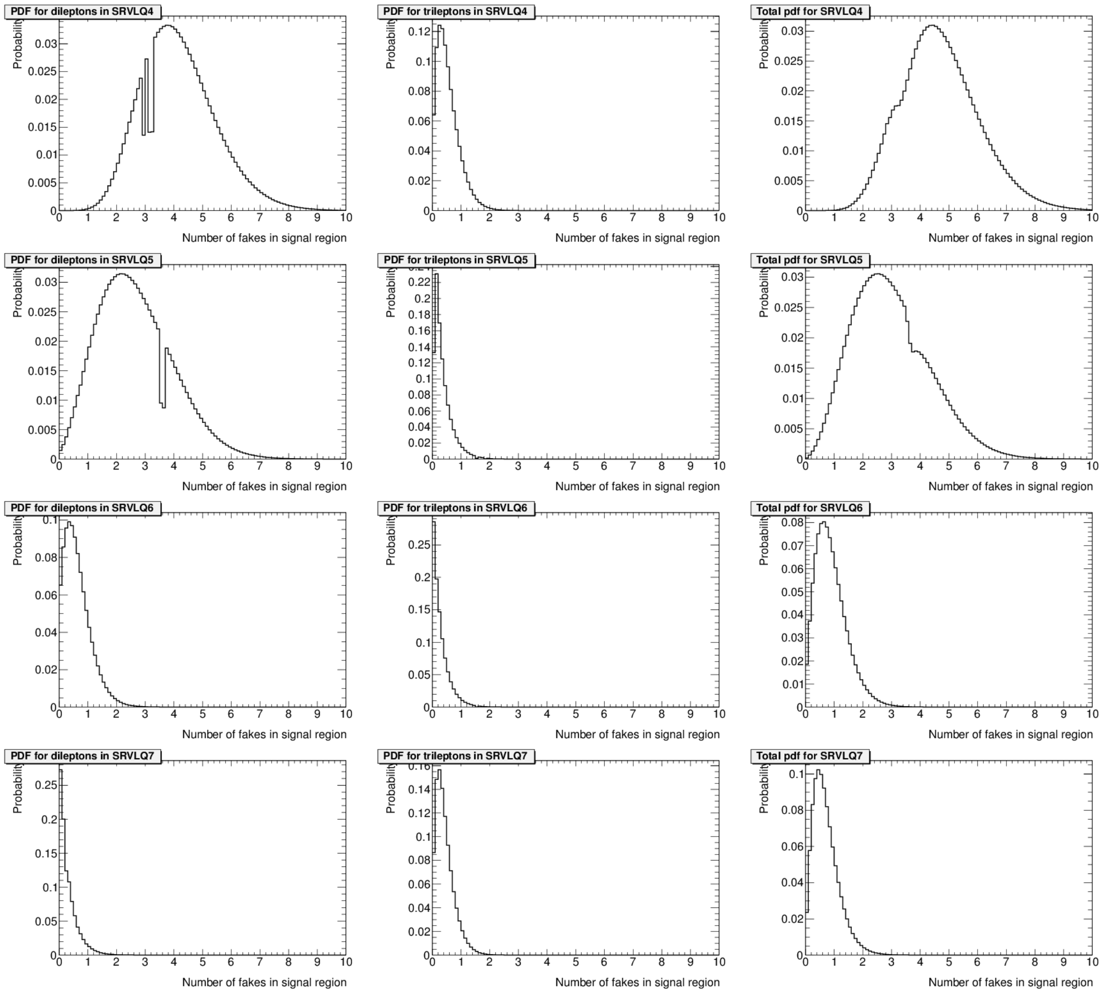

Figure 6.8: Probability density functions for the fake/non-prompt yield computed as described in the text, for signal regions SRVLQ4-SRVLQ7. The contribution from dilepton events is shown in the left-most plots, from trilepton events in the center plots, and the total in the right-hand plots. Discontinuities in some distributions arise from occasional non-convergence of the likelihood fit. These have a negligible impact on the statistical uncertainties used in the analysis. [110]

6.4 Study of Multivariate Analysis

The event selection described in this chapter is an example of the cut and count method. This means that the signal region is defined by placing a set of requirements or "cuts" on variables separately. An alternate approach is to implement a multivariate analysis (MVA) which can make better use of the information contained in the data and the MC simulation. In an MVA a number of variables are used together to produce a weight that characterizes the likelihood that an event is signal or background. This has the advantage that it can account for correlations between variables to better isolate regions of phase space with a large signal to background ratio ideal for performing the search. A method known as the Boosted Decision Tree (BDT) is an example of an MVA used often in particle physics searches. A study was carried out using a subset of the data collected in 2012 to assess the potential benefits of a BDT analysis for the full 2012 data set. A comparison was made between the results of a simple cut and count analysis and a BDT analysis. Details on the BDT method and the software package used to implement it for this study can be found in Ref. [125]

A BDT uses a large number of "trees", each of which applies a sequence of cuts on different variables to each event. Each tree consists of a series of nodes that branch out from one another starting from an initial node and ending with a group of terminal nodes. With the exception of the terminal nodes, each node is connected by branches to two nodes in the next level of nodes below it. At each node a cut is applied on a particular variable. The result of the cut determines which of the two connected nodes the event is passed to. The number of trees, number of nodes per tree, the variables used and the number of different cut values attempted at each node are configurable. Within each tree the cuts are determined to maximally separate signal and background. The variables and cut values at each node are chosen so that signal-like events fall into certain terminal nodes with higher probability than background-like events and vice versa. For each tree a weight is produced for an event based on the terminal node in which it falls. This weight expresses the likelihood that it is a signal event. The final weight for the event is an average taken across all the trees in the BDT.

The BDT is trained using a subset of events from MC simulation to distinguish between signal and background. Another subset of the MC events, orthogonal to that used for training, is used to test the trained BDT. The distribution of the weights for the events used for testing should roughly match the distribution of the training events. If they do not match well the BDT may have been over trained. This occurs when there are either too few events in the training sample, too many trees or too many nodes per tree causing the BDT to reflect random fluctuations in the training sample. Once the BDT is trained and tested it is used to determine a weight for data and the remaining MC events not used in training or testing. The signal region can then be defined by placing a cut on this weight rather than placing a series of cuts on individual variables. A disadvantage of a BDT analysis is that some fraction of the signal and background MC events must be used to train and test the BDT. These events cannot be used to compare with data. As a consequence there are fewer MC events available and the statistical error is larger.

The comparison was carried out using 14.3 fb^{-1} of data collected in the first part of 2012. It was done with a simpler cut and count analysis than that described in this dissertation. Details on the earlier version of the analysis, including the results of this simpler cut and count selection, are documented in Ref. [124]. Only same-sign dilepton events were considered with three channels for ee, $e\mu$ and $\mu\mu$ events rather than eight SR categories. The event selection for the cut and count analysis required $E_{\mathrm{T}}^{\mathrm{miss}} > 40$ GeV and $H_{\mathrm{T}} > 550$ GeV. The variables used by the BDT are H_{T}, $E_{\mathrm{T}}^{\mathrm{miss}}$, N_{jets}, N_{b-jets} and η of the second leading jet. Four hundred trees were used with five nodes per tree and twenty attempts at finding the optimal cut value per variable at each node. The BDT was trained with the full background and a combination of vector-like bottom and top isosinglets with masses 600, 700 and 800 GeV. The events in each MC sample are numbered from one to the total number of events in that sample. Only even events were used for the training and testing in order to reserve MC events for comparison with data.

The results of the BDT are shown in Fig. 6.9. Figure 6.9 (a) shows the distribution of the BDT weight for the events used in training and testing. It shows that there is good separation between signal and background and that the BDT is not overtrained. Figure 6.9 (b) shows the signal and background efficiency as well as the signal significance (defined as $s/\sqrt{s+b}$) as a function of the cut placed on the BDT weight. The optimal cut value to maximize significance is 0.0527. Figure 6.10 shows the distribution of BDT weights for signal and background events and data for the ee, $e\mu$ and $\mu^+\mu^-$ channels. Here the signal and background are correctly normalized to the integrated luminosity of the data sample. The data is only shown below the cut value. This was done to avoid looking at the data in what would have become the signal region in the event that the BDT approach was adopted. The estimation of the background was not finalized at the time so the analysis was still blinded (see Chapter 7). The limits produced by placing a cut on the BDT weight are shown in Fig. 6.11 for vector-like bottom and top singlets. Table 6.12 summarizes the limits produced for the 14.3 fb^{-1} data set using the simple cut and count analysis and using the BDT analysis. The table shows both mass limits and cross-section limits for vector-like bottom and top signals of mass 600 GeV. The mass limits produced with the BDT analysis show a slight improvement with respect to the limits produced with the cut and count analysis. The mass limit for vector-like bottom increases by 4.5% and those for vector-like top increase by 2.4%. Although the BDT analysis shows an improvement in the limits the improvement is very slight. Ultimately it was decided that the categorization method described in Section 6.2 was the best option for the analysis of the full 2012 data on the basis of the optimization study done with the $t\bar{t}t\bar{t}$ signal.

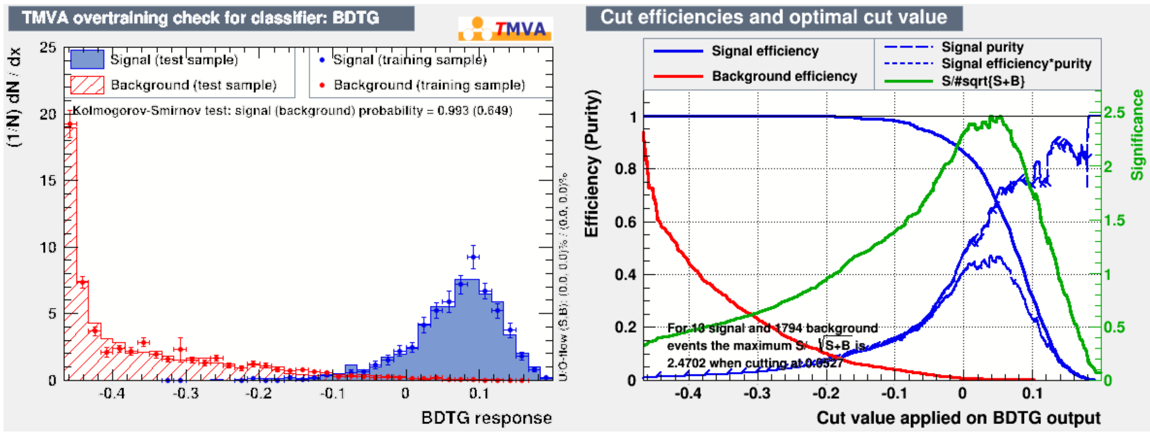

(a) BDT Weight (b) BDT Cut Value

Figure 6.9: Distribution of BDT weights (a) for signal and background MC events used in training and testing. The distributions are not normalized to the integrated luminosity of the data set. Plots of signal and background efficiency (b) as well as signal significance (defined as $s/\sqrt{s+b}$) as a function of the cut placed on the BDT weight.

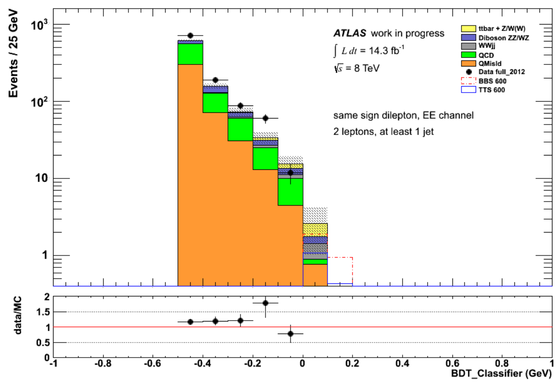

(a) ee

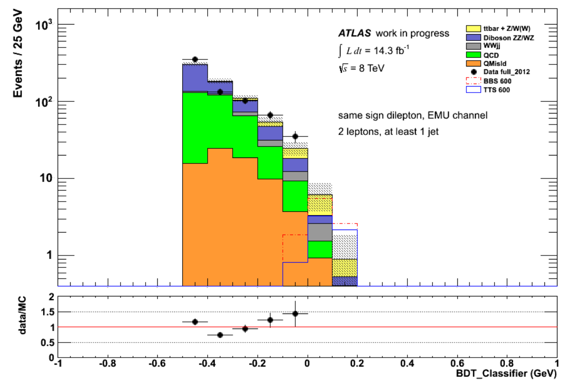

(b) $e\mu$

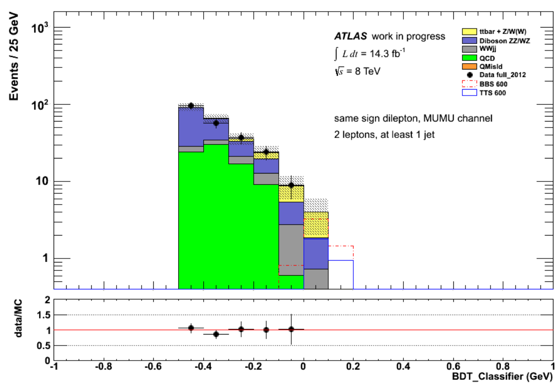

(c) $\mu\mu$

Figure 6.10: Distribution of BDT weights for signal and background MC events as well as data for the ee, $e\mu$ and $\mu\mu$. The MC events are normalized to 14.3 fb^{-1}. The data is only shown below the proposed cut value on the BDT weight.

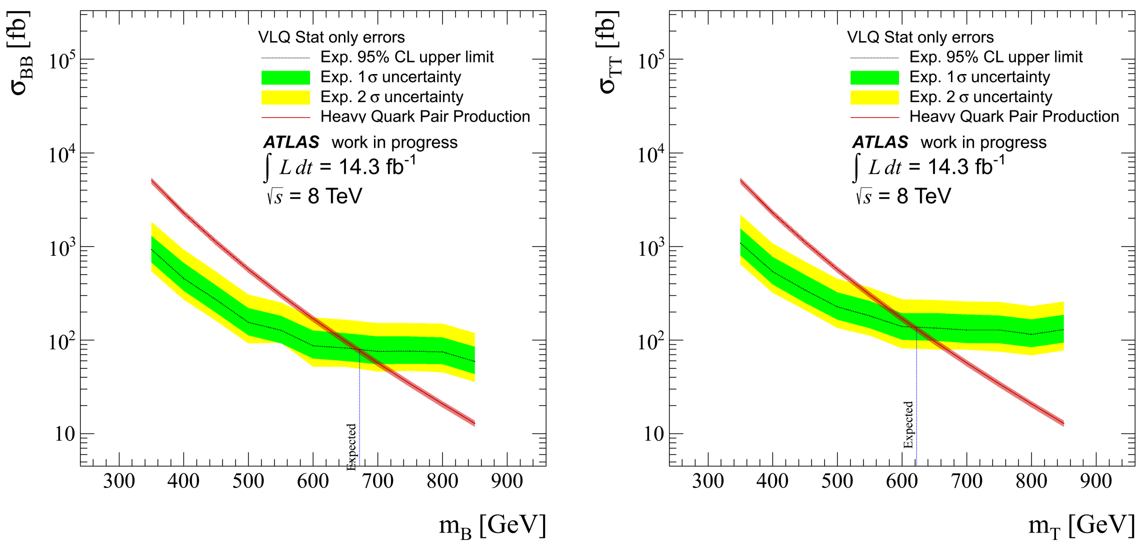

(a) vector-like bottom

(b) vector-like top

Figure 6.11: Expected limits produced at 95 % CL on the production cross-section for pair production of vector-like bottom (a) and top (b) using the BDT analysis. These limits only account for statistical error

Table 6.12: Comparison of expected limits on the production cross section for pair production of vector-like bottom and top isosinglets with a mass of 600 GeV produced with a cut and count analysis and a BDT analysis. Also shown is a comparison of the expected mass limits for vector-like bottom and top isosinglets for the cut an count analysis and the BDT analysis.

expected limts				
analysis	95 % CLs σ_{UL} (fb)		mass limit (GeV)	
	BBS600	TTS600	BBS	TTS
cut and count	109	157	643	607
BDT	87 (-20%)	140 (-11%)	672 (+4.5%)	622 (+2.4%)

CHAPTER 7

Background Estimation and Validation

The standard procedure in an analysis involving a search for new physics is to compare the data in a particular region of phase space to the background only and signal-plus-background hypotheses. An excess in data above the background expectation can be interpreted as a sign of new physics depending on the significance of the excess. As such, a crucial step is the estimation of the background contribution to the signal region. The background for this analysis can be divided into two broad categories: the irreducible background from SM processes that produce the same final state as the signal and instrumental background arising from limitations of the detector and reconstruction software in accurately determining the final state. The irreducible background is estimated using MC simulations described in detail in Chapter 4. Since the effects that give rise to the instrumental background occur in a wide variety of physical processes and also involve the detector response they can be difficult to model with MC simulations and thus are estimated using data-driven methods. Both the MC simulations and the data-driven techniques are validated by comparing kinematic distributions of data and the total background estimate in a series of validation regions orthogonal to the signal region.

While the background estimation is being developed and validated the analysis is said to be blind. This means that the analysis team does not look at the data in the signal region. This is done to avoid the possibility that the background estimation is influenced by knowledge of the data in the signal region. Once the techniques used for estimating the background are finalized the analysis is unblinded and the data in the signal region can be analyzed.

7.1 Irreducible Background from Standard Model Processes

SM processes that can produce either three leptons or a same-sign dilepton pair in the final state, and thus contribute to the signal region, include associated production of $t\bar{t}$ with bosons ($t\bar{t}$+$W/Z/H/WW$), diboson production ($ZZ \rightarrow \ell^+\ell^-\ell^+\ell^-$, $WZ/\gamma^* \rightarrow \ell\nu\ell^+\ell^-$, $W^{\pm}W^{\pm} \rightarrow \ell^{\pm}\nu\ell^{\pm}\nu$), triboson production ($WWW^* \rightarrow \ell\nu\ell\nu\ell\nu$, $ZWW^* \rightarrow \ell\ell\ell\nu\ell\nu$), associated production of a single top quark with a Higgs boson (tH where $H \rightarrow WW$, $H \rightarrow ZZ$ and $H \rightarrow \tau\tau$ decays are included) and associated production of a single top quark with a WZ pair (tWZ). The same-sign W background ($W^{\pm}W^{\pm} \rightarrow \ell^{\pm}\nu\ell^{\pm}\nu$) includes a component arising from double parton interactions (DPI) where two separate pairs of partons inside the colliding protons scatter and each produces a W boson in association with jets. The Feynman diagrams for each of these processes are shown in Fig. 7.1 through Fig. 7.3. Table 4.2 lists important information for each of the background samples including the MC generators used to produce them, the parton distribution function (PDF), cross-section, K-factor relating the LO and NLO cross-sections, the integrated luminosity corresponding to each sample and the detector simulation used.

The irreducible background sources are estimated from the following MC samples:

- Associated production of $t\bar{t}$ and bosons:
  - $t\bar{t}W$+jets, $t\bar{t}Z$+jets and $t\bar{t}W^+W^-$ were generated at leading-order (LO) with MadGraph 5.1 [102], showered and hadronized with Pythia 6.4 [126]. The cross-sections for the $t\bar{t}W/Z$+jets samples are rescaled to next-to-leading-order (NLO) calculations [127, 128];
  - $t\bar{t}H$ with $H \rightarrow W^+W^-, ZZ, \tau^+\tau^-$ and $\tau^+\tau^- \rightarrow \ell h$ were generated at LO with Pythia 8 [104]. The cross-sections are rescaled to NLO computation [129, 130];
- Diboson production:

- $W^{\pm}W^{\pm}$, WZ/γ^* and ZZ samples were generated at LO using Sherpa 1.4 [105]. The accepted vector boson decays were restricted to $W^{\pm}W^{\pm} \rightarrow \ell\nu\ell\nu$, $WZ \rightarrow \ell\ell\ell\nu$ and $ZZ \rightarrow \ell\ell\ell\ell$, where all three generations of leptons are allowed. The cross-sections are normalized to NLO theoretical calculations using MC for FeMtobarn processes (MCFM) [131];
- WWjj production from Double Parton Interaction of Wj [132] was generated using Pythia 8 [104];
- WH and ZH samples were generated at LO using Pythia 8 [104]. The cross-sections are rescaled to NLO computation [129, 130];

- Triboson production: $WWW^* \rightarrow \ell\nu\ell\nu\ell\nu$ and $ZWW^* \rightarrow \ell\ell\ell\nu\ell\nu$ were generated with MadGraph 5.1 [102], showered and hadronized with Pythia 6.4 [126].

- Associated production of a single top quark with a WZ pair (tWZ): produced with MadGraph v.5 [102], showered and hadronized with Pythia6.4 [126].

- Associated production of a single top quark with a Higgs boson (tH) is generated by the means of MadGraphv.5 [102], showered and hadronized with Pythia 8 [104];. This contribution includes $H \rightarrow WW$, $H \rightarrow ZZ$ and $H \rightarrow \tau\tau$ decays.

7.2 Data-Driven Instrumental Background

The two sources of instrumental background in this analysis are events containing final state objects which are misidentified as prompt leptons from the hard scattering process and events containing real opposite-sign dilepton pairs where one of the leptons has its charge misidentified leading to a same-sign dilepton pair. They are referred to as the fake/non-prompt lepton and electron charge misidentification [19] backgrounds respectively. Their contributions to our signal region are estimated with data-driven methods.

[19] charge misidentification is negligible for muons, see Section 7.2.2

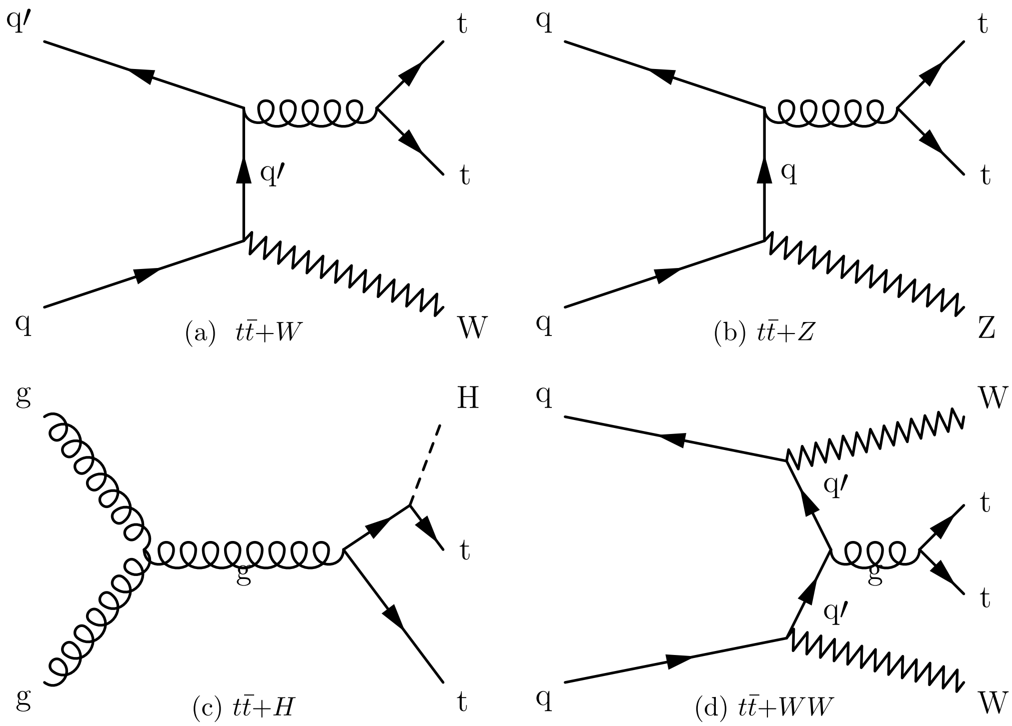

Figure 7.1: Leading order Feynman diagrams for production of top-antitop pair with associated boson(s).

7.2.1 Fake/Non-Prompt Leptons

The fake/non-prompt lepton background includes events containing objects, such as jets, which are misidentified as leptons as well as events containing true leptons that are not from the hard scattering process but rather some secondary process such as the decay of a heavy flavor hadron in the final state. The first category is referred to as fake leptons while the second is referred to as non-prompt leptons. Since the principles of detection and reconstruction of leptons differ greatly for electrons and muons the physical sources of fake and non-prompt leptons depend heavily on lepton flavor. For muons, the primary sources are semi-leptonic decay of b-hadrons and c-hadrons and extremely energetic particles in jets that punch through the calorimeter and reach the muon spectrometer. Fake or non-prompt electrons can come from semi-leptonic decay of b-hadrons and c-hadrons (as for muons), photon conversions that occur near the primary vertex, a photon or π^0 that showers in the

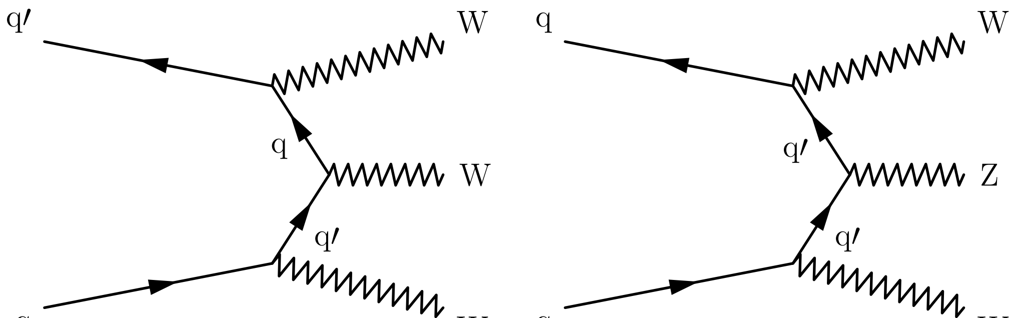

(a) WWW^* (b) ZWW^*

Figure 7.2: Leading order Feynman diagrams for production of three bosons.

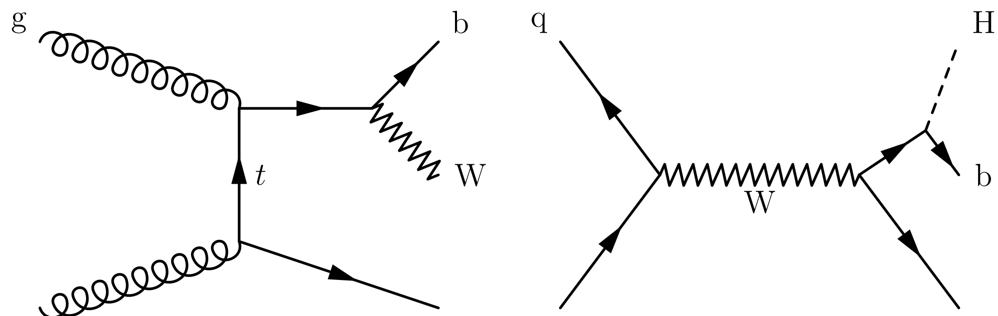

(a) tWZ (b) tH

Figure 7.3: Leading order Feynman diagrams for production of a single top quark with boson(s).

EM calorimeter and happens to overlap a charged hadron in the inner detector and hadronic showers that contain an abnormally large number of π^0s and shower mostly in the EM calorimeter. The method used to estimate the fake/non-prompt lepton background is known as the matrix method. The implementation of the matrix method in this analysis follows the techniques developed by the TopFakes subgroup in ATLAS in the context of final states containing top quarks using the ATLAS 2012 *pp* data set [133]. The matrix method relies primarily on data but also makes use of MC samples of single lepton $t\bar{t}$, W+jets, Z+jets, single-top and diboson events. Details on these MC samples including the MC generator, PDF and ATLAS sample ID are given in Table 7.1. The way these MC samples are used in the estimation is described below.

The matrix method uses two different lepton definitions known as loose (L) and tight (T). The tight lepton definition matches that used in the analysis described

Process	ATLAS SampleID	Generator	Shower	PDF	Normalization
$t\bar{t}$	117050	POWHEG [134]	PYTHIA 6.4 [126]	HERAPDF15NLO	NNLO+NNLL
W+jets	117680-126605	ALPGEN [135]	PYTHIA 6.4	CTEQ6L1	NNLO
Z+jets	117650-110816	ALPGEN	PYTHIA 6.4	CTEQ6L1	NNLO
t (s-,Wt-channel)	110141	POWHEG	PYTHIA 6.4	CT10	NLO+NNLL
$WW/WZ/ZZ$	107100-110832	ALPGEN	HERWIG 6.5	CTEQ6L1	NLO

Table 7.1: Single lepton MC samples used in the estimation of the fakes/non-prompt lepton background

in Chapter 5, while the loose definition is derived from the tight by relaxing one or more of its requirements. The way in which the lepton definitions are relaxed is analysis-dependent and generally varies with lepton flavor. In this analysis, the loose muon definition is equal to the tight muon definition with the isolation requirement removed. For electrons, the loose definition is equal to the tight with the isolation requirement removed and the electron ID criteria relaxed from *Tight* to *Medium*. However the requirement of a hit in the innermost vertexing layer of the pixel detector in order to veto electrons from photon conversions (included in *Tight* but not *Medium*) is retained in the loose electron definition. The main differences between *Tight* and *Medium* electrons that are removed for the loose definition are:

- a cut on the $\Delta\phi$ and $\Delta\eta$ between the calorimeter cluster and the extrapolated ID track.
- a requirement on a minimum number of high threshold hits, characteristic of electrons, in the TRT.
- a requirement on the ratio of cluster energy to track momentum E/p.

The loose signal region is a superset of the signal region where the tight lepton definition is replaced with the loose definition. The matrix method relates the number of events in the signal region with different combinations of tight and anti-tight (loose but not tight) leptons to the number of events in the loose signal region with different combinations of real and fake leptons. The expressions relating these two sets of numbers involve the real and fake efficiencies r and f. These are the probabilities that a real or fake lepton passing the loose definition also passes the tight definition. These equations can be cast into a matrix form and solved to find the number of events containing fake leptons in the signal region. The form of these equations for the same-sign dilepton and the trilepton channels is given below but first a discussion of the real and fake efficiencies is necessary.

The real and fake efficiencies r and f are measured in single lepton control regions in data that are highly enriched in either real or fake leptons. For muons, r is measured in events with a single muon and high W transverse mass ($m_W^T>$ 100 GeV), while f is measured in events with a single muon with a transverse impact parameter whose significance exceeds 5 standard deviations ($\mid d0_{sig} \mid > 5$). For electrons, r is measured in events with a single electron and high missing transverse energy ($E_{\mathrm{T}}^{\mathrm{miss}}>$ 150 GeV), while f is measured in events with a single electron and low $E_{\mathrm{T}}^{\mathrm{miss}}$ and m_W^T ($m_W^T<$ 20 GeV and $m_W^T+E_{\mathrm{T}}^{\mathrm{miss}}<$ 60 GeV). For both electrons and muons, the real enriched regions are dominated by events with real leptons from W boson decay from $t\bar{t}$, W+jets and single-top events, while the fake enriched regions are dominated by multi-jet events. The residual contribution to the fake enriched regions from events containing real leptons ($\approx 7\%$ for electrons and $\approx 2\%$ for muons) is removed with $t\bar{t}$, W+jets, Z+jets, single-top and diboson MC samples.

Events with a single lepton and large $E_{\mathrm{T}}^{\mathrm{miss}}$ are predominantly real lepton events since the main source of large $E_{\mathrm{T}}^{\mathrm{miss}}$ is neutrinos from leptonic decay of W bosons. In contrast single lepton events with low $E_{\mathrm{T}}^{\mathrm{miss}}$ are more likely to contain fake leptons. This is because the only way to produce a single lepton in a proton-proton collision is through production of a W boson (or another resonance that decays to a W boson such as a top-quark) followed by the leptonic decay $W \to \ell\nu$. Thus the same process that produces a single real lepton also produces a neutrino which is seen as large $E_{\mathrm{T}}^{\mathrm{miss}}$. Events with a single lepton and a large m_W^T are also predominantly real since W bosons are most often produced centrally leading to large m_W^T. In contrast multi-jet events, which can contain fake leptons, are typically lower energy and concentrated in the forward region of the detector leading to low m_W^T. Requiring a large $\mid d0_{sig} \mid$ produces a sample enriched in fake muons because the tracks of non-prompt muons from the leptonic decay of long-lived b-hadrons generally have a large impact parameter with respect to the primary vertex.

The efficiencies r and f depend on the kinematic properties of the lepton and the event. To account for this they are parametrized as a function of a set of kinematic variables. The electron efficiencies are parametrized in terms of leading jet p_{T}, electron η and the distance between the electron and the nearest jet $\Delta\mathrm{R}(\mathrm{e},\mathrm{jet})$. The muon efficiencies are parametrized in terms of muon p_{T}, muon η and the distance between the muon and the nearest jet $\Delta\mathrm{R}(\mu,\mathrm{jet})$. For electrons, the efficiencies are measured separately for events containing no b-tagged jets and events containing at least one b-tagged jet. The efficiencies for both electrons and muons are measured separately for leptons matched to each of the triggers used in the analysis (described in Chapter 4) as well as additional e and μ triggers equivalent to the low p_{T} triggers used in the analysis but with no isolation requirement.

Plots showing the dependencies of r and f on the parameters listed above for each trigger and b-jet multiplicity (for electrons) are shown in Fig. 7.5 through Fig. 7.7. These plots show a strong dependence of the efficiencies on the trigger matched to the lepton. This dependence arises from the isolation requirement included in the low lepton p_{T} triggers which biases the efficiencies for leptons matched to them high. The need to account for this bias is the motivation for measuring the efficiencies for events passing the low lepton p_{T} non-isolated triggers in addition to the triggers used in the analysis. More details on exactly how this bias is handled are given below.

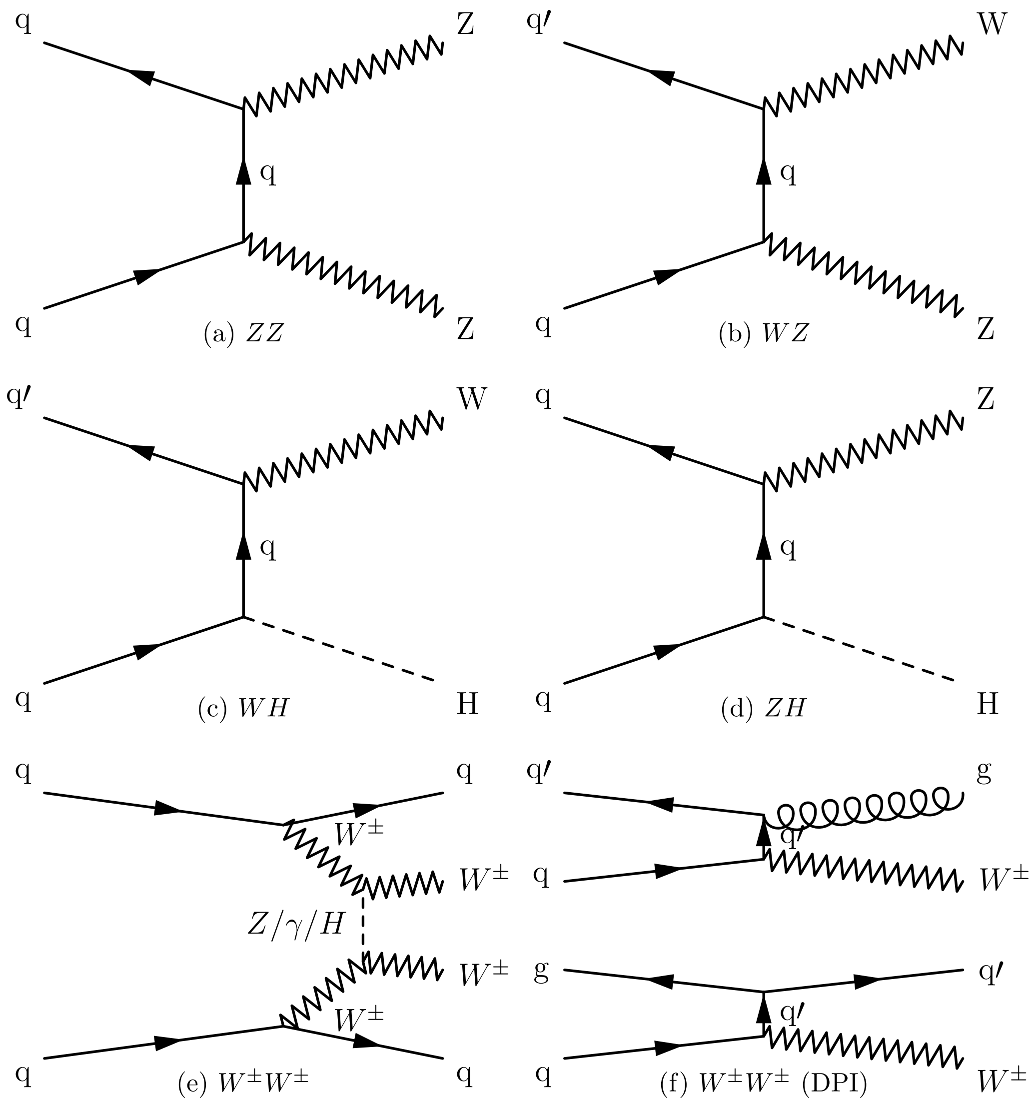

Figure 7.4: Leading order Feynman diagrams for production of two bosons.

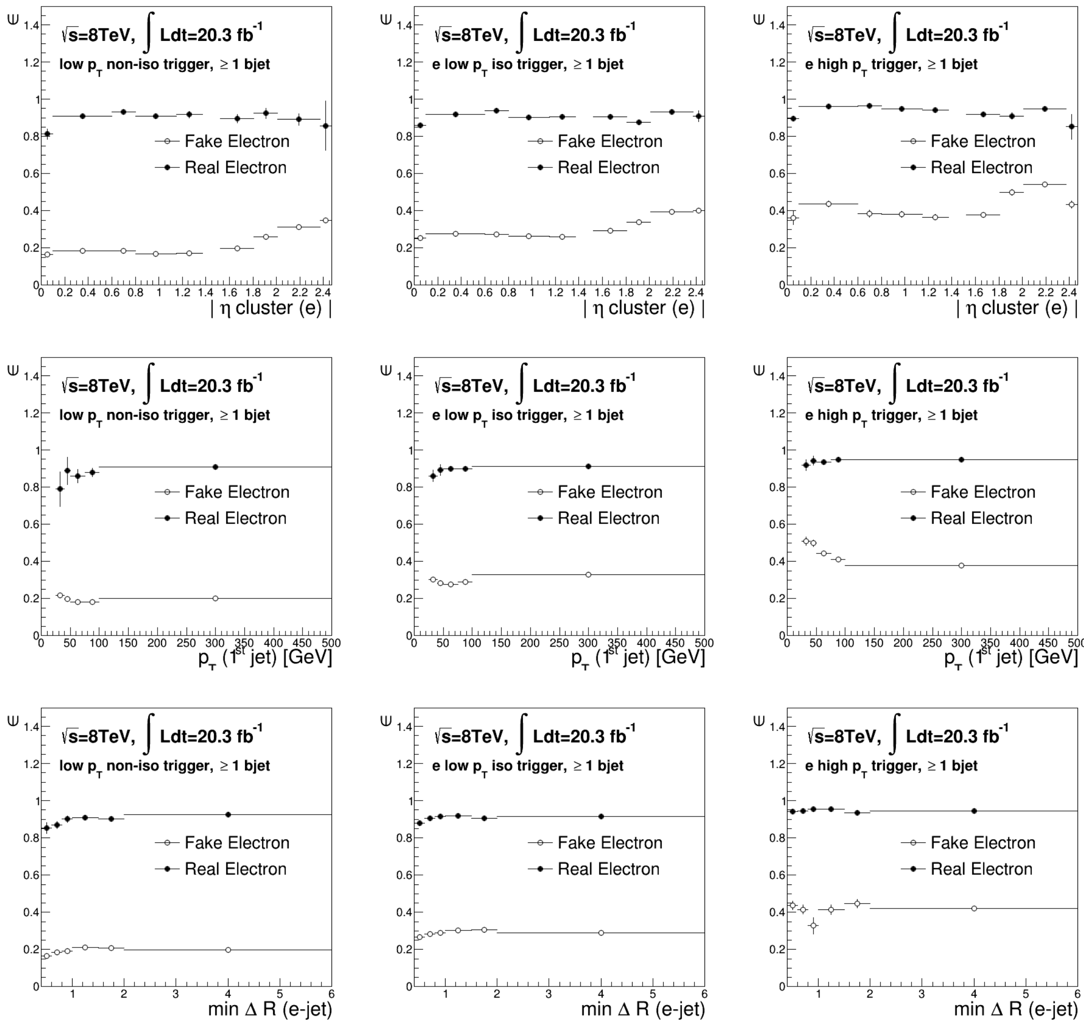

Figure 7.5: Efficiency for loose real and non-prompt/fake electrons to pass the tight selection criteria as a function of the electron η, leading jet p_{T}, and the distance $\Delta R(e, \mathrm{j}et)$ between the electron and the nearest jet. The control sample used to calculate these efficiencies required events to have at least one b-tagged jet. The plots on the left show efficiencies for electrons that match the e24vh trigger, the plots in the middle are for electrons that match e24vhi, and the plots on the right for electrons that match e60.

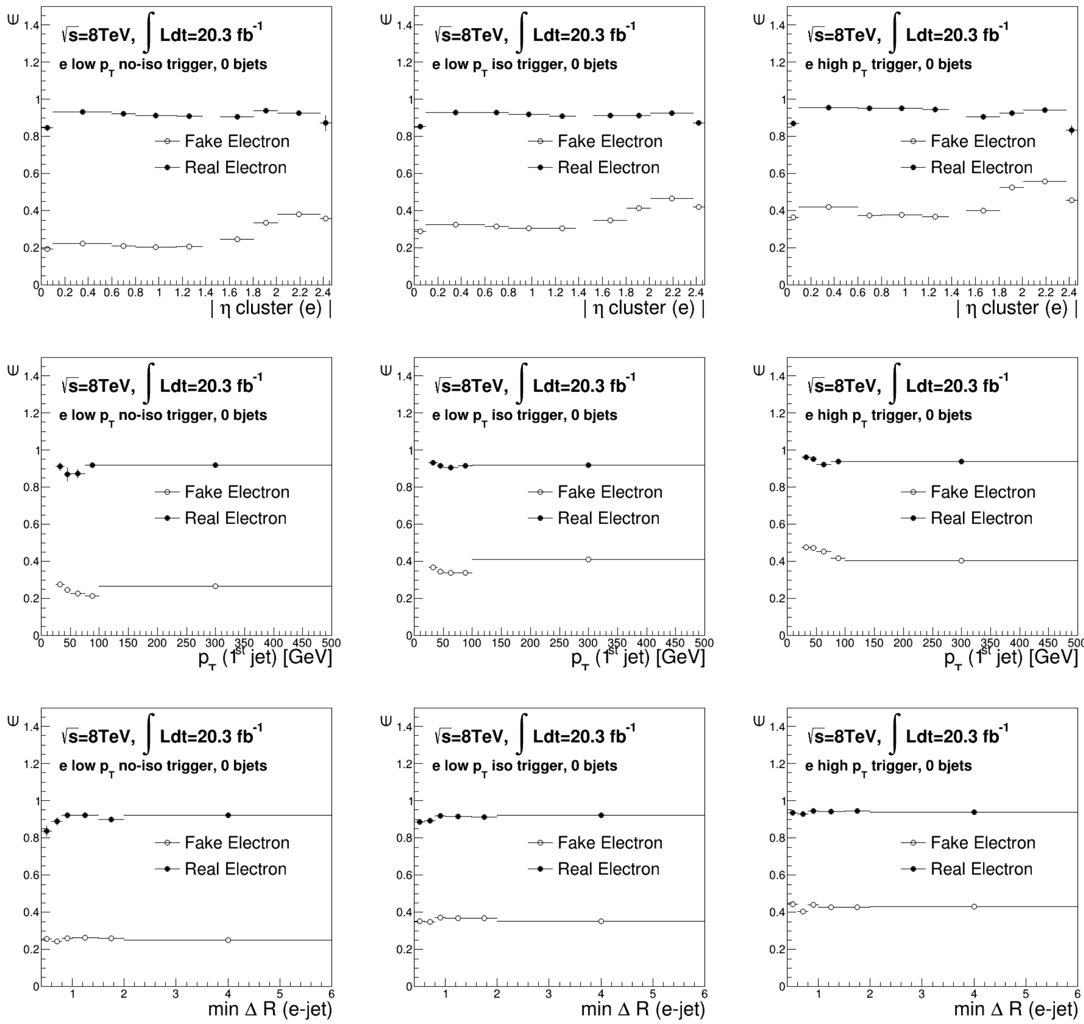

Figure 7.6: Efficiency for loose real and non-prompt/fake electrons to pass the tight selection criteria as a function of the electron η, leading jet p_{T}, and the distance $\Delta R(e, \mathrm{j}et)$ between the electron and the nearest jet. The control sample used to calculate these efficiencies required events to have zero b-tagged jets. The plots on the left show efficiencies for electrons that match the e24vh trigger, the plots in the middle are for electrons that match e24vhi, and the plots on the right for electrons that match e60.

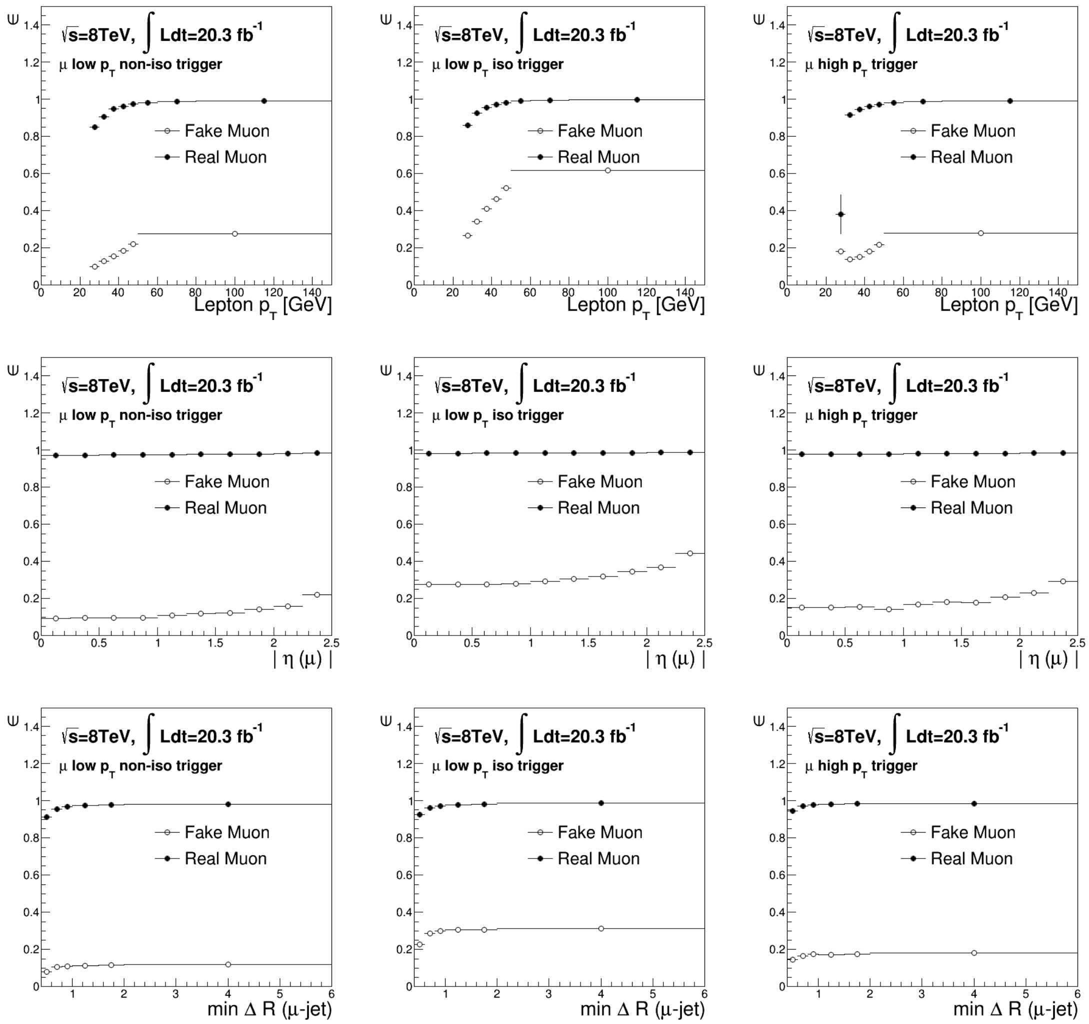

Figure 7.7: Efficiency for loose real and non-prompt/fake muons to pass the tight criteria as a function of muon p_{T}, η, and the distance between the muon and the nearest jet. The plots on the left show efficiencies for muons that match the mu24 trigger, the plots in the middle are for muons that match mu24i, and the plots on the right for muons that match mu36.

A system of equations is derived to estimate the number of events in the signal region containing fake leptons. For the same-sign dilepton channel the equations can be cast into the following 4×4 matrix equation

$$\begin{pmatrix} N^{\mathrm{tt}} \\ N^{\mathrm{t\bar{t}}} \\ N^{\mathrm{\bar{t}t}} \\ N^{\mathrm{\bar{t}\bar{t}}} \end{pmatrix} = \mathbf{M} \begin{pmatrix} N^{\mathrm{ll}}_{\mathrm{rr}} \\ N^{\mathrm{ll}}_{\mathrm{rf}} \\ N^{\mathrm{ll}}_{\mathrm{fr}} \\ N^{\mathrm{ll}}_{\mathrm{ff}} \end{pmatrix} \tag{7.1}$$

where the matrix M is given by

$$\mathbf{M} = \begin{pmatrix} r_1 r_2 & r_1 f_2 & f_1 r_2 & f_1 f_2 \\ r_1 \overline{r_2} & r_1 \overline{f_2} & f_1 \overline{r_2} & f_1 \overline{f_2} \\ \overline{r_1} r_2 & \overline{r_1} f_2 & \overline{f_1} r_2 & \overline{f_1} f_2 \\ \overline{r_1 r_2} & \overline{r_1 f_2} & \overline{f_1 r_2} & \overline{f_1 f_2} \end{pmatrix} \tag{7.2}$$

The values on the left hand side N_{tt}, $N_{t\bar{t}}$, $N_{\bar{t}t}$ and $N_{\bar{t}\bar{t}}$ represent the numbers of events where the leading and sub-leading leptons (ordered by p_{T}) are either tight (t) or not tight ($\bar{t}$). This is indicated by the subscripts where the first subscript corresponds to the leading lepton and the second corresponds to the sub-leading lepton. The values on the right hand side N^{II}_{rr}, N^{II}_{rf} , N^{II}_{fr} , N^{II}_{ff} represent the numbers of events in the loose signal region where the leading and sub-leading leptons are either real or fake following the same subscript scheme. The loose signal region is equivalent to the signal region except that it contains two loose leptons which may or may not be tight instead of two tight leptons. The elements of M are written in terms of the real and fake efficiencies for the leading and sub-leading leptons denoted by (r_1, f_1) and (r_2, f_2). The notation $\bar{r}$ and $\bar{f}$ is shorthand notation for (1-r) and (1-f) respectively. The values on the left hand side of Eq. 7.1 are measured directly while those on the right hand side must be solved for by inverting the matrix M. From these values we can obtain the corresponding values for the signal region (N^{tt}) by applying the appropriate product of efficiencies. Then the fakes estimate for the signal region (N^{tt}_{fake}) is the sum of all events containing at least one fake lepton given by

$$
\begin{aligned}
N^{\mathrm{tt}}_{\mathrm{fake}} &= N^{tt}_{\mathrm{rf}} + N^{\mathrm{tt}}_{\mathrm{fr}} + N^{\mathrm{tt}}_{\mathrm{ff}} \\
&= r_1 f_2 N^{\mathrm{ll}}_{\mathrm{rf}} + f_1 r_2 N^{\mathrm{ll}}_{\mathrm{fr}} + f_1 f_2 N^{\mathrm{ll}}_{\mathrm{ff}} \\
&= \alpha r_1 f_2 \left[-\bar{f_1}\bar{r_2} N^{\mathrm{tt}} + \bar{f_1} r_2 N^{\mathrm{t\bar{t}}} + f_1 \bar{r_2} N^{\mathrm{\bar{t}t}} - f_1 r_2 N^{\mathrm{\bar{t}\bar{t}}} \right] \\
&\quad +\alpha f_1 r_2 \left[-\bar{r_1}\bar{f_2} N^{\mathrm{tt}} + \bar{r_1} f_2 N^{\mathrm{t\bar{t}}} + r_1 \bar{f_2} N^{\mathrm{\bar{t}t}} - r_1 f_2 N^{\mathrm{\bar{t}\bar{t}}} \right] \\
&\quad +\alpha f_1 f_2 \left[\bar{r_1}\bar{r_2} N^{\mathrm{tt}} - \bar{r_1} r_2 N^{\mathrm{t\bar{t}}} - r_1 \bar{r_2} N^{\mathrm{\bar{t}t}} + r_1 r_2 N^{\mathrm{\bar{t}\bar{t}}} \right]
\end{aligned}
\tag{7.3}
$$

where

$$\alpha = \frac{1}{(r_1 - f_1)(r_2 - f_2)}.$$

Since the efficiencies in this expression depend on the kinematics of the lepton and of the event, Eq. 7.3 is recast as a weight to be applied to each event in the loose signal region. This is done by replacing the values N_{tt}, $\mathrm{N}_{t\bar{t}}$ ... by Boolean values that indicate whether the leptons in each event are tight or not. The weighted sum of all events in the loose signal region then yields the fakes estimate for the signal region.

Since the same-sign dilepton channel allows for the presence of additional loose leptons beyond the two tight same-sign leptons, we must estimate the contribution of these events to the fakes yield. Because these events contain more than two leptons we must decide which two to use in the 4×4 matrix method described above. To do this we subdivide the signal region into four sub-regions according to the p_{T} ordering of the leading three leptons in the event. The sub-regions are TT, TTL, TLT and LTT. TT contains events with two tight same-sign leptons only and the other three contain events with two tight same-sign leptons and one or more additional non-tight leptons with the leading non-tight lepton being either first second or third in p_{T} ordering. We then apply the 4×4 matrix method to the leading two leptons in each sub-region and sum the number of fakes from each to get the full fakes estimate.

The fakes for the trilepton channel are also calculated using the matrix method where M is now an 8×8 matrix given by

$$\begin{pmatrix} N^{\mathrm{ttt}} \\ N^{\mathrm{tt\bar{t}}} \\ N^{\mathrm{t\bar{t}t}} \\ N^{\mathrm{t\bar{t}\bar{t}}} \\ N^{\mathrm{\bar{t}tt}} \\ N^{\mathrm{\bar{t}t\bar{t}}} \\ N^{\mathrm{\bar{t}\bar{t}t}} \\ N^{\mathrm{\bar{t}\bar{t}\bar{t}}} \end{pmatrix} = \begin{pmatrix} r_1r_2r_3 & r_1r_2f_3 & r_1f_2r_3 & r_1f_2f_3 & f_1r_2r_3 & f_1r_2f_3 & f_1f_2r_3 & f_1f_2f_3 \\ r_1r_2\overline{r_3} & r_1r_2\overline{f_3} & r_1f_2\overline{r_3} & r_1f_2\overline{f_3} & f_1r_2\overline{r_3} & f_1r_2\overline{f_3} & f_1f_2\overline{r_3} & f_1f_2\overline{f_3} \\ r_1\overline{r_2}r_3 & r_1\overline{r_2}f_3 & r_1\overline{f_2}r_3 & r_1\overline{f_2}f_3 & f_1\overline{r_2}r_3 & f_1\overline{r_2}f_3 & f_1\overline{f_2}r_3 & f_1\overline{f_2}f_3 \\ r_1\overline{r_2}\,\overline{r_3} & r_1\overline{r_2}\,\overline{f_3} & r_1\overline{f_2}\,\overline{r_3} & r_1\overline{f_2}\,\overline{f_3} & f_1\overline{r_2}\,\overline{r_3} & f_1\overline{r_2}\,\overline{f_3} & f_1\overline{f_2}\,\overline{r_3} & f_1\overline{f_2}\,\overline{f_3} \\ \overline{r_1}r_2r_3 & \overline{r_1}r_2f_3 & \overline{r_1}f_2r_3 & \overline{r_1}f_2f_3 & \overline{f_1}r_2r_3 & \overline{f_1}r_2f_3 & \overline{f_1}f_2r_3 & \overline{f_1}f_2f_3 \\ \overline{r_1}r_2\overline{r_3} & \overline{r_1}r_2\overline{f_3} & \overline{r_1}f_2\overline{r_3} & \overline{r_1}f_2\overline{f_3} & \overline{f_1}r_2\overline{r_3} & \overline{f_1}r_2\overline{f_3} & \overline{f_1}f_2\overline{r_3} & \overline{f_1}f_2\overline{f_3} \\ \overline{r_1}\,\overline{r_2}r_3 & \overline{r_1}\,\overline{r_2}f_3 & \overline{r_1}\,\overline{f_2}r_3 & \overline{r_1}\,\overline{f_2}f_3 & \overline{f_1}\,\overline{r_2}r_3 & \overline{f_1}\,\overline{r_2}f_3 & \overline{f_1}\,\overline{f_2}r_3 & \overline{f_1}\,\overline{f_2}f_3 \\ \overline{r_1}\,\overline{r_2}\,\overline{r_3} & \overline{r_1}\,\overline{r_2}\,\overline{f_3} & \overline{r_1}\,\overline{f_2}\,\overline{r_3} & \overline{r_1}\,\overline{f_2}\,\overline{f_3} & \overline{f_1}\,\overline{r_2}\,\overline{r_3} & \overline{f_1}\,\overline{r_2}\,\overline{f_3} & \overline{f_1}\,\overline{f_2}\,\overline{r_3} & \overline{f_1}\,\overline{f_2}\,\overline{f_3} \end{pmatrix} \begin{pmatrix} N^{\mathrm{lll}}_{\mathrm{rrr}} \\ N^{\mathrm{lll}}_{\mathrm{rrf}} \\ N^{\mathrm{lll}}_{\mathrm{rfr}} \\ N^{\mathrm{lll}}_{\mathrm{rff}} \\ N^{\mathrm{lll}}_{\mathrm{frr}} \\ N^{\mathrm{lll}}_{\mathrm{frf}} \\ N^{\mathrm{lll}}_{\mathrm{ffr}} \\ N^{\mathrm{lll}}_{\mathrm{fff}} \end{pmatrix} \tag{7.4}$$

and the expression for the fakes estimate is a straightforward generalization of Eq. 7.3

$$\begin{aligned} N^{\mathrm{ttt}}_{\mathrm{fake}} &= N^{\mathrm{ttt}}_{\mathrm{rrf}} + N^{\mathrm{ttt}}_{\mathrm{rfr}} + N^{\mathrm{ttt}}_{\mathrm{rff}} + N^{\mathrm{ttt}}_{\mathrm{frr}} + N^{\mathrm{ttt}}_{\mathrm{frf}} + N^{\mathrm{ttt}}_{\mathrm{ffr}} + N^{\mathrm{ttt}}_{\mathrm{fff}} \\ &= r_1r_2f_3N^{\mathrm{lll}}_{\mathrm{rrf}} + r_1f_2r_3N^{\mathrm{lll}}_{\mathrm{rfr}} + r_1f_2f_3N^{\mathrm{lll}}_{\mathrm{rff}} + f_1r_2r_3N^{\mathrm{lll}}_{\mathrm{frr}} \\ &\quad + f_1r_2f_3N^{\mathrm{lll}}_{\mathrm{frf}} + f_1f_2r_3N^{\mathrm{lll}}_{\mathrm{ffr}} + f_1f_2f_3N^{\mathrm{lll}}_{\mathrm{fff}} \end{aligned} \tag{7.5}$$

An added complication to the fakes estimation in this analysis arises due to the strong dependence of the real and fakes efficiencies on the trigger matched to the lepton. Figures 7.5-7.7 clearly show that leptons matched to the low p_{T} triggers used in the analysis have efficiencies that are biased toward higher values due to the isolation requirement included in the trigger. Since only one lepton is required to satisfy a trigger for the event to enter the loose signal region, the event may also contain low p_{T} leptons that are not isolated. Thus it is inappropriate to use these efficiencies.

To handle this issue efficiencies are also measured for low p_{T} non-isolated, prescaled triggers. The decision of which efficiency to apply to each lepton in each event is made according to the following procedure. If any lepton in the event matches the high p_{T} trigger, then the event selection is not biased by the isolation requirement and unbiased trigger efficiencies are applied to each lepton in the event. If no lepton in the event matches the high p_{T} trigger, the low p_{T} biased trigger efficiency is applied to the leading p_{T} lepton that matches that trigger and unbiased efficiencies are applied to the remaining leptons in the event. This procedure is outlined in detail in Table 7.2

Event trigger	p_{T} rank among trigger-matched leptons	Lepton p_{T} range	Efficiency applied
≥ 1 lepton matches high-p_{T} trigger	Any	high	high-p_{T}
≥ 1 lepton matches high-p_{T} trigger	Any	low	low-p_{T} unbiased
No lepton matches high-p_{T} trigger	Leading	Any	low-p_{T} biased
No lepton matches high-p_{T} trigger	Subleading	high	high-p_{T} unbiased
No lepton matches high-p_{T} trigger	Subleading	low	low-p_{T} unbiased

Table 7.2: Selection probabilities r and f applied to each lepton, depending on the characteristics of the lepton and the event trigger. High- and low-p_{T} are defined here by the boundary between the p_{T} thresholds of the triggers that require isolation and those that do not. For electrons, low-p_{T} means the range $24 < p_{\mathrm{T}} < 61$ GeV while for muons the range is $24 < p_{\mathrm{T}} < 37$ GeV [110]

A number of cross checks were carried out to test the matrix method and to verify that the efficiencies shown in Fig. 7.5- Fig. 7.7 can be applied to the estimation of the fake/non-prompt lepton background in the signal region for this analysis. A closure test was carried out to show that the efficiencies can be used to accurately calculate the fake/non-prompt lepton background in the single lepton control regions where the fake efficiencies are measured. In addition to this, a test was carried out where the matrix method was applied to $t\bar{t}$ MC events with the same event selection applied as for the signal region in the analysis. The fake/non-prompt lepton estimate calculated with the matrix method is then compared to the fake estimate determined from the MC truth information. The results of these tests are described in the following two sections.

7.2.1.1 Fakes Estimation in Single Lepton Fake Enriched Control Regions

In an effort to validate the matrix method used for estimating the fake/non-prompt lepton background a test was performed in which estimates were calculated for the single lepton control regions used to measure the fake efficiencies (f) for the analysis. Strictly speaking this isn't a true closure test as the estimates also use the real efficiencies (r) which are measured using different samples. For electrons f is measured using a single-electron control sample that requires $m_T(W) < 20$ GeV and

$E_{\mathrm{T}}^{\mathrm{miss}} + m_T(W) < 60$ GeV while for muons it is measured using a single muon control sample where the impact parameter of the muon with respect to the primary vertex has a significance of > 5. For electrons the efficiencies are extracted separately for events with 0 b-tagged jets and with one or more b-tagged jets. These regions are dominated by multijet events.

The real and fake efficiencies used to produce fakes estimates for the multi-lepton regions in our analysis, using the 4x4 marix method described in section 4.2.1, are here used to estimate the fakes contribution to these single lepton control regions using the 2x2 matrix method. The 2x2 matrix method follows the same logic as the 4x4 and 8x8 matrix methods described in section 4.2.1 except that the equations are much simplified due to the fact that each event contains only a single lepton. The full method is described in detail in [136]. The expression which gives the fake yield, corresponding to Eq. 7.3 and 7.6 in Section 7.2.1 is

$$N_{\mathrm{fake}}^{\mathrm{t}} = \frac{f}{r - f} \cdot (r \cdot N^l - N^t). \tag{7.6}$$

Since the efficiencies in Eq. 7.6 depend upon the kinematics of each event the above expression can be rewritten as a weight to be applied to the loose sample on an event by event basis. The weight for the ith event in the sample is

$$w_i = \frac{f}{r - f} \cdot (r \cdot 1 - isTight(i)), \tag{7.7}$$

where *isTight* is a Boolean that is equal to one for tight events and zero for non-tight events. The same parametrizations of r and f for electrons and muons are used as in the analysis.

Figures 7.8-7.12 show a comparison of events in data to Monte Carlo and the fake/non-prompt lepton background for these single lepton + jets fake enriched samples. The events are shown distributed with respect to lepton p_{T}, leading jet p_{T}, $E_{\mathrm{T}}^{\mathrm{miss}}$, $m_T(W)$, and the ΔR between the lepton and the closest jet. Comparison plots are shown for the pretag sample and the sample containing at least one b-tag for electrons and muons.

The distribution of electron p_{T} shows a large discrepancy in the lowest bin as well as a large positive slope in the ratio plot in the low p_{T} range. This becomes more prominent when we consider the b-tagged sample. There is also a clear slope in the distribution of $E_{\mathrm{T}}^{\mathrm{miss}}$, for electrons. For muons the distributions show good agreement for the pretag sample but a clear excess of fakes on the order of $\sim 20\%$ in the b-tagged sample. There is also a slope in the distribution of leading jet p_{T}. All of these features have been observed in the analyses done by the TopFakes subgroup detailed in [136]. The poor shape agreement in electron p_{T} is explained by the fact that electron p_{T} is not used in the parametrization of r and f for electrons. Leading jet p_{T} is used instead. This parametrization was chosen because both r and f were seen to depend on a number of variables that measure the level of hadronic activity in the event such as jet multiplicity, $E_{\mathrm{T}}^{\mathrm{miss}}$ and leading jet p_{T}. The more hadronic activity the lower the fake efficiency due to the isolation cut. Since lepton p_{T} is also correlated to leading jet p_{T} using leading jet p_{T} in the parametrization was an effort to capture the dependence on hadronic activity and on lepton p_{T} with a single variable. In most control regions, in particular the multilepton control regions in this analysis, this parametrization accurately describes the fakes background. The excess of fakes in the muon b-tagged region is explained by the fact that the muon efficiencies used in this analysis are not split by b-tag multiplicity as the electron efficiencies are. This was the initial recommendation of the TopFakes group because originally there did not appear to be a large difference between the fakes estimates calculated with pretag efficiencies and efficiencies split by b-tag multiplicity. Later on, after reproducing background samples and applying updated b-tagging scale factors, the difference was seen to be larger. Figure 7.12 shows the same comparison as in Figure 7.11 except that here the fake/non-prompt lepton background is calculated using efficiencies measured with events in the same fake enriched region as defined above for muons with the added requirement that the events contain at least one b-tagged jet. With these efficiencies the $\sim 20\%$ excess seen in Figure 7.11 is gone. This can be seen in Fig. 7.12. As a consequence of the improved agreement in this fake enriched region b-tag splitting for muons has been adopted by the TopFakes group but this was after our analysis was frozen due to unblinding. Regardless, the $\sim 20\%$ excess in fakes seen here is well within the 70% systematic uncertainty used in this analysis. The estimation of this systematic is described in Section 8.3.1.

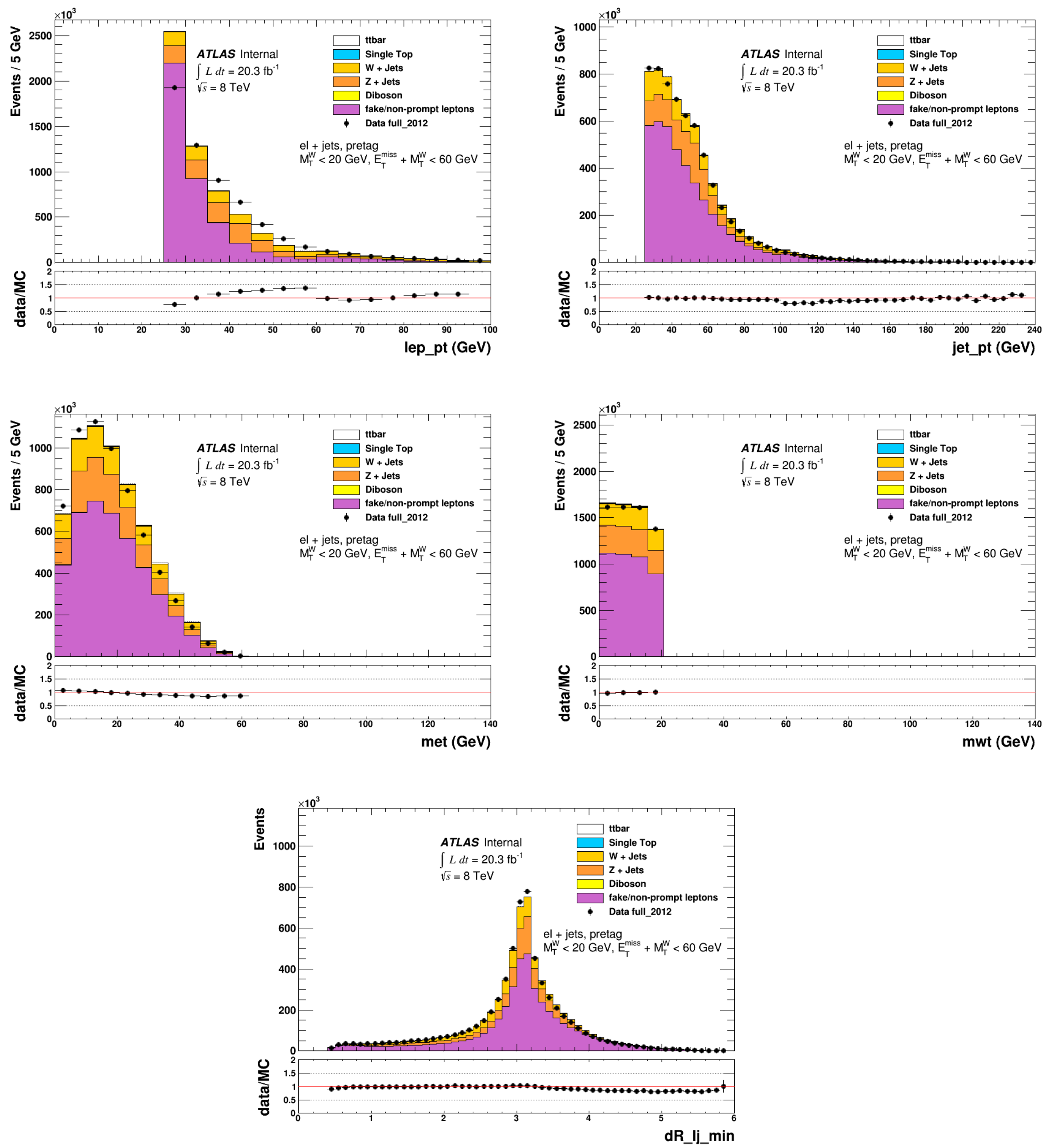

Figure 7.8: Distributions of some kinematic variables in the single lepton fake enriched control regions. The plots above compare data with background, including fakes, for the pretag selection in the e+jets channel

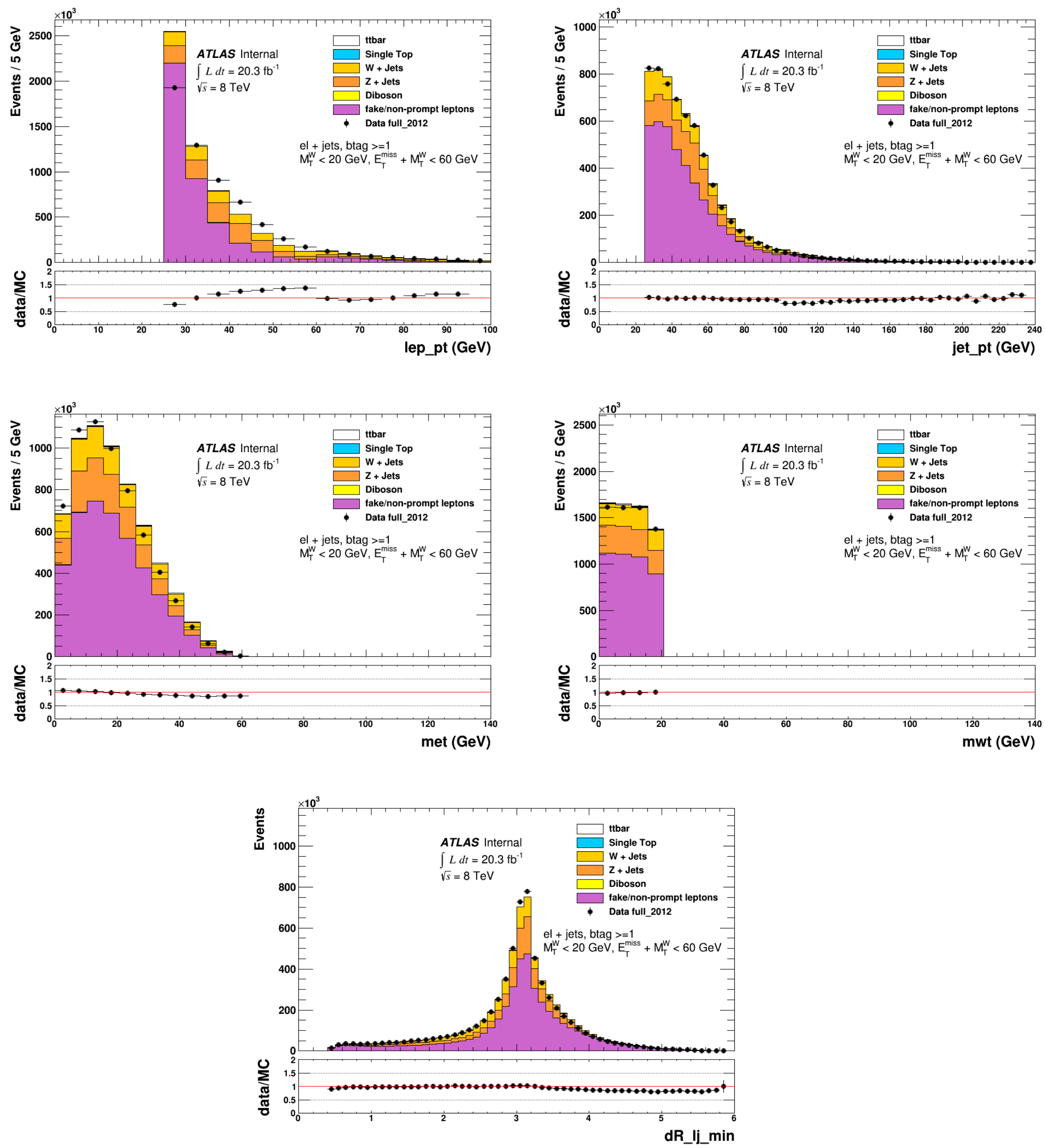

Figure 7.9: Distributions of some kinematic variables in the single lepton fake enriched control regions. The plots above compare data with background, including fakes, for the b-tagged selection in the e+jets channel

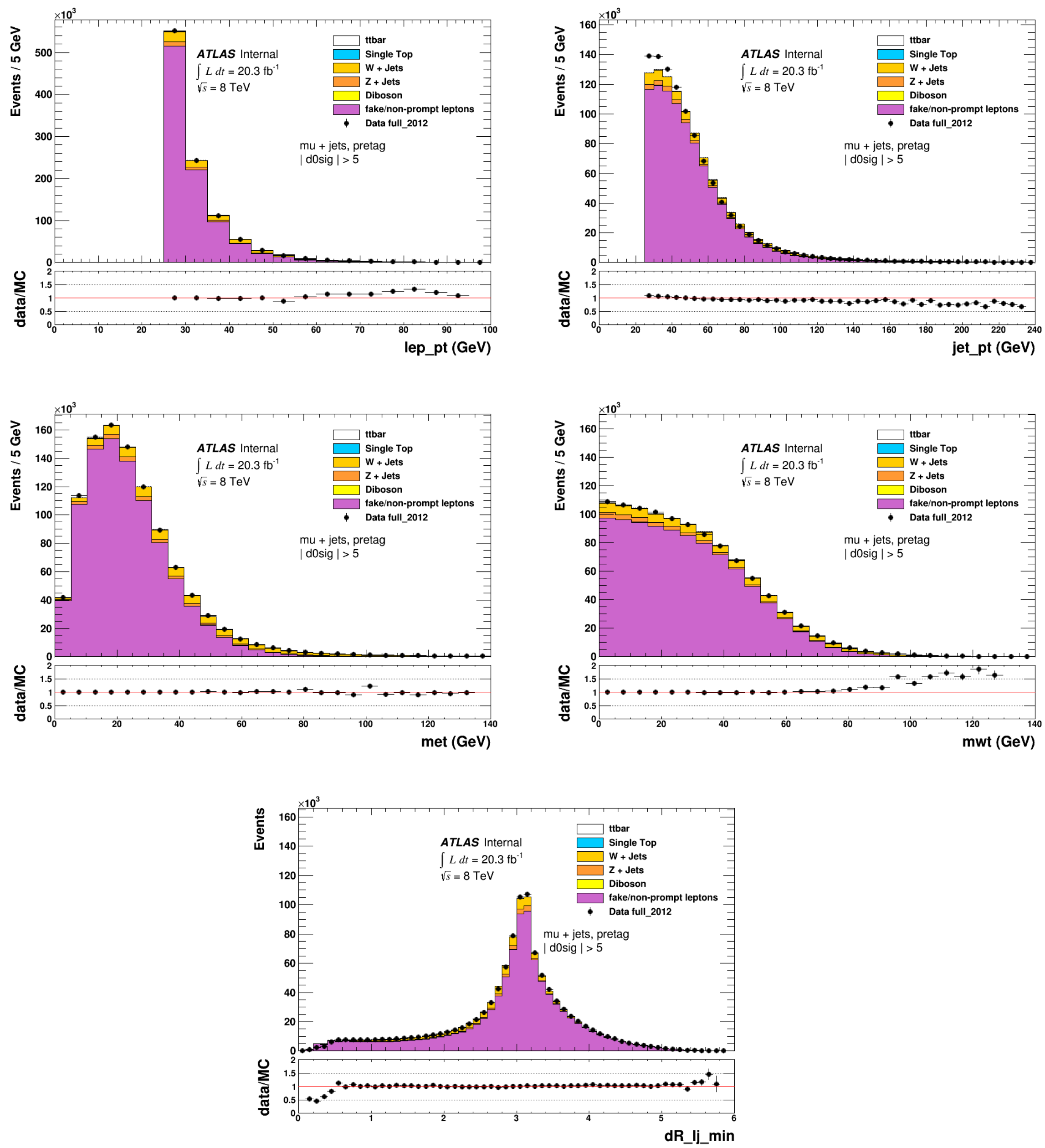

Figure 7.10: Distributions of some kinematic variables in the single lepton fake enriched control regions. The plots above compare data with background, including fakes, for the pretag selection in the μ+jets channel

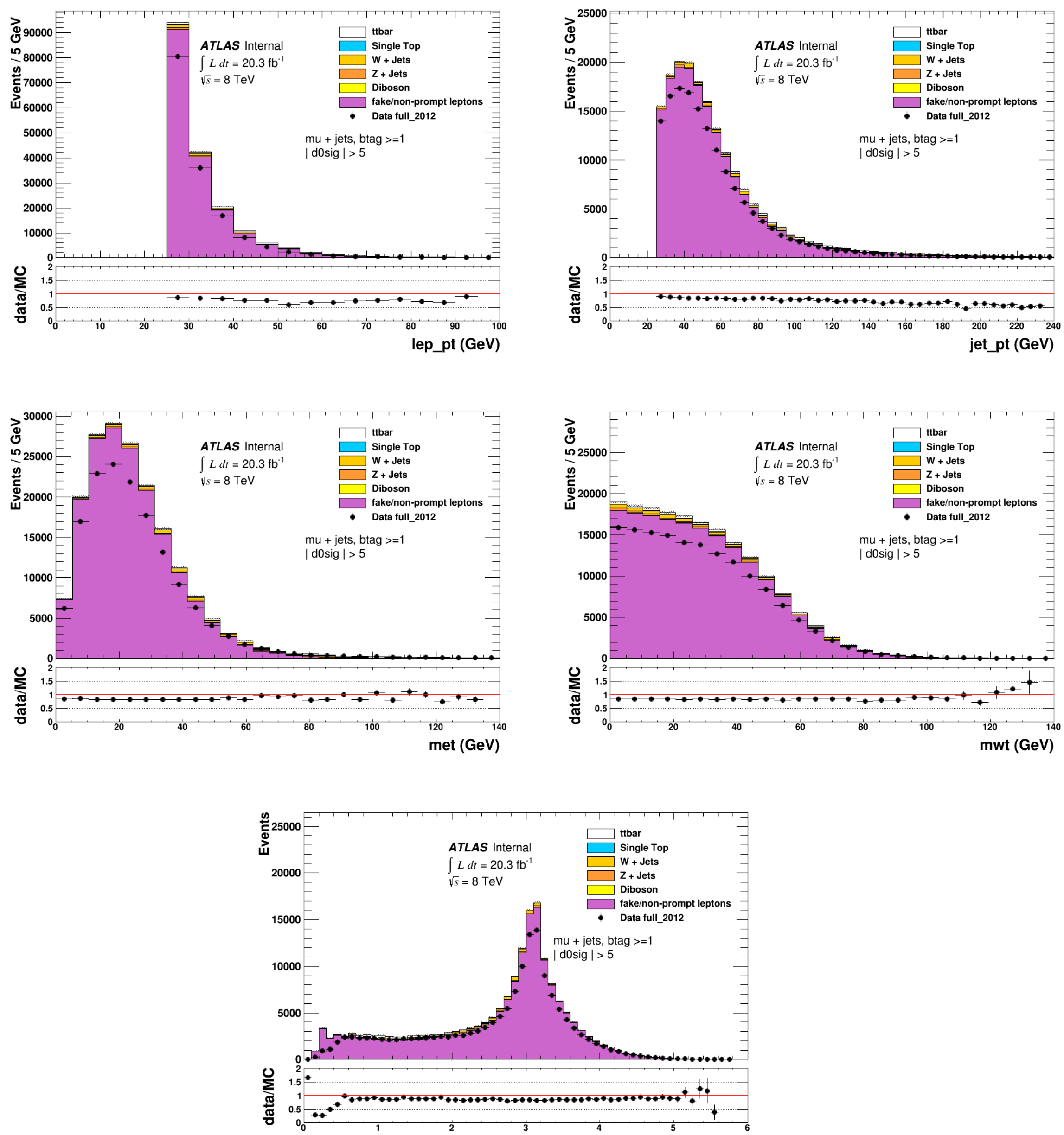

Figure 7.11: Distributions of some kinematic variables in the single lepton fake enriched control regions. The plots above compare data with background, including fakes, for the b-tagged selection in the μ+jets channel

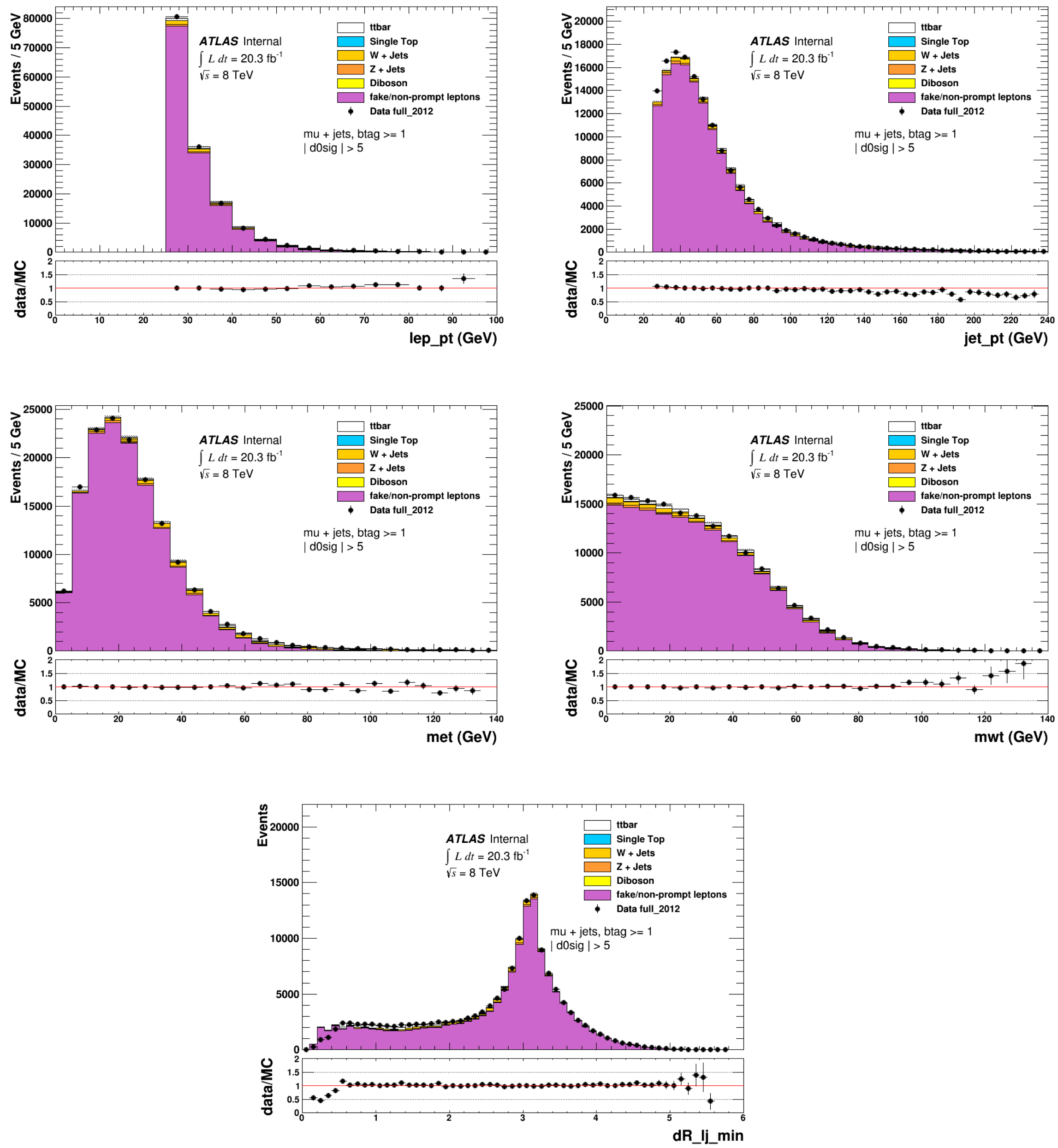

Figure 7.12: Distributions of some kinematic variables in the single lepton fake enriched control regions. The plots above compare data with background, including fakes, for the b-tagged selection in the μ+jets channel using efficiencies measured with events containing at least one b-tag

7.2.1.2 Validation of Matrix Method for Fakes Estimation in Signal Region Using a Monte Carlo $t\bar{t}$ Sample

In addition to validating the matrix method in both single lepton and combined trilepton and same sign dilepton control regions in data, a study was carried out to validate the method in our signal regions using a Monte Carlo $t\bar{t}$ sample. In particular the aim was to show that efficiencies measured in our control regions are applicable in our signal regions. In the study estimates of the fake/non-prompt lepton background calculated using the matrix method were compared to the truth fake yields for each of the eight signal regions defined in Table 6.3. The truth fake yields were determined by requiring that events contain at least one lepton that is not matched to a true lepton as determined by the MCTruthClassifier which takes leptons from W/Z and tau decay to be true (including trident electrons). The matrix method fake estimates were calculated by applying the same loose and tight lepton definitions as in the analysis to the MC dilepton $t\bar{t}$ sample and using efficiencies measured in single lepton and multijet MC samples rather than in real and fake enriched control regions in data. Although the analysis considers both trilepton and same sign dilepton events, only dilepton events were considered in this comparison. This is sufficient to validate our procedure as these events dominate our signal regions. In addition to same sign dilepton events which are contained in our signal regions we also perform the comparison for opposite sign dilepton pairs in order to cross check an alternate region with better statistics. The real efficiencies were calculated as the fraction of events in a combination of single lepton MC samples, made up of $t\bar{t}$, Z+jets, W+jets, diboson and single top, using the loose lepton definition which also satisfy the tight lepton definition. The fake efficiencies were calculated as the same fraction but in a multijet MC sample which includes heavy flavor multijet events. The same technique for deciding which efficiencies to apply to each lepton as used in the analysis, summarized in Table 7.2, was used here. Both the truth and the matrix method fake yields are normalized to an integrated luminosity of 20.3 fb^{-1}, however no additional event weights are applied since we are not comparing MC to data.

The plots in Figure 7.13 show the comparison between the truth yields and the matrix method estimates for the fake/non-prompt lepton background for both same sign and opposite sign dilepton events. The first row shows the comparison for each of the eight SR categories defined for the VLQ signals (SRVLQ0 - SRVLQ7). The second row shows the comparison for the three low H_T regions (SRVLQ0 - SRVLQ2) and the five high H_T regions (SRVLQ3 - SRVLQ7) combined. All plots show the combined yields for all three categories of dilepton events (ee, $\mu\mu$, eμ). We see that the matrix method overestimates the fake/non-prompt lepton background in the low H_T regions with the largest discrepancy in the single b-tag region (SRVLQ0). Although the significance of the excess is large in this region it is considered acceptable as it is less than the 70% systematic uncertainty applied to the matrix method fakes estimation. In the other regions the matrix method estimate is consistent with the truth yield within uncertainty. The slight discrepancies that we see, for example in SRVLQ6, are consistent with fluctuations in the $t\bar{t}$ dilepton sample due to low statistics. In fact in this region we see a deficit of the matrix method estimate for same sign events and an excess for opposite sign events. The plots in Figures 7.14 and 7.15 show how the matrix method and truth fakes are distributed with respect to H_T, E_T^{miss} and N_{b-jets}. The distributions in Figure 7.14 are for same sign events in the low H_T regions on the left and high H_T regions on the right. Figure 7.15 shows the same distributions for opposite sign events. As in Figure 7.13 all categories of dilepton events (ee, $\mu\mu$, eμ) are included. The excess of matrix method fakes in the low H_T control regions is not concentrated in any particular range of these distributions. No shape disagreement is seen although the error in the high H_T regions, and in particular the high H_T same sign region, is very large due to low statistics. In all of the plots only the statistical error is shown.

7.2.2 Electron Charge Misidentification

The background from charge misidentification (misid) consists of opposite-sign lepton pairs, primarily from $t\bar{t}$ and Z+jets events, where the charge of one of the leptons

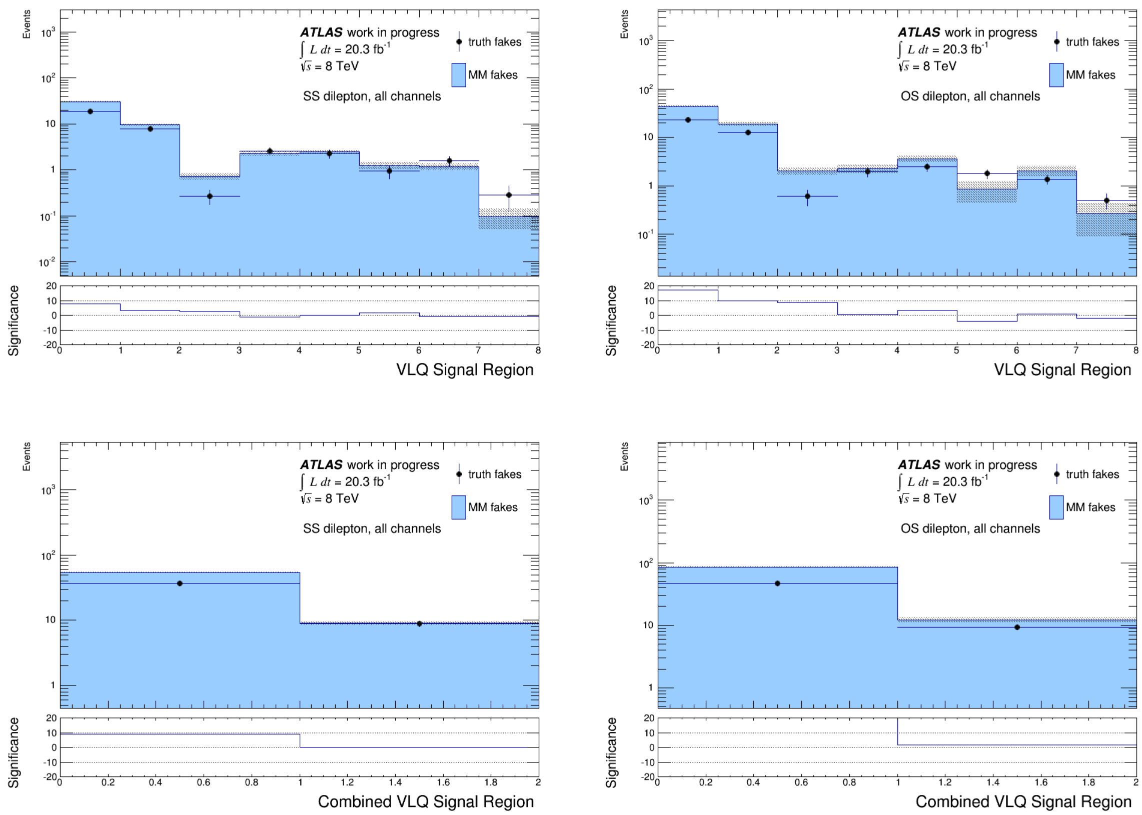

Figure 7.13: Comparison of truth fake yield and matrix method fake estimate for the signal regions defined for heavy quark and four top signals. The comparison is shown for same sign and opposite sign lepton pairs in the left and right columns respectively. The first row shows the comparison for the eight signal regions separately while the second row shows a combined low H_T region that combines signal regions SRVLQ0 - SRVLQ2 and a single high H_T control region that combines SRVLQ3 - SRVLQ7. The error bars shown include statistical uncertainty only

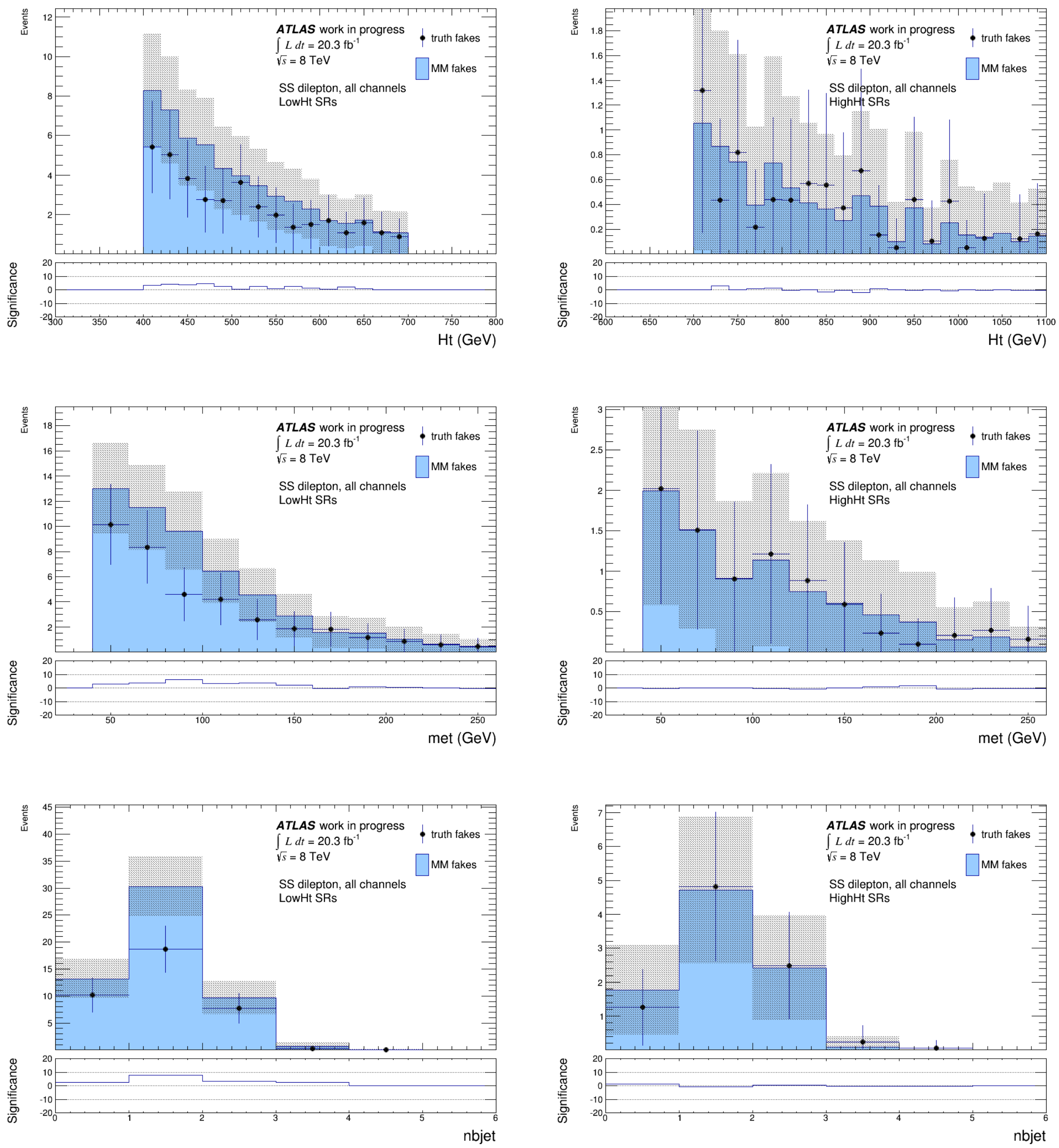

Figure 7.14: Distributions of H_T, E_T^{miss} and b-jet multiplicity for same sign dilepton events in low H_T signal regions SRVLQ0 - SRVLQ2 (left) and high H_T signal regions SRVLQ3 - SRVLQ7 (right). The error bars shown include statistical uncertainty only

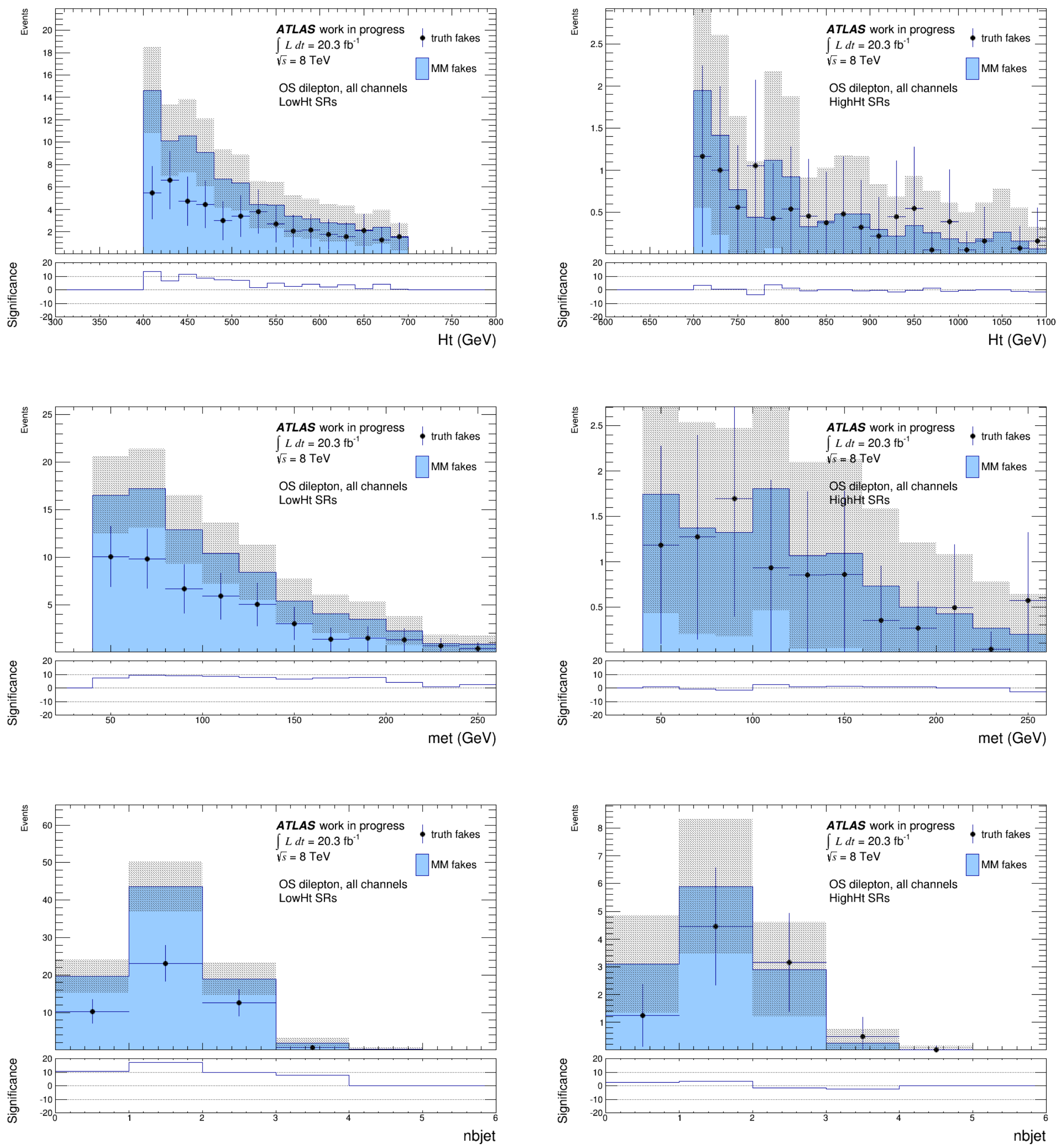

Figure 7.15: Distributions of H_T, E_T^{miss} and b-jet multiplicity for opposite sign dilepton events in low H_T signal regions SRVLQ0 - SRVLQ2 (left) and high H_T signal regions SRVLQ3 - SRVLQ7 (right). The error bars shown include statistical uncertainty only

in the pair is mis-measured causing the event to satisfy the selection criteria for a same-sign dilepton pair. A full description of the method used to estimate this background is given in Ref. [137]. The charge misid background only contributes to the same-sign dilepton channel and not the trilepton channel since no requirement is made on lepton charge for trilepton events. Furthermore it only contributes to ee and eμ events, since the probability of mis-measuring the charge of a muon is negligible. The dominant sources of charge misidentified electrons are high p_{T} electrons where the radius of curvature of the track is large leading to large uncertainty in the charge measurement, and trident electrons where the prompt electron radiates a photon which subsequently undergoes pair production in the direction of the original electron. Trident electrons lead to three particle tracks close to one another in the inner detector, one of which has the opposite-sign charge to the prompt electron. In this case, if the calorimeter cluster is matched to the wrong track the electron's charge is mis-measured.

The charge misid background is negligible for muons for three reasons. Muons' charge is measured in both the inner detector and muon spectrometer so there are two independent measurements. The lever arm in the muon system is larger than that in the inner detector by a factor of 10 (see Section 3.2) so the charge measurement is more precise. The large mass of the muon compared to the electron suppresses bremsstrahlung radiation so trident muons are rarely produced.

The charge misid background is estimated using data by measuring the probability of an electron charge mis-measurement in $Z \rightarrow ee$ events in data where no requirement is made on the charge of the electrons. The data sample contains both opposite-sign and same-sign dilepton pairs where, the same-sign events come from charge mis-measurement of one of the electrons. It is assumed that the rate at which an electron's charge is mis-measured depends on η and p_{T} of the electron, but is uncorrelated between the two electrons in the event. Given the assumption that the sample consists entirely of opposite-sign dilepton events the number of same-sign events arising from charge mis-measurement with electrons in the (i, k) and (j, l)

η-p_{T} bins can be expressed as

$$N_{ss}^{ik,jl} \approx N^{ik,jl}(\varepsilon_{ik} + \varepsilon_{jl}) \tag{7.8}$$

where $N^{ik,jl}$ is the total number of events with an electron in the (i, k) η-p_{T} bin and another in the (j, l) η-p_{T} bin and ε_{ik} and ε_{jl} are the charge misid rates in those η-p_{T} bins. The value of ϵ for each η and p_{T} bin is determined by minimizing a Poisson likelihood function for the observed number of total events and same-sign events using the above equation. The likelihood function has the form

$$-ln[L(\varepsilon|N_{ss}, N)] = \sum_{ik,jl} ln[(\varepsilon_{ik} + \varepsilon_{jl})N^{ik,jl}]N_{ss}^{ik,jl} - (\varepsilon_{ik} + \varepsilon_{jl})N^{ik,jl}$$

Once the rates are measured, the number of charge misid events in the signal region is determined by selecting events with the same criteria used to define the signal region except with opposite-sign rather than same-sign lepton pairs. Each event is then multiplied by the weight $\varepsilon_{ik} + \varepsilon_{jl}$ where the electrons in the event fall in the (i, k) and (j, l) η and p_{T} bins. In the case of an eμ event one ε is zero. This event then enters the signal region as part of the charge misid background along with a weight characterizing the likelihood that one or the other, but not both of its electrons has its charge mis-measured.

This method suffers from an important limitation. Since electrons from Z boson decay rarely have $p_{\mathrm{T}}>$ 100 GeV the measurement of the charge misid rates for very high p_{T} electrons has large uncertainty due to low statistics in the data. To mitigate this the misid rates are also measured in $t\bar{t}$ MC simulated events. The rates are matched to the rates measured in data for the low p_{T} range covered by the $Z \rightarrow ee$ data and the rates for high p_{T} electrons ($p_{\mathrm{T}} > 100$ GeV) are determined according to

$$\varepsilon(|\eta|, p_{\mathrm{T}}; p_{\mathrm{T}} > 100 \text{ GeV}) = \varepsilon(|\eta|, p_{\mathrm{T}} \in [80, 100] \text{ GeV}) \times \alpha_{t\bar{t}}(|\eta|, p_{\mathrm{T}}; p_{\mathrm{T}} > 100 \text{ GeV})$$

where $\varepsilon(|\eta|, p_{\mathrm{T}} \in [80, 100]$ GeV) is computed with the likelihood procedure described above, and

$$\alpha_{t\bar{t}}(|\eta|, p_{\mathrm{T}}) = \frac{\varepsilon(|\eta|, p_{\mathrm{T}})_{t\bar{t}}}{\varepsilon(|\eta|, p_{\mathrm{T}} \in [80, 100]\ \mathrm{GeV})_{t\bar{t}}}$$

where $\varepsilon(|\eta|, p_{\mathrm{T}})_{t\bar{t}}$ is computed using truth matching on the simulated $t\bar{t}$ MC sample. The correction factors $\alpha_{t\bar{t}}$ and the charge misid rates corrected with these factors are shown parametrized as a function of η and p_{T} in Fig. 7.16a and Fig. 7.16b.

A closure test is carried out in which the rates in Fig. 7.16b were used to predict the number of charge misid events, for the $Z \to ee$ data where they were measured. Figure 7.17 shows a comparison of the same-sign events in the data and the charge misid estimate produced by applying the procedure described above to the opposite-sign events in the $Z \to ee$ data. The events are shown distributed as a function of leading lepton p_{T} without any p_{T} dependence in red and with the p_{T} dependence including the high p_{T} correction in blue. The agreement between data and the charge misid estimate for events with $p_{\mathrm{T}}^{leading} > 100$ GeV is improved significantly after applying the corrections from $t\bar{t}$ MC simulation. The number of data events in this region is 702 and the charge misid estimate is 407 ± 16 before the correction and 671^{+165}_{-159} afterward.

Another important complication that must be accounted for in estimating the charge misid background is the overlap with the fake/non-prompt lepton background. Trident electrons, which are a leading cause of charge misid events, also contribute to the fake/non-prompt lepton background since they are less likely to be isolated than leptons that do not emit hard radiation and thus are captured in the matrix method described in Section 7.2.1. In order to avoid double counting these events the charge misid rates are remeasured from the $Z \to ee$ data after applying the matrix method to it and removing the fakes component. Figure 7.18a shows a plot of the invariant mass of the ee system before and after the removal of fakes and Fig. 7.18b shows the ratio of the misid rates before and after the removal of fakes as a function of η and p_{T}. The final misid rates after both the high p_{T} correction and the fakes overlap removal are shown in Fig. 7.19 and listed in Table 7.3. These are the rates used to produce the charge misid yields for the analysis using Eq. 7.8

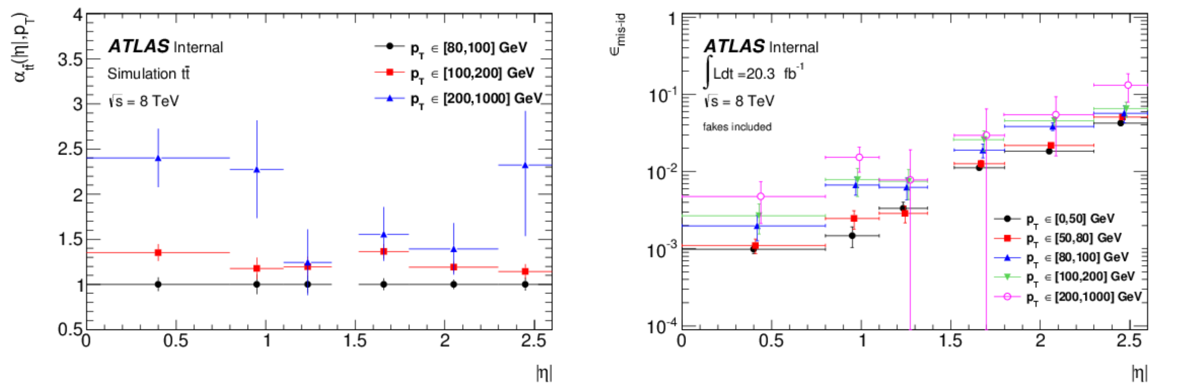

(a) Correction factor for high p_{T} charge misid rates extracted from simulated $t\bar{t}$ events.

(b) Charge misid rates as a function of η and p_{T}, including the high p_{T} correction factor.

Figure 7.16: Charge misid rates [110]

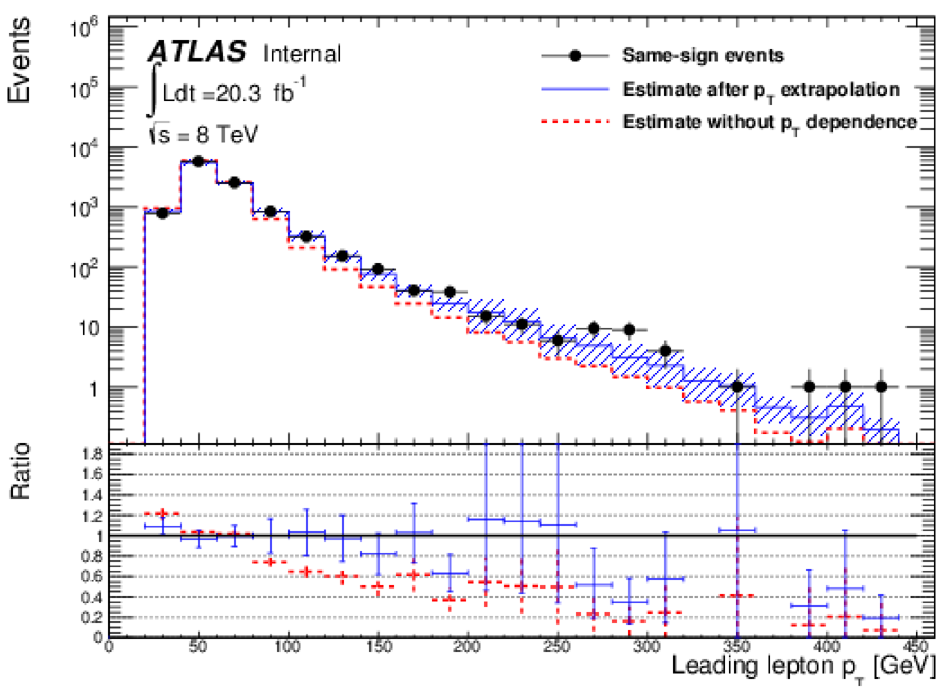

Figure 7.17: Distribution in data of the leading electron p_{T} for Z events. The $e^{\pm}e^{\pm}$ events are displayed as black points. The charge misid estimate using reweighted $e^{+}e^{-}$ events is shown with the dashed line when no p_{T}-dependence is applied (i.e. the charge misid rates are determined without any p_{T} dependence in the likelihood and no p_{T} correction factor is applied) and with the solid line when the p_{T}-dependence is applied. [110]

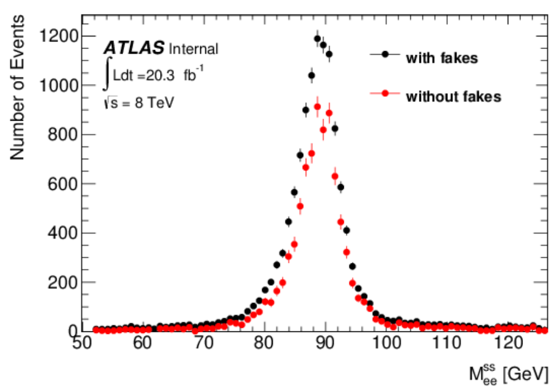

(a) Z peak coming from same-sign events, before and after removing the fakes component.

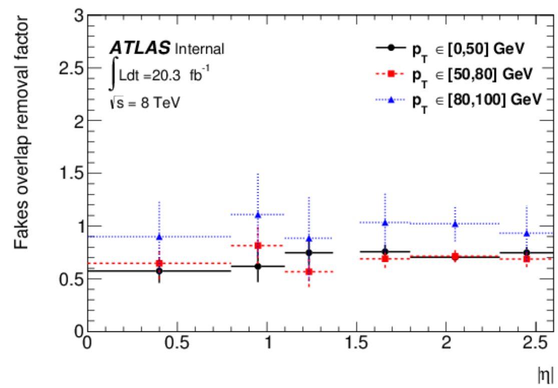

(b) Ratio between the charge misid rates after and before removing the fakes component.

Figure 7.18: Removal of fakes in the charge misid rates. [110]

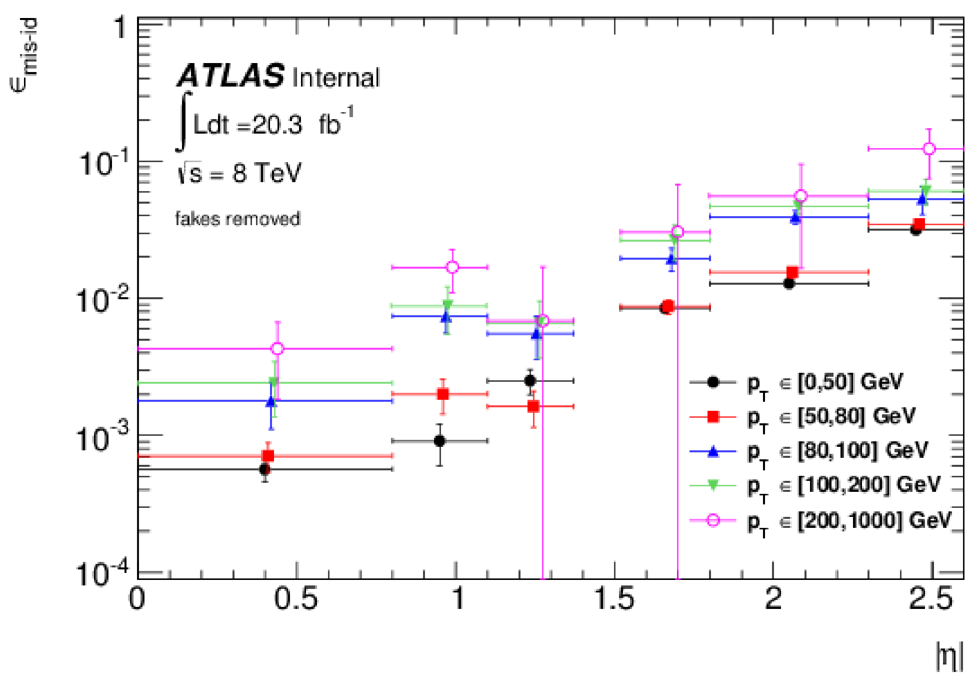

Figure 7.19: Charge misid rates as a function of η and p_{T}, including the high p_{T} correction factor and after removal of the fakes contamination. [110]

Table 7.3: Charge misidentification rates as a function of $|\eta|$ and p_{T}. [110]

	p_{T} range				
$|\eta|$ range	$[0, 50]$ GeV	$[50, 80]$ GeV	$[80, 100]$ GeV	$[100, 200]$ GeV	$[200, 1000]$ GeV
$[0, 0.8]$	0.000565	0.000708	0.00178	0.0024	0.00427
$[0.8, 1.1]$	0.000909	0.002	0.00739	0.00869	0.0168
$[1.1, 1.37]$	0.0025	0.00162	0.00552	0.0066	0.00686
$[1.52, 1.8]$	0.00844	0.0087	0.0195	0.0266	0.0303
$[1.8, 2.3]$	0.0128	0.0155	0.0393	0.0467	0.055
$[2.3, 2.6]$	0.0315	0.0349	0.053	0.0606	0.123

7.3 Background Validation

To validate the MC simulations used to model the irreducible SM backgrounds and the data-driven methods used to estimate the instrumental backgrounds the total background is compared to data in a number of regions orthogonal to the signal region. The validation compares the total yield as well as the distribution of data and background events for a number of important kinematic variables in each region. The variables considered are those that show the strongest discrimination between signal and background. It is crucial that the background is well modeled for these variables as they are used to define the signal region. Although same-sign dilepton and trilepton events are considered together in the signal region due to limited statistics, they are validated separately. Furthermore, within each category the events are separated by lepton flavor. This amounts to a more rigorous test of the background estimation. The regions used for the validation must have negligible contribution from signal and have a background composition as similar as possible to the signal region. To understand the composition of the signal region, an alternate background estimate is produced entirely with MC, replacing the fakes/non-prompt and charge misid backgrounds with the following simulated samples

- $t\bar{t}$ and single top,
- W+jets and Z+jets,
- $W\gamma$ and $Z\gamma$,
- W^+W^-,
- WZ and ZZ decaying to a single lepton or two leptons of opposite charge.

which are the dominant SM processes that contribute to these instrumental backgrounds. This estimate is referred to as the *full MC background estimate* while the estimate including the MC samples listed in Table 4.2 and the data-driven background estimates described in Section 7.2 is referred to as the *standard background estimate*. The full MC background estimate is considered only to better understand the composition of the signal region in order to determine the ideal regions for the validation of the standard background estimate. It cannot be used to model the background in the signal region directly since instrumental effects are not expected to be very accurately simulated, particularly in extreme kinematic regions such as the signal region.

The first step is to validate the full MC background estimate by comparing it to data in a number of regions orthogonal to the signal region but potentially different from the regions that are ultimately defined for validating the standard background estimate. Once there is confidence in the full MC background estimate it is used to model the background in a region that is very close to the signal region. This region is not identical to the signal region used in the analysis but has a large overlap with it. It was used instead of the true signal region since this step of the validation was done while the signal region was still being optimized. The exact definition of the signal region and the way it is broken into categories was not settled yet at this point in the analysis so a more generic region that is very close to the final signal region was used. Later after the signal region was defined the full MC background estimate was also used to model the true signal region and the results are in good agreement with the standard background estimate. However this more generic early version of the signal region is discussed here since it was used to determine the regions for the validation of the standard background estimate which was then frozen after unblinding since it relies on data-driven techniques which cannot be changed significantly after looking at the data in the signal region. The validation regions are determined on the basis of the full MC background estimate in this generic early version of the signal region. The final step is to compare the standard background estimate to the data in these validation regions.

7.3.1 Validation of the Full MC Background Estimate

Before using the full MC sample to understand the composition of the signal region it must be validated itself to be sure that we have included all the MC samples necessary to account for the instrumental backgrounds. In particular we assume that the contribution from QCD ($pp \rightarrow$ jets) is negligible since it would only enter the signal region if there were two fake/non-prompt leptons which is unlikely. This assumption must be checked. To do this we chose two control regions that contain no signal, referred to as the Low $E_{\mathrm{T}}^{\mathrm{miss}}$ and Low H_{T} regions. They are defined by the preselection in Section 6.1 plus an upper bound on $E_{\mathrm{T}}^{\mathrm{miss}}$ ($E_{\mathrm{T}}^{\mathrm{miss}} < 40$ GeV) and H_{T} ($100 < H_{\mathrm{T}} < 400$ GeV) respectively. Tables 7.4 and 7.5 show the validation of the full MC background estimate against the data for the same-sign dilepton channel in the Low $E_{\mathrm{T}}^{\mathrm{miss}}$ and Low H_{T} regions. Figures 7.20 through 7.22 show distributions of these events with respect to H_{T}, $E_{\mathrm{T}}^{\mathrm{miss}}$, N_{jets} and N_{b-jets}. Tables 7.6-7.7 and Fig. 7.23-7.26 show the same validation for the trilepton channel. The full MC background estimate is in very good agreement with the data for both same-sign dilepton and trilepton events for both control regions considered.

Table 7.4: Yields in the Low $E_{\mathrm{T}}^{\mathrm{miss}}$ control region for the same-sign dilepton channels using the full MC background estimate. [110]

Sample	ee	$e\mu$	$\mu\mu$
$Z + jets$	$1741.53 \pm 59.65 \pm 260.19$	$63.45 \pm 21.34 \pm 7.38$	$9.45 \pm 23.09 \pm 1.70$
$W + jets$	$48.91 \pm 12.40 \pm 5.93$	$79.88 \pm 13.80 \pm 10.75$	$1.45 \pm 10.38 \pm 0.31$
$W/Z + \gamma$	$235.06 \pm 6.68 \pm 56.80$	$96.69 \pm 5.75 \pm 21.51$	$0.32 \pm 0.78 \pm 0.10$
$t, t\bar{t}$ mis-id	$50.31 \pm 4.02 \pm 4.72$	$71.47 \pm 5.01 \pm 6.35$	0.00 ± 0.63
$t, t\bar{t}$ fakes	$22.00 \pm 2.55 \pm 1.82$	$38.72 \pm 3.34 \pm 3.22$	$6.23 \pm 1.39 \pm 0.55$
$t\bar{t} + X$ fakes/mis-id	$0.17 \pm 0.03 \pm 0.02$	$0.33 \pm 0.04 \pm 0.03$	$0.07 \pm 0.02 \pm 0.01$
VV mis-id	$15.72 \pm 1.45 \pm 2.71$	$10.74 \pm 1.09 \pm 2.30$	0.00 ± 0.74
VV fakes	$8.09 \pm 0.94 \pm 1.75$	$22.13 \pm 1.36 \pm 4.55$	$11.31 \pm 1.04 \pm 2.48$
VH fakes/mis-id	0.56 ± 0.17	0.92 ± 0.09	0.42 ± 0.08
VVV fakes/mis-id	0.01 ± 0.00	0.04 ± 0.01	0.02 ± 0.00
$t\bar{t}W(W)$	$1.71 \pm 0.11 \pm 0.34$	$5.16 \pm 0.20 \pm 0.98$	$3.39 \pm 0.17 \pm 0.69$
$t\bar{t}Z$	$0.71 \pm 0.07 \pm 0.13$	$1.86 \pm 0.10 \pm 0.34$	$1.06 \pm 0.08 \pm 0.19$
$t\bar{t}H$	$0.28 \pm 0.04 \pm 0.03$	$0.77 \pm 0.06 \pm 0.07$	$0.49 \pm 0.05 \pm 0.05$
VV	$83.58 \pm 2.07 \pm 18.11$	$181.69 \pm 2.92 \pm 40.42$	$77.60 \pm 1.92 \pm 17.13$
VH	1.18 ± 0.30	3.16 ± 0.46	3.08 ± 0.56
VVV	0.15 ± 0.02	0.51 ± 0.04	0.33 ± 0.03
Total bkg.	$2209.99 \pm 61.54 \pm 267.06$	$577.53 \pm 26.96 \pm 48.42$	$115.23 \pm 25.49 \pm 17.42$
Data	2196	626	122

Table 7.5: Yields in the low H_{T} control region for the same-sign dilepton channels using the full MC bacground estimate. [110]

Sample	ee	$e\mu$	$\mu\mu$
$Z + jets$	$1821.61 \pm 59.99 \pm 274.27$	$77.82 \pm 21.57 \pm 8.48$	$13.14 \pm 23.15 \pm 2.32$
$W + jets$	$96.96 \pm 14.07 \pm 11.79$	$153.51 \pm 16.76 \pm 20.30$	$4.45 \pm 10.47 \pm 0.70$
$W/Z + \gamma$	$255.86 \pm 7.61 \pm 56.33$	$158.98 \pm 7.81 \pm 36.32$	$0.33 \pm 0.78 \pm 0.10$
$t, t\bar{t}$ mis-id	$175.99 \pm 7.83 \pm 15.46$	$228.71 \pm 8.82 \pm 20.57$	0.00 ± 0.63
$t, t\bar{t}$ fakes	$61.48 \pm 4.29 \pm 5.28$	$101.46 \pm 5.54 \pm 8.56$	$18.72 \pm 2.49 \pm 1.57$
$t\bar{t} + X$ fakes/mis-id	$0.60 \pm 0.07 \pm 0.08$	$0.74 \pm 0.06 \pm 0.07$	$0.15 \pm 0.02 \pm 0.01$
VV mis-id	$19.54 \pm 1.50 \pm 3.37$	$16.80 \pm 1.19 \pm 3.81$	0.00 ± 0.74
VV fakes	$20.39 \pm 1.14 \pm 4.70$	$51.35 \pm 1.67 \pm 11.60$	$27.07 \pm 1.30 \pm 6.32$
VH fakes/mis-id	1.07 ± 0.17	2.38 ± 0.11	1.08 ± 0.09
VVV fakes/mis-id	0.08 ± 0.01	0.16 ± 0.02	0.06 ± 0.01
$t\bar{t}W(W)$	$4.93 \pm 0.20 \pm 1.09$	$15.16 \pm 0.35 \pm 3.30$	$9.46 \pm 0.29 \pm 2.12$
$t\bar{t}Z$	$1.06 \pm 0.08 \pm 0.23$	$3.21 \pm 0.14 \pm 0.68$	$1.57 \pm 0.10 \pm 0.32$
$t\bar{t}H$	$0.55 \pm 0.05 \pm 0.05$	$1.75 \pm 0.09 \pm 0.17$	$0.98 \pm 0.07 \pm 0.09$
VV	$145.49 \pm 2.48 \pm 33.62$	$344.32 \pm 3.69 \pm 80.53$	$157.82 \pm 2.48 \pm 36.57$
VH	2.89 ± 0.45	9.16 ± 0.82	6.75 ± 0.80
VVV	0.83 ± 0.05	2.36 ± 0.08	1.49 ± 0.07
Total bkg.	$2609.33 \pm 62.81 \pm 282.79$	$1167.88 \pm 30.57 \pm 94.57$	$243.06 \pm 25.73 \pm 37.29$
Data	2498	1259	260

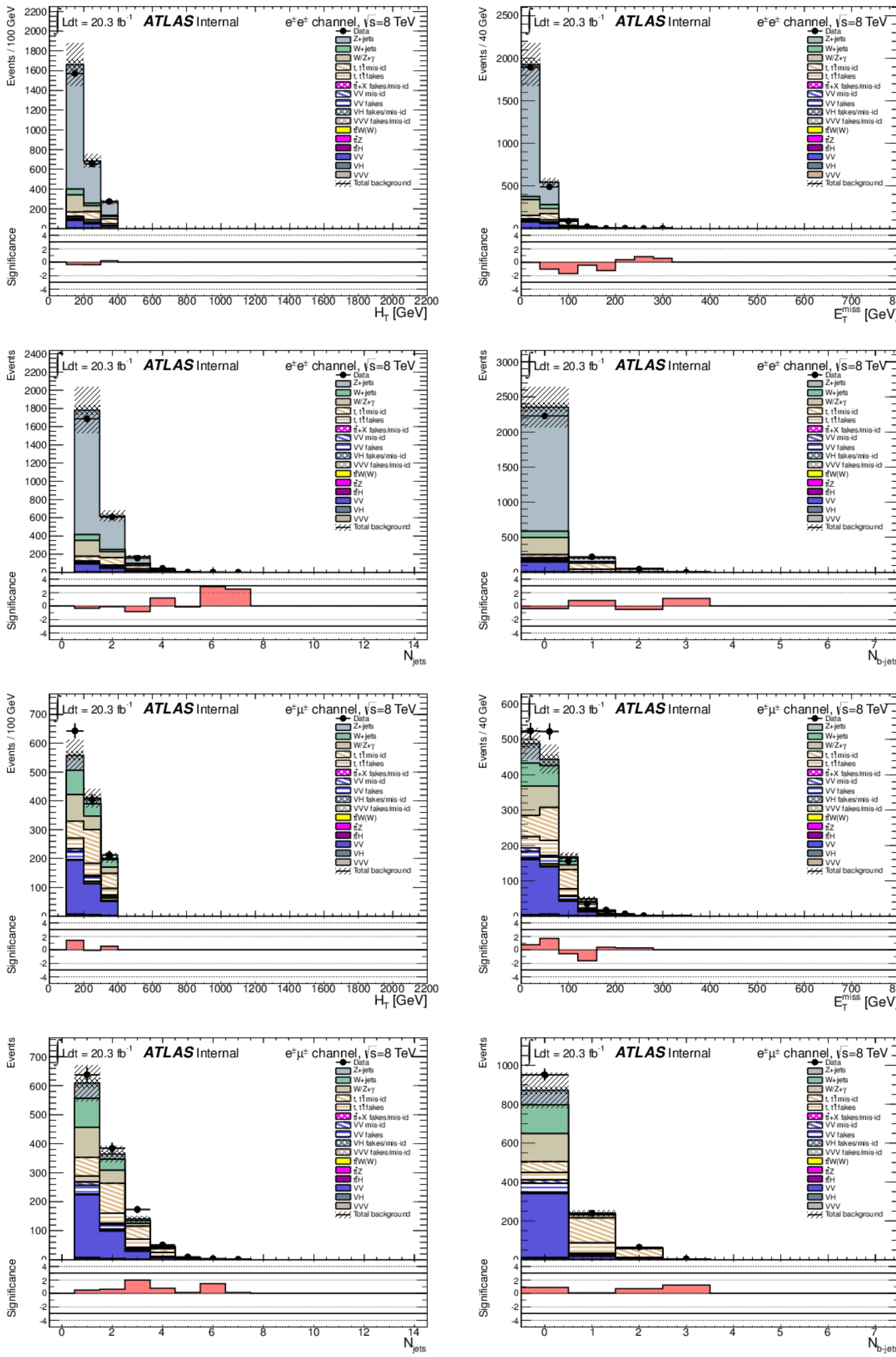

Figure 7.20: Distributions of some kinematic variables in the ee and $e\mu$ channels, in the low H_{T} control region for both the full MC background estimation and the data. [110]

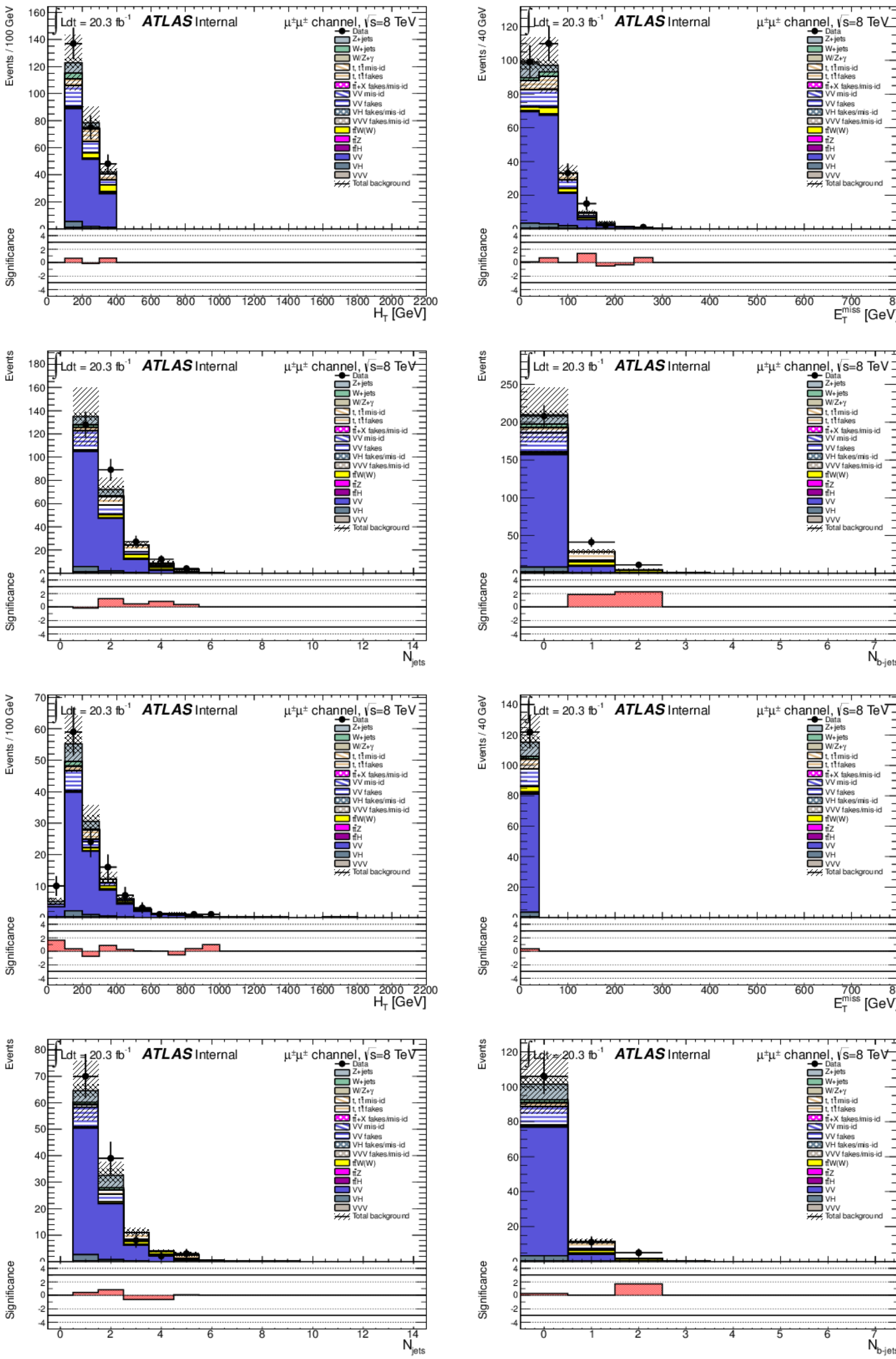

Figure 7.21: Distributions of some kinematic variables in the $\mu\mu$ channel, in the low H_{T} (top) and low $E_{\mathrm{T}}^{\mathrm{miss}}$ (bottom) control regions for both the full MC background estimation and the data. [110]

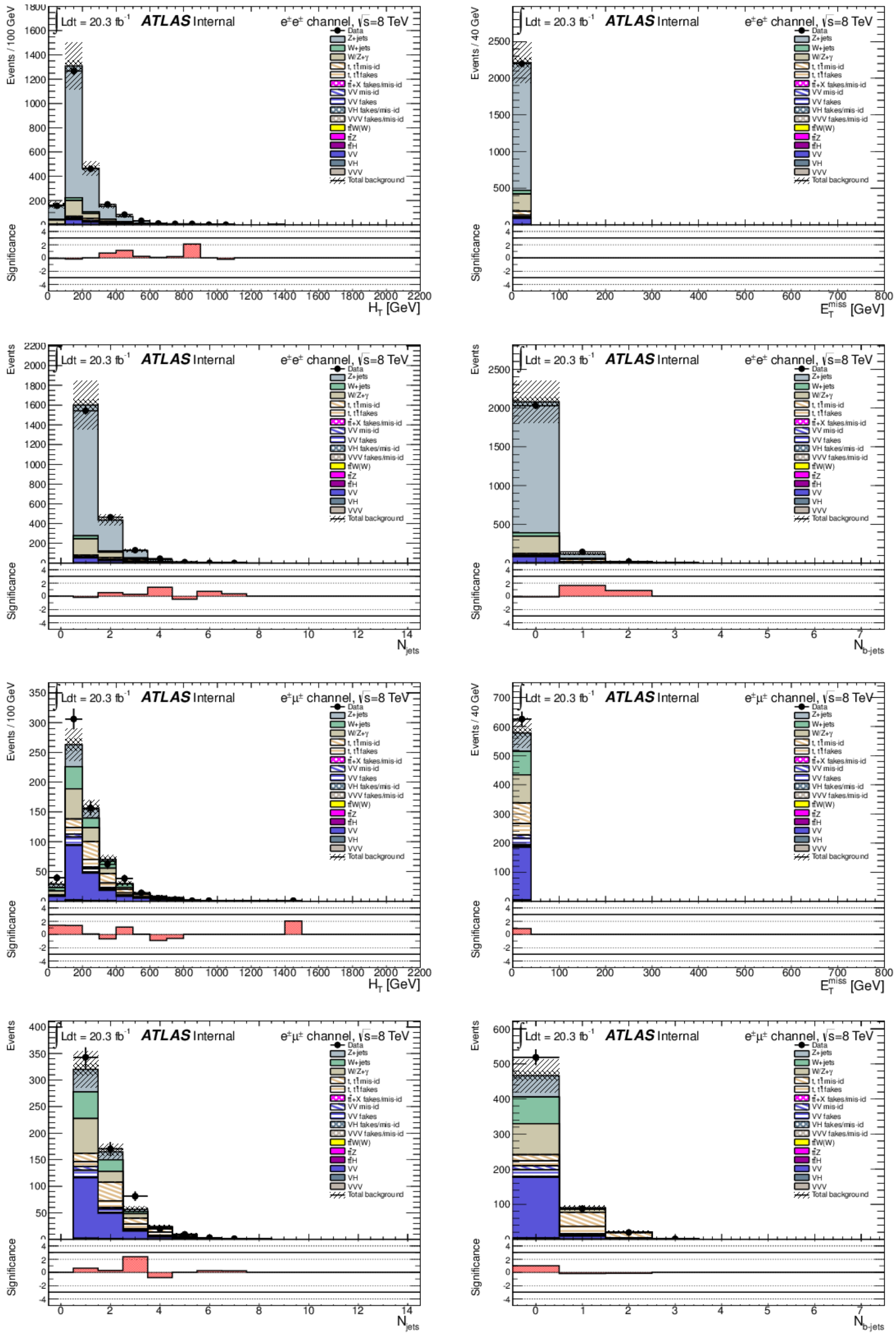

Figure 7.22: Distributions of some kinematic variables in the ee and $e\mu$ channels, in the low $E_{\mathrm{T}}^{\mathrm{miss}}$ control region for both the full MC background estimation and the data. [110]

Table 7.6: Yields in the low $E_{\mathrm{T}}^{\mathrm{miss}}$ control region for the trilepton channels using the full MC background estimate. [110]

Sample	eee	$ee\mu$	$e\mu\mu$	$\mu\mu\mu$
$Z+jets$	$21.51 \pm 21.04 \pm 2.59$	$0.75 \pm 21.02 \pm 0.18$	$34.96 \pm 21.40 \pm 5.25$	$0.36 \pm 22.98 \pm 0.11$
$W+jets$	0.00 ± 10.50	0.00 ± 10.50	0.00 ± 10.50	0.00 ± 10.45
$W/Z+\gamma$	$14.75 \pm 1.48 \pm 4.42$	0.00 ± 0.76	$23.73 \pm 1.83 \pm 7.12$	0.00 ± 0.76
$t, t\bar{t}$ fakes	$0.43 \pm 0.65 \pm 0.04$	$4.01 \pm 1.20 \pm 0.40$	$1.41 \pm 0.89 \pm 0.14$	$0.59 \pm 0.68 \pm 0.06$
$t\bar{t}+X$ fakes	$0.01 \pm 0.01 \pm 0.00$	$0.03 \pm 0.02 \pm 0.00$	$0.04 \pm 0.02 \pm 0.01$	0.00 ± 0.01
VV fakes	$2.76 \pm 0.80 \pm 0.58$	$3.13 \pm 0.85 \pm 0.65$	$4.99 \pm 0.94 \pm 0.96$	$3.91 \pm 0.88 \pm 0.77$
VH fakes	0.00 ± 0.08	0.00 ± 0.08	0.01 ± 0.08	0.00 ± 0.08
VVV fakes	0.01 ± 0.00	0.02 ± 0.00	0.01 ± 0.00	0.01 ± 0.00
$t\bar{t}W(W)$	$0.10 \pm 0.03 \pm 0.02$	$0.48 \pm 0.06 \pm 0.09$	$0.51 \pm 0.06 \pm 0.10$	$0.18 \pm 0.04 \pm 0.03$
$t\bar{t}Z$	$0.93 \pm 0.07 \pm 0.17$	$1.32 \pm 0.09 \pm 0.23$	$1.54 \pm 0.10 \pm 0.29$	$1.79 \pm 0.11 \pm 0.32$
$t\bar{t}H$	$0.05 \pm 0.01 \pm 0.00$	$0.15 \pm 0.02 \pm 0.01$	$0.20 \pm 0.03 \pm 0.02$	$0.10 \pm 0.02 \pm 0.01$
VV	$69.54 \pm 2.07 \pm 14.44$	$66.30 \pm 1.84 \pm 14.77$	$106.20 \pm 2.62 \pm 22.08$	$109.53 \pm 2.48 \pm 24.40$
VH	0.46 ± 0.06	0.62 ± 0.07	0.73 ± 0.08	1.06 ± 0.10
VVV	0.10 ± 0.02	0.24 ± 0.02	0.28 ± 0.03	0.11 ± 0.01
Total bkg.	$110.64 \pm 23.68 \pm 15.33$	$77.04 \pm 23.63 \pm 14.80$	$174.61 \pm 24.09 \pm 23.81$	$117.65 \pm 25.40 \pm 24.42$
Data	98	84	190	121

Table 7.7: Yields in the low H_{T} control region for the trilepton channels using the full MC background estimate. [110]

Sample	eee	$ee\mu$	$e\mu\mu$	$\mu\mu\mu$
$Z+jets$	$23.51 \pm 21.33 \pm 2.80$	$0.70 \pm 21.02 \pm 0.18$	$38.87 \pm 21.48 \pm 5.98$	$0.90 \pm 22.98 \pm 0.16$
$W+jets$	0.00 ± 10.50	0.00 ± 10.50	0.00 ± 10.50	0.00 ± 10.45
$W/Z+\gamma$	$14.05 \pm 1.43 \pm 4.15$	0.00 ± 0.76	$24.49 \pm 1.86 \pm 7.35$	0.00 ± 0.76
$t, t\bar{t}$ fakes	$3.96 \pm 1.17 \pm 0.40$	$10.50 \pm 1.83 \pm 1.05$	$6.81 \pm 1.43 \pm 0.66$	$0.99 \pm 0.79 \pm 0.10$
$t\bar{t}+X$ fakes	$0.03 \pm 0.02 \pm 0.00$	$0.09 \pm 0.02 \pm 0.01$	$0.12 \pm 0.03 \pm 0.01$	$0.02 \pm 0.02 \pm 0.00$
VV fakes	$7.33 \pm 0.97 \pm 1.50$	$7.50 \pm 0.98 \pm 1.61$	$11.91 \pm 1.14 \pm 2.42$	$9.19 \pm 1.03 \pm 1.95$
VH fakes	0.00 ± 0.08	0.00 ± 0.08	0.01 ± 0.08	0.00 ± 0.08
VVV fakes	0.02 ± 0.01	0.07 ± 0.01	0.06 ± 0.01	0.04 ± 0.01
$t\bar{t}W(W)$	$0.42 \pm 0.06 \pm 0.09$	$1.51 \pm 0.10 \pm 0.30$	$1.96 \pm 0.12 \pm 0.43$	$0.95 \pm 0.09 \pm 0.20$
$t\bar{t}Z$	$1.24 \pm 0.08 \pm 0.27$	$1.85 \pm 0.11 \pm 0.39$	$2.29 \pm 0.12 \pm 0.47$	$2.50 \pm 0.13 \pm 0.54$
$t\bar{t}H$	$0.11 \pm 0.02 \pm 0.01$	$0.37 \pm 0.04 \pm 0.03$	$0.45 \pm 0.04 \pm 0.04$	$0.18 \pm 0.03 \pm 0.01$
VV	$102.66 \pm 2.29 \pm 22.92$	$114.15 \pm 2.25 \pm 27.74$	$168.96 \pm 3.03 \pm 37.62$	$188.82 \pm 3.01 \pm 46.00$
VH	0.89 ± 0.09	1.19 ± 0.11	1.53 ± 0.13	1.75 ± 0.14
VVV	0.31 ± 0.02	0.82 ± 0.04	1.08 ± 0.05	0.60 ± 0.03
Total bkg.	$154.53 \pm 23.97 \pm 23.51$	$138.74 \pm 23.71 \pm 27.81$	$258.53 \pm 24.24 \pm 38.88$	$205.95 \pm 25.47 \pm 46.05$
Data	147	142	296	209

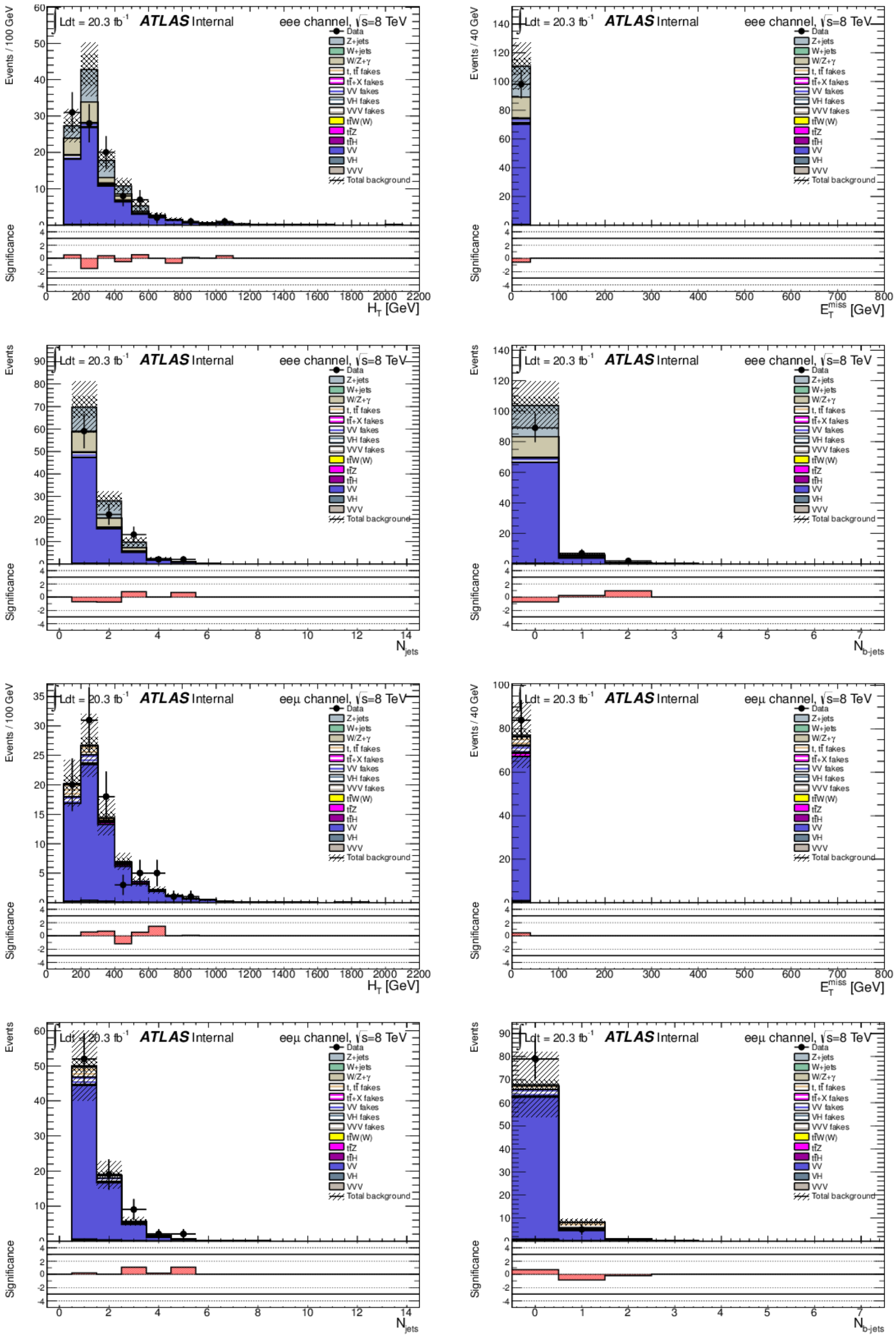

Figure 7.23: Distributions of some kinematic variables in the eee and $ee\mu$ channels, in the low $E_{\mathrm{T}}^{\mathrm{miss}}$ control region for both the full MC background estimation and the data. [110]

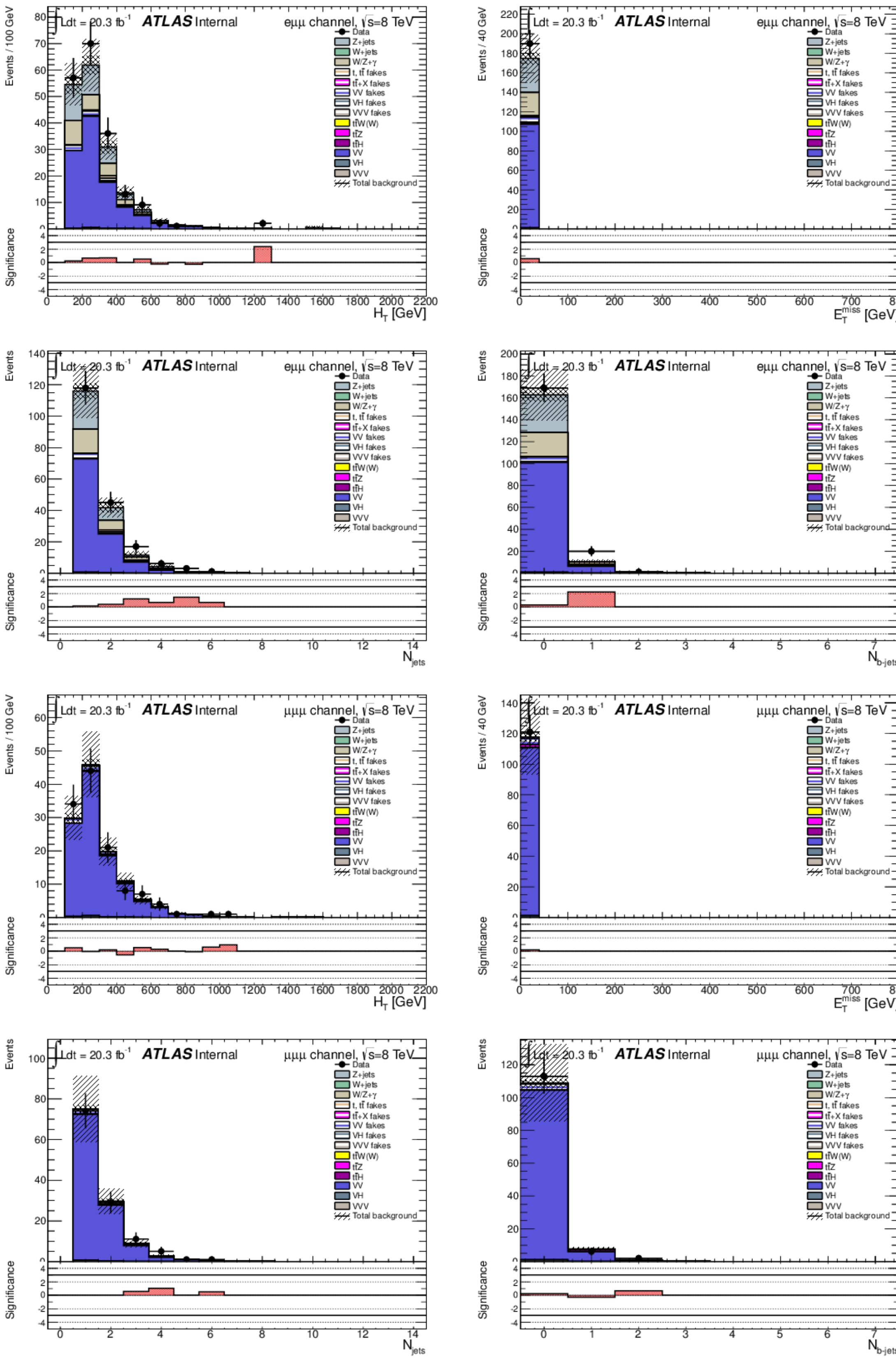

Figure 7.24: Distributions of some kinematic variables in the $e\mu\mu$ and $\mu\mu\mu$ channels, in the low $E_{\mathrm{T}}^{\mathrm{miss}}$ control region for both the full MC background estimation and the data. [110]

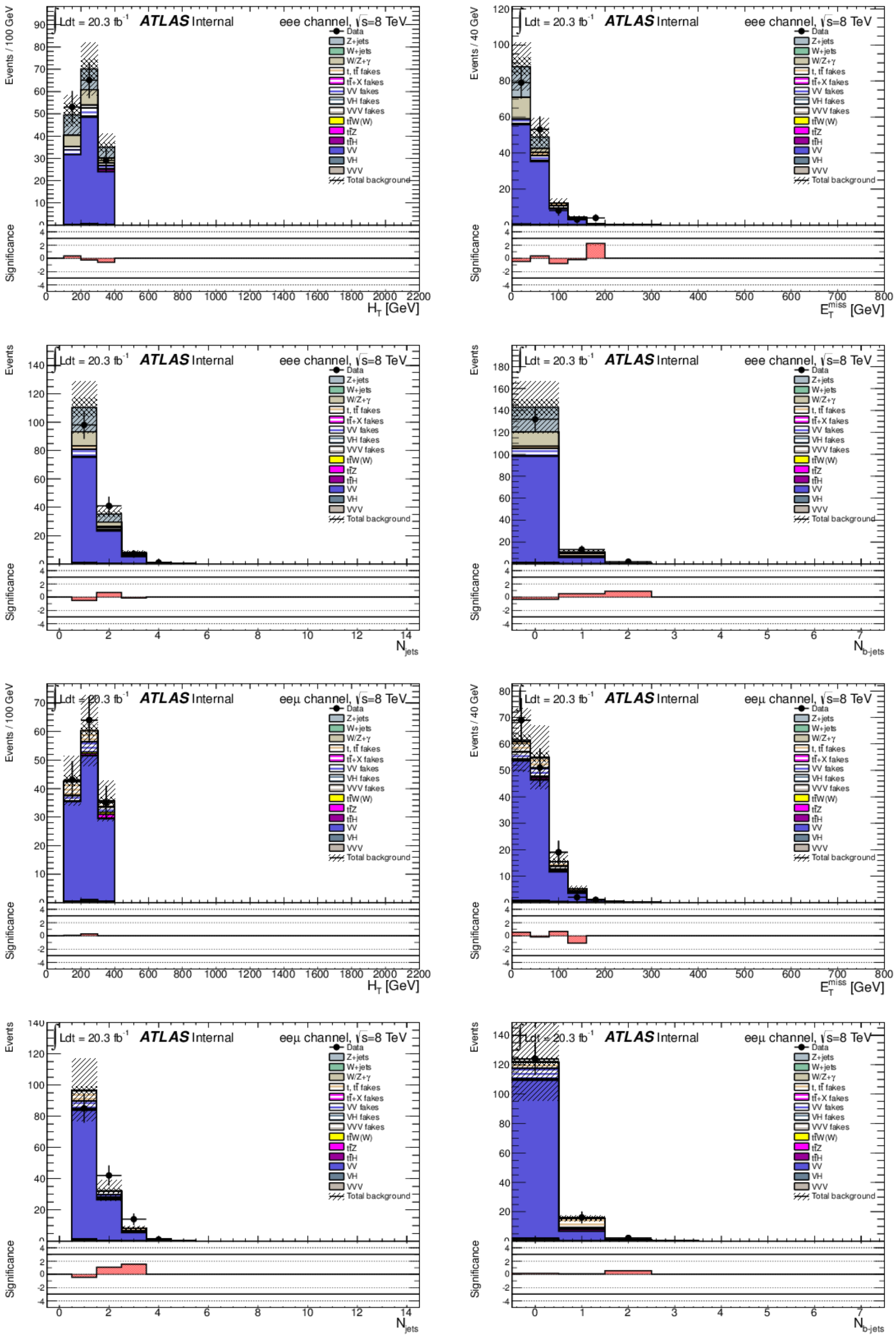

Figure 7.25: Distributions of some kinematic variables in the eee and $ee\mu$ channels, in the low H_{T} control region for both the full MC background estimation and the data. [110]

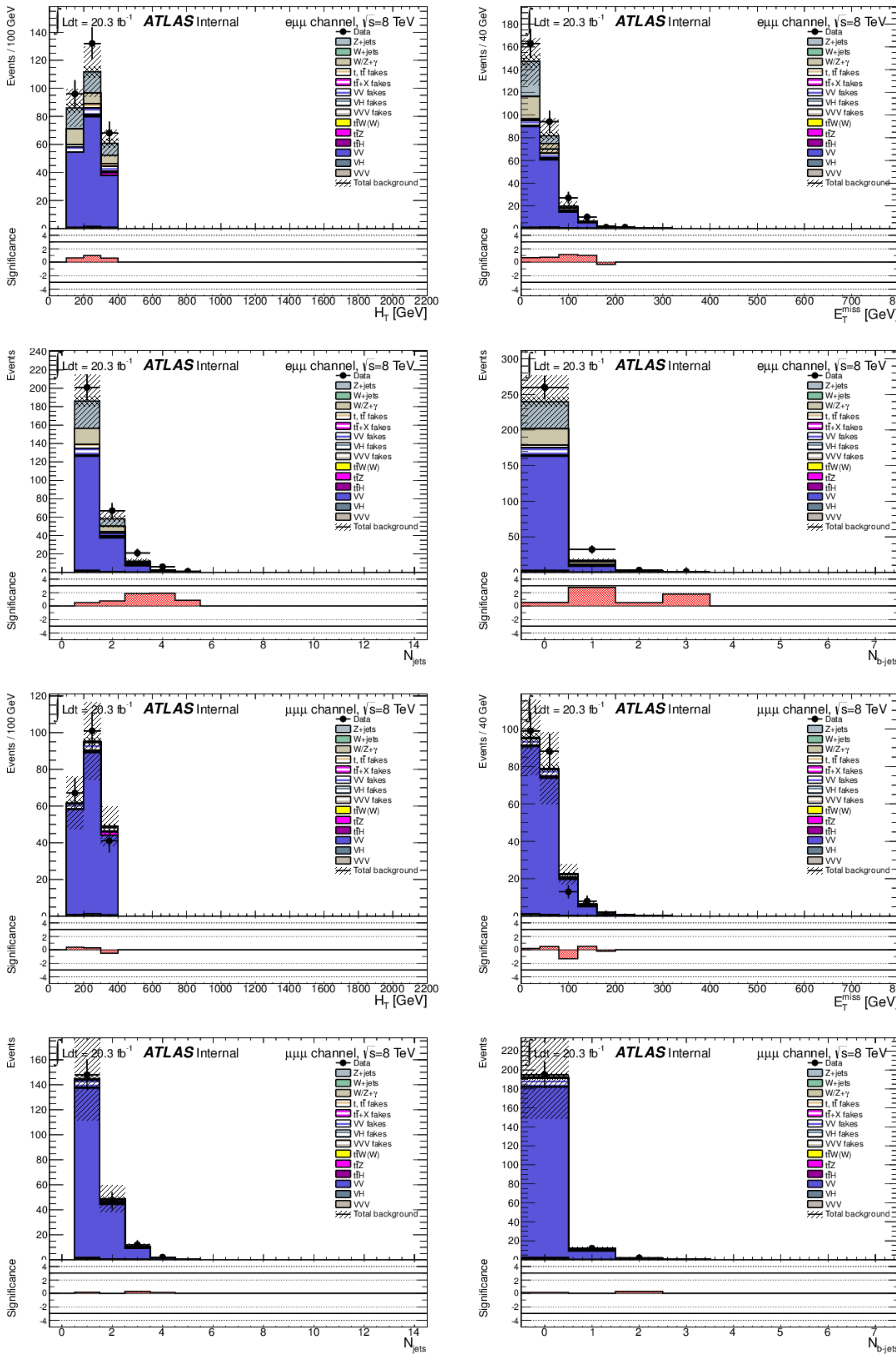

Figure 7.26: Distributions of some kinematic variables in the $e\mu\mu$ and $\mu\mu\mu$ channels, in the low H_{T} control region for both the full MC background estimation and the data. [110]

7.3.2 Composition of the Background in the Generic Signal Region

The results in the previous section show that the full MC estimate accurately describes the background and can be used to analyze the composition of the background in the signal region. The generic signal region considered here (different from the signal region in our analysis, see Section 7.3) is defined as having at least two jets, one b-jet, $E_{\mathrm{T}}^{\mathrm{miss}} > 40$ GeV, $H_{\mathrm{T}} > 650$ GeV and a Z/quarkonia-veto in the ee channel. The event yields for the full MC estimate are shown in Table 7.8 and Table 7.9 for the same-sign dilepton and trilepton channels. The dominant backgrounds are $t\bar{t}$ and $t\bar{t}$+W/Z in the same-sign dilepton channel and $t\bar{t}$+W/Z, WZ and $t\bar{t}$ (eeμ only) in the trilepton channel.

Table 7.8: Yields in the signal region for the same-sign dilepton channels using the full MC background estimate. The first error is statistical and the second is systematic. [110]

Sample	ee	$e\mu$	$\mu\mu$
$Z + jets$	$0.45 \pm 21.02 \pm 0.10$	0.00 ± 21.02	$0.15 \pm 22.98 \pm 0.04$
$W + jets$	$0.58 \pm 10.51 \pm 0.17$	0.00 ± 10.50	0.00 ± 10.45
$W/Z + \gamma$	$0.37 \pm 0.73 \pm 0.08$	$0.04 \pm 0.69 \pm 0.01$	0.00 ± 0.76
$t, t\bar{t}$ mis-id	$4.73 \pm 1.24 \pm 0.42$	$4.93 \pm 1.33 \pm 0.49$	0.00 ± 0.63
$t, t\bar{t}$ fakes	$2.01 \pm 0.96 \pm 0.20$	$2.68 \pm 1.05 \pm 0.27$	$0.30 \pm 0.66 \pm 0.03$
$t\bar{t} + X$ fakes/mis-id	$0.16 \pm 0.02 \pm 0.01$	$0.18 \pm 0.03 \pm 0.01$	$0.06 \pm 0.02 \pm 0.01$
VV mis-id	$0.01 \pm 0.74 \pm 0.00$	$0.01 \pm 0.74 \pm 0.00$	0.00 ± 0.74
VV fakes	$0.54 \pm 0.81 \pm 0.14$	$0.43 \pm 0.74 \pm 0.08$	$0.09 \pm 0.74 \pm 0.02$
VH fakes/mis-id	0.00 ± 0.08	0.00 ± 0.08	0.00 ± 0.08
VVV fakes/mis-id	0.00 ± 0.00	0.00 ± 0.00	0.00 ± 0.00
$t\bar{t}W(W)$	$1.29 \pm 0.08 \pm 0.22$	$3.51 \pm 0.14 \pm 0.62$	$1.95 \pm 0.10 \pm 0.35$
$t\bar{t}Z$	$0.42 \pm 0.05 \pm 0.08$	$1.06 \pm 0.07 \pm 0.21$	$0.40 \pm 0.04 \pm 0.08$
$t\bar{t}H$	$0.22 \pm 0.03 \pm 0.02$	$0.80 \pm 0.06 \pm 0.08$	$0.43 \pm 0.04 \pm 0.04$
VV	$0.43 \pm 0.15 \pm 0.08$	$1.42 \pm 0.21 \pm 0.26$	$0.66 \pm 0.16 \pm 0.10$
VH	0.00 ± 0.08	0.00 ± 0.08	0.10 ± 0.11
VVV	0.00 ± 0.00	0.00 ± 0.00	0.00 ± 0.00
Total bkg.	$11.21 \pm 23.59 \pm 0.59$	$15.07 \pm 23.59 \pm 0.90$	$4.14 \pm 25.29 \pm 0.38$

Table 7.9: Yields in the signal region for the trilepton channels using the full MC background estimate. The first error is statistical and the second is systematic. [110]

Sample	eee	$ee\mu$	$e\mu\mu$	$\mu\mu\mu$
$Z + jets$	0.00 ± 21.02	0.00 ± 21.02	0.00 ± 21.02	0.00 ± 22.98
$W + jets$	0.00 ± 10.50	0.00 ± 10.50	0.00 ± 10.50	0.00 ± 10.45
$W/Z + \gamma$	0.00 ± 0.76	0.00 ± 0.76	0.00 ± 0.76	0.00 ± 0.76
$t, t\bar{t}$ fakes	0.00 ± 0.63	$0.44 \pm 0.68 \pm 0.04$	$0.14 \pm 0.61 \pm 0.01$	0.00 ± 0.63
$t\bar{t} + X$ fakes	$0.01 \pm 0.01 \pm 0.00$	$0.03 \pm 0.02 \pm 0.00$	$0.03 \pm 0.02 \pm 0.00$	0.00 ± 0.01
VV fakes	$0.06 \pm 0.74 \pm 0.01$	$0.07 \pm 0.74 \pm 0.02$	$0.09 \pm 0.74 \pm 0.02$	$0.11 \pm 0.74 \pm 0.03$
VH fakes	0.00 ± 0.08	0.00 ± 0.08	0.00 ± 0.08	0.00 ± 0.08
VVV fakes	0.00 ± 0.00	0.00 ± 0.00	0.00 ± 0.00	0.00 ± 0.00
$t\bar{t}W(W)$	$0.08 \pm 0.02 \pm 0.02$	$0.30 \pm 0.04 \pm 0.05$	$0.34 \pm 0.04 \pm 0.06$	$0.16 \pm 0.03 \pm 0.03$
$t\bar{t}Z$	$0.62 \pm 0.05 \pm 0.12$	$0.95 \pm 0.07 \pm 0.17$	$1.03 \pm 0.07 \pm 0.19$	$1.10 \pm 0.08 \pm 0.20$
$t\bar{t}H$	$0.07 \pm 0.02 \pm 0.01$	$0.16 \pm 0.03 \pm 0.01$	$0.22 \pm 0.03 \pm 0.02$	$0.08 \pm 0.02 \pm 0.01$
VV	$0.44 \pm 0.16 \pm 0.11$	$0.72 \pm 0.16 \pm 0.16$	$0.94 \pm 0.20 \pm 0.24$	$1.35 \pm 0.26 \pm 0.28$
VH	0.00 ± 0.02	0.00 ± 0.02	0.00 ± 0.02	0.00 ± 0.02
VVV	0.00 ± 0.00	0.00 ± 0.00	0.00 ± 0.00	0.00 ± 0.00
Total bkg.	$1.28 \pm 23.53 \pm 0.16$	$2.67 \pm 23.53 \pm 0.25$	$2.79 \pm 23.53 \pm 0.31$	$2.82 \pm 25.27 \pm 0.35$

7.3.3 Validation of the Standard Background Estimate

The ideal control regions for background validation should contain no signal but have the same background composition as our signal region. In general it is nontrivial to find control regions that satisfy both of these requirements. Figures 7.20-7.21 show that a Low H_{T} region with at least one b-tagged jet is a good region for validating the leading backgrounds. As expected it is dominated by $t\bar{t}$ in particular in the eμ channel. In the ee channel there is a large contribution from Z+jets. This can be validated with a region where the Z-peak is selected. The $\mu\mu$ channel contains a non-negligible contribution from WZ which can be controlled by looking in a region with Low H_{T} and zero b-tagged jets. To summarize, the control regions for the same-sign dilepton channels are the following:

- low H_{T}+1b: preselection defined in Section 6.1, 100< H_{T} < 400 GeV, at least one b-tagged jet. This is the main control region, used to validate the $t\bar{t}(+Z/W)$ background, in particular in the $e\mu$ channel;

- low H_{T}+0b: preselection defined in Section 6.1, 100< H_{T} < 400 GeV, zero b-tagged jets. This control region is necessary to validate the description of the WZ background that enters in the low H_{T}+1b control region, for the $\mu\mu$ channel only.

- Z-peak: preselection defined in Section 6.1, removal of the Z/quarkonia veto in the ee channel, $81<m_{ee}<101$ GeV. This control region is necessary to validate the description of the $Z + jets$ background that enters in the low $H_{\mathrm{T}}+1b$ control region, for the ee channel only

The trilepton control regions must be able to validate the $t\bar{t}$+W/Z and WZ backgrounds as well as the $t\bar{t}$ background in the eeμ channel. The $H_{\mathrm{T}} + 0b$ and $H_{\mathrm{T}} + 1b$ control regions defined for the same-sign dilepton channel can also be used here to validate the WZ and $t\bar{t}$ backgrounds respectively. It is not possible however to find a region to validate the $t\bar{t}$+WZ background without allowing significant signal contamination.

Tables 7.10 and 7.11 show the same-sign dilepton yields in data in the $H_{\mathrm{T}} + 1b$ control region compared to both the standard and the full MC background estimates. Figures 7.29 through 7.31 show the distribution of same-sign dilepton events in data compared to the standard background estimate in the $H_{\mathrm{T}} + 1b$, $H_{\mathrm{T}} + 0b$ and Z-peak regions. Tables 7.12 and 7.15 show the trilepton yields in data in the $H_{\mathrm{T}} + 1b$ control region compared to both the standard and the full MC background estimates. Figures 7.32 through 7.34 show the distribution of trilepton events in data compared to the standard background estimate in the $H_{\mathrm{T}} + 1b$, $H_{\mathrm{T}} + 0b$ control regions. The yields in all the tables and plots in this section include statistical and systematic errors. The systematic error includes only the leading systematics in the analysis namely the uncertainty on the cross-section of the MC backgrounds and a 30% uncertainty on the fake/non-prompt and charge misid backgrounds. The standard background estimate is consistent with the data within uncertainty in each of the validation regions considered.

Table 7.10: Yields in the low H_{T}+1b control region for the same-sign dilepton channels. The first error is statistical and the second is systematic. [110]

Sample	ee	$e\mu$	$\mu\mu$
Q Mis-id	$135.68 \pm 1.80 \pm 40.70$	$117.99 \pm 1.44 \pm 35.40$	—
Non-prompt/fakes	$152.68 \pm 11.23 \pm 120.21$	$224.94 \pm 10.45 \pm 175.98$	$28.82 \pm 3.10 \pm 22.84$
$t\bar{t}W(W)$	$3.80 \pm 0.18 \pm 0.85$	$11.72 \pm 0.31 \pm 2.56$	$7.24 \pm 0.25 \pm 1.64$
$t\bar{t}Z$	$0.77 \pm 0.07 \pm 0.17$	$2.44 \pm 0.12 \pm 0.52$	$1.19 \pm 0.09 \pm 0.25$
$t\bar{t}H$	$0.39 \pm 0.04 \pm 0.04$	$1.31 \pm 0.08 \pm 0.13$	$0.76 \pm 0.06 \pm 0.07$
VV	$5.57 \pm 0.45 \pm 1.08$	$15.90 \pm 0.78 \pm 2.93$	$9.00 \pm 0.58 \pm 1.79$
VH	0.28 ± 0.16	0.63 ± 0.28	0.20 ± 0.08
VVV	0.04 ± 0.01	0.12 ± 0.02	0.07 ± 0.01
Total bkg.	$299.21 \pm 11.39 \pm 126.93$	$375.05 \pm 10.59 \pm 179.55$	$47.29 \pm 3.17 \pm 22.97$
Data	271	307	52

Table 7.11: Yields in two control regions for the same-sign dilepton channels using the full MC background estimate. The first error is statistical and the second is systematic. [110]

	"low H_{T}+1b"			"low H_{T}+0b"
Sample	ee	$e\mu$	$\mu\mu$	$\mu\mu$
$Z + jets$	$53.28 \pm 22.01 \pm 4.67$	$2.34 \pm 21.00 \pm 0.33$	$0.61 \pm 22.98 \pm 0.10$	$12.52 \pm 23.15 \pm 2.31$
$W + jets$	$7.03 \pm 10.56 \pm 0.93$	$5.47 \pm 10.54 \pm 0.80$	0.00 ± 10.45	$4.45 \pm 10.47 \pm 0.70$
$W/Z + \gamma$	$14.63 \pm 1.86 \pm 3.24$	$15.37 \pm 2.61 \pm 3.85$	0.00 ± 0.76	$0.33 \pm 0.78 \pm 0.10$
$t, t\bar{t}$ mis-id	$131.68 \pm 6.58 \pm 11.96$	$173.06 \pm 7.64 \pm 15.63$	0.00 ± 0.63	0.00 ± 0.63
$t, t\bar{t}$ fakes	$38.36 \pm 3.39 \pm 3.44$	$62.22 \pm 4.20 \pm 5.51$	$12.22 \pm 2.09 \pm 1.05$	$6.50 \pm 1.37 \pm 0.52$
$t\bar{t} + X$ fakes/mis-id	$0.46 \pm 0.06 \pm 0.06$	$0.53 \pm 0.05 \pm 0.05$	$0.12 \pm 0.02 \pm 0.01$	$0.03 \pm 0.01 \pm 0.00$
VV mis-id	$0.40 \pm 0.73 \pm 0.08$	$0.58 \pm 0.74 \pm 0.13$	0.00 ± 0.74	0.00 ± 0.74
VV fakes	$1.20 \pm 0.76 \pm 0.26$	$4.57 \pm 0.85 \pm 0.82$	$1.93 \pm 0.78 \pm 0.41$	$25.14 \pm 1.27 \pm 5.92$
VH fakes/mis-id	0.06 ± 0.08	0.17 ± 0.08	0.08 ± 0.08	1.00 ± 0.09
VVV fakes/mis-id	0.01 ± 0.01	0.00 ± 0.00	0.01 ± 0.00	0.06 ± 0.01
$t\bar{t}W(W)$	$3.80 \pm 0.18 \pm 0.85$	$11.72 \pm 0.31 \pm 2.56$	$7.24 \pm 0.25 \pm 1.64$	$2.22 \pm 0.14 \pm 0.48$
$t\bar{t}Z$	$0.77 \pm 0.07 \pm 0.17$	$2.44 \pm 0.12 \pm 0.52$	$1.19 \pm 0.09 \pm 0.25$	$0.38 \pm 0.05 \pm 0.08$
$t\bar{t}H$	$0.39 \pm 0.04 \pm 0.04$	$1.31 \pm 0.08 \pm 0.13$	$0.76 \pm 0.06 \pm 0.07$	$0.21 \pm 0.03 \pm 0.02$
VV	$5.57 \pm 0.45 \pm 1.08$	$15.90 \pm 0.78 \pm 2.93$	$9.00 \pm 0.58 \pm 1.79$	$148.82 \pm 2.41 \pm 34.81$
VH	0.28 ± 0.16	0.63 ± 0.28	0.20 ± 0.08	6.55 ± 0.80
VVV	0.04 ± 0.01	0.12 ± 0.02	0.07 ± 0.01	1.42 ± 0.07
Total bkg.	$257.96 \pm 25.60 \pm 13.78$	$296.44 \pm 25.24 \pm 17.50$	$33.44 \pm 25.38 \pm 2.69$	$209.62 \pm 25.63 \pm 35.40$
Data	271	307	52	208

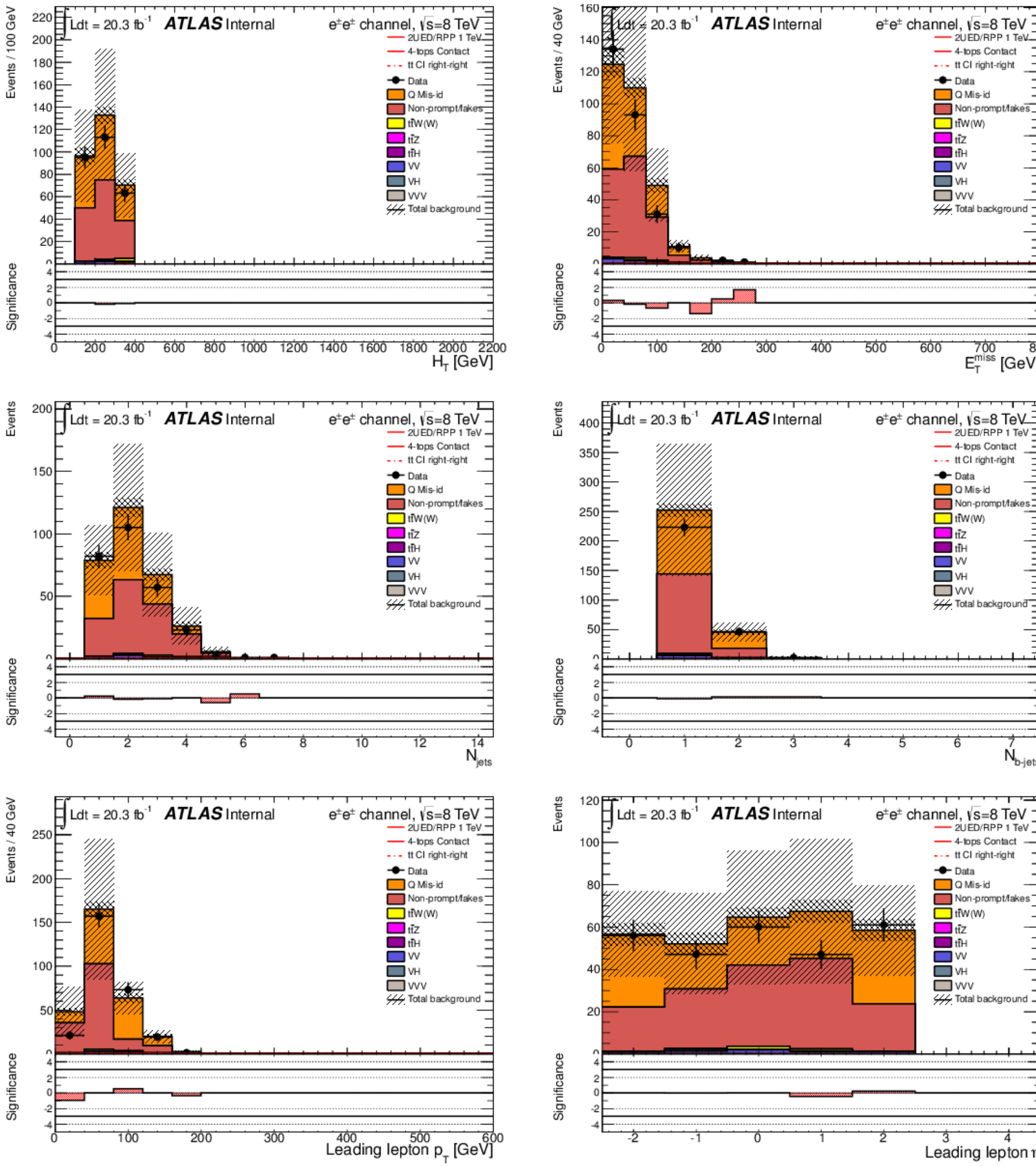

Figure 7.27: Distributions of some kinematic variables in the ee channel, in the low H_{T}+1b control region for both the background estimation and the data. [110]

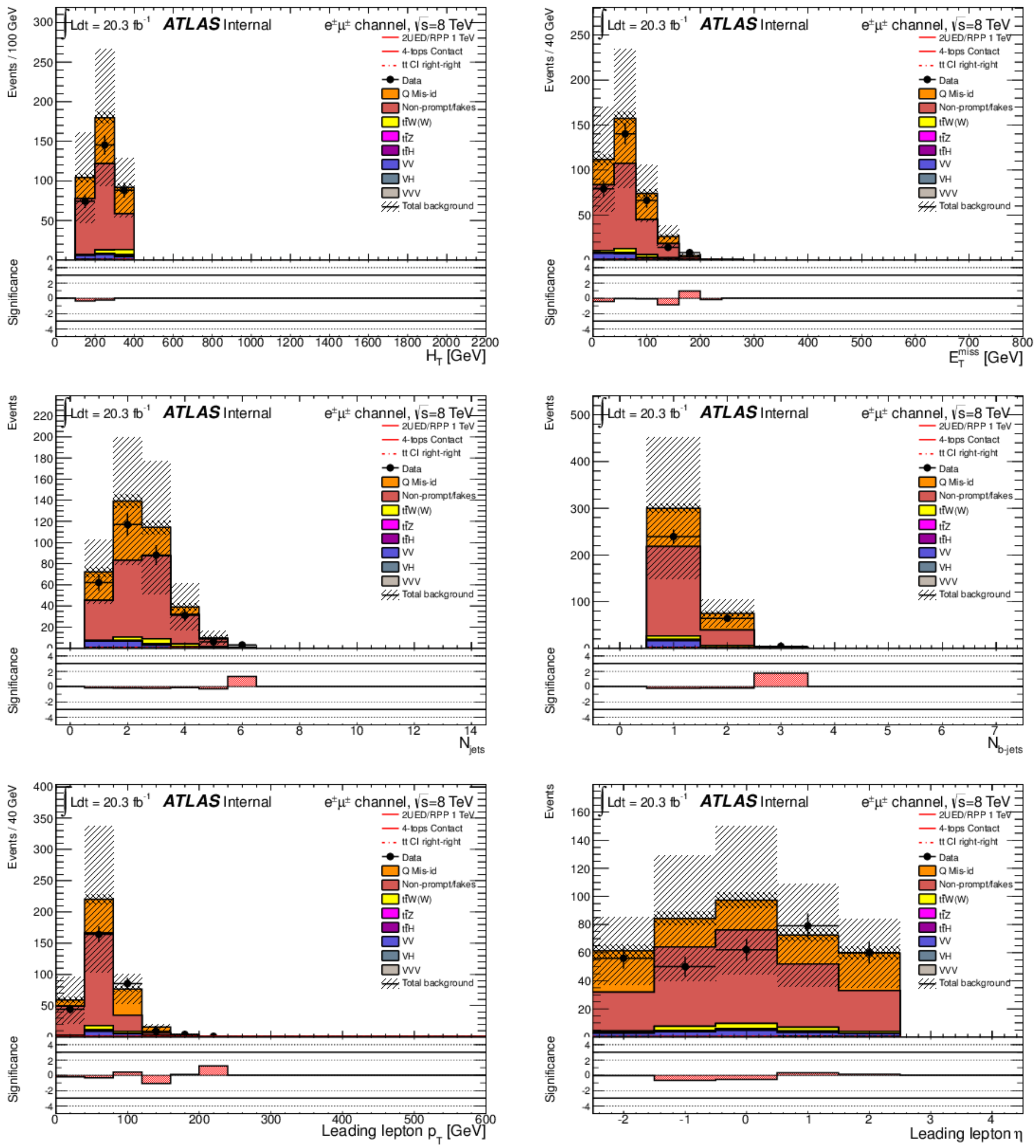

Figure 7.28: Distributions of some kinematic variables in the $e\mu$ channel, in the low H_{T}+1b control region for both the background estimation and the data. [110]

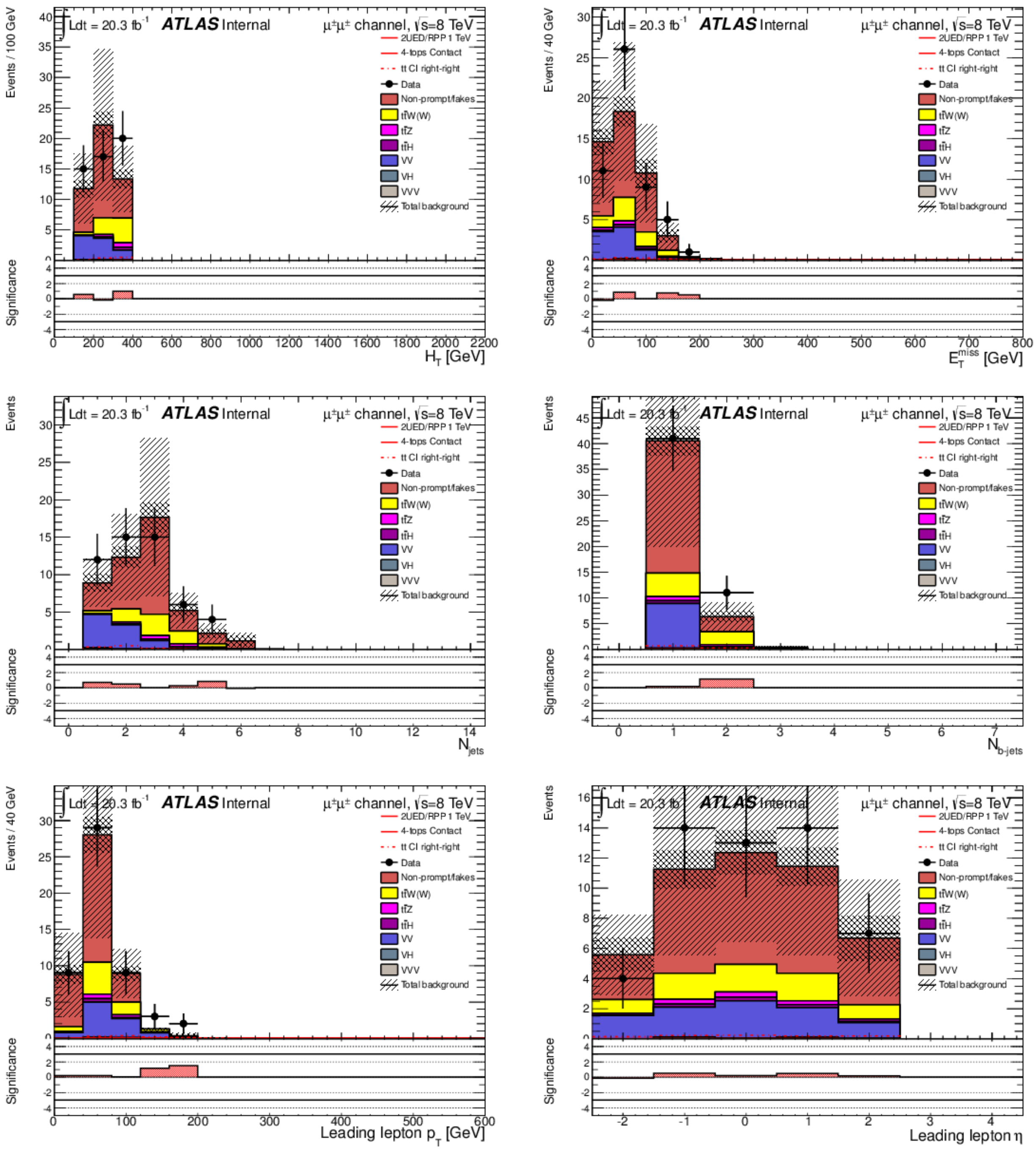

Figure 7.29: Distributions of some kinematic variables in the $\mu\mu$ channel, in the low H_{T}+1b control region for both the background estimation and the data. [110]

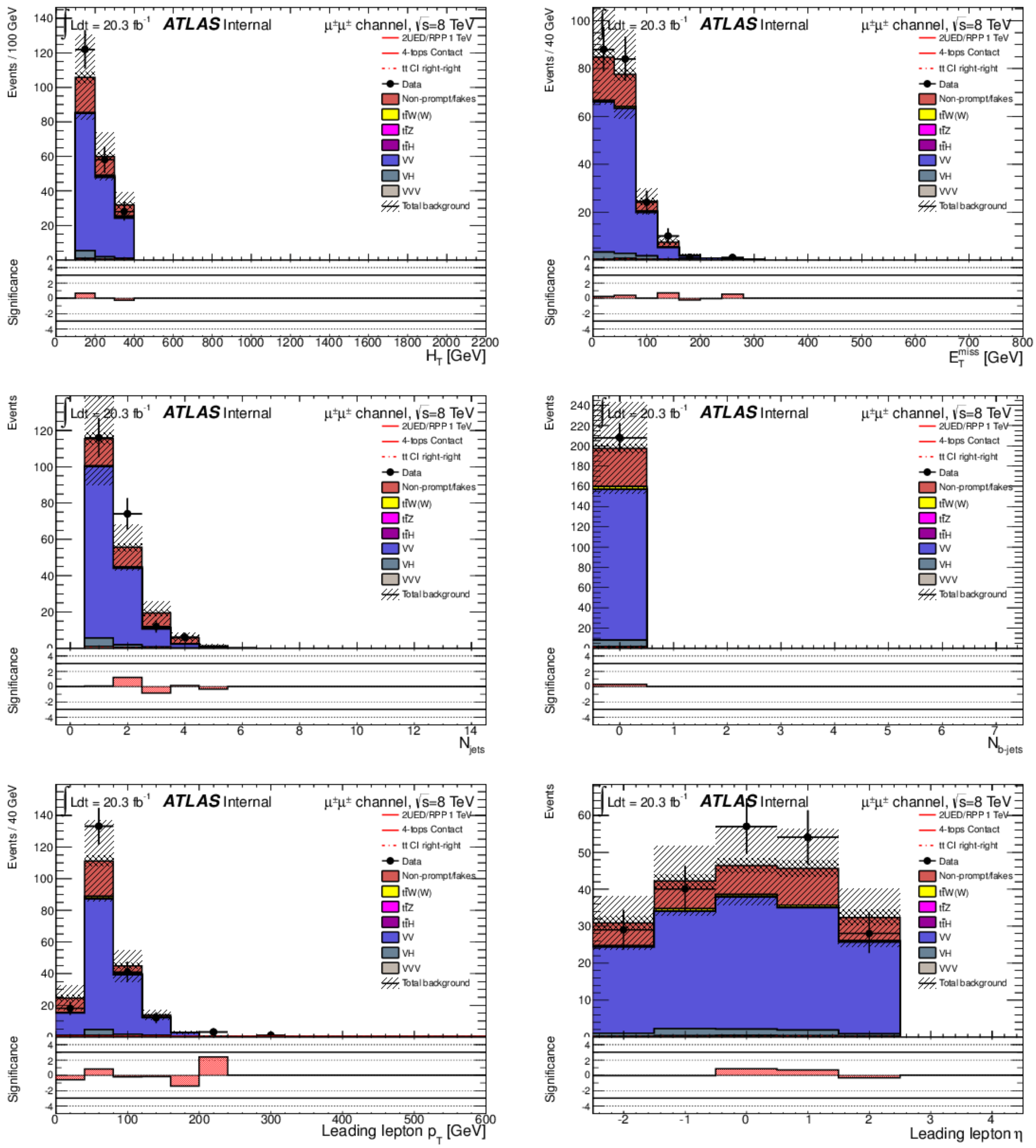

Figure 7.30: Distributions of some kinematic variables in the $\mu\mu$ channel, in the low $H_{\rm T}$+0b control region for both the background estimation and the data. [110]

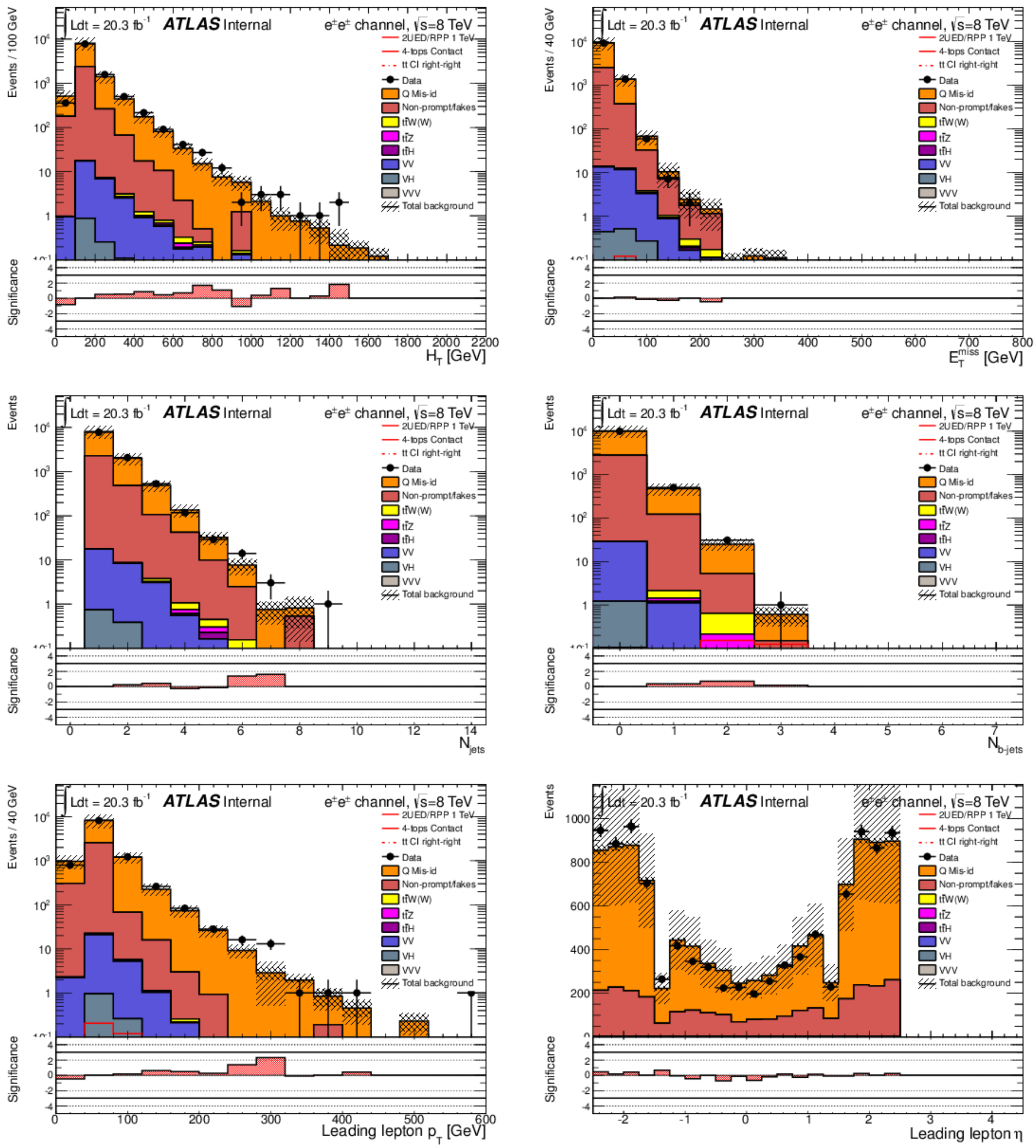

Figure 7.31: Distributions of some kinematic variables in the *ee* channel, in the Z-peak control region for both the background estimation and the data. [110]

Table 7.12: Yields in the low H_{T}+0b control region for the trilepton channels. The first error is statistical and the second is systematic. [110]

Sample	eee	$ee\mu$	$e\mu\mu$	$\mu\mu\mu$
Non-prompt/fakes	$38.57 \pm 6.60 \pm 30.85$	$17.13 \pm 3.89 \pm 13.70$	$63.83 \pm 7.15 \pm 51.06$	$-0.01 \pm 1.65 \pm 0.01$
$t\bar{t}W(W)$	$0.11 \pm 0.03 \pm 0.02$	$0.34 \pm 0.05 \pm 0.06$	$0.36 \pm 0.05 \pm 0.07$	$0.19 \pm 0.04 \pm 0.04$
$t\bar{t}Z$	$0.33 \pm 0.04 \pm 0.06$	$0.47 \pm 0.05 \pm 0.09$	$0.51 \pm 0.06 \pm 0.10$	$0.56 \pm 0.06 \pm 0.12$
$t\bar{t}H$	$0.04 \pm 0.01 \pm 0.00$	$0.09 \pm 0.02 \pm 0.01$	$0.13 \pm 0.02 \pm 0.01$	$0.05 \pm 0.02 \pm 0.00$
VV	$96.88 \pm 2.23 \pm 21.81$	$107.36 \pm 2.17 \pm 26.46$	$160.54 \pm 2.98 \pm 35.94$	$179.59 \pm 2.94 \pm 44.29$
VH	0.87 ± 0.09	1.12 ± 0.11	1.44 ± 0.13	1.62 ± 0.13
VVV	0.29 ± 0.02	0.78 ± 0.04	1.06 ± 0.05	0.58 ± 0.03
Total bkg.	$137.09 \pm 6.97 \pm 37.78$	$127.30 \pm 4.46 \pm 29.80$	$227.86 \pm 7.75 \pm 62.44$	$182.57 \pm 3.38 \pm 44.29$
Data	132	124	260	195

Table 7.13: Yields in the low H_{T}+1b control region for the trilepton channels. The first error is statistical and the second is systematic. [110]

Sample	eee	$ee\mu$	$e\mu\mu$	$\mu\mu\mu$
Non-prompt/fakes	$8.04 \pm 2.32 \pm 6.44$	$13.20 \pm 2.41 \pm 10.56$	$17.87 \pm 2.77 \pm 14.30$	$1.34 \pm 0.55 \pm 1.07$
$t\bar{t}W(W)$	$0.30 \pm 0.05 \pm 0.07$	$1.17 \pm 0.09 \pm 0.24$	$1.60 \pm 0.11 \pm 0.36$	$0.76 \pm 0.08 \pm 0.16$
$t\bar{t}Z$	$0.90 \pm 0.07 \pm 0.21$	$1.38 \pm 0.09 \pm 0.29$	$1.78 \pm 0.11 \pm 0.38$	$1.94 \pm 0.11 \pm 0.42$
$t\bar{t}H$	$0.07 \pm 0.02 \pm 0.01$	$0.28 \pm 0.03 \pm 0.03$	$0.32 \pm 0.03 \pm 0.03$	$0.14 \pm 0.02 \pm 0.01$
VV	$5.78 \pm 0.51 \pm 1.14$	$6.78 \pm 0.57 \pm 1.33$	$8.42 \pm 0.57 \pm 1.78$	$9.23 \pm 0.65 \pm 1.82$
VH	0.02 ± 0.02	0.07 ± 0.02	0.09 ± 0.03	0.13 ± 0.04
VVV	0.02 ± 0.01	0.04 ± 0.01	0.03 ± 0.01	0.02 ± 0.01
Total bkg.	$15.14 \pm 2.38 \pm 6.54$	$22.92 \pm 2.48 \pm 10.65$	$30.11 \pm 2.83 \pm 14.42$	$13.56 \pm 0.86 \pm 2.16$
Data	15	18	36	14

Table 7.14: Yields in the low H_{T}+0b control region for the trilepton channels using the full MC background estimate. The first error is statistical and the second is systematic. [110]

Sample	eee	$ee\mu$	$e\mu\mu$	$\mu\mu\mu$
$Z + jets$	$22.47 \pm 21.32 \pm 2.76$	$0.45 \pm 21.02 \pm 0.13$	$38.11 \pm 21.48 \pm 5.96$	$0.87 \pm 22.98 \pm 0.15$
$W + jets$	0.00 ± 10.50	0.00 ± 10.50	0.00 ± 10.50	0.00 ± 10.45
$W/Z + \gamma$	$13.21 \pm 1.40 \pm 3.90$	0.00 ± 0.76	$22.69 \pm 1.79 \pm 6.81$	0.00 ± 0.76
$t, t\bar{t}$ fakes	$1.58 \pm 0.87 \pm 0.16$	$4.22 \pm 1.25 \pm 0.42$	$3.48 \pm 1.06 \pm 0.33$	$0.59 \pm 0.73 \pm 0.06$
$t\bar{t} + X$ fakes	$0.02 \pm 0.01 \pm 0.00$	$0.03 \pm 0.02 \pm 0.00$	$0.02 \pm 0.01 \pm 0.00$	$0.02 \pm 0.01 \pm 0.00$
VV fakes	$6.98 \pm 0.96 \pm 1.45$	$7.12 \pm 0.97 \pm 1.55$	$11.18 \pm 1.11 \pm 2.31$	$8.57 \pm 1.01 \pm 1.82$
VH fakes	0.00 ± 0.08	0.00 ± 0.08	0.01 ± 0.08	0.00 ± 0.08
VVV fakes	0.02 ± 0.01	0.07 ± 0.01	0.06 ± 0.01	0.03 ± 0.01
$t\bar{t}W(W)$	$0.11 \pm 0.03 \pm 0.02$	$0.34 \pm 0.05 \pm 0.06$	$0.36 \pm 0.05 \pm 0.07$	$0.19 \pm 0.04 \pm 0.04$
$t\bar{t}Z$	$0.33 \pm 0.04 \pm 0.06$	$0.47 \pm 0.05 \pm 0.09$	$0.51 \pm 0.06 \pm 0.10$	$0.56 \pm 0.06 \pm 0.12$
$t\bar{t}H$	$0.04 \pm 0.01 \pm 0.00$	$0.09 \pm 0.02 \pm 0.01$	$0.13 \pm 0.02 \pm 0.01$	$0.05 \pm 0.02 \pm 0.00$
VV	$96.88 \pm 2.23 \pm 21.81$	$107.36 \pm 2.17 \pm 26.46$	$160.54 \pm 2.98 \pm 35.94$	$179.59 \pm 2.94 \pm 44.29$
VH	0.87 ± 0.09	1.12 ± 0.11	1.44 ± 0.13	1.62 ± 0.13
VVV	0.29 ± 0.02	0.78 ± 0.04	1.06 ± 0.05	0.58 ± 0.03
Total bkg.	$142.80 \pm 23.95 \pm 22.37$	$122.06 \pm 23.66 \pm 26.51$	$239.59 \pm 24.21 \pm 37.14$	$192.67 \pm 25.46 \pm 44.32$
Data	132	124	260	195

Table 7.15: Yields in the low H_{T}+1b control region for the trilepton channels using the full MC background estimate. The first error is statistical and the second is systematic. [110]

Sample	eee	$ee\mu$	$e\mu\mu$	$\mu\mu\mu$
$Z + jets$	$1.05 \pm 21.02 \pm 0.22$	$0.25 \pm 21.02 \pm 0.05$	$0.76 \pm 21.01 \pm 0.12$	$0.03 \pm 22.98 \pm 0.01$
$W + jets$	0.00 ± 10.50	0.00 ± 10.50	0.00 ± 10.50	0.00 ± 10.45
$W/Z + \gamma$	$0.84 \pm 0.81 \pm 0.25$	0.00 ± 0.76	$1.80 \pm 0.90 \pm 0.54$	0.00 ± 0.76
$t, t\bar{t}$ fakes	$2.38 \pm 0.97 \pm 0.24$	$6.27 \pm 1.46 \pm 0.63$	$3.34 \pm 1.13 \pm 0.33$	$0.40 \pm 0.65 \pm 0.04$
$t\bar{t} + X$ fakes	$0.02 \pm 0.01 \pm 0.00$	$0.06 \pm 0.02 \pm 0.01$	$0.09 \pm 0.03 \pm 0.01$	$0.01 \pm 0.01 \pm 0.00$
VV fakes	$0.35 \pm 0.75 \pm 0.07$	$0.38 \pm 0.74 \pm 0.07$	$0.72 \pm 0.73 \pm 0.12$	$0.62 \pm 0.75 \pm 0.13$
VH fakes	0.00 ± 0.08	0.00 ± 0.08	0.00 ± 0.08	0.00 ± 0.08
VVV fakes	0.00 ± 0.00	0.00 ± 0.00	0.00 ± 0.00	0.01 ± 0.00
$t\bar{t}W(W)$	$0.30 \pm 0.05 \pm 0.07$	$1.17 \pm 0.09 \pm 0.24$	$1.60 \pm 0.11 \pm 0.36$	$0.76 \pm 0.08 \pm 0.16$
$t\bar{t}Z$	$0.90 \pm 0.07 \pm 0.21$	$1.38 \pm 0.09 \pm 0.29$	$1.78 \pm 0.11 \pm 0.38$	$1.94 \pm 0.11 \pm 0.42$
$t\bar{t}H$	$0.07 \pm 0.02 \pm 0.01$	$0.28 \pm 0.03 \pm 0.03$	$0.32 \pm 0.03 \pm 0.03$	$0.14 \pm 0.02 \pm 0.01$
VV	$5.78 \pm 0.51 \pm 1.14$	$6.78 \pm 0.57 \pm 1.33$	$8.42 \pm 0.57 \pm 1.78$	$9.23 \pm 0.65 \pm 1.82$
VH	0.02 ± 0.02	0.07 ± 0.02	0.09 ± 0.03	0.13 ± 0.04
VVV	0.02 ± 0.01	0.04 ± 0.01	0.03 ± 0.01	0.02 ± 0.01
Total bkg.	$11.73 \pm 23.55 \pm 1.23$	$16.68 \pm 23.57 \pm 1.52$	$18.94 \pm 23.55 \pm 1.97$	$13.28 \pm 25.28 \pm 1.88$
Data	15	18	36	14

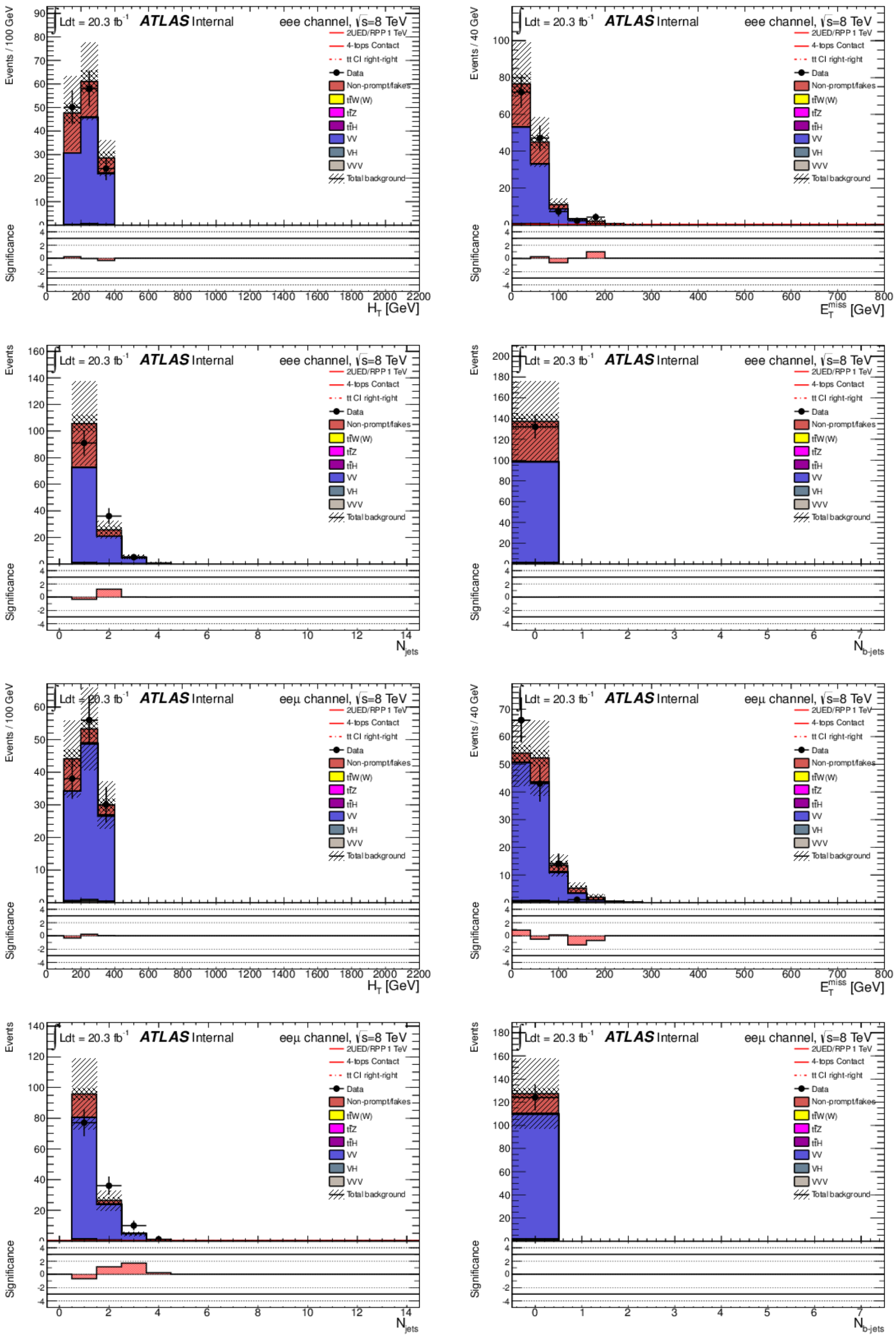

Figure 7.32: Distributions of some kinematic variables in the eee and $ee\mu$ channels, in the low H_{T}+0b control region for both the background estimation and the data. [110]

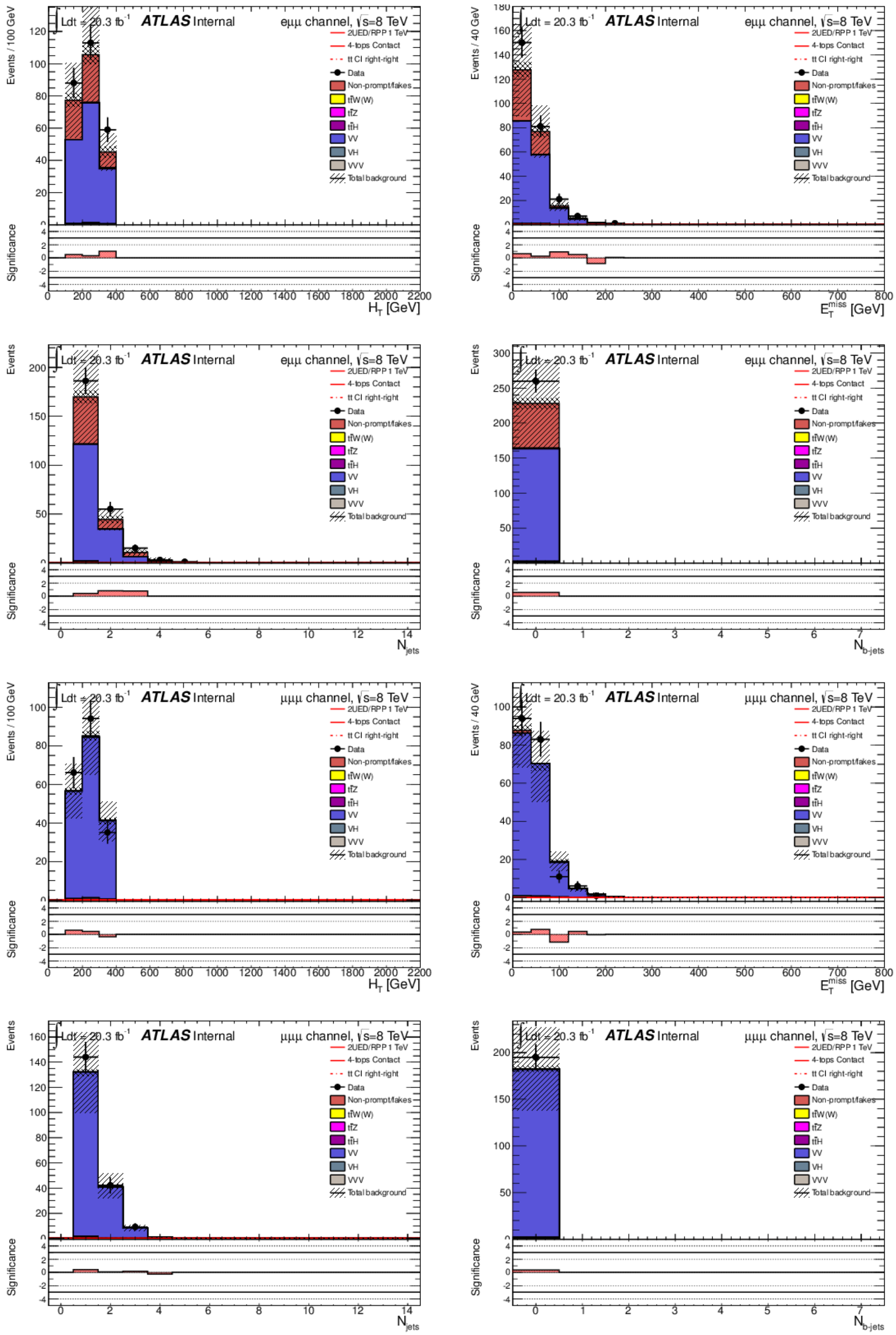

Figure 7.33: Distributions of some kinematic variables in the $e\mu\mu$ and $\mu\mu\mu$ channels, in the low H_{T}+0b control region for both the background estimation and the data. [110]

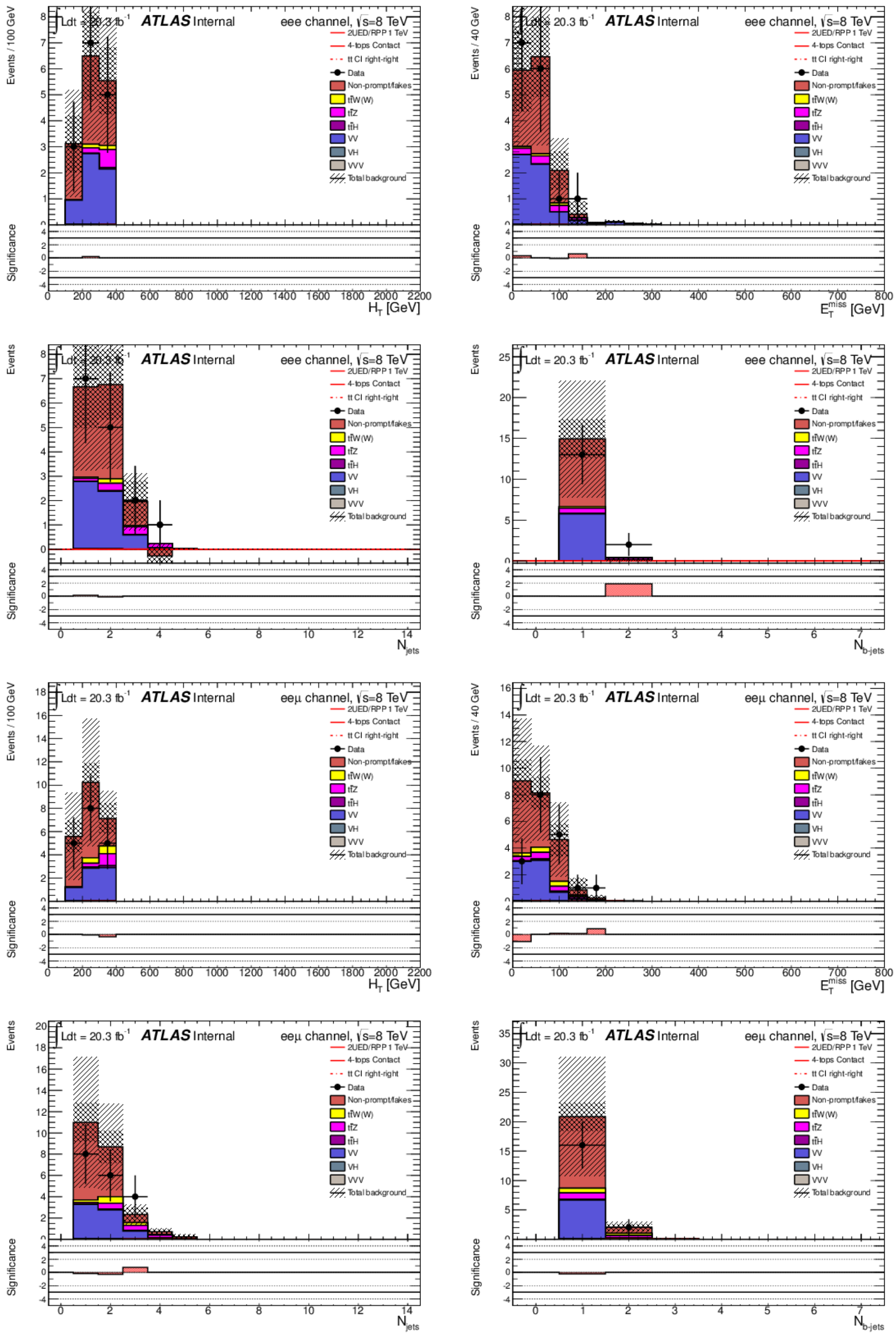

Figure 7.34: Distributions of some kinematic variables in the eee and $ee\mu$ channels, in the low H_{T}+1b control region for both the background estimation and the data. [110]

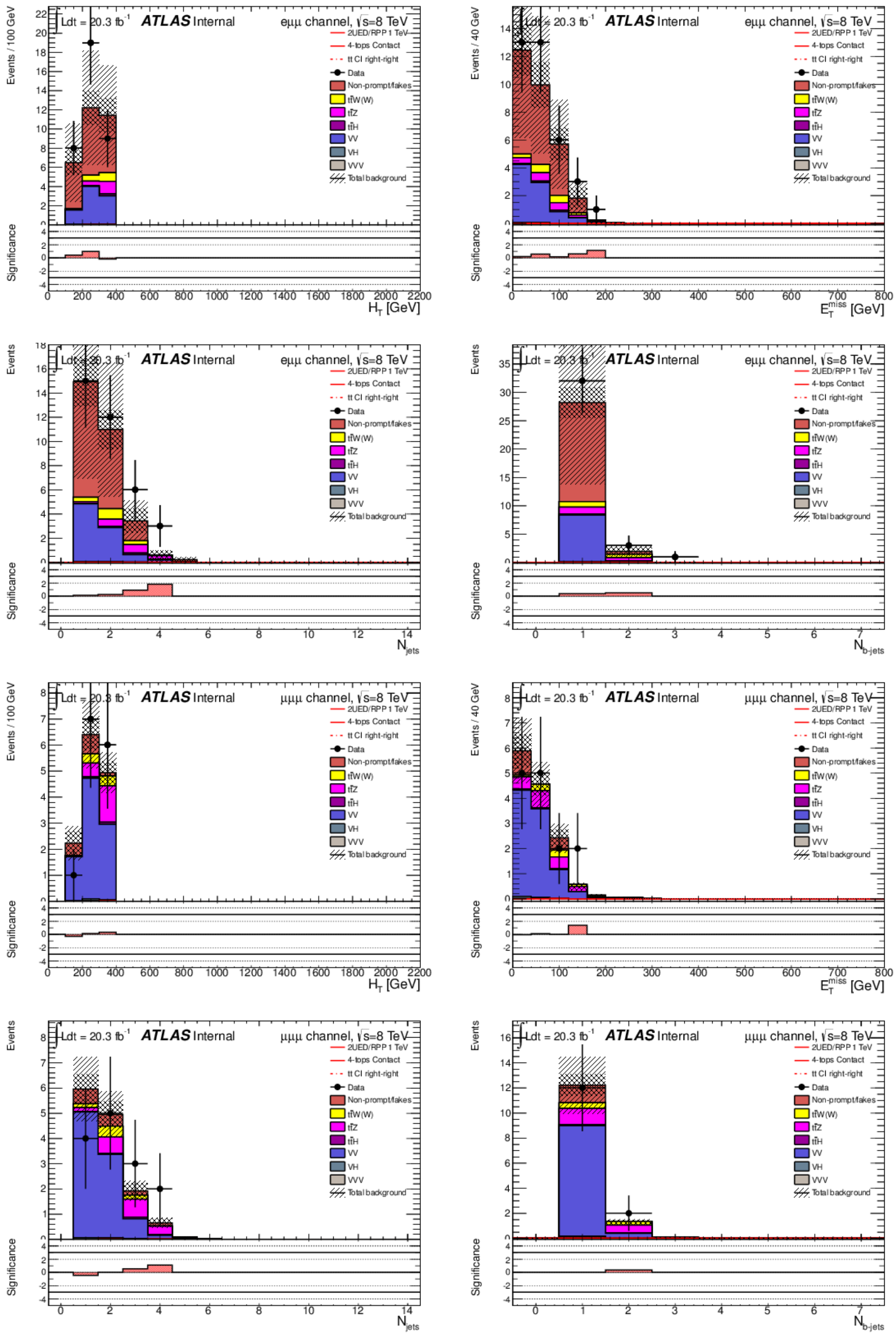

Figure 7.35: Distributions of some kinematic variables in the $e\mu\mu$ and $\mu\mu\mu$ channels, in the low H_{T}+1b control region for both the background estimation and the data. [110]

CHAPTER 8

Systematic Uncertainties

The estimation of uncertainty is an extremely important part of any experimental measurement. In particular in a particle physics search it factors heavily in the statistical interpretation of the data in the context of the background-only and the signal-plus-background hypotheses. The uncertainty can be divided into two components: statistical and systematic. Statistical uncertainty derives from random fluctuations in measurement that are either unknown or unpredictable. In the context of a particle physics analysis these fluctuations follow a Poisson distribution with mean μ and standard deviation $\sqrt{\mu}$. This error can be significant in extreme regions of phase space where N is small, however it decreases as more data is collected. It is straightforward to evaluate and scales with the inverse square root of the integrated luminosity of the data. [20] In contrast the systematic uncertainty is generally not straightforward to evaluate and does not decrease as the integrated luminosity increases. Identifying and controlling all the sources of systematic error is a crucial and non-trivial part of the analysis.

The main result of a particle physics search is the significance which quantifies the agreement of data with the background expectation and, in the case of no excess, the exclusion limits for the signal(s) being investigated. The details of their calculation are given in Chapter 9. They are calculated directly from the event yields observed in data and the expected signal and background event yields. The former is determined by simply counting the number of events in data that pass the selection defining the signal region while the latter are determined with Eq. 6.1. The uncertainty on the expected signal and background yields has both a statistical and systematic

[20] For signal and background event yields the statistical uncertainty is the quadratic sum of the weights applied to the MC events and scales with the inverse square root of the size of the MC sample.

component. The systematics arise from theoretical and experimental uncertainties that affect the cross-section, the integrated luminosity and the selection efficiency. These uncertainties contribute to the overall uncertainty on the event yield which affects the calculation of the significance and exclusion limits. Greater systematic uncertainty makes it more difficult to distinguish between the background-only and the signal-plus-background hypotheses and thus fundamentally limits the sensitivity of the search. For these reasons it is critical to identify all sources of systematic error and to minimize them as much as possible. The remainder of this chapter lists the leading sources of systematic uncertainty for this analysis. In each case a parameter subject to some uncertainty is varied and the systematic uncertainty is estimated by comparing the yields calculated with the variation to the nominal yield. For each systematic there are three yields, x_{nom}, x_{up} and x_{down} corresponding to the nominal value of the parameter and the value shifted up and down by one standard deviation. These three values are used to determine the probability distribution functions for the nuisance parameters $\pi(\nu_j)$ (described in Section 9.1) used for setting limits. In some cases the nominal values are smeared by a Gaussian producing a single shifted value which is then symmetrized to get x_{up} and x_{down} and determine $\pi(\nu_j)$. Tables 8.1 and 8.2 show the leading systematic uncertainties on the combined background yield and on the yield for a representative signal (600 GeV vector-like bottom pair production) for each SR category.

	VLQ signal region number							
Source	0	1	2	3	4	5	6	7
Cross section	±8.0	±13.6	±15.1	±11.1	±12.1	±16.8	±25.2	±23.8
Fake/non-prompt leptons	±33	±18	±25	±23	±26	±16	±1.5	±3.8
Charge misID	$^{+5.9}_{-5.7}$	$^{+9.3}_{-9.1}$	$^{+5.4}_{-5.1}$	$^{+7.4}_{-6.7}$	$^{+5.0}_{-4.6}$	$^{+8.7}_{-8.1}$	$^{+9.0}_{-8.5}$	$^{+11.0}_{-10.1}$
Jet energy scale	$^{+1.7}_{-1.6}$	$^{+1.2}_{-1.8}$	$^{+1.4}_{-1.7}$	$^{+1.8}_{-2.1}$	$^{+2.6}_{-4.2}$	$^{+3.8}_{-1.5}$	$^{+8.5}_{-4.8}$	$^{+7.3}_{-2.9}$
b-tagging efficiency	±1.0	±2.6	$^{+5.7}_{-5.5}$	$^{+1.9}_{-2.0}$	$^{+1.6}_{-1.7}$	$^{+3.8}_{-3.7}$	$^{+5.1}_{-5.0}$	$^{+8.3}_{-8.2}$
Lepton ID efficiency	±1.3	±1.6	±1.6	$^{+2.1}_{-2.0}$	$^{+2.1}_{-2.0}$	$^{+2.2}_{-2.1}$	$^{+2.8}_{-2.2}$	±2.5
Jet energy resolution	±0.5	±0.2	±3.1	±1.9	±0.3	±0.9	±0.8	±3.4
Luminosity	±0.9	±1.1	±1.3	±1.4	±1.5	±1.5	±2.1	±1.9

Table 8.1: Uncertainty (in %) on the total background yield for each SR category due to the leading sources of systematic uncertainty. [39]

	VLQ signal region number							
Source	0	1	2	3	4	5	6	7
Jet energy scale	$^{+11.3}_{-9.0}$	$^{+11.5}_{-6.3}$	$^{+28.0}_{-17.3}$	$^{+3.7}_{-2.1}$	$^{+5.4}_{-2.4}$	$^{+3.9}_{-2.0}$	$^{+4.5}_{-6.5}$	$^{+6.6}_{-3.0}$
b-tagging efficiency	$^{+2.5}_{-3.0}$	$^{+6.3}_{-6.1}$	$^{+16.4}_{-15.9}$	$^{+3.1}_{-3.7}$	$^{+3.4}_{-4.0}$	$^{+7.4}_{-7.2}$	$^{+7.6}_{-7.4}$	$^{+12.1}_{-11.9}$
Lepton ID efficiency	±2.9	±2.9	±2.8	±2.9	$^{+3.2}_{-3.1}$	±2.9	$^{+3.2}_{-3.1}$	$^{+3.0}_{-2.9}$
Jet energy resolution	±0.8	±2.5	±3.9	±0.3	±0.7	±0.7	±1.0	±0.1
Luminosity	±2.8	±2.8	±2.8	±2.8	±2.8	±2.8	±2.8	±2.8

Table 8.2: Uncertainty (in %) on the yield of a representative signal (600 GeV vector-like B pair production) for each SR category due to the leading sources of experimental systematic uncertainty. [39]

8.1 Uncertainties on Monte Carlo Samples

8.1.1 Trigger and Object Reconstruction

The trigger and object reconstruction efficiencies described in Chapters 4 and 5 are not the same in MC simulation and data. This is because the detector simulation is imperfect and can only approximate the true detector response. The trigger efficiencies in both MC simulation and data are shown in Fig. 4.1 and Fig. 4.2. The object reconstruction efficiencies in MC simulation and data are shown in Fig. 5.3, 5.9 and 5.10 for jets, electrons and muons respectively. The difference between the efficiencies measured in MC simulation and those measured in data must be accounted for in order to accurately compare MC event yields with observed event yields. This is done by scaling the efficiencies in the MC simulation to agree with those in data. Scale factors are evaluated as the ratio

$$SF = \frac{\epsilon_{data}(\eta, p_{\mathrm{T}})}{\epsilon_{MC}(\eta, p_{\mathrm{T}})}$$

They are parametrized as the efficiencies are in terms of object η and p_{T}. The scale factors used in this analysis for each of the trigger and object reconstruction efficiency corrections follow the recommendations of the relevant physics Combined Performance (CP) group. The CP groups and the software tags used for each correction is given in Table 8.3

Efficiency Correction	CP Group	Software Tag
muon trigger	Muon	TrigMuonEfficiency-00-02-48
electron trigger	E/gamma	ElectronEfficiencyCorrection-00-00-50
jet reco	Jet/EtMiss	JetEffiProvider-00-00-05
electron reco	E/gamma	ElectronEfficiencyCorrection-00-00-50
muon reco	Muon	MuonEfficiencyCorrections-02-01-19-02

Table 8.3: Combined Performance (CP) groups and software tags for each efficiency correction

The uncertainty on these scale factors constitutes a systematic uncertainty on the final signal and background yields. Each efficiency correction is treated as a separate uncorrelated systematic. To estimate the effect of these systematics the full event selection is applied using the nominal values of the scale factors and using the scale factors shifted up and down by one standard deviation.

8.1.2 Object Scales and Resolutions

The energy of final state objects measured in the detector can deviate significantly from the energy of the underlying particles that produced them. The detector aims to accurately measure the energy or momentum of the particle. However for a variety of reasons there can be a mismatch between the measured energy and the true energy of the particle. Despite this mismatch the measured energy is found to be proportional to the true energy and so must be calibrated to agree with it. This is generally done by comparing the true energy to the reconstructed energy for MC simulated events and producing calibration factors. In addition to these calibration factors measured in MC simulated events, *in situ* techniques are applied to data to assess the difference in the detector response in data and MC simulation. The calibration factors measured in MC simulation are applied directly to the MC signal and background samples. The calibration factors measured in MC simulation and then corrected with *in situ* data-driven techniques are applied to the data. The uncertainty in the difference between the calibration factors applied to the MC samples and data introduces a systematic uncertainty on the final event yields.

The largest object scale systematic is the Jet Energy Scale (JES). The reconstructed energy of a jet can deviate significantly from the energy of the underlying parton (quark or gluon) that produces it. The effects that contribute to this deviation include:

- Ratio of calorimeter response to electromagnetic showers and hadronic showers e/h is >1 for non-compensating calorimeters. The mechanisms by which electrons, photons and hadrons interact in the calorimeter (described in Section 3.2.3) are very different. Hadrons interact with nuclei in the calorimeter material often breaking them up into smaller nuclei. The energy expending by the incident particle in breaking up these nuclei is not recovered by the calorimeter and thus is missing from the reconstructed energy.

- Energy lost in un-instrumented regions of the detector (dead material)

- Loss of energy deposits from part of the shower which falls outside the calorimeter (leakage, punch through)
- Energy deposits in the calorimeter due to processes other than the hard scatter of interest, including the underlying event, multiple parton-parton interactions and pile-up.
- Detector and electronic noise
- The fraction of the jet energy excluded due to the finite size of the jet (out-of-cone corrections)

ATLAS uses a calibration scheme that applies η and p_{T} dependent JES correction factors to restore on average the measured jet energy to its initial value. The methods used to evaluate the JES uncertainty are described in detail in Ref. [138]. The correction factors are measured in MC simulation and then a residual JES correction is applied to account for differences between MC simulation and data. This correction and its systematic uncertainty are evaluated in bins of jet η and p_{T}. They are estimated using a combination of *in situ* techniques exploiting the transverse momentum balance between a jet and a reference object such as a photon or Z boson. The effect of multiple parton-parton interactions is corrected for and an uncertainty is evaluated using *in situ* techniques. The JES uncertainty is shown as a function of p_{T}^{jet} and η in Fig. 8.1. The values of the JES uncertainty are given for a number of p_{T}^{jet} and η bins in Table 8.4.

In addition to the energy scale of final state objects the difference between the object energy resolution in MC simulation and data introduces another systematic uncertainty. As with energy scale systematics the largest energy resolution systematic is the Jet Energy Resolution (JER). Compared to electromagnetic objects, jets usually have a much poorer resolution due to large shower-by-shower fluctuations in their hadronic showers referred to as intrinsic fluctuations. The energy deposited by jets in the calorimeter is split into two parts:

$$E_{dep} = E_{dep}^{EM} + E_{dep}^{had}$$

E_{dep}^{EM} is the energy deposited in the electromagnetic shower within the jet due to the presence of neutral pions and photons. E_{dep}^{had} is the energy deposited in the hadronic shower within the jet. It arises from strong interactions between hadrons in the jet and nuclei in the calorimeter and is subject to large fluctuations compared to E_{dep}^{EM}. These fluctuations derive in part from the fact that not all of E_{dep}^{had} is visible in the calorimeter. Some fraction of this energy is lost to nuclear binding energy in breaking up nuclei in the calorimeter. This fraction varies from shower to shower and thus contributes to the intrinsic fluctuations mentioned above.

Measurements of jet energy in MC simulation and data show that the JER is poorer in data. This results from the failure of the detector simulation to adequately simulate the intrinsic fluctuations of hadronic showers. To correct for this the energy of jets in MC simulation is smeared with the difference between JER in data and MC simulation. The smearing is done with a Gaussian distribution with standard deviation:

$$\sigma_{smear} = \sqrt{(\sigma_{MC} + \Delta\sigma)^2 - \sigma_{MC}^2}$$

The value of σ_{smear} is determined with *in situ* measurements and is subject to uncertainty. This uncertainty gives rise to the a systematic uncertainty in the event yields for the MC samples. The smeared MC samples are used for physics analysis and the difference between the smeared and unsmeared samples is used to determine the systematic uncertainty. The full analysis selection is applied to both sets of samples producing a nominal and a smeared yield for each MC signal and background sample for each SR category. For the purposes of limit setting where three values are needed to determine the prior for each systematic $\pi(\nu_j)$ (x_{nom}, x_{up} and x_{down}, see Section 9.1) the smeared value is symmetrized to produce x_{up} and x_{down} ($x_{\text{nom}} \pm x_{smear}$).

In addition to the JES and JER described here, object scale and resolution systematics are also evaluated for electrons and muons. However these systematics are small compared to JES and JER.

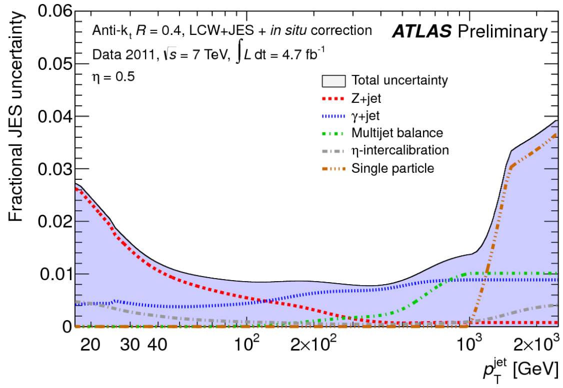

(a) $\eta = 0.5$

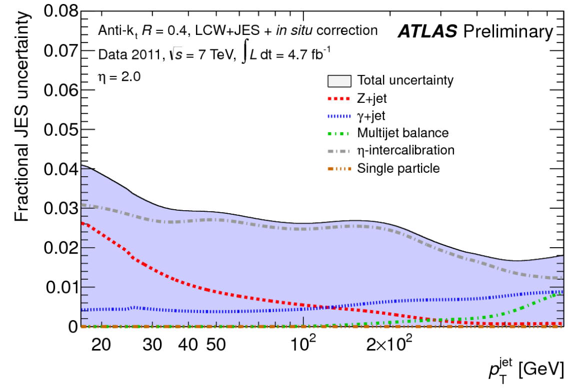

(b) $\eta = 2.0$

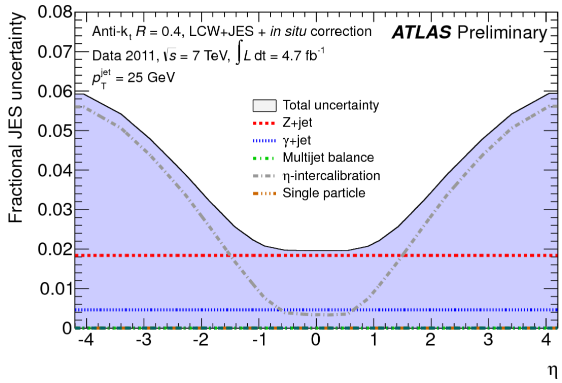

(c) $p_{\mathrm{T}}^{jet} = 25$ GeV

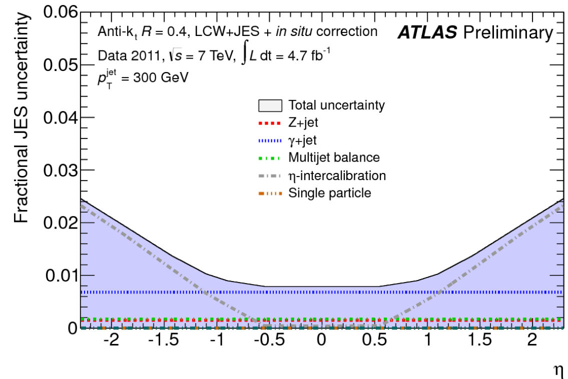

(d) $p_{\mathrm{T}}^{jet} = 300$ GeV

Figure 8.1: Fractional *in situ* jet energy scale systematic uncertainty as a function of p_{T} (8.1a, 8.1a) and jet pseudorapidity (8.1c, 8.1d) for anti-k$_t$ jets with distance parameter of R = 0.4 calibrated using the LCW+JES calibration scheme. The contributions from each *in situ* method are shown separately. [138]

$\|\eta\|$ region	Fractional JES uncertainty				
	p_T^{jet} = 20 GeV	p_T^{jet} = 40 GeV	p_T^{jet} = 200 GeV	p_T^{jet} = 800 GeV	p_T^{jet} = 1.5 TeV
$\|\eta\| = 0.1$	2.4%	1.2%	0.8%	1.3%	3.2%
$\|\eta\| = 0.5$	2.5%	1.2%	0.8%	1.3%	3.2%
$\|\eta\| = 1.0$	2.6%	1.4%	1.1%	1.3%	3.2%
$\|\eta\| = 1.5$	3.1%	2.1%	1.7%	1.4%	3.3%
$\|\eta\| = 2.0$	3.9%	2.9%	2.6%	1.8%	
$\|\eta\| = 2.5$	4.6%	3.9%	3.4%		
$\|\eta\| = 3.0$	5.2%	4.6%	3.9%		
$\|\eta\| = 3.5$	5.8%	5.2%	4.5%		
$\|\eta\| = 4.0$	6.2%	5.5%	5.1%		

Table 8.4: Summary of *in situ* LCW+JES jet energy scale systematic uncertainty for different p_T^{jet} and η values for anti-k$_t$ jets with R = 0.4. These values do not include pile-up, flavor or topology uncertainties. [138]

8.1.3 B-tagging Uncertainties

The uncertainties for the calibration scale factors for the b-tagging efficiency, c-jet mistag rate and light jet rejection rate are shown in Fig. 5.5 - 5.7. These uncertainties give rise to a systematic uncertainty on the selection efficiency and in turn on the signal and background MC yields. A separate systematic is evaluated for each of these three sets of scale factors. For each, the scale factors are varied by $\pm\sigma$ and the systematic is taken as the fractional change in the event yield. The largest effect is from the variation of the b-tagging scale factors.

8.1.4 Luminosity and Production Cross Sections

The integrated luminosity of the data set used for this analysis is 20.3 fb^{-1}. This is determined with the LumiCalc tool [97] and depends on the triggers used for the analysis, the GoodRunsList (GRL) recommended by the Top Working Group, and the instantaneous luminosity measured per LumiBlock for each run. The measurement of instantaneous luminosity is described in Section 4.1 and in further detail in [96]. It is determined by measuring the inelastic event rate at the interaction point. A variety of different detectors and counting algorithms are used and the results are compared in order to estimate the experimental uncertainty. This uncertainty leads to a systematic uncertainty on the integrated luminosity and the event yields. The method used to determine the systematic uncertainty on the yields follows that described in [139]. For the ATLAS 2012 data set the systematic uncertainty derived from the uncertainty on the integrated luminosity is 2.8%.

Theoretical uncertainties on the background cross-sections arise from a variety of sources. The factors that contribute to this uncertainty are the normalization and factorization mass scales, the modeling of initial and final state radiation (ISR/FSR), the parton distribution functions (PDFs) and higher order corrections in perturbation theory. [21] These parameters are varied in order to estimate the effect that their uncertainty can have on the event yields. The cross-section uncertainties for each of the backgrounds considered in this analysis are summarized in Table 8.5. The details of the calculation of the systematic uncertainty for the cross-section of the leading irreducible background $t\bar{t}W/Z$ are given in Section 8.2. The calculations for the other irreducible backgrounds are detailed in the references given in Table 8.5.

Table 8.5: Summary of the Monte Carlo backgrounds production cross section systematic uncertainties.. [110]

Background	Variations		Comment
$t\bar{t}W/Z$	−43%	+43%	see details in Section 8.2
$t\bar{t}H$	−10%	+10%	conservative estimate from [129, 130]
$t\bar{t}W^+W^-$	−26%	+38%	estimate from MadGraph (scales variation)
WZ/ZZ	−30%	+30%	conservative estimate using dedicated study with VBFNLO for high multiplicity events [140]
WH/ZH	−10%	+10%	conservative estimate from [130]
$W^{\pm}W^{\pm}$jj	−25%	+25%	estimate from MadGraph (scales variation)
VVV	−10%	+10%	conservative estimate from [141]
tH	−10%	+10%	conservative estimate from [142]
tWZ	−10%	+10%	conservative estimate from [143]

[21] See Section 2 for a discussion of perturbation theory in Quantum Field Theory

8.1.5 PDF Uncertainties

In addition to affecting the cross-section measurement, varying the PDF can also affect the distributions of events in a number of kinematic variables. This can affect the selection efficiency since the signal region is defined by placing cuts on these variables. The evaluation of the systematic uncertainty resulting from this is done by generating additional samples with three NLO PDF sets: `NNPDF23_nlo_as_119`, `CT10` and `MSTW2008NLO2008`. The uncertainty is estimated according to the TopPDFUncertainty page recommendations, varying the intra-PDF and inter-PDF uncertainties. The resulting deviations form an envelope which is taken as the amplitude of the systematic uncertainty [144]. The amplitude of the systematic uncertainty is corrected to account only for acceptance effects.

8.2 Determination of the systematic uncertainty for the $t\bar{t}W/Z$ background

Following the same procedure as the same-sign dilepton SUSY analysis [145], the total systematic uncertainty on the production cross section of the $t\bar{t}W$ and $t\bar{t}Z$ processes is determined from four sources: theoretical uncertainty, shape uncertainty, parton shower modeling, alternate MC generators. The various contributions and the global uncertainty are given in Table 8.6. The uncertainty on the yield is evaluated separately for each SR category. The largest of these is taken as the systematic applied across all SR categories. This leads to a conservative estimate of 43%.

8.2.1 Theoretical uncertainty

From the theoretical NLO predictions of [127, 128], the systematic uncertainty on the production cross section is 22%, largely dominated by the scale variations (see Appendix L of [145]).

8.2.2 Shape uncertainty

Since MadGraph is an LO generator, its shape uncertainty is estimated by varying the generator parameters. An extensive study performed by the SUSY group (see

Table 8.6: Systematic uncertainties (in %) from the various sources for each SR category. The sum in quadrature is shown in the last column. The "Worst case" corresponds to the conservative estimate, taking the largest contribution from each source. [110]

Region	Theory	Shape	Parton shower	Generators			Total
				Alt. MG	Alpgen	Final	
SRVLQ0	22	3.8	2.5	23	0.9	23	32
SRVLQ1	22	2.1	2.7	14	2.5	14	26
SRVLQ2	22	9.2	7.0	7.3	13	13	28
SRVLQ3	22	9.4	5.5	27	12	27	36
SRVLQ4	22	9.4	< 0.1	7.1	6.2	7.1	25
SRVLQ5	22	11	1.3	22	17	22	33
SRVLQ6	22	11	0	3.0	34	34	42
SRVLQ7	22	13	7.8	3.7	4.1	4.1	27
Worst case SRVLQ	22	13	7.8			34	43

Appendix L of [145]) concluded that, by far, the dominant uncertainty comes from the variation of ISR. Therefore, only these samples were used in estimating the uncertainty (DSID 176897, 176905 and 176913 for the $t\bar{t}W$ with ISR up; 176921, 176929 and 176937 for the $t\bar{t}Z$ with ISR up; 176898, 176906 and 176914 for the $t\bar{t}W$ with ISR down; 176922, 176930 and 176938 for $t\bar{t}Z$ with ISR down). Only NTUP_TRUTH samples are available, thus the full analysis is not possible with these varied samples. The estimate is then based on a similar selection as the analysis but only on the truth particles, still performing the same object selection (cuts on p_{T} and η, overlap removals) and applying weights to take into account the 70% efficiency on b-jets. The cuts on $E_{\mathrm{T}}^{\mathrm{miss}}$ which are part of the definition of the SR categories in Table 6.3 are not applied in this study. This is because there was no good definition of $E_{\mathrm{T}}^{\mathrm{miss}}$ in the MC samples.

The basic selection requires the presence of at least three leptons or two leptons with the same electric charge, and at least two jets. For SR categories 0-2, we require 400 GeV$< H_{\mathrm{T}} <$ 700 GeV. For SR categories 3-7, the cut is $H_{\mathrm{T}}>$ 700 GeV. Since there are no cuts on $E_{\mathrm{T}}^{\mathrm{miss}}$, SR categories 3 and 4 have the same estimate, as do 5 and 6. The variation observed in each SR category is shown in Table 8.6. The largest one is 13%, which is consistent with the 12% value observed in the SUSY analysis.

8.2.3 Parton shower modeling

The default $t\bar{t}W/Z$ simulated samples used in the analysis (see Table 4.2) are split into three sub-samples: $t\bar{t}V + 0$ parton exclusive, $t\bar{t}V + 1$ parton exclusive and $t\bar{t}V + 2$ partons inclusive. In order to take into account variations in the parton shower modeling, an alternative estimate is performed replacing the $t\bar{t}V + 1$ parton exclusive and $t\bar{t}V + 2$ partons inclusive samples by a $t\bar{t}V + 1$ parton inclusive sample (DSID 119354 for $t\bar{t}W$ and 119356 for $t\bar{t}Z$). The difference between the two estimates is taken as a systematic uncertainty and is shown in Table 8.6 for each SR category.

8.2.4 Difference between several generators

Three different $t\bar{t}W/Z$ simulated samples are available: the nominal one has been produced with MadGraph, while an Alpgen set and an alternative MadGraph set can be used. Differences between the alternative samples and the nominal ones are shown in Table 8.6 for each SR category. The final value is taken as the largest difference in each region.

The complete list of $t\bar{t}W/Z$ MC samples used is shown in Table 8.7. The nominal MadGraph samples have been generated with on-shell Z bosons, including up to two additional partons at the MadGraph level, but excluding b quarks. Therefore, additional $b\bar{b}$ pairs may be present in the final state, but only coming from gluon splitting at the Pythia level. In the alternative MadGraph samples, the top quarks and the W and Z bosons are decayed within MadGraph. Moreover, the additional parton for the samples 117488 and 117490 may be a b quark. For the alternative Alpgen samples, up to three additional partons are included at the Alpgen level, but they do not include b quarks. Moreover, the statistics of $t\bar{t}W$ Alpgen samples is roughly ten times smaller than the MadGraph samples.

Table 8.7: Monte Carlo samples used for the $t\bar{t}W/Z$ background estimation (ℓ means any kind of charged lepton). The sample identifier is the sample number in the ATLAS production. The K-factor is the rescaling factor between LO and NLO cross sections. $\mathcal{L}$ is the integrated luminosity corresponding to each sample, in fb^{-1}.

Sample	Process	Generator	Cross-section [pb]	K-factor	$\mathcal{L}$ [fb^{-1}]
Nominal MadGraph samples					
119353	$t\bar{t}W$	MadGraph+Pythia	0.104	1.17	3284
174830	$t\bar{t}W$+j	MadGraph+Pythia	0.053	1.17	6404
174831	$t\bar{t}W$+jj (incl.)	MadGraph+Pythia	0.041	1.17	8237
119355	$t\bar{t}Z$	MadGraph+Pythia	0.068	1.35	4377
174832	$t\bar{t}Z$+j	MadGraph+Pythia	0.045	1.35	6532
174833	$t\bar{t}Z$+jj (incl.)	MadGraph+Pythia	0.040	1.35	7446
Alternative MadGraph samples (with single lepton filter)					
117487	$t\bar{t}W$	MadGraph+Pythia	0.072	1.29	5405
117488	$t\bar{t}W$+j/b (incl.)	MadGraph+Pythia	0.062	1.29	6249
117489	$t\bar{t}Z$ ($Z \to \nu\bar{\nu}, q\bar{q}$), $t\bar{t}\ell^+\ell^-$	MadGraph+Pythia	0.048	1.40	7410
117490	$t\bar{t}\ell^+\ell^-$+j/b (incl.)	MadGraph+Pythia	0.013	1.40	5692
Alternative Alpgen samples					
174233	$t\bar{t}W$ ($W \to \ell\nu$)+Np0	Alpgen+Herwig	0.027	1.0	556.5
174234	$t\bar{t}W$ ($W \to \ell\nu$)+Np1	Alpgen+Herwig	0.018	1.0	543.4
174235	$t\bar{t}W$ ($W \to \ell\nu$)+Np2	Alpgen+Herwig	0.0095	1.0	528.4
174236	$t\bar{t}W$ ($W \to \ell\nu$)+Np3 (incl.)	Alpgen+Herwig	0.0065	1.0	459.4
174248	$t\bar{t}Z$ ($Z \to \ell^+\ell^-$)+Np0	Alpgen+Herwig	0.0080	1.0	6275
174249	$t\bar{t}Z$ ($Z \to \ell^+\ell^-$)+Np1	Alpgen+Herwig	0.0077	1.0	5846
174250	$t\bar{t}Z$ ($Z \to \ell^+\ell^-$)+Np2	Alpgen+Herwig	0.0052	1.0	5519
174251	$t\bar{t}Z$ ($Z \to \ell^+\ell^-$)+Np3 (incl.)	Alpgen+Herwig	0.0039	1.0	5641

8.3 Uncertainties on Data-Driven Backgrounds

Table 8.1 shows that for most of the SR categories the leading systematic uncertainties are those associated with the data driven backgrounds. The estimation of the systematic uncertainty on the fake/non-prompt lepton and the electron charge misid backgrounds are described in the following section.

8.3.1 Fake/Non-Prompt Lepton Background

The systematic uncertainty on the fake/non-prompt lepton background derives from the uncertainties on the real and fake efficiencies used in the matrix method to calculate fake weights. These efficiencies represent the probability that a real or fake lepton which passes the loose lepton definition will also pass the tight lepton definition. Three sources of uncertainty in the calculation of the efficiencies were considered:

i) choice of the real and fake enriched control regions used to measure them

ii) MC model used to subtract events with real leptons from the fake/non-prompt control region

iii) limited statistics in the control regions

To assess the effect of *i*), fakes yields are estimated using efficiencies measured in alternate real and fake control regions. These yields are then compared to the yields produced with the nominal efficiencies and the difference is taken as the systematic. The real and fake control regions used for measuring the efficiencies in the analysis are described in Section 7.2.1. In the following these regions are referred to as the nominal control regions. For electrons the alternate real control region is defined as having $E_{\mathrm{T}}^{\mathrm{miss}} > 175$ GeV, while the alternate fake control region is defined as having $E_{\mathrm{T}}^{\mathrm{miss}} < 20$ GeV. For muons the alternate real control region has $m_W^T > 110$ GeV, while the alternate fake control region has $m_W^T < 20$ GeV and $m_W^T + E_{\mathrm{T}}^{\mathrm{miss}} < 60$ GeV. The $E_{\mathrm{T}}^{\mathrm{miss}}$ and m_W^T cuts used for the alternate real control regions must be increased with respect to the nominal control regions as any decrease would allow a non-negligible number of events containing fake/non-prompt leptons to enter the region. The increased cut values were chosen so that the alternate real control regions would contain half the number of events in the nominal control regions. Effect *ii*) is accounted for by remeasuring the efficiencies after varying the normalization of the MC samples used for the subtraction up and down by 10%. As for effect *i*), the yields calculated with these efficiencies are compared to the nominal yields to estimate the systematic. Effect *iii*) is dealt with by dividing each control region up into four equal subregions and calculating efficiencies and yields separately in each subregion. The standard deviation of these four yield values divided by two is taken as the systematic for this effect. The factor of one half is included since there are approximately four times as many events in the nominal control regions as in each of the subregions.

Figures 8.2 - 8.7 show how the efficiencies for electrons and muons vary due to effects *i*) and *ii*). The use of alternate fake control regions has the largest effect on the value of the efficiencies for both electrons and muons. The magnitude of each component of the systematic uncertainty depends on the specific selection applied. In control regions such as the high H_{T}+1b region the leading systematic is that due to effect *i*) which is $\sim 30\%$ while the others are at the few percent level. In our signal region the overall systematic uncertainty is much larger. The overall systematic shift for each SR category is shown in Table 8.8. The large systematic uncertainty there is caused by reduced statistics in the signal region and possible differences between the efficiencies in the control regions, where they are measured, and the signal regions, where they are applied. The reduced statistics means that leptons which happen to fall into bins of the efficiency plots with atypically large variations can significantly impact the shift in yield. To mitigate the problem of low statistics SR categories with similar characteristics are combined to form larger subsets of the full signal region where the systematics are reevaluated. The systematic uncertainty in these regions is shown in Table 8.9. The values range from $\sim 50\%$ to 70%. Based on the variations seen in these combined regions a flat conservative value of 70% is taken for the fake/non-prompt systematic across all SR categories.

Section 7.2.1.2 describes a study that was carried out to assess the effect of differences between the efficiencies in the control regions where they were measured and the signal regions. In the study efficiencies were measured in the same control regions as in the analysis in MC simulation and applied to estimate the fake/non-prompt lepton estimate in the same SR categories as in the analysis for an MC $t\bar{t}$ sample. The fake/non-prompt lepton estimate from the matrix method was then compared to the fake/non-prompt lepton background from truth information. The study concluded that they agree within the 70% systematic uncertainty assigned to the fake/non-prompt lepton estimation.

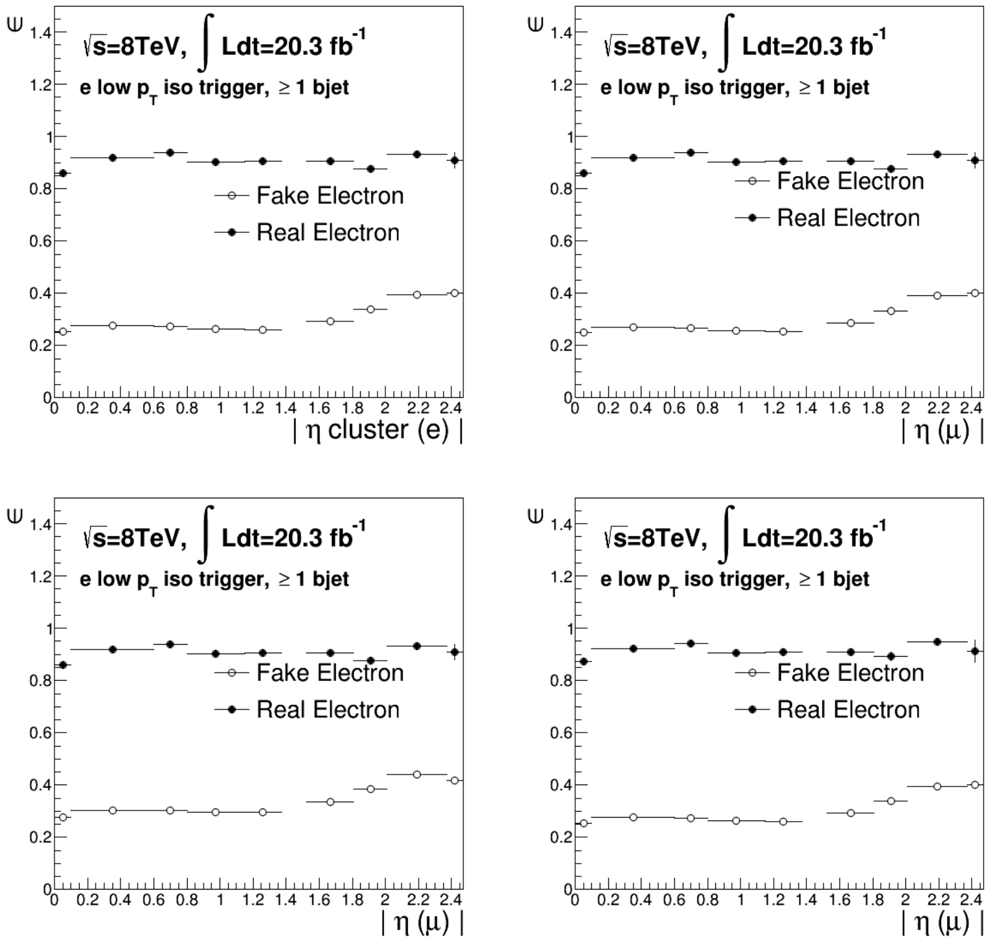

Figure 8.2: Electron real and fake efficiencies for electrons that match the low-p_{T} trigger EF_e24vhi_medium1, parameterized as a function of the electron η. The upper left plot is the default, the upper right plot shows the effect of increasing the MC normalization to remove real electrons from the fake/non-prompt control region, the lower left shows efficiencies calculated using the alternate fake/non-prompt control region, and the lower right shows efficiencies calculated using the alternate real control region. [110]

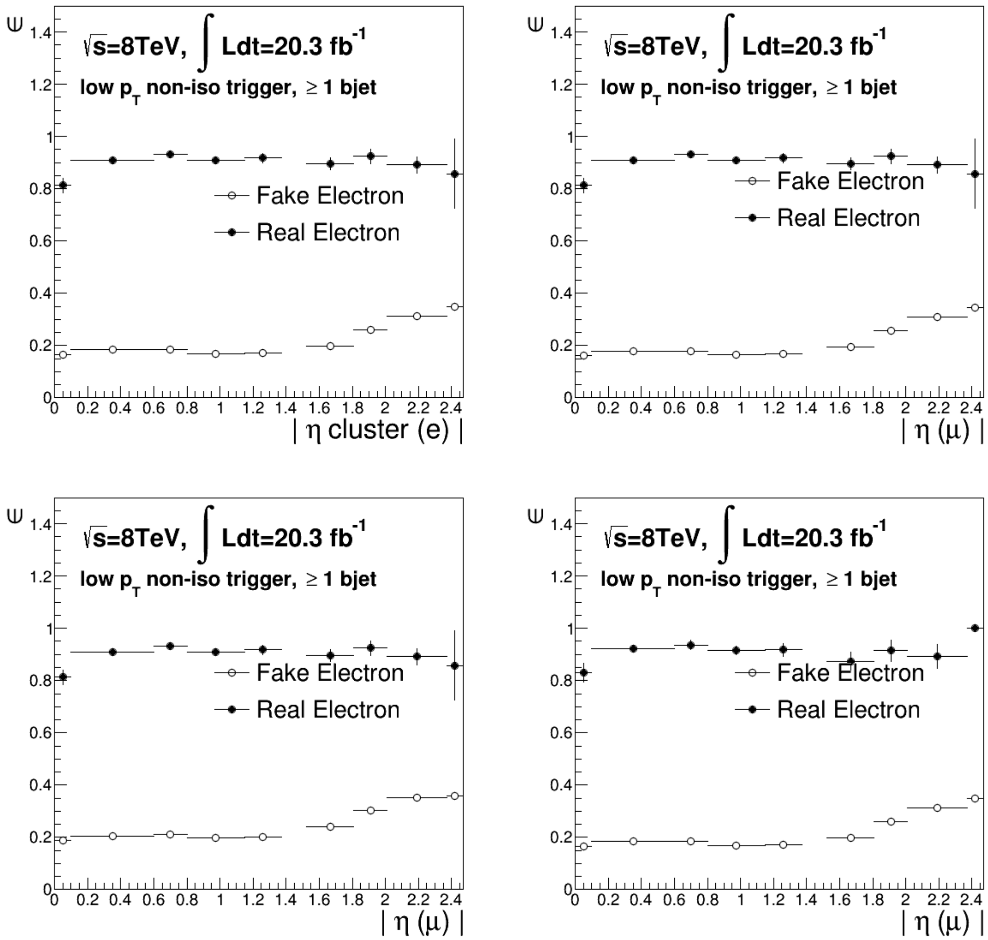

Figure 8.3: Electron real and fake efficiencies for electrons that match the prescaled low-p_{T} trigger `EF_e24vh_medium1`, parameterized as a function of the electron η. The upper left plot is the default, the upper right plot shows the effect of increasing the MC normalization to remove real electrons from the fake/non-prompt control region, the lower left shows efficiencies calculated using the alternate fake/non-prompt control region, and the lower right shows efficiencies calculated using the alternate real control region. [110]

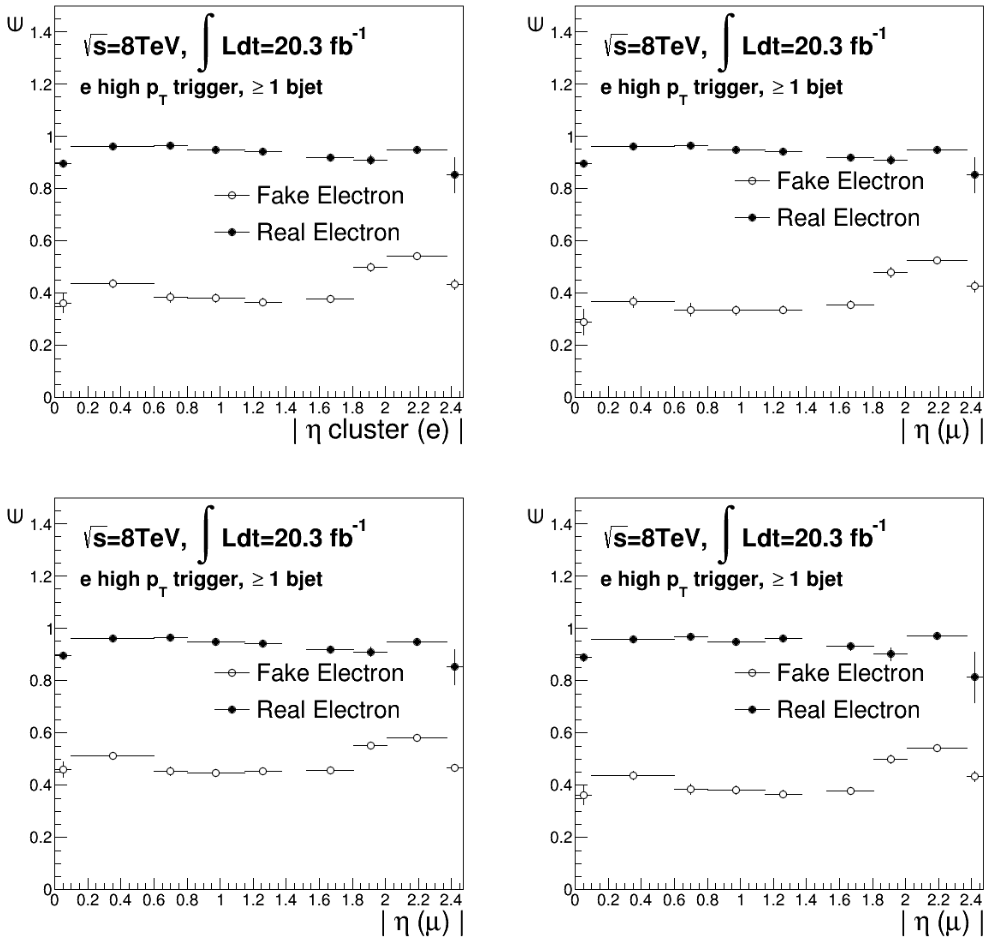

Figure 8.4: Electron real and fake efficiencies for electrons that match the high-p_{T} trigger `EF_e60_medium1`, parameterized as a function of the electron η. The upper left plot is the default, the upper right plot shows the effect of increasing the MC normalization to remove real electrons from the fake/non-prompt control region, the lower left shows efficiencies calculated using the alternate fake/non-prompt control region, and the lower right shows efficiencies calculated using the alternate real control region. [110]

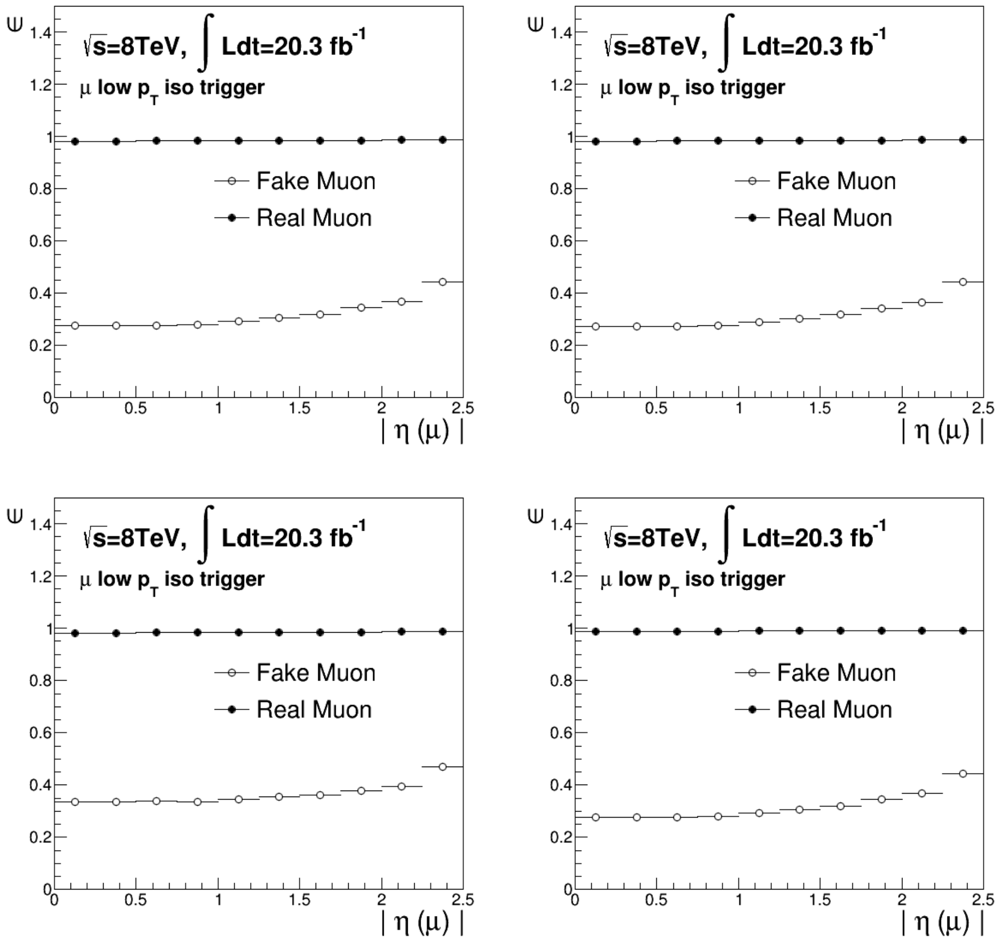

Figure 8.5: Muon real and fake efficiencies for muons that match the low-p_{T} trigger `EF_mu24i_tight`, parameterized as a function of the muon η. The upper left plot is the default, the upper right plot shows the effect of increasing the MC normalization to remove real muons from the fake/non-prompt control region, the lower left shows efficiencies calculated using the alternate fake/non-prompt control region, and the lower right shows efficiencies calculated using the alternate real control region. [110]

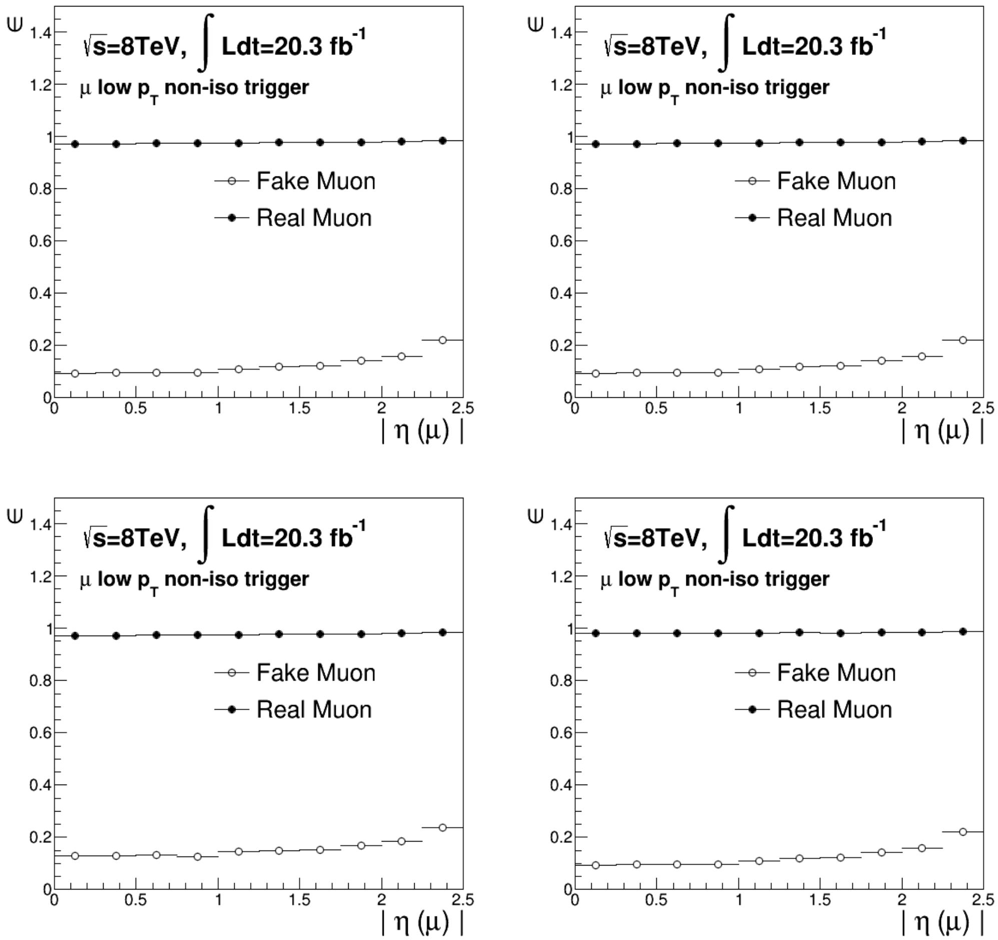

Figure 8.6: Muon real and fake efficiencies for muons that match the prescaled low-p_{T} trigger `EF_mu24_tight`, parameterized as a function of the muon η. The upper left plot is the default, the upper right plot shows the effect of increasing the MC normalization to remove real muons from the fake/non-prompt control region, the lower left shows efficiencies calculated using the alternate fake/non-prompt control region, and the lower right shows efficiencies calculated using the alternate real control region. [110]

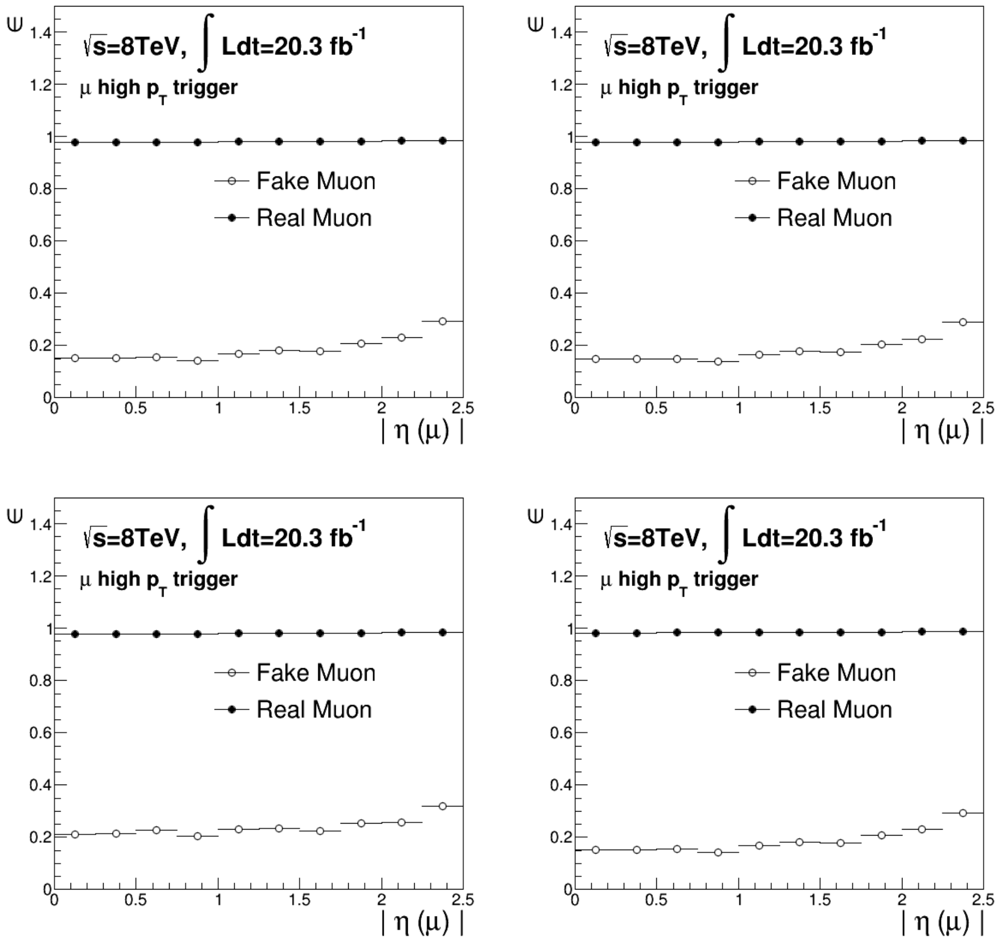

Figure 8.7: Muon real and fake efficiencies for muons that match the high-p_{T} trigger `EF_mu36_tight`, parameterized as a function of the muon η. The upper left plot is the default, the upper right plot shows the effect of increasing the MC normalization to remove real muons from the fake/non-prompt control region, the lower left shows efficiencies calculated using the alternate fake/non-prompt control region, and the lower right shows efficiencies calculated using the alternate real control region. [110]

Table 8.8: Systematic uncertainties on the fake/non-prompt yield obtained from applying the procedure described in the text to each signal region. A fractional uncertainty cannot be assigned in SRVLQ6/4t3 since the central value of the estimated yield is zero. [110]

Signal region	Fake/non-prompt uncertainty (%)
SRVLQ0	+51/-48
SRVLQ1/4t0	±66
SRVLQ2/4t1	±62
SRVLQ3	+69/-70
SRVLQ4	±57
SRVLQ5/4t2	+105/-103
SRVLQ6/4t3	–
SRVLQ7/4t4	+200/-195

Table 8.9: Systematic uncertainties on the fake/non-prompt yield obtained from applying the procedure described in the text to signal regions combined according to their requirements on H_{T} and the number of b-tagged jets. [110]

Signal region characteristic	Fake/non-prompt uncertainty (%)
$H_{\mathrm{T}} < 700$ GeV	±53
$H_{\mathrm{T}} > 700$ GeV	±65
Exactly 1 b-tagged jet	±52
Exactly 2 b-tagged jets	±69
≥ 2 b-tagged jets	+68/-67
≥ 3 b-tagged jets	±57

8.3.2 Electron Charge Mis-Identification Background

The systematic uncertainty on the charge mis-identification background is calculated by shifting the charge misid rate for each η-p_{T} bin ($\epsilon(\eta{,}p_{\mathrm{T}})$) up and down by $\sigma_{\epsilon}(\eta{,}p_{\mathrm{T}})$ and comparing the charge misid yields in each case to the yield calculated with the nominal values of $\epsilon(\eta{,}p_{\mathrm{T}})$. The rate uncertainty is the quadratic sum of six different contributions:

- the statistical uncertainty on the charge misid rates from the likelihood method $\sigma_{\varepsilon}^{likelihood}(|\eta|, p_{\mathrm{T}}) \times \alpha_{t\bar{t}}(|\eta|, p_{\mathrm{T}})$,

- the statistical uncertainty on the p_{T} dependent correction factor $\varepsilon^{likelihood}(|\eta|, p_{\mathrm{T}}) \times \sigma_{\alpha_{t\bar{t}}}(|\eta|, p_{\mathrm{T}})$. This uncertainty only affects the region where the electron $p_{\mathrm{T}} > 100$ GeV.

- the difference between the rates measured with the 2D likelihood method and truth-matching on simulated $Z \to e^+e^-$ events,

- half of the difference between the true rates measured for electrons and positrons. This uncertainty is taken into account only in the $(|\eta|, p_{\mathrm{T}})$ configurations where the ratio on these rates is not compatible with one within uncertainties,

- the variation of the rates due to the variation of the Z peak region definition when the background is extracted. In this case, the different regions have been variated by 1σ,

- the difference on the correction factor using different simulated $t\bar{t}$ samples (MC@NLO+Herwig instead of POWHEG+Pythia). The uncertainty is taken into account only in the $(|\eta|, p_{\mathrm{T}})$ configurations where the ratio on the different correction factors is not compatible with one within uncertainties. It affects only the region where the electron $p_{\mathrm{T}} > 100$ GeV.

The contributions from each source are shown in Fig. 8.8. The total systematic uncertainty on the rates are given for each η-p_{T} bin in Table 8.10. The combination of all six of these effects leads to a total systematic uncertainty on the charge misid yields of approximately 26-45% depending on the SR category.

An additional systematic is introduced because of the removal of the fake/non-prompt lepton background from the $Z \to ee$ events that are used to measure the charge misid rates. The uncertainty on the fake/non-prompt lepton background that is subtracted from the Z peak region leads to an uncertainty on the measured charge misid rates and ultimately on the charge misid yields. This uncertainty is evaluated by varying the fake/non-prompt lepton background in the Z peak region according to the three sources of uncertainty *i*)-*iii*) described in the previous section.

Table 8.10: Charge mis-identification rates (in %) as a function of $|\eta|$ and p_{T}. The uncertainty is the total systematic uncertainty on the rates, without taking into account the effect from the overlap removal. [110]

	p_{T} range				
$\vert\eta\vert$ range	$[0, 50]$ GeV	$[50, 80]$ GeV	$[80, 100]$ GeV	$[100, 200]$ GeV	$[200, 1000]$ GeV
$[0, 0.8]$	0.0565 ± 0.0104	0.0708 ± 0.0171	0.178 ± 0.067	0.240 ± 0.103	0.427 ± 0.24
$[0.8, 1.1]$	0.0909 ± 0.0305	0.2 ± 0.0563	0.739 ± 0.183	0.869 ± 0.335	1.68 ± 0.58
$[1.1, 1.37]$	0.250 ± 0.051	0.162 ± 0.0474	0.552 ± 0.194	0.660 ± 0.294	0.686 ± 1.004
$[1.52, 1.8]$	0.844 ± 0.060	0.87 ± 0.104	1.95 ± 0.37	2.66 ± 0.780	3.03 ± 3.66
$[1.8, 2.3]$	1.28 ± 0.058	01.55 ± 0.150	3.93 ± 0.44	4.67 ± 0.58	5.5 ± 3.9
$[2.3, 2.6]$	3.15 ± 0.178	3.49 ± 0.31	5.30 ± 1.23	6.06 ± 1.27	12.3 ± 4.8

Tables 8.11 and 8.12 show the charge misid rates measured with the fake/non-prompt lepton background varied up and down by these three effects. The final systematic uncertainty applied to the charge misid background to account for the fakes/non-prompt - charge misid overlap removal ranges from 5-6% depending on the SR category. Since an upward shift in the fakes/non-prompt lepton background would cause a downward shift in the charge misid background (since fewer events would be subtracted from the Z peak region) this systematic is anti-correlated with the 70% systematic uncertainty on the fakes/non-prompt lepton background.

Table 8.11: Charge mis-identification rates (in %) as a function $|\eta|$ and p_{T}, for the downward variation of the non-prompt/fakes background. [110]

	p_{T} range				
$\lvert\eta\rvert$ range	$[0, 50]$ GeV	$[50, 80]$ GeV	$[80, 100]$ GeV	$[100, 200]$ GeV	$[200, 1000]$ GeV
$[0, 0.8]$	0.0678	0.861	0.193	0.261	0.464
$[0.8, 1.1]$	0.104	0.215	0.763	0.898	1.74
$[1.1, 1.37]$	0.276	0.208	0.596	0.713	0.742
$[1.52, 1.8]$	0.917	1.01	1.96	2.67	3.05
$[1.8, 2.3]$	1.40	1.71	3.95	4.69	5.50
$[2.3, 2.6]$	3.32	3.89	5.43	6.20	12.6

Table 8.12: Charge mis-identification rates (in %) as a function $|\eta|$ and p_{T}, for the upward variation of the non-prompt/fakes background. [110]

	p_{T} range				
$\lvert\eta\rvert$ range	$[0, 50]$ GeV	$[50, 80]$ GeV	$[80, 100]$ GeV	$[100, 200]$ GeV	$[200, 1000]$ GeV
$[0, 0.8]$	0.0452	0.0555	0.162	0.219	0.390
$[0.8, 1.1]$	0.0774	0.185	0.714	0.840	1.63
$[1.1, 1.37]$	0.223	0.117	0.507	0.606	0.631
$[1.52, 1.8]$	0.771	0.732	1.94	2.64	3.01
$[1.8, 2.3]$	1.16	1.39	3.91	4.65	5.45
$[2.3, 2.6]$	2.98	3.09	5.18	5.92	12.0

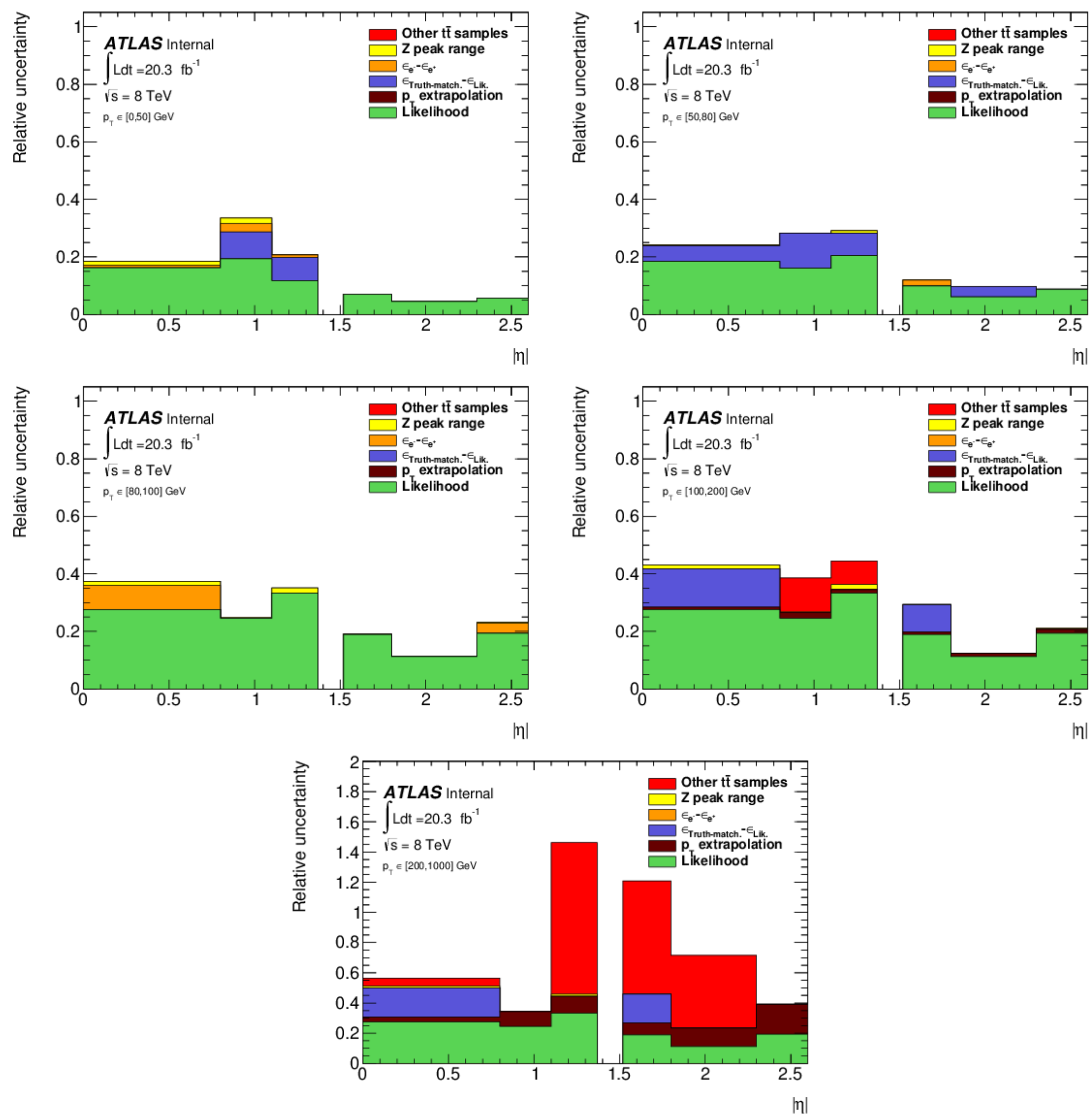

Figure 8.8: Relative systematic uncertainties contributions on the charge mis-identification rate, for different bins in p_{T} and $|\eta|$. [110]

CHAPTER 9

Results

9.1 Statistical Interpretation

Once the event selection defining the signal region has been determined, it is applied to data and to the signal and background MC simulations. The number of data events that pass the selection is then compared with the number of signal and background events that pass in order to test the consistency of the data with two hypotheses: the signal-plus-background hypothesis and the null, or background-only, hypothesis. From this comparison exclusion limits are produced that quantify the likelihood that the signal could exist.

If the number of data events is closer to the background-only expectation then it is more consistent with the null hypothesis and strong exclusion limits are set. Conversely, if it is closer to the signal-plus-background expectation weaker limits are set. In the latter case, the significance of the excess in data above the background-only expectation is used to interpret the results. If the significance is less than two standard deviations it may be the result of a fluctuation in data or the first sign of new physics. A significance of five standard deviations or greater is interpreted as a discovery of new physics. An intermediate significance between two and five standard deviations is inconclusive and requires more data to understand. Many searches in particle physics show no significant excess and lead to exclusion limits that rule out an increasingly large region of phase space for the new physics signal as more data is collected. Eventually the signal may be ruled out all together. Occasionally, analyses produce an excess which grows over time as more data is collected eventually leading to a discovery when the excess surpasses five standard deviations. What follows in this section is a description of the technique used for setting limits in this analysis, known as the CL_s method.

9.1.1 The CLs Method

The CL_s method is a modified frequentist model widely used in particle physics to set exclusion limits on new physics signals [146, 147]. It defines a test statistic (q) which is maximally different for the signal-plus-background and background-only hypotheses. The value of the test statistic is calculated from the events observed in data and compared with distributions of values calculated from a large number of pseudo-experiments. One set of pseudo-experiments assumes the signal-plus-background hypothesis while another assumes the background-only hypothesis. The test statistic chosen here, known as the Log Likelihood Ratio (LLR), is defined as:

$$q = LLR = -2 \ln \frac{\mathcal{L}(x \mid s+b)}{\mathcal{L}(x \mid b)} \tag{9.1}$$

where $\mathcal{L}$(x | s+b) and $\mathcal{L}$(x | b) are the likelihood functions for data (or the result of the pseudo-experiments) in each hypothesis. They are Poisson probability distributions with the mean taken as the signal-plus-background expectation and the background-only expectation respectively. The distributions are given by

$$\mathcal{L}(x \mid s+b) = \frac{e^{-(s+b)}(s+b)^x}{x!}$$

$$\mathcal{L}(x \mid b) = \frac{e^{-(b)}(b)^x}{x!}$$

where s and b are calculated with Eq. 6.1. If the signal region is made up of multiple channels, as in this analysis where it consists of the eight SR categories defined in Section 6.2, the likelihood functions become a product of the above expressions for each individual channel.

$$\mathcal{L}(x \mid s+b) = \prod_i \frac{e^{-(s_i+b_i)}(s_i+b_i)^{x_i}}{x_i!} \tag{9.2}$$
$$\mathcal{L}(x \mid b) = \prod_i \frac{e^{-(b_i)}(b_i)^{x_i}}{x_i!}$$

The observed LLR value is calculated from the above expression by setting x to the observed number of data events in each channel of the signal region. In addition, an LLR value is calculated for each pseudo-experiment by setting x to the observed number of events for that pseudo-experiment. This produces distributions of LLR values denoted f(q | s+b) and f(q | b) for the signal-plus-background and background-only hypotheses. In this notation the test statistic q is the LLR value. For values of x that are more consistent with the signal-plus-background hypothesis the likelihood ratio is greater than one and thus the LLR is negative. Similarly values of x that are more consistent with the background-only hypothesis are positive. An example of f(q | s+b) and f(q | b) as well as the observed LLR value for a vector-like bottom quark of mass 650 GeV is shown in Fig. 9.1.

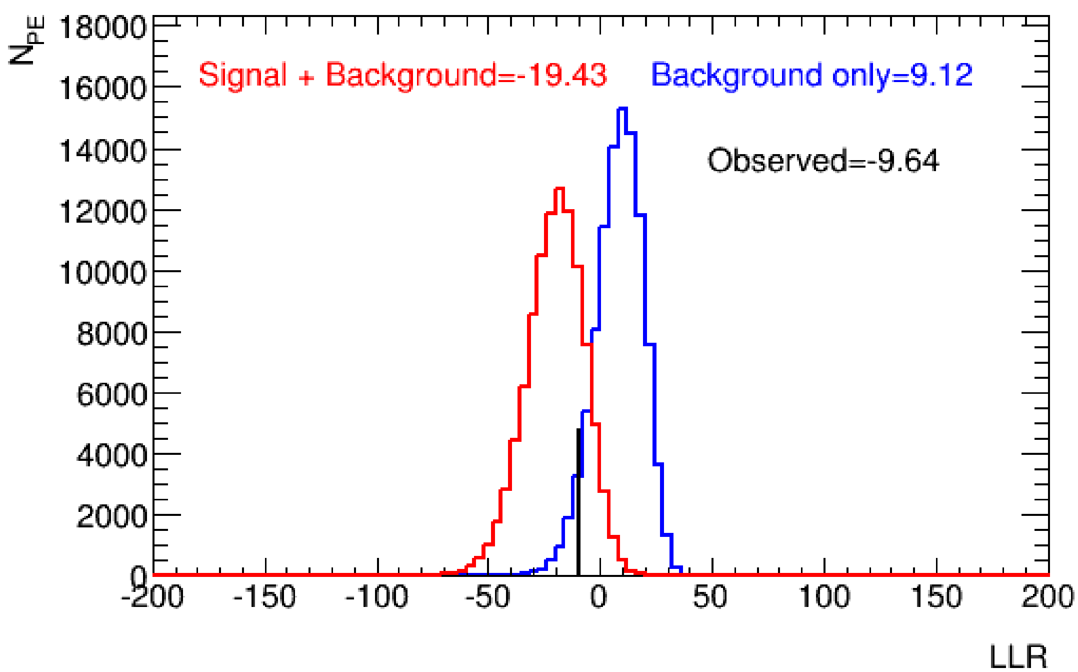

Figure 9.1: Distribution of LLR values for pseudo-experiments in the signal-plus-background and background-only hypotheses for a vector-like bottom with a mass of 650 GeV. For each hypothesis 100,000 pseudo-experiments are carried out. Also shown is the observed LLR value calculated using the observed number of data events in the signal region.

From the distributions of LLR values and the observed LLR value, p-values are defined which characterize the likelihood that each hypothesis could have produced the observed data. The p-values are defined as integrals of the LLR distributions for all values that show equal or lesser compatibility with the given hypothesis. These can be expressed as

$$p_{s+b} = \int_{q_{obs}}^{\infty} f(q \mid s+b) dq \tag{9.3}$$
$$p_b = \int_{-\infty}^{q_{obs}} f(q \mid b) dq$$

The CL_s value is then defined as the ratio

$$CL_s = \frac{p_{s+b}}{1 - p_b}$$

The signal-plus-background hypothesis is considered ruled out at the Confidence Level (CL) of 1 - α when $CL_s < \alpha$. By convention α is taken to be 0.05 corresponding to a CL of 95%.

In earlier versions of the method the upper bound was placed on p_{s+b} directly. This has been replaced by the current method which places the upper bound on the CL_s value. It is clear that to exclude the signal one should require p_{s+b} to be small as it represents the probability of obtaining the observed data under the signal-plus-background hypothesis. Placing the upper bound on the value of CL_s rather than p_{s+b} enforces the condition that both p_{s+b} and p_b are small. By requiring that p_b is small the method avoids excluding signals in analyses with low sensitivity when there is a downward fluctuation of the background. Many exotic searches are limited in the signal sensitivity they can achieve due to the small cross-section of signal compared to background. When this happens the distributions f(q | s+b) and f(q | b) are less separated and have large overlap. In this case a downward fluctuation of the background leads to a larger value for the observed LLR that can cause p_{s+b} to fall below 0.05. If the upper bound were placed on p_{s+b} itself rather than CL_s this signal would be excluded despite the low sensitivity of the search. We avoid this unwanted exclusion by using CL_s instead of p_{s+b}. Although p_{s+b} is small in this case, p_b is large. This drives up the value of CL_s making it more difficult to exclude a signal. Given that p_b is always greater than zero CL_s is always greater than p_{s+b}. This makes the CL_s method a more conservative technique for setting limits than its predecessor where only p_{s+b} was considered.

Typically the BSM theory being considered contains a number of free parameters that define a phase space within which the new particle may exist. In order to be exhaustive the search must consider the entire phase space. In practice this is done by dividing the phase space into bins defined by appropriate intervals of these free parameters and treating each bin as a separate signal. The CL_s method is applied within each bin to determine if the signal is excluded there. In this way, exclusion limits are set on the free parameters in the theory and regions of phase space are ruled out.

In most BSM theories, as in the Standard Model, the masses of the particles in the theory are free parameters and thus form part of the phase space that must be explored [22]. There are often constraints placed on the value of these masses using electroweak precision measurements. However they are not determined exactly by theory and so searches must be carried out over a large mass range. Depending on the specific VLQ model considered the number of free parameters is either one or three. In the VLQ Singlet Model the only free parameter is the VLQ mass. If we consider a broader range of models the branching ratios for the three allowed decay modes of VLQ are not fixed as they are in the Singlet Model. This is described in more detail in Chapter 2. Given the constraint that the branching ratios sum to one this adds another two free parameters to the phase space of the search.

The CL_s value as defined above can only be used to determine whether or not the signal is excluded at 95% CL. In order to calculate the 95% CL upper limit on the signal cross-section we must scale it by a factor μ and look at the dependence of the CL_s value on μ. This multiplies the right hand side of Eq. 6.1 by μ and changes the value of s that is used in the limit calculation. This shifts the LLR distributions

[22] The masses of SM particles are not predicted by theory and so prior to their discovery were unknown

for both the signal+background and background only hypotheses. The value of μ where CL_s crosses 0.05 is known as the signal strength. The 95% CL upper limit is the product of the signal strength and the theoretical signal cross-section.

$$\sigma_{95\%CL} = \mu \times \sigma_{th}$$

Signals for which $CL_s < 0.05$ with $\mu = 1$ are excluded. The signal strength for such signals is less than one meaning that the upper limit on the cross-section is less than the theoretical cross-section. Signals for which $CL_s > 0.05$ with $\mu = 1$ are not excluded. The signal strength in this case is greater than one meaning that the upper limit on the cross-section is greater than the theoretical cross-section. By calculating cross-section limits within each separate region of phase space we obtain more information about the signal there than simply determining whether or not it is excluded.

In addition to the observed limits, expected limits are calculated to show the limits that would be expected in the absence of signal. This provides a guideline for the observed limits that are the results of the search. If no excess is seen in data the observed limits should be at least as restrictive as the expected limits. Only when there is an excess do we see the observed and expected limits disagree beyond the level of about two standard deviations. In the case of a discovery one should see the observed limit peak far above the expected limits in a particular region of phase space. Expected limits are calculated in the same way as observed limits except that the data is replaced with the median value of the test statistic from the pseudo-experiments carried out under the background-only hypothesis (i.e. the median of f(q | b)). This essentially assumes that the data is just what one would expect if the signal did not exist and then calculates limits based on that assumption. In addition to this median expected limit, expected limits are calculated using f_{mean}(q | b) shifted up and down by one and two standard deviations. This provides the error bands around the expected median used to compare the observed and expected limits.

Systematic uncertainties are incorporated into the CL_s method as nuisance parameters that influence the signal and background yields in each SR category (s_i and b_i). These yields influence the test statistic (LLR) via Eq. 9.1 and thus effect the final limits produced for each VLQ signal. The functional dependence of s_i can be written as $s_i(\mu,\nu_j)$ where μ is the scale factor applied to the signal cross-section, which is the parameter of interest, and ν_j are the remaining parameters referred to as nuisance parameters. Similarly b_i can be written as $b_i(\nu_j)$ where μ is not included as there is no scale factor applied to the background cross-section. The nuisance parameters are not central to the calculation but nonetheless effect the values of s_i and b_i. Examples include the theoretical uncertainties on the cross-sections introduced due to higher order corrections in perturbation theory and uncertainties in the parton distribution function (PDF). The complete list of systematic uncertainties in this analysis is given in Chapter 8. The full systematic uncertainty for each signal and background in each of the SR categories is given in Tables 6.4, 6.5 and 6.9. With the addition of systematic uncertainties the likelihood functions are redefined as

$$\mathcal{L}(x \mid s+b) = \prod_i \frac{e^{-(s_i+b_i)}(s_i+b_i)^x}{x!} \prod_j \pi_j(\mu,\nu_j) \tag{9.4}$$
$$\mathcal{L}(x \mid b) = \prod_i \frac{e^{-(b_i)}(b_i)^x}{x!} \prod_j \pi_j(\nu_j)$$

where the index i runs over the SR categories as before, and the index j runs over all nuisance parameters. The functions π_j are probability distribution functions for the nuisance parameters, also known as priors. They are assumed to be Gaussian and are determined from the values x_{nom}, x_{up} and x_{down} for each systematic uncertainty. These are the nominal yield and the yields obtained from shifting the systematic uncertainties up and down. Each signal and background sample is statistically varied independently. Correlations of the systematic uncertainties across all samples and channels are taken into account. The incorporation of systematic uncertainties via priors in this way is what makes the CL_s method a 'modified' rather than a 'pure' frequentist method. This means that it doesn't rely entirely on pseudo-experiments. The generalized definition of $\mathcal{L}$ in Eq. 9.4 increases the width of the distributions in Fig. 9.1 leading to greater overlap between f(q | s+b) and f(q | b), larger CL_s values and weaker limits.

9.2 Expected and Observed Event Yields

A comparison of the expected background to the data for each SR category is presented in Table 9.1 and Fig. 9.2. In addition to the yields, Table 9.1 shows the p-values characterizing the probability that the observed yield could arise from the background-only hypothesis. Figure 9.2 shows the significance of the disagreement between the background expectation and the observed yield in each SR category. These significance values are related to the p-values in Table 9.1 by the following expression:

$$p = \int_z^\infty \frac{1}{\sqrt{2\pi}} e^{\frac{-x^2}{2}} dx$$

where z is the significance in units of standard deviations. The p-values are the background only p-values (p_b) calculated in the CL$_s$ method described in the previous section. However the values shown are calculated separately for each individual SR category. This means that the likelihood functions consist of a single Poisson distribution function rather than the products across all categories shown in Eq. 9.2. Although the definition of p_b contains a reference to a particular signal, via the test statistic LLR, the p-values themselves are independent of this signal. Varying the signal shifts both the observed LLR value and the distribution of values in the background only hypothesis from which p_b is calculated. They shift to the right if the signal increases and to the left if it decreases. They shift together such that the integral in Eq. 9.3 is unchanged.

Figure 9.2 shows an excess in data above the background expectation with the excess concentrated mostly in SR categories with at least 2 b-jets and high H_{T} (SRVLQ6 and SRVLQ7). In these SR categories the local significance reaches approximately two standard deviations.

Although the p-value and significance for each SR category is independent of the particular signal being considered this is not true for the full signal region consisting of the combination of all SR categories. To combine SR categories we simply take the product of the likelihood functions for each SR category as shown in Eq. 9.2. This corresponds to adding the expressions for the LLR of each SR category. With this definition of LLR, varying the signal does affect the p-value. As in the case of a single SR category both the observed LLR and the background distribution of LLRs shift but in such a way that the p-value changes. The p-value is interpreted as the probability that the cross-section for a particular signal model is zero. For models that lead to events being concentrated in SRVLQ6 and SRVLQ7 the data is more consistent with those models existing, so the p-value is small. On the other hand models with events concentrated in any of the other SR categories have a larger p-value since there's no excess in those regions. Since higher mass vector-like quarks produce more events with high H_{T} that populate SRVLQ6 and SRVLQ7 they have smaller p-values.

The p-value and corresponding significance for the full signal region (SRVLQ0-7) are shown in Fig. 9.3 as a function of VLQ mass for vector-like top and vector-like bottom quarks. The significance is greater for the vector-like top quark because the signal region is only sensitive to five of the six possible decay modes of vector-like top while it is sensitive to all six of the decay modes of vector-like bottom. TT$\rightarrow WbWb$ cannot produce a trilepton or a same sign dilepton event. This means the expected signal yield is lower for the vector-like top quark leading to a smaller p-value (p_b) and a larger significance. For the same reason the significance increases with VLQ mass for both vector-like top and vector-like bottom. Higher mass resonances have lower expected yields. For the range of masses not already excluded by Ref. [124] the significance lies between one and two standard deviations with the significance reaching ~ 1.9 standard deviations for a vector-like top with a mass > 0.75 TeV.

	SRVLQ0	SRVLQ1/SR4t0	SRVLQ2/SR4t1
$t\bar{t}+W/Z$	16.2 ± 0.3 ± 7.0	12.6 ± 0.3 ± 5.4	1.24 ± 0.09 ± 0.53
$t\bar{t}+H$	2.5 ± 0.1 ± 0.3	1.8 ± 0.1 ± 0.2	0.26 ± 0.03 ± 0.05
Dibosons	11.2 ± 0.6 ± 2.8	0.95 ± 0.19 ± 0.25	0.07 ± 0.12 ± 0.05
Fake/Non-prompt	42.1 ± 5.4 ± 24.6	8.61 ± 2.34 ± 5.02	1.17 ± 0.82 ± 0.68
Q mis-Id	20.8 ± 0.7 ± 5.2	15.1 ± 0.6 ± 3.5	0.7 ± 0.11 ± 0.18
Other bkg.	1.76 ± 0.13 ± 0.17	0.75 ± 0.04 ± 0.1	0.1 ± 0.08 ± 0.03
Total bkg.	94.5 ± 5.4 ± 24.9	40.0 ± 2.4 ± 7.3	3.6 ± 0.9 ± 0.8
Data	107	54	6
p-value	0.36	0.12	0.24

	SRVLQ3	SRVLQ4
$t\bar{t}+W/Z$	2.07 ± 0.11 ± 0.89	3.14 ± 0.13 ± 1.35
$t\bar{t}+H$	0.4 ± 0.04 ± 0.07	0.57 ± 0.05 ± 0.07
Dibosons	2.36 ± 0.29 ± 0.61	2.03 ± 0.25 ± 0.49
Fake/Non-prompt	3.09 ± 1.29 ± 1.80	4.24 ± 1.59 ± 2.47
Q mis-Id	1.72 ± 0.22 ± 0.63	1.45 ± 0.17 ± 0.52
Other bkg.	0.22 ± 0.08 ± 0.03	0.41 ± 0.10 ± 0.06
Total bkg.	9.87 ± 1.35 ± 2.10	11.9 ± 1.6 ± 2.8
Data	7	10
p-value	0.83	0.71

	SRVLQ5/SR4t2	SRVLQ6/SR4t3	SRVLQ7/SR4t4
$t\bar{t}+W/Z$	1.87 ± 0.09 ± 0.8	2.46 ± 0.11 ± 1.06	0.57 ± 0.05 ± 0.25
$t\bar{t}+H$	0.31 ± 0.04 ± 0.05	0.44 ± 0.04 ± 0.006	0.08 ± 0.02 ± 0.2
Dibosons	0.33 ± 0.14 ± 0.10	0.04 ± 0.12 ± 0.03	0.00 ± 0.12 ± 0.00
Fake/Non-prompt	1.03 ± 0.97 ± 0.60	0.00 ± 1.02 ± 0.28	0.04 ± 0.83 ± 0.24
Q mis-Id	1.17 ± 0.16 ± 0.38	1.09 ± 0.14 ± 0.34	0.30 ± 0.09 ± 0.10
Other bkg.	0.16 ± 0.08 ± 0.02	0.23 ± 0.08 ± 0.05	0.14 ± 0.08 ± 0.08
Total bkg.	4.86 ± 1.00 ± 1.01	4.25 ± 1.05 ± 1.11	1.12 ± 0.85 ± 0.37
Data	6	12	6
p-value	0.46	0.029	0.036

Table 9.1: Expected and observed number of events with statistical (first) and systematic (second) uncertainties for the SR categories defined for VLQ production searches. The p-values for the agreement between the observed yield and the expected background in each SR category are reported. [39]

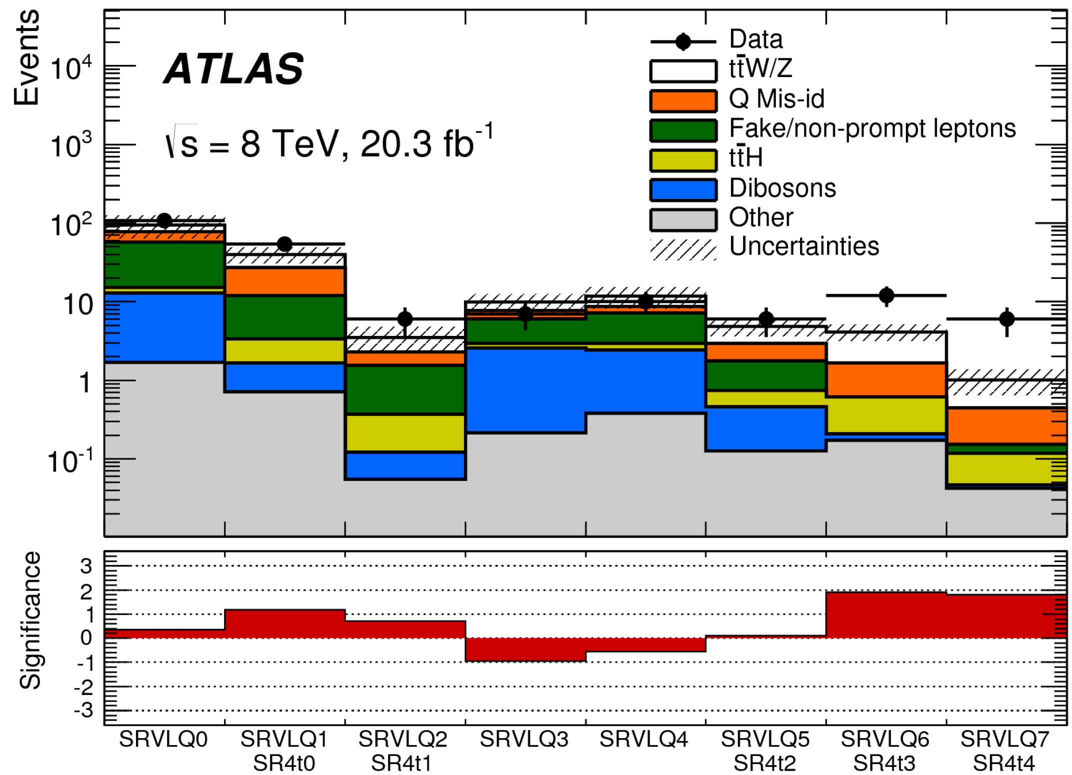

Figure 9.2: Expected background yields and observed data events in all SR categories. The difference between data and expectations is quantified by the means of the significance, computed from the p-values from Tables 9.1. [39]

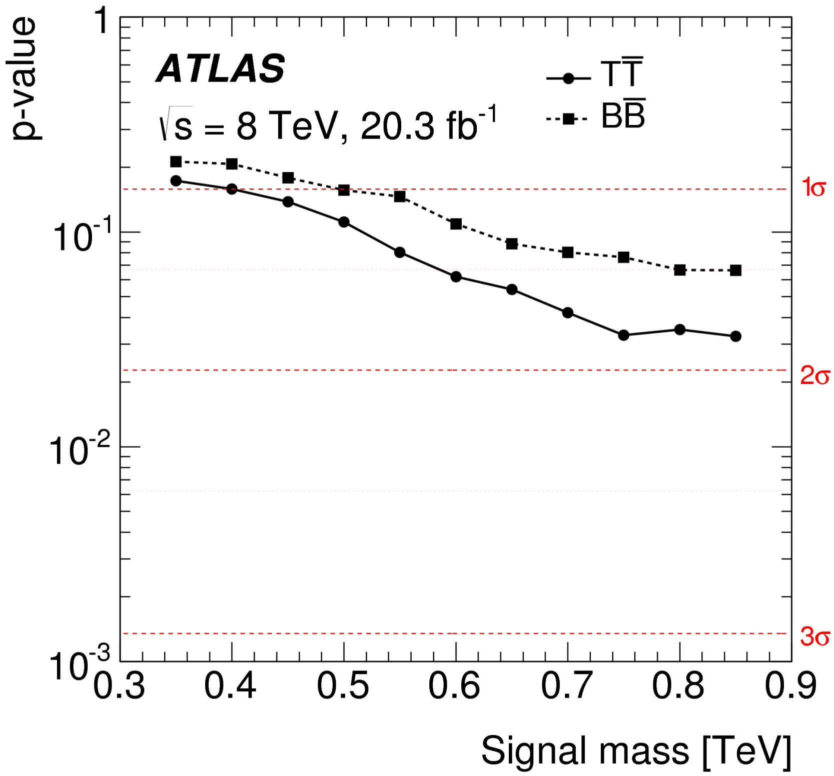

Figure 9.3: Probability for the data in the VLQ signal regions (SRVLQ0-SRVLQ7) to be consistent with a zero cross section for vector-like top and bottom, as a function of the quark mass.

9.3 Cross-Checks of Data Excess

A number of cross-checks were carried out to verify that the excesses seen in SR categories six and seven are legitimate and not the result of an error in the analysis. A number of these cross-checks consist of scrutinizing various properties of the events in the signal region to ensure that they should indeed pass the selection. Others involve running additional tests to further validate the techniques for estimating the background, described in Chapter 7. The results of each of these cross-checks are given below. None of the cross-checks uncover anything that leads the analysis team to doubt the excess seen in data or the significance assigned to it.

Tables 9.2 and 9.3 give details on the properties of the data events observed in the SR categories where there we see an excess. They show that for most events the H_{T} and $E_{\mathrm{T}}^{\mathrm{miss}}$ are well above the required threshold values that define these regions. Of the events in these regions only two in SRVLQ6 and one in SRVLQ7 have values of H_{T} that are close to the threshold value of 700 GeV and even these events are above the threshold by more than 5 GeV. All events have $E_{\mathrm{T}}^{\mathrm{miss}}$ well above the threshold values of 100 GeV in SRVLQ6 and 40 GeV in SRVLQ7.

Figures 9.4 and 9.5 show distributions of the data events along with the signal and background expectation for a number of variables in SRVLQ6 and SRVLQ7. The signal distributions shown are not for VLQ but rather for two of the $t\bar{t}t\bar{t}$ models considered in the same analysis. In general when there is an excess in data, the shape of the events in the excess can be used to understand whether they are more consistent with being signal events or fluctuations of the background. However, the statistics are too low to make this distinction. Figure 9.4 (a) shows that most of the excess in SRVLQ6 falls in a lower H_{T} range than that expected for $t\bar{t}t\bar{t}$ events. However the expected H_{T} range of VLQ events (not shown in the plot) is lower but still large enough to populate this region. Non of the other distributions show anything unusual. Given the low statistics in these regions, it is not possible to determine on the basis of these distributions whether the more likely source of the excess is signal or a background fluctuation.

Type	N_j	H_{T} [GeV]	$E_{\mathrm{T}}^{\mathrm{miss}}$ [GeV]
e^-e^-	3	807	171
e^+e^+	5	862	268
e^+e^+	5	868	113
μ^-e^-	6	1346	353
$e^+\mu^+$	5	810	106
$e^-\mu^-$	3	707	184
$e^-\mu^-$	2	706	174
μ^+e^+	8	882	150
μ^+e^+	4	860	112
$\mu^+\mu^+$	5	888	111
$\mu^-e^+e^+$	5	773	197
$\mu^-e^+e^+$	9	968	355

Table 9.2: List of data events in the SRVLQ6 category (by definition, all events have exactly two b-jets, the $E_{\mathrm{T}}^{\mathrm{miss}}$ is above 100 GeV and the H_{T} above 700 GeV). [39]

Type	N_j	N_b	H_{T} [GeV]	$E_{\mathrm{T}}^{\mathrm{miss}}$ [GeV]
e^+e^+	4	3	709	298
e^+e^+	6	3	800	137
$e^+\mu^+$	5	3	744	216
$e^+\mu^+$	4	3	888	155
μ^+e^+	3	3	1439	239
$\mu^-\mu^+\mu^-$	4	4	1072	175.9

Table 9.3: List of data events in the SRVLQ7 category (by definition, the $E_{\mathrm{T}}^{\mathrm{miss}}$ is above 40 GeV and the H_{T} above 700 GeV). [39]

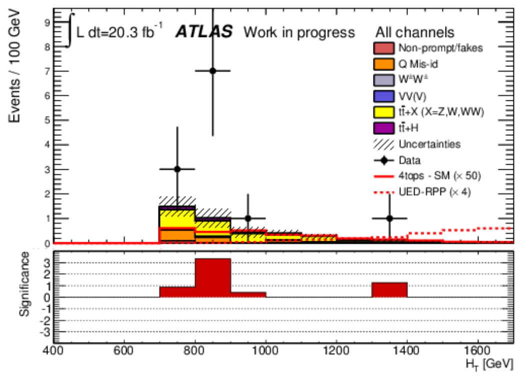

(a)

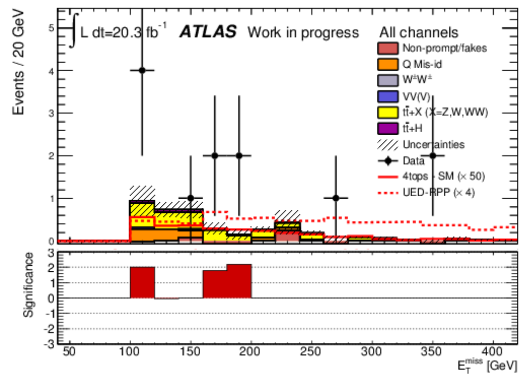

(b)

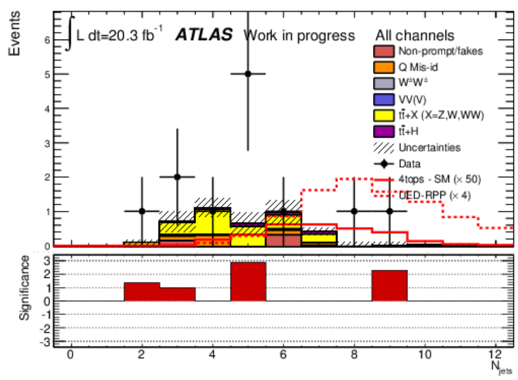

(c)

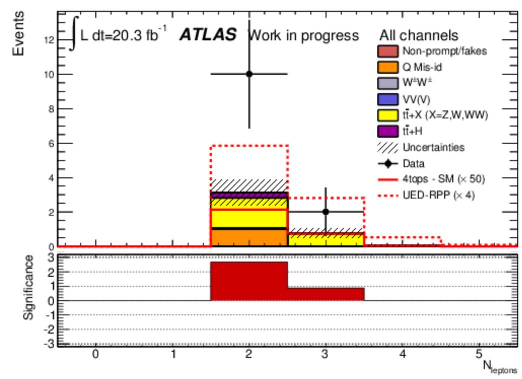

(d)

Figure 9.4: Distributions of H_{T} (a), $E_{\mathrm{T}}^{\mathrm{miss}}$ (b), number of jets (c) and number of leptons (d) (including loose leptons) in the SRVLQ6 category, for the expected background and the observed events in data. The number of b-jets in this category is two by construction. The signals shown are for the production of $t\bar{t}t\bar{t}$ in the SM and in a BSM theory involving two extra dimensions in the real projective plane. These signals were also considered in this analysis since they produce final states very close to VLQ final states. The Feynman diagrams for these signal processes are shown in Fig. 6.1. [39]

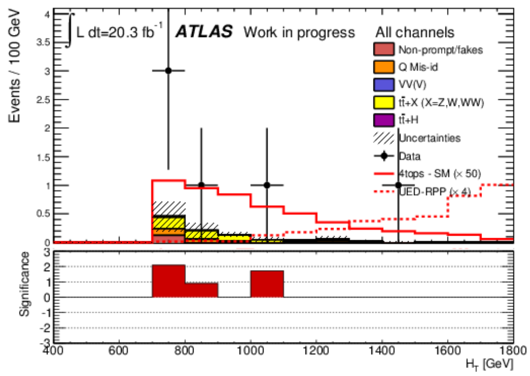

(a)

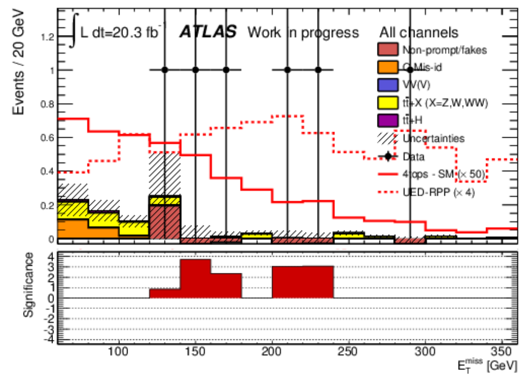

(b)

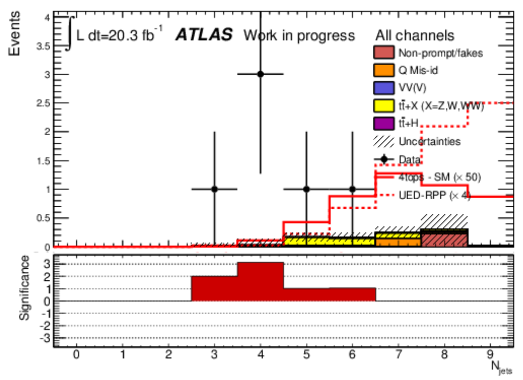

(c)

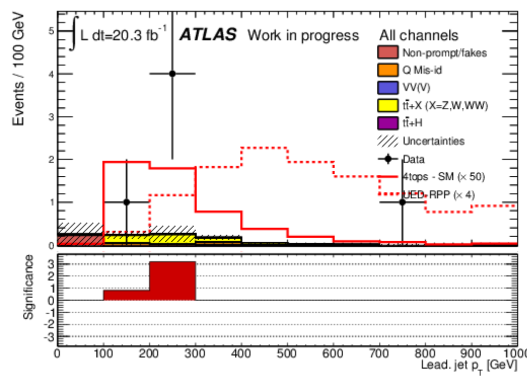

(d)

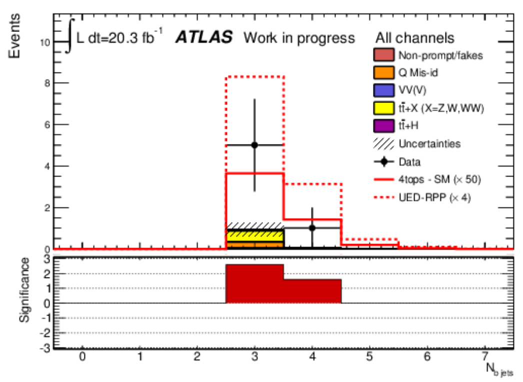

(e)

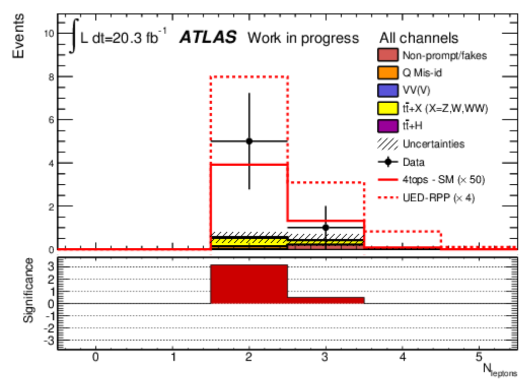

(f)

Figure 9.5: Distributions of H_{T} (a), $E_{\mathrm{T}}^{\mathrm{miss}}$ (b), number of jets (c), leading jet p_{T} (d), number of b-jets (e) and number of leptons (f) (including loose leptons) in the SRVLQ7 category, for the expected background and the observed events in data. The signals shown are for the production of $t\bar{t}t\bar{t}$ in the SM and in a BSM theory involving two extra dimensions in the real projective plane. These signals were also considered in this analysis since they produce final states very close to VLQ final states. The Feynman diagrams for these signal processes are shown in Fig. 6.1. [39]

The plots in Fig. 9.6 show the distribution of events observed in data and the expected background yields plotted against the data taking period in Run I for each of the SR categories. The background yields for each data period were calculated by scaling the number of events in the MC simulation for each background to the integrated luminosity of each data period rather than the full integrated luminosity collected in 2012. This is an effort to ensure that the excess events did not arise from some technical problem with the LHC or ATLAS that was not flagged by the DQMF. These plots show that the events observed in all SR categories are evenly distributed with respect to data taking period. In particular, the excesses seen in SRVLQ6 and SRVLQ7 are not concentrated in any particular period.

Figures 9.7 shows the distribution of the isolation variable used in this analysis known as mini-isolation for data and the background expectation. Mini-isolation is defined as:

$$I = \frac{\sum_{tracks} p_{\mathrm{T}}}{p_{\mathrm{T}}^{\ell}}$$

where p_{T}^{ℓ} is the p_{T} of the lepton and the sum is over all tracks within a cone of radius $\Delta R = 10$ GeV$/p_{\mathrm{T}}^{\ell}$ of the lepton. The leptons are considered to be isolated if $I < 0.05$. This definition is designed to try to capture more real prompt leptons from the decay of boosted objects which may not pass a fixed cone isolation requirement. These distributions show that all the leptons in the signal region are very well isolated.

Figures 9.8 and 9.9 show the distribution of the weights produced by the MV1 algorithm which characterize the likelihood that a jet contains a b-hadron. The plots show the MV1 for all b-tagged jets in SRVLQ6 and SRVLQ7. In order to be tagged as b-jets the MV1 weight must be greater than 0.7892. These distributions show that all b-jets in these regions have an MV1 weight well above this threshold value. This means that no events have b-jets that were very close to the threshold and so perhaps only passed the selection due to a fluctuation.

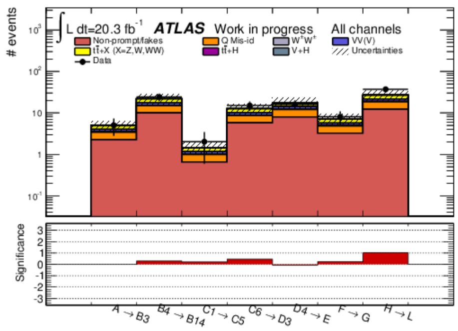

(a) SRVLQ0

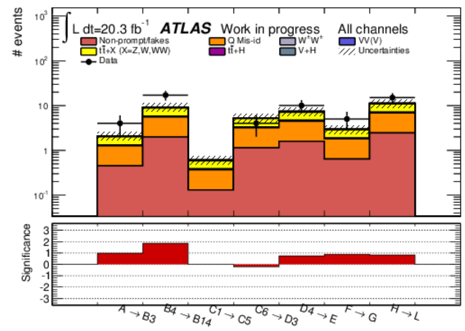

(b) SRVLQ1/SR4t0

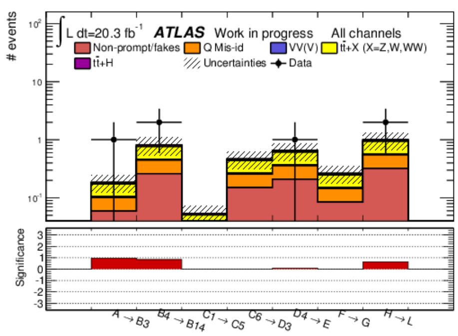

(c) SRVLQ2/SR4t1

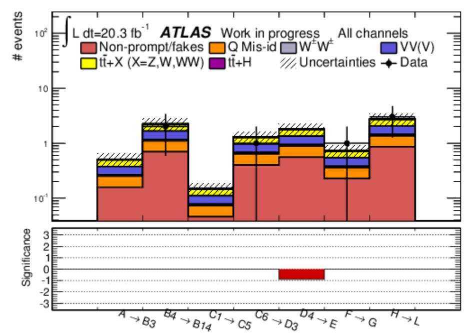

(d) SRVLQ3

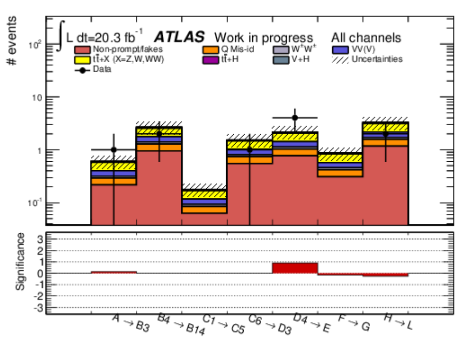

(e) SRVLQ4

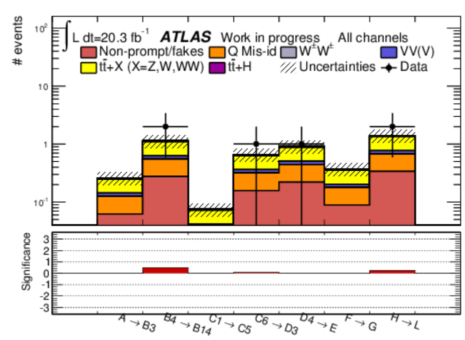

(f) SRVLQ5/SR4t2

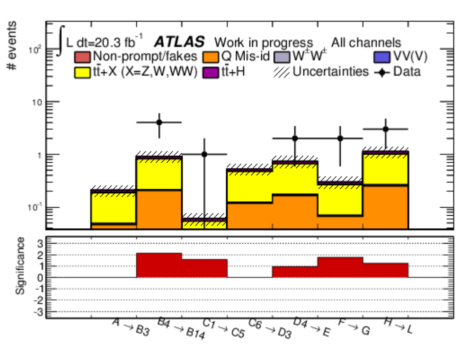

(g) SRVLQ6/SR4t3

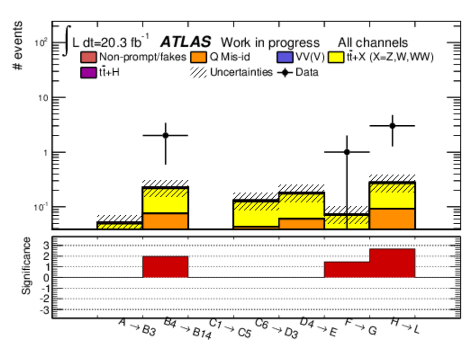

(h) SRVLQ7/SR4t4

Figure 9.6: Observed number of events in data and expected background yields v.s. data period.

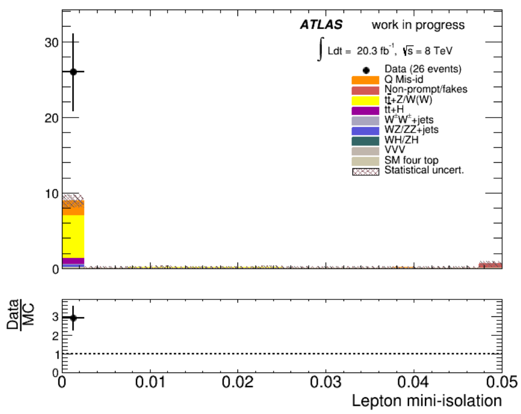

Figure 9.7: Lepton isolation (mini-isolation as defined in the text) in the SR4t3/VLQ6 (left) and SR4t4/VLQ7 (right) categories.

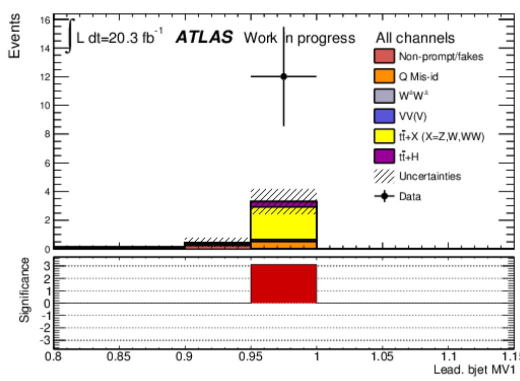

Figure 9.8: Distributions of the MV1 value (b-tagging weight) for the first (left) and second (right) b-tagged jet in the SR4t3/VLQ6 category.

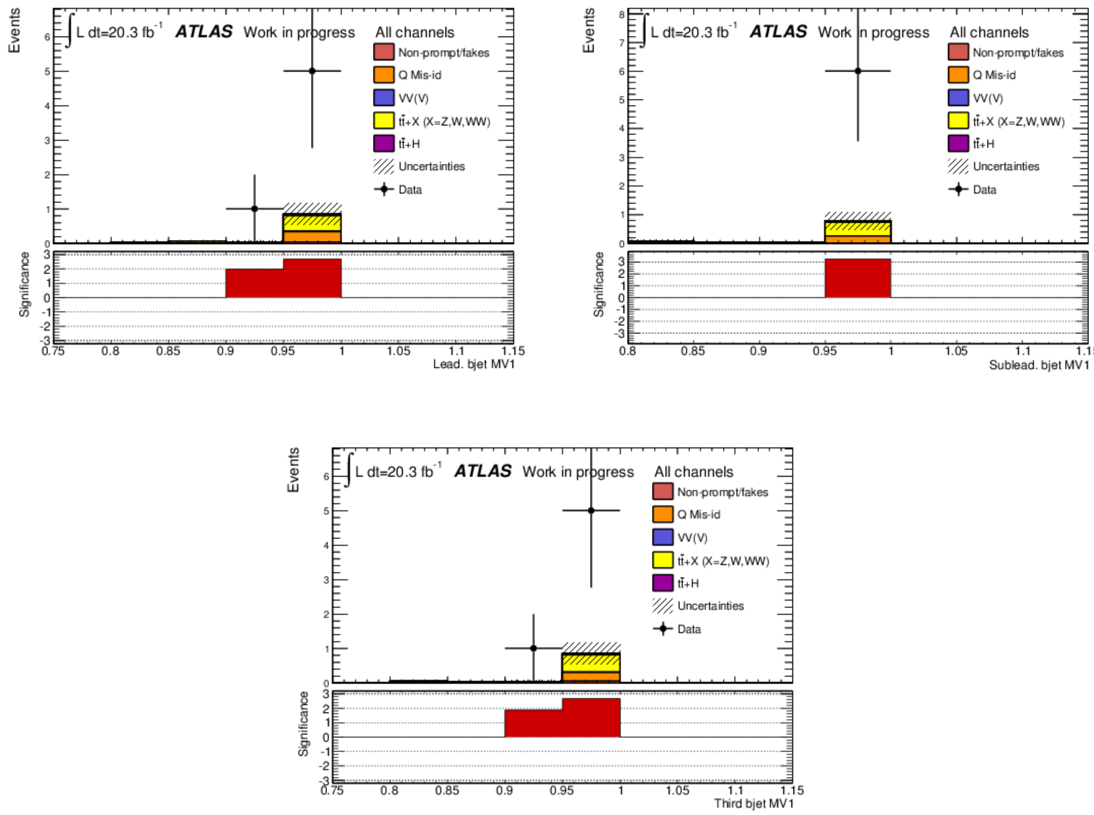

Figure 9.9: Distributions of the MV1 value (b-tagging weight) for the first (top left), second (top right) and third (bottom) b-tagged jet in the SR4t4/VLQ7 category.

Expected yields for the $t\bar{t}W$ and $t\bar{t}Z$ processes were produced using two alternate sets of MC samples in addition to those used for the nominal yields. These processes are the dominant contributions to the irreducible SM background. The alternate sets of MC samples are listed in Table 8.7 and the differences between them are described in Section 8.2.4. A comparison of the total background yield as well as the components due to $t\bar{t}W$ and $t\bar{t}Z$ are shown in Table 9.4 for the nominal and each of the alternate MC samples. For the nominal estimate of the total background the uncertainty includes both statistical and systematic uncertainties. For the $t\bar{t}W$ and $t\bar{t}Z$ the uncertainties are only statistical. The comparison shows that the yields for both the nominal and each of the alternate MC estimates are in agreement within their uncertainties.

Region	Nominal MadGraph	Alternative MadGraph	Alternative Alpgen	Observed
Total bkg. SRVLQ0	95 ± 25	98	95	107
• $t\bar{t}W$	9.43 ± 0.25	11.29 ± 0.21	8.8 ± 0.7	
• $t\bar{t}Z$	6.79 ± 0.20	8.66 ± 0.18	7.55 ± 0.20	
Total bkg. SR4t0/VLQ1	39.8 ± 6.8	41.5	40.1	54
• $t\bar{t}W$	7.91 ± 0.23	8.30 ± 0.18	7.5 ± 0.7	
• $t\bar{t}Z$	4.69 ± 0.16	6.04 ± 0.15	5.41 ± 0.17	
Total bkg. SR4t1/VLQ2	3.6 ± 1.1	3.5	3.4	6
• $t\bar{t}W$	0.75 ± 0.07	0.64 ± 0.05	0.73 ± 0.21	
• $t\bar{t}Z$	0.49 ± 0.05	0.51 ± 0.04	0.36 ± 0.04	
Total bkg. SRVLQ3	9.9 ± 2.4	10.4	10.1	7
• $t\bar{t}W$	1.02 ± 0.07	1.17 ± 0.07	1.10 ± 0.28	
• $t\bar{t}Z$	1.05 ± 0.07	1.46 ± 0.08	1.23 ± 0.09	
Total bkg. SRVLQ4	11.9 ± 3.1	12.1	11.7	10
• $t\bar{t}W$	1.89 ± 0.11	1.97 ± 0.09	1.68 ± 0.33	
• $t\bar{t}Z$	1.25 ± 0.08	1.39 ± 0.07	1.27 ± 0.09	
Total bkg. SR4t2/VLQ5	4.9 ± 1.1	5.3	5.2	6
• $t\bar{t}W$	0.91 ± 0.06	1.04 ± 0.06	1.01 ± 0.26	
• $t\bar{t}Z$	0.97 ± 0.07	1.24 ± 0.07	1.18 ± 0.08	
Total bkg. SR4t3/VLQ6	4.3 ± 1.0	4.2	5.1	12
• $t\bar{t}W$	1.52 ± 0.09	1.40 ± 0.07	2.4 ± 0.4	
• $t\bar{t}Z$	0.94 ± 0.07	0.98 ± 0.06	0.90 ± 0.07	
Total bkg. SR4t4/VLQ7	1.12 ± 0.38	1.10	1.10	6
• $t\bar{t}W$	0.30 ± 0.09	0.288 ± 0.033	0.25 ± 0.13	
• $t\bar{t}Z$	0.256 ± 0.035	0.257 ± 0.030	0.29 ± 0.04	

Table 9.4: Comparison of the event yields for the total background and the $t\bar{t}W$ and $t\bar{t}Z$ components using the nominal samples and two sets of alternate MC samples for these processes. For the nominal estimate of the total background the uncertainty includes both statistical and systematic uncertainties. For the $t\bar{t}W$ and $t\bar{t}Z$ the uncertainties are only statistical.

In addition to the standard background estimate that makes use of both MC simulation and data-driven techniques, a background estimate was produced which consists entirely of MC simulation. This background estimate is referred to as the *full MC background estimate* and is described in Section 7.3. It was initially developed to better understand the composition of the signal region in order to select the best regions to validate the standard background estimate. As an additional cross-check the *full MC background estimate* is applied to the signal region directly and compared to the standard background estimate. A comparison of the yields from each of these estimates and the data is shown in Table 9.5 for each SR category defining the signal region. The uncertainties for the *full MC background estimate* are not shown because they are very large, due to the low integrated luminosity of some of the samples

Since $t\bar{t}$ is the dominant process contributing to the instrumental background, an alternate full MC background estimate has been produced by replacing the standard $t\bar{t}$ sample (DSID 117050) with a set of alternate samples (DSIDs 201020-4, 201220-4, 201027-8). These alternate samples include $t\bar{t}$ + heavy flavor events ($t\bar{t}b\bar{b}$ and $t\bar{t}c\bar{c}$). Since Heavy Flavor Overlap Removal was not available for these samples we expect an overestimate of the $t\bar{t}$ + heavy flavor component. In general each of the full MC background estimates agree with the standard background estimate. The exception is in SRVLQ6 where the alternate full MC estimate shows an excess with respect to the others in the ee and $e\mu$ channels. In this SR category the full MC estimate gives 1.1 $\pm$ 1.0 ee and 1.1 $\pm$ 1.0 $e\mu$ events while the alternate full MC estimate gives 1.9 $\pm$ 1.0 ee and 2.4 $\pm$ 1.0 $e\mu$ events. The uncertainties given here are only statistical.

Region	Data-driven	Full MC	Full MC (alt. $t\bar{t}$)	Observed
SRVLQ0	93.4 ± 18.5	77.3	87.6	107
SR4t0/VLQ1	39.3 ± 6.4	37.5	44.8	54
SR4t1/VLQ2	3.53 ± 1.04	2.87	2.80	6
SRVLQ3	9.72 ± 2.09	8.00	10.4	7
SRVLQ4	11.7 ± 2.8	9.83	13.0	10
SR4t2/VLQ5	4.78 ± 1.05	4.53	6.04	6
SR4t3/VLQ6	4.17 ± 1.11	5.33	7.70	12
SR4t4/VLQ7	1.10 ± 0.40	1.12	1.17	6

Table 9.5: Comparison of the number of events in data to the standard background estimate and the full MC background estimate for each SR category. Column four shows yields produced from an alternate full MC background estimate that uses different $t\bar{t}$ samples.

9.4 Exclusion Limits

9.4.1 Vector-Like T and B Pair Production

The expected and observed 95% CL cross-section limits calculated with the CL_s method for vector-like top and vector-like bottom quarks in the Singlet model are shown in Fig. 9.10. The branching ratios used in producing the signal yields that enter in the limit calculation are those shown in Fig. 2.4. When compared with the theoretical cross-section these limits exclude vector-like top masses below 0.59 TeV and vector-like bottom masses below 0.62 TeV at 95% CL. For comparison with the background-only hypothesis the expected mass limits are 0.66 TeV and 0.69 TeV respectively. The observed limits are consistently above the expected limits across the full mass range due to the excess seen in data. The limits on vector-like bottom are stronger then those on vector-like top because the signal region is sensitive to all six decay modes of the vector-like bottom and only five of the six decay modes of vector-like top. As mentioned in the previous section the TT→ $WbWb$ decay mode cannot produce a trilepton or a same sign dilepton event.

Figures 9.11 and 9.12 show expected and observed exclusion limits for vector-like

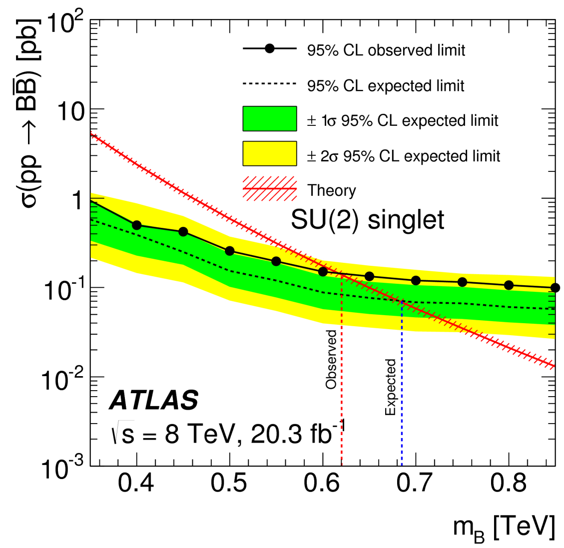

(a)

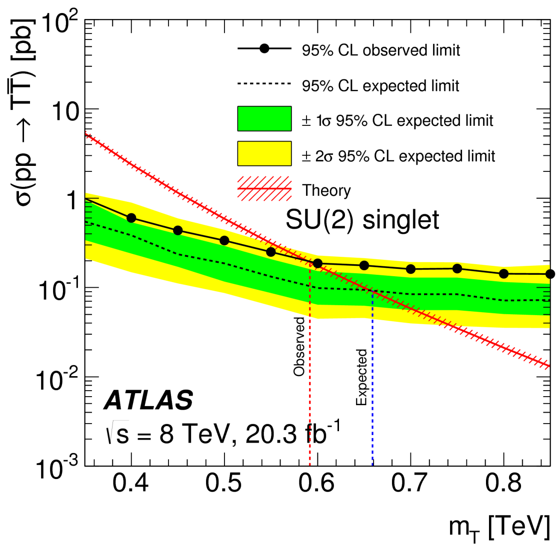

(b)

Figure 9.10: Observed limits on the pair production cross section as a function of mass for (a) vector-like B and (b) vector-like T quarks. These limits assume branching ratios given by the model where the B and T quarks exist as singlets. These branching ratios can be found in Ref. [106].

bottom and vector-like top as a function of the branching ratios to the three decay modes. The axes in the plane represent the branching ratios for two of the three decay modes with the third determined by the constraint that the branching ratios add to one. Each point in the plane corresponds to a unique combination of branching ratios. The vertical axis represented in color indicates the mass limit. These limits explore the full phase space of the vector-like quarks in a model independent way.

For vector-like bottom quarks, the strongest mass limits are produced in the region of the plane corresponding to a high branching ratio to Wt. For vector-like top, the strongest mass limits are produced in the region of the plane corresponding to a low branching ratio to Wb. These results reflect the sensitivity of the signal region to the various topologies of the VLQ final states discussed in Section 2.3. As with the limits for the Singlet VLQ models, the expected limits are stronger than the observed limits for the model independent limits shown here. This is caused by the excess in data over the background expectation which is the same regardless of the signal. Also, consistent with the Singlet VLQ limits, the model independent limits are stronger for vector-like bottom quarks than for vector-like top quarks. More of the plane is excluded for any given mass for vector-like bottom quarks than for vector-like top quarks. This is again consistent with what the limits on the singlet VLQ models show. Figures 9.13 and 9.14 show the same model independent limits in a different format and also indicate the points on the plane that correspond to the Singlet and Doublet benchmark VLQ models.

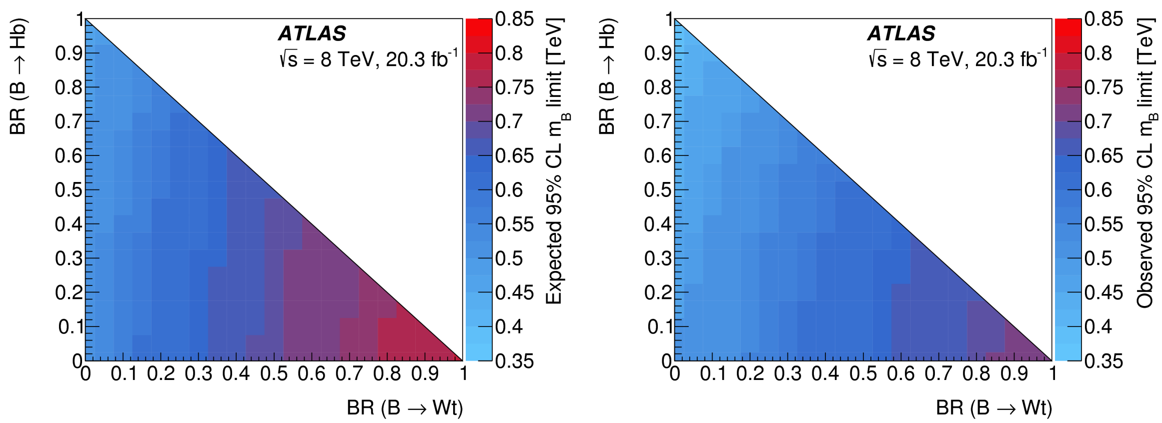

(a) (b)

Figure 9.11: Expected (a) and observed (b) vector-like B quark mass hypotheses excluded at 95% CL as a function of the assumed branching ratios.

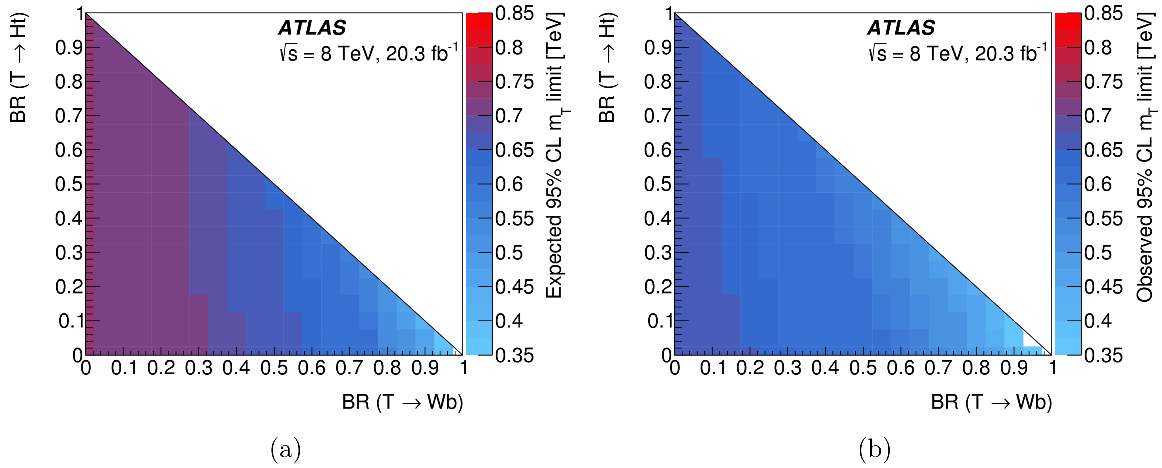

Figure 9.12: Expected (a) and observed (b) vector-like T quark mass hypothesis excluded at 95% CL as a function of the assumed branching ratios

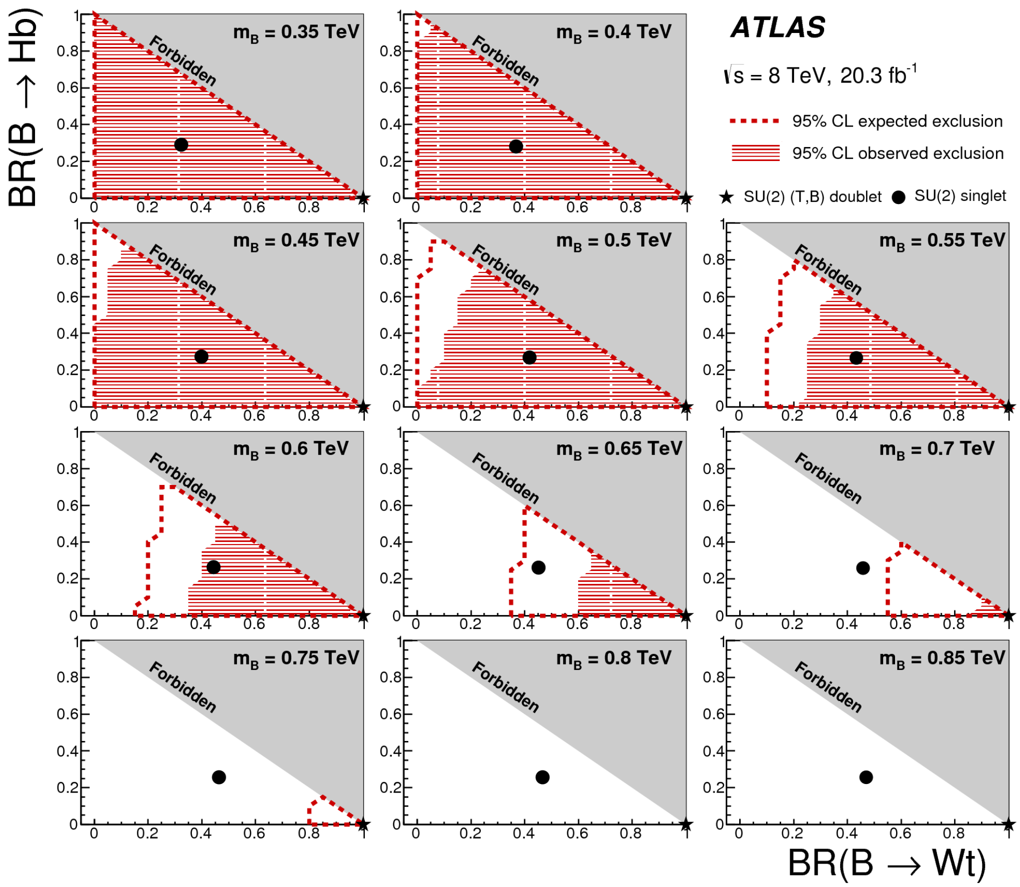

Figure 9.13: B branching fractions excluded at 95% CL for several B mass hypotheses. The branching fractions expected in models where the B appears in a SU(2) singlet are indicated by a circle, and those expected when the B appears in a (T, B) doublet are indicated by a star.

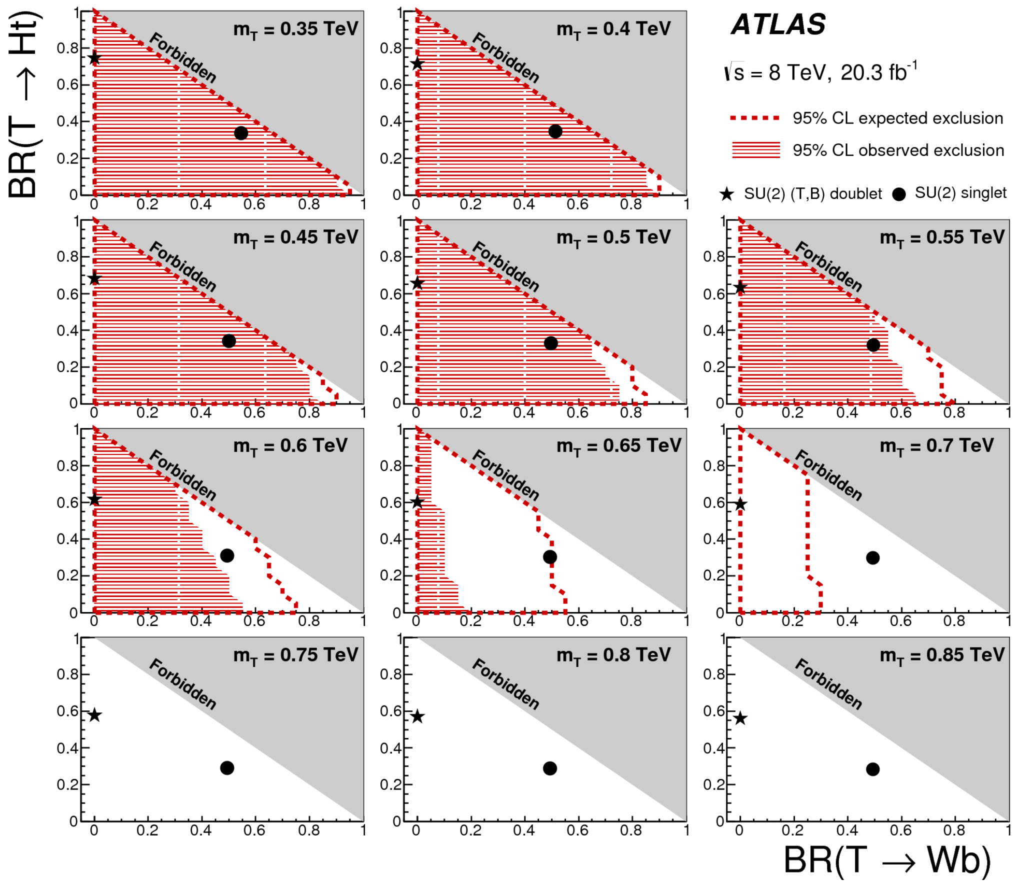

Figure 9.14: T branching fractions excluded at 95% CL for several T mass hypotheses. The branching fractions expected in models where the T appears in a SU(2) singlet are indicated by a circle, and those expected when the T appears in a (T, B) doublet are indicated by a star.

9.4.2 Vector-Like $T_{5/3}$ Pair and Single Production

95% CL cross-section limits for pair production and pair production combined with single production are calculated for the vector-like quark $T_{5/3}$. Three scenarios are considered: pair production only and combined pair production and single production with two values of the coupling constant λ defined in Section 2.3 ($\lambda = 0.5$ and 1.0).

The pair production limits are shown in Fig. 9.15a, and correspond to an observed mass limit of 0.74 TeV and an expected mass limit of 0.81 TeV. The limits on pair plus single production with $\lambda = 0.5$ are show in Fig. 9.15b, where the observed mass limit is 0.75 TeV and the expected limit is 0.81 TeV. Finally, the limits on pair plus single production with $\lambda = 1.0$ are shown in Fig. 9.15c, where again the observed mass limit is 0.75 TeV and the expected limit is 0.81 TeV. The cross section limits for combined pair production and single production for both values of λ are weaker than for pair production alone since the overall selection efficiency is less for the singly produced $T_{5/3}$ than for $T_{5/3}$ produced in pairs. This is particularly true in the high H_{T} SR categories. This is why the difference increases with mass, since a higher mass $T_{5/3}$ is more likely to populate one of the high H_{T} regions. For $\lambda = 1$ the combined pair production and single production cross section limits are $\sim 12\%$ larger than pair production alone for 600 GeV and $\sim 30\%$ for 1000 GeV. Despite this, the mass limits are marginally stronger for the combination of single and pair production because the theoretical cross sections are larger. However the difference is very small (~ 1 GeV)[23]

[23] This is rounded to 10 GeV for the final mass limits.

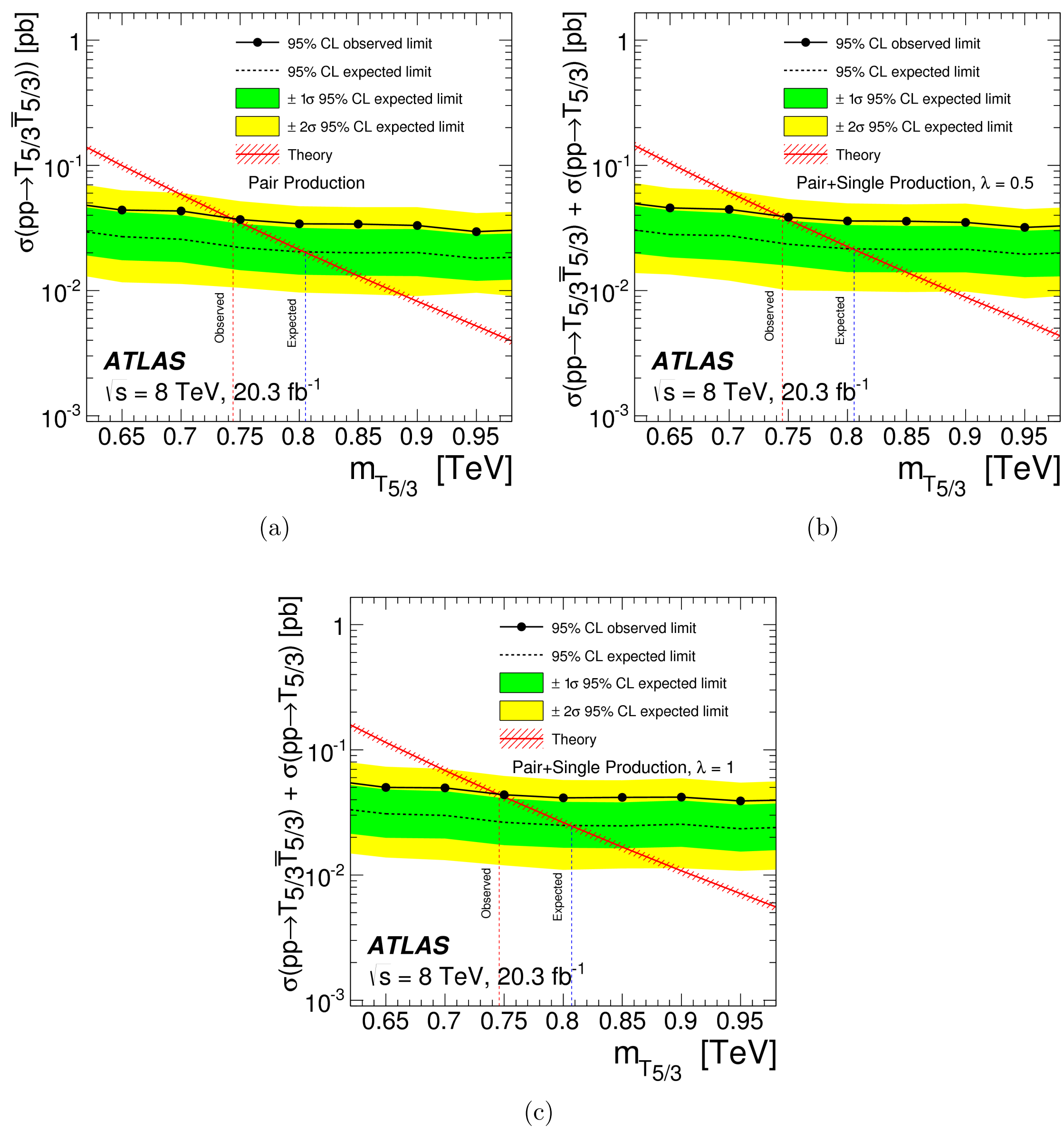

Figure 9.15: Expected and observed limits as a function of mass on (a) $T_{5/3}$ pair production, (b) $T_{5/3}$ pair plus single production for coupling $\lambda = 0.5$, and (c) $T_{5/3}$ pair plus single production for $\lambda = 1.0$.

CHAPTER 10

Conclusion

This dissertation presents a search for vector-like quarks in 20.3 fb^{-1} of proton-proton collision data collected in 2012 with the ATLAS detector at a center-of-mass energy of $\sqrt{s} = 8$ TeV. The analysis considers trilepton and same-sign dilepton final states, which are rarely produced in the SM but are significantly enhanced by the presence of vector-like quarks. The data are interpreted in the context of several vector-like quark models including vector-like top (T) and vector-like bottom (B) quarks with electric charge 2/3 and -1/3 respectively as well as the $\text{T}_{5/3}$ with electric charge 5/3.

For T and B, only pair production via gluon fusion is considered since single production cannot produce either a trilepton or a same-sign dilepton final state. For $\text{T}_{5/3}$, both single and pair production are considered since a singly produced $\text{T}_{5/3}$ can give rise to a same-sign dilepton pair. A variety of BSM models are considered in which T and B appear as isosinglets or as part of isodoublets or isotriplets with other vector-like quarks. Depending on the model, T and B can decay into a W, Z or H boson together with a third generation SM quark. The branching ratios for these decay modes are specified by the model. This leads to a very broad range of different final state topologies from the decay of $T\bar{T}$ and $B\bar{B}$ pairs, many of which are trilepton or same-sign dilepton states. $\text{T}_{5/3}$ decays exclusively to Wt, which can also give rise to trilepton and same-sign dilepton final states.

The event selection is optimized to maximize the contribution from vector-like quark signals while minimizing leading backgrounds such as $t\bar{t}$+W/Z, the fake/non-prompt lepton and electron charge misidentification backgrounds. In addition to the trilepton and same-sign dilepton signatures, events containing vector-like quarks are distinguished from SM background events by having large total transverse momentum, large missing transverse momentum, and a large number of jets including b-tagged jets. The signal region consists of eight categories defined in terms of these four discriminating variables: H_{T}, $E_{\mathrm{T}}^{\mathrm{miss}}$, N_{jets} and N_{b-jets}, (see Table 6.3). In six of the eight categories the event yields in data are consistent with the expectation from the SM background. In the remaining two categories, characterized by large H_{T} and a large number of b-tagged jets, there is an excess in data above the background expectation. In SRVLQ6, 12 events are observed in data while only $4.25 \pm 1.05 \pm 1.11$ [24] are expected from the SM background. In SRVLQ7, 6 events are observed in data while only $1.12 \pm 0.85 \pm 0.37$ are expected. These combined excesses correspond to a significance of $\sim$1.9 standard deviations for a vector-like top with mass > 0.75 TeV. These excesses are interesting, however the significances are too low to claim discovery of any new physics. At this level, they are consistent with fluctuations of the SM background. More data is needed to determine if they are indeed the result of fluctuations or if they are the first signs of new physics.

Exclusion limits are produced at 95% CL on the cross-section for pair production of vector-like quarks in BSM models in which T and B occur as isosinglets. These limits are produced as a function of vector-like quark mass. Combined with the theoretical cross-sections for vector-like quark pair production, the cross-section limits are used to constrain the vector-like quark mass. Lower limits on the mass of vector-like top and bottom quarks, in the isosinglet scenario, are set at 0.59 TeV and 0.62 TeV respectively. In addition, 95% CL exclusion limits are produced directly on the mass of both T and B in a model independent way. These limits are represented as two dimensional plots showing the mass limit as a function of the branching ratios for each of the decay modes for vector-like quarks. Each point in the plane corresponds to a unique combination of branching ratios for each decay mode and the mass limit is represented with the color scale.

Exclusion limits are also produced at 95% CL on the production cross-section for the $\mathrm{T}_{5/3}$ vector-like quark. The limits are produced for three scenarios: pair production only and combined pair and single production with two different values for the weak coupling constant λ between $\mathrm{T}_{5/3}$ and Wt ($\lambda = 0.5$ and 1.0). When

[24] The first uncertainty is statistical and the second is systematic

compared with the theoretical cross-sections in each of these scenarios these limits constrain the mass of the $T_{5/3}$. If only pair production is significant (λ=0), the $T_{5/3}$ is excluded below a mass of 0.74 TeV. If both pair production and single production are significant (λ=0.5 or 1.0) it is excluded below a mass of 0.75 TeV.

A previous search by the ATLAS collaboration, using an integrated luminosity of 1.04 fb^{-1} of pp collisions at a center-of-mass energy $\sqrt{s} = 7$ TeV observed no significant excess in same-sign dilepton events [148]. This result was used to set a lower limit of 450 GeV on the mass of a heavy down-type quark, under the assumption that the branching ratio to Wt is 100%. A more recent search with a similar final state carried out by the ATLAS collaboration, using 2012 data also observed no excess in these events [149]. This analysis uses 20.3 fb^{-1} of pp collisions at a center-of-mass energy of 8 TeV. It differs from the search described in this dissertation in that it does not require the presence of b-jets and was not used to set limits on VLQ signals but rather considered a variety of SUSY models.

The CMS collaboration also carried out searches with same-sign dilepton and trilepton final states using data collected in 2012 and observed no significant excesses. These analyses use 19.5 fb^{-1} of pp collisions at a center-of-mass energy of 8 TeV collected with the CMS detector. Ref. [150] did not require the presence of b-jets and was not used to set limits on VLQ signals. The analysis in Ref. [151] set a lower limit on the mass of the vector-like top T by considering final states with either a single lepton, a same-sign or opposite sign dilepton pair or three leptons. The multi-lepton final states require the presence of at least one b-jet. The lower limit lies between 687 GeV and 782 GeV for all possible values of the branching fractions into the three allowed decay modes. The analysis in Ref. [152] sets a lower limit on the mass of the $T_{5/3}$ at 800 GeV by considering a final state involving a pair of same-sign leptons.

10.1 Future Outlook

At the beginning of 2013 the LHC and ATLAS entered an extended shutdown period known as LS1 (Long Shutdown 1). The first three years of operation of the LHC that preceded LS1 from 2010 to 2012 are referred to collectively as Run I. LS1 was needed for scheduled maintenance and repairs as well as upgrades necessary to prepare both the LHC and ATLAS for higher energy and luminosity. After approximately two years in LS1 the LHC began its second phase of operation known as Run II in June 2015. The first data of Run II were recorded on June 3, 2015. During Run I the LHC ran with a collision energy of 7 TeV in 2010-2011 and 8 TeV in 2012. The beam luminosity was on the order of 10^{33} cm^{-2} s^{-1}, reaching a peak value of 7.3×10^{33} cm^{-2} s^{-1} in 2012. Approximately 25 fb^{-1} of collision data was recorded. In Run II the LHC will reach the full design energy and luminosity of 14 TeV and 10^{34} cm^{-2} s^{-1}. The current collision energy at the LHC is 13 TeV. It will remain at this value for some time, eventually rising to 14 TeV later in Run II.

Work is already in progress to continue the search for VLQ in trilepton and same-sign dilepton final states with the Run II ATLAS data. The increased luminosity means that more data ($\sim$ 75 - 100 fb^{-1}) will be available for analysis. The increased collision energy means that the production cross-sections for the VLQ signals will increase significantly. Both of these factors will lead to higher signal yields in Run II. Although the expected background yields will increase as well for the same reasons, they will increase by less so that the sensitivity of the search will improve.

In general it is difficult to predict the increase in the expected background because of the component arising from instrumental effects. The increase in the SM background yields can be easily calculated with Eq. 6.1 given the integrated luminosity and the increase in the cross-section due to the higher collision energy. The cross-sections for the leading SM background in this analysis $t\bar{t}W/Z$ are a factor of $\sim$ 2-5 times larger, depending on jet multiplicity of the sample, at 13 TeV than at 8 TeV. The cross-sections for VLQ pair production are a factor of $\sim$ 10 larger at 13 TeV than 8 TeV. This is an approximation as the actual increase depends on the VLQ mass. If there were no instrumental background to consider the sensitivity of the analysis would necessarily improve by virtue of the more significant increase of the signal cross-sections compared to the background cross-sections. There is no straightforward way to predict the change in the contribution from instrumental background which relies on data-driven techniques. However, in general these techniques improve over time leading to an overall reduction of the background.

Figure 10.1 shows projections for the expected limits on pair production of vector-like bottom and top quarks at 13 TeV compared to those produced in 2012 at 8 TeV. The plots show limits for a variety of values of the integrated luminosity and the increase in the total background. The signal yields are normalized to the 13 TeV cross-section values and a variety of different values of the integrated luminosity. The background yields are obtained by simply scaling the 2012 background yields by factors of three and five to approximate the possible increase in Run II. These projected limits show that with a minimum of 2 fb^{-1} of data the Run II expected mass limits will exceed those produced in 2012.

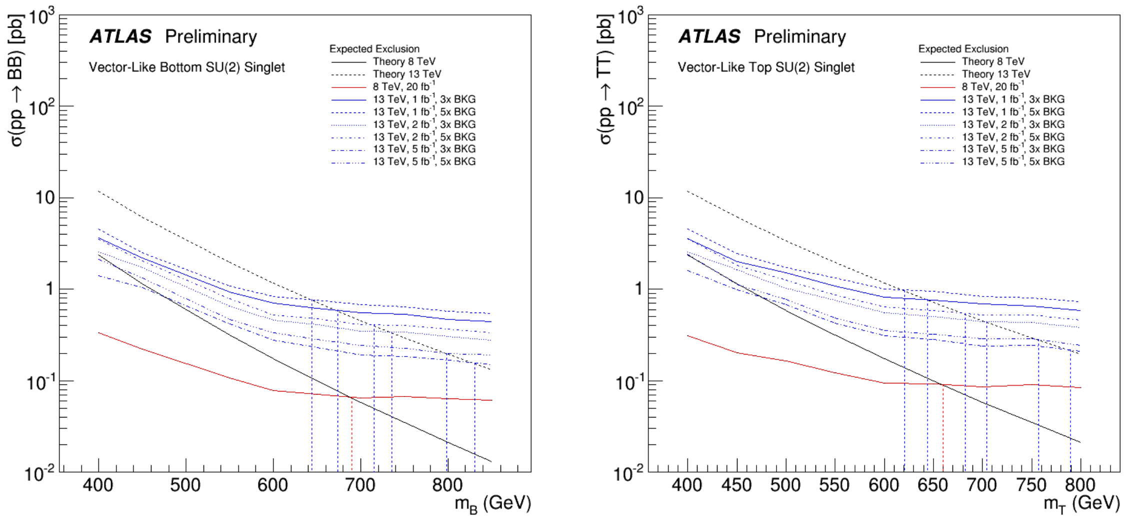

(a) (b)

Figure 10.1: Projections for the expected limits on pair production of vector-like bottom (a) and top (b) quarks in Run II. The signal yields are normalized to the 13 TeV cross-section values and a variety of different values of the integrated luminosity. The background yields are obtained by scaling the 2012 background yields by factors of three and five.

The projected limits in Fig. 10.1 assume the same analysis techniques as in 2012. There are a number of ways in which the Run II analysis could be modified to potentially improve the sensitivity with respect to the 2012 analysis. The most obvious improvement comes from reduced systematic uncertainties. Generally the longer an experiment is running the better its operation is understood so that systematic uncertainties tend to reduce over time. As an example, the systematic uncertainty associated with the luminosity measurement decreased from 3.6% in 2011 to 2.8% in 2012. Many of the systematic uncertainties described in Chapter 8 should decrease in Run II leading to improved sensitivity in searches and stronger limits. In addition to this the analysis could be improved by making use of the shape of events in the signal region and by implementing a multivariate selection rather than following a simple cut and count procedure. The power of such techniques is limited by the statistics of the data sample. This is why they were not applied in Run I. However, there may be sufficient statistics in Run II to make them worthwhile. Another possibility is the introduction of techniques designed to select hadronically decaying objects that are boosted such that some or all of the decay products are merged into a single jet. These boosted objects will be far more common at the higher energies in Run II.

The search described in this dissertation is a cut and count analysis. This means that the signal region is defined by placing requirements or "cuts" on variables such as H_{T} and $E_{\mathrm{T}}^{\mathrm{miss}}$ separately and that only the total number of events in the signal region is considered in setting limits. One way to improve a cut and count experiment is to use distributions of events in the signal region to set limits rather than simply counting the total number. By using distributions, the data can be compared to the background only and signal+background hypotheses in each bin of the distribution. Ideally the variable used for the distribution is highly discriminant between signal and background. To set limits, the likelihood functions given in Eq. 9.2 would be a product over all categories that define the signal region as well as every bin of the distributions in each category. A major limitation of this approach is that there must be large enough statistics that the true shape of the events can be seen. This is only a concern for the data and the data-driven background since one can always generate more MC events if necessary. If there are too few events no consistent shape will emerge from the distributions. Also, the statistical error will be large due to the very small number of events in each bin. Given sufficient statistics distributions can be used to exploit differences in the shape of signal and background events and increase the overall signal significance for the analysis.

An alternative to defining the signal region with a set of cuts on separate variables is to implement a multivariate analysis (MVA). In an MVA a weight is determined based on several variables which characterizes the likelihood that an event is signal or background. By using a single multivariate function an MVA can account for correlations between variables in order to better isolate regions of phase space with high signal sensitivity. The signal region can be defined by placing a cut on the

MVA weight. Alternatively the weight can be used as a distribution from which to set limits. A study was carried out using a subset of the data collected in 2012 to explore the possibility to implementing an MVA known as a Boosted Decision Tree (BDT) in the analysis of the full 2012 data set. A comparison was made between the results of a simple cut and count analysis and a BDT analysis. The results of this comparison are given in Section 6.4. The expected limits produced by the BDT analysis were slightly better than those produced by the cut and count analysis. Despite this, ultimately it was decided to proceed with the cut and count approach with the categorization of the signal region outlined in Table 6.3. It was decided on the basis of the optimization study carried out on the $t\bar{t}t\bar{t}$ signal (see Section 6.2) to implement the categorization method outlined in Table 6.3 rather than this MVA approach.

Higher energy collisions produce boosted final state objects whose decay products are collimated. Already in the 2012 analysis, techniques were introduced to account for this. The variable ΔR requirement applied to muons and the mini-isolation requirement applied to both electrons and muons were introduced to accept more boosted events from signal. These requirements are described in detail in Section 5.1. Although this allows leptons to be less isolated in boosted events the selection still requires each final state particle to produce a resolved object in the detector. In many high energy events, particles are so boosted that their decay products produce a single very large jet in the detector. These large jets can be reconstructed using the anti-k_t algorithm described in Section 5.1.1 with a large value of the constant R used in the definition of the distance parameter d_{ij}. Many other analyses in 2012 have added channels that look for such large R jets and reconstruct them as boosted W bosons or top quarks. An example is the search for $t\bar{t}$ resonances in the lepton+jets channel carried out with the ATLAS 2012 data [153]. Adding such channels may be very beneficial for the Run II continuation of this analysis.

Figure 10.1 shows that the increase in luminosity and collision energy alone in Run II will significantly improve the sensitivity of the search for vector-like quarks in trilepton and same-sign dilepton events. In addition to this, the analysis may be improved further by introducing techniques such as the use of distributions in comparing data with background and signal+background models, multivariate techniques such as BDTs and the addition of extra channels for boosted events. These techniques were not applied in Run I due to limited statistics in the signal region. Run II should provide sufficient statistics to make them valuable. The large increase in the luminosity and energy of the LHC in Run II, as well as the possibility of improved analysis techniques, mean that there is great potential to continue the search for vector-like quarks in this unique final state and further investigate the intriguing excess in data seen in Run I.

REFERENCES

[1] R. Bouchendira, P. Clade, S. Guellati-Khelifa, F. Nez, and F. Biraben, *New Determination of the fine structure constant and test of the quantum electrodynamics*, Phys.Rev.Lett **106** (2011) 0801, `arXiv:1012.3227 [physics.atom-ph]`.

[2] J. Thompson, *Cathode Rays*, The Electrician **39** (1987) 104–109.

[3] Particle Data Group Collaboration, K. Olive et al., *Review of Particle Physics*, Chin.Phys. **C38** (2014) 090001.

[4] *Observation of a new particle in the search for the Standard Model Higgs boson with the ATLAS detector at the LHC*, Physics Letters B **716** no. 1, (2012) 1 – 29.

[5] V. Mitsou et al., *The ATLAS Transition Radiation Tracker*, tech. rep., CERN, Geneva, Nov, 2003. `arXiv:0311058v1 [hep-ex]`.

[6] P. W. Higgs, *Broken Symmetries and the Masses of Gauge Bosons*, Phys.Rev.Lett. **13** (1964) 508–509.

[7] F. Englert and R. Brout, *Broken Symmetry and the Mass of Gauge Vector Mesons*, Phys.Rev.Lett. **13** (1964) 321–323.

[8] Planck Collaboration, P. Ade et al., *Planck 2013 Results. I. Overview of products and scientific results*, Astron.Astrophys **571** (2014), `arXiv:1303.5062 [astro-phys]`.

[9] M. L. Perl, G. S. Abrams, A. M. Boyarski, M. Breidenbach, D. D. Briggs, F. Bulos, W. Chinowsky, J. T. Dakin, G. J. Feldman, C. E. Friedberg, D. Fryberger, G. Goldhaber, G. Hanson, F. B. Heile, B. Jean-Marie, and et

al., *Evidence for anomalous lepton production in e^+e^- annihilation*, Physical Review Letters **35** (1975) 1489–1492.

[10] F. Abe, H. Akimoto, A. Akopian, M. G. Albrow, S. R. Amendolia, D. Amidei, J. Antos, C. Anway-Wiese, S. Aota, G. Apollinari, and et al., *Observation of Top Quark Production in pp Collisions with the Collider Detector at Fermilab*, Physical Review Letters **74** (1995) 2626–2631, `arXiv:9503002 [hep-ph]`.

[11] S. Abachi, B. Abbott, M. Abolins, B. S. Acharya, I. Adam, D. L. Adams, M. Adams, S. Ahn, H. Aihara, G. Álvarez, and et al., *Search for High Mass Top Quark Production in pp Collisions at s = 1.8 TeV*, Physical Review Letters **74** (1995) 2422–2426, `arXiv:9411001 [hep-ph]`.

[12] B. A. Dobrescu and C. T. Hill, *Electroweak symmetry breaking via top condensation seesaw*, Phys.Rev.Lett. **81** (1998) 2634–2637, `arXiv:9712319 [hep-ph]`.

[13] R. S. Chivukula, B. A. Dobrescu, H. Georgi, and C. T. Hill, *Top quark seesaw theory of electroweak symmetry breaking*, Phys.Rev. **D59** (1999) 075003, `arXiv:9809470 [hep-ph]`.

[14] H.-J. He, C. T. Hill, and T. M. Tait, *Top quark seesaw, vacuum structure and electroweak precision constraints*, Phys.Rev. **D65** (2002) 055006, `arXiv:0108041 [hep-ph]`.

[15] C. T. Hill and E. H. Simmons, *Strong dynamics and electroweak symmetry breaking*, Phys.Rept. **381** (2003) 235–402, `arXiv:0203079 [hep-ph]`.

[16] R. Contino, L. Da Rold, and A. Pomarol, *Light custodians in natural composite Higgs models*, Phys.Rev. **D75** (2007) 055014, `arXiv:0612048 [hep-ph]`.

[17] C. Anastasiou, E. Furlan, and J. Santiago, *Realistic Composite Higgs Models*, Phys.Rev. **D79** (2009) 075003, `arXiv:0901.2117 [hep-ph]`.

[18] K. Kong, M. McCaskey, and G. W. Wilson, *Multi-lepton signals from the top-prime quark at the LHC*, JHEP **1204** (2012) 079, arXiv:1112.3041 [hep-ph].

[19] A. Carmona, M. Chala, and J. Santiago, *New Higgs Production Mechanism in Composite Higgs Models*, JHEP **1207** (2012) 049, arXiv:1205.2378 [hep-ph].

[20] M. Gillioz, R. Grober, C. Grojean, M. Muhlleitner, and E. Salvioni, *Higgs Low-Energy Theorem (and its corrections) in Composite Models*, JHEP **1210** (2012) 004, arXiv:1206.7120 [hep-ph].

[21] A. Davidson and K. C. Wali, *Family mass hierarchy from universal seesaw mechanism*, Phys. Rev. Lett. **60** (1988) 1813–1816.

[22] K. S. Babu and R. N. Mohapatra, *Solution to the strong* CP *problem without an axion*, Phys. Rev. D **41** (1990) 1286–1291.

[23] B. Grinstein, M. Redi, and G. Villadoro, *Low Scale Flavor Gauge Symmetries*, JHEP **1011** (2010) 067, arXiv:1009.2049 [hep-ph].

[24] D. Guadagnoli, R. N. Mohapatra, and I. Sung, *Gauged Flavor Group with Left-Right Symmetry*, JHEP **1104** (2011) 093, arXiv:1103.4170 [hep-ph].

[25] N. Arkani-Hamed, A. Cohen, E. Katz, and A. Nelson, *The Littlest Higgs*, JHEP **0207** (2002) 034, arXiv:0206021 [hep-ph].

[26] T. Han, H. E. Logan, B. McElrath, and L.-T. Wang, *Phenomenology of the little Higgs model*, Phys.Rev. **D67** (2003) 095004, arXiv:0301040 [hep-ph].

[27] M. Perelstein, M. E. Peskin, and A. Pierce, *Top quarks and electroweak symmetry breaking in little Higgs models*, Phys.Rev. **D69** (2004) 075002, arXiv:0310039 [hep-ph].

[28] M. Schmaltz and D. Tucker-Smith, *Little Higgs review*, Ann.Rev.Nucl.Part.Sci. **55** (2005) 229–270, arXiv:0502182 [hep-ph].

[29] M. S. Carena, J. Hubisz, M. Perelstein, and P. Verdier, *Collider signature of T-quarks*, Phys.Rev. **D75** (2007) 091701, arXiv:0610156 [hep-ph].

[30] S. Matsumoto, T. Moroi, and K. Tobe, *Testing the Littlest Higgs Model with T-parity at the Large Hadron Collider*, Phys.Rev. **D78** (2008) 055018, arXiv:0806.3837 [hep-ph].

[31] E. Noether, *Invariant Variation Problems*, Math-phys. Klasse (1918) 235–257.

[32] R. Feynman, *Mathematical Formulation of the Quantum Theory of Electromagnetic Interaction*, Physical Review **80(3)** (1950) 440–457.

[33] Particle Data Group Collaboration, K. Nakamura et al., *Review of particle physics*, 2010.

[34] ATLAS, CMS Collaboration, G. Aad et al., *Combined Measurement of the Higgs Boson Mass in pp Collisions at $\sqrt{s} = 7$ and 8 TeV with the ATLAS and CMS Experiments*, Phys.Rev.Lett. **114** (2015) 191803, arXiv:1503.07589 [hep-ex].

[35] J.-L. Kneur and A. Neveu, $\Lambda^{\mathrm{QCD}}_{\overline{\mathrm{MS}}}$ *from Renormalization Group Optimized Perturbation*, Phys.Rev. **D85** (2012) 014005, arXiv:1108.3501 [hep-ph].

[36] R. Placakyte, *Parton Distribution Functions*, in *Proceedings, 31st International Conference on Physics in collisions (PIC 2011)*. 2011. arXiv:1111.5452 [hep-ph]. http://inspirehep.net/record/954990/files/arXiv:1111.5452.pdf.

[37] D. Grifiths, *Introduction to Elementary Particles.* Wiley-VCH, Weinheim, 2008.

[38] C. Amsler et al., *Review of Particle Physics*, Physics Letters B **667** (2008).

[39] D. E. Boumediene, E. Busato, D. Calvet, S. Calvet, E. Dubreuil, S. Grancagnolo, R. Kukla, H. Lacker, X. Lei, R. Nayyar, F. Oǵrady, D. Paredes Hernandez, D. Simon, D. Sperlich, L. Valery, and E. Varnes, *Study of events with b-jets and two leptons of the same charge or three leptons in pp collisions at* $\sqrt{s} = 8$ *TeV with the ATLAS detector*, Tech. Rep. ATL-COM-PHYS-2014-1425, CERN, Geneva, Oct, 2014. `https://cds.cern.ch/record/1966200`.

[40] CMS Collaboration Collaboration, D. Pagano, *Search for exotic heavy quark partners*, Tech. Rep. CMS-CR-2013-150, CERN, Geneva, Jun, 2013. `http://cds.cern.ch/record/1558645`.

[41] G. D. Kribs, T. Plehn, M. Spannowsky, and T. M. Tait, *Four Generations and Higgs Physics*, Phys.Rev **D76** (2006), `arXiv:0706.3718 [hep-ph]`.

[42] CMS Collaboration Collaboration, S. Chatrchyan et al., *Observation of a new boson at a mass of 125 GeV with the CMS experiment at the LHC*, Phys.Lett. **B716** (2012) 30–61, `arXiv:1207.7235 [hep-ex]`.

[43] O. Eberhardt, G. Herbert, H. Lacker, A. Lenz, A. Menzel, et al., *Impact of a Higgs boson at a mass of 126 GeV on the standard model with three and four fermion generations*, Phys.Rev.Lett. **109** (2012) 241802, `arXiv:1209.1101 [hep-ph]`.

[44] A. Djouadi and A. Lenz, *Sealing the fate of a fourth generation of fermions*, Phys. Lett. **B715** (2012) 310–314, `arXiv:1204.1252 [hep-ph]`.

[45] O. Eberhardt, G. Herbert, H. Lacker, A. Lenz, A. Menzel, et al., *Joint analysis of Higgs decays and electroweak precision observables in the Standard Model with a sequential fourth generation*, `arXiv:1204.3872 [hep-ph]`.

[46] O. Eberhardt, A. Lenz, A. Menzel, U. Nierste, and M. Wiebusch, *Status of the fourth fermion generation before ICHEP2012: Higgs data and electroweak precision observables*, `arXiv:1207.0438 [hep-ph]`.

[47] A. Denner, S. Dittmaier, A. Muck, G. Passarino, M. Spira, et al., *Higgs Production and Decay with a Fourth Standard-Model-Like Fermion Generation*, Eur.Phys.J. **C72** (2012) 1992, `arXiv:1111.6395 [hep-ph]`.

[48] G. Passarino, C. Sturm, and S. Uccirati, *Complete Electroweak Corrections to Higgs production in a Standard Model with four generations at the LHC*, Phys.Lett. **B706** (2011) 195–199, `arXiv:1108.2025 [hep-ph]`.

[49] S. Bar-Shalom, M. Geller, S. Nandi, and A. Soni, *Two Higgs doublets, a 4th generation and a 125 GeV Higgs: A review.*, Adv. High Energy Phys. **2013** (2013) 672972, `arXiv:1208.3195 [hep-ph]`.

[50] F. del Aguila and M. J. Bowick, *The Possibility of New Fermions With Δ I = 0 Mass*, Nucl.Phys. **B224** (1983) 107.

[51] ATLAS Collaboration, G. Aad et al., *Search for production of vector-like quark pairs and of four top quarks in the lepton-plus-jets final state in pp collisions at* $\sqrt{s} = 8$ *TeV with the ATLAS detector*, `arXiv:1505.04306 [hep-ex]`.

[52] *Search for pair and single production of new heavy quarks that decay to a Z boson and a third generation quark in pp collisions at* $\sqrt{s} = 8$ *TeV with the ATLAS detector*, Tech. Rep. ATLAS-CONF-2014-036, CERN, Geneva, Jul, 2014. `http://cds.cern.ch/record/1735195`.

[53] J. Aguilar-Saavedra, R. Benbrik, S. Heinemeyer, and M. Prez-Victoria, *Handbook of vectorlike quarks: Mixing and single production*, Phys.Rev. **D88** no. 9, (2013) 094010, `arXiv:1306.0572 [hep-ph]`.

[54] M. Buchkremer, G. Cacciapaglia, A. Deandrea, and L. Panizzi, "Feynrules Exotic (X,T) doublet model." `http://feynrules.irmp.ucl.ac.be/wiki/VLQ_xtdoubletvl`.

[55] M. Buchkremer, G. Cacciapaglia, A. Deandrea, and L. Panizzi, *Model Independent Framework for Searches of Top Partners*, Nucl.Phys. **B876** (2013) 376–417, arXiv:1305.4172 [hep-ph].

[56] O. S. Bruning, P. Collier, P. Lebrun, S. Myers, R. Ostojic, J. Poole, and P. Proudlock, *LHC Design Report Volume 1.* CERN, Geneva, 2004.

[57] O. S. Bruning, P. Collier, P. Lebrun, S. Myers, R. Ostojic, J. Poole, and P. Proudlock, *LHC Design Report Volume 2.* CERN, Geneva, 2004.

[58] C. Campagnari and M. Franklin, *The Discovery of the top quark*, Rev.Mod.Phys. **69** (1997) 137–212, arXiv:hep-ex/9608003 [hep-ex].

[59] "www.maalpu.org." http://maalpu.org/lhc/LHC.main.htm.

[60] M. Benedikt, P. Collier, V. Mertens, J. Poole, and K. Schindl, *LHC Design Report.* CERN, Geneva, 2004.

[61] T. Lenzi, *Development and Study of Different Muon Track Reconstruction Algorithms for the Level-1 Trigger for the CMS Muon Upgrade with GEM Detectors*, arXiv:1306.0858 [physics.ins-det].

[62] A. Team, "Computer-generated diagram of an LHC dipole. Schma d'un diple du LHC." CERN-DI-9809007, Sep, 1998.

[63] ATLAS Collaboration, W. Armstrong et al., *ATLAS: Technical proposal for a general-purpose p-p experiment at the Large Hadron Collider at CERN*,. CERN-LHCC-94-43.

[64] ATLAS Collaboration, *ATLAS detector and physics performance: Technical Design Report, 1.* Technical Design Report ATLAS. CERN, Geneva, 1999. Electronic version not available.

[65] ATLAS Collaboration, *ATLAS detector and physics performance: Technical Design Report, 2*. Technical Design Report ATLAS. CERN, Geneva, 1999. Electronic version not available.

[66] ATLAS Collaboration, G. Aad, S. Bentvelsen, G. J. Bobbink, and K. Bos, *The ATLAS Experiment at the CERN Large Hadron Collider*, J. Instrum. **3** (2008) S08003. 437 p. Also published by CERN Geneva in 2010.

[67] ATLAS Collaboration, G. Aad et al., *Studies of the performance of the ATLAS detector using cosmic-ray muons*, Eur.Phys.J. **C71** (2011) 1593, `arXiv:1011.6665 [physics.ins-det]`.

[68] M. Skaarup, *Diffractive pp interactions: A study of diffractive pp interactions at the LHC using a tagged proton at* , Master's thesis, University of Copenhagen, 2013. `http://discoverycenter.nbi.ku.dk/teaching/thesis_page/Mikkel-Thesis.pdf`. Presented 15 October 2013.

[69] ATLAS Collaboration, *ATLAS inner detector: Technical Design Report, 1*. Technical Design Report ATLAS. CERN, Geneva, 1997.

[70] ATLAS Collaboration, *ATLAS inner detector: Technical design report. Vol. 2*,.

[71] ATLAS Collaboration, G. Aad et al., *Operation and performance of the ATLAS semiconductor tracker*, JINST **9** (2014) P08009, `arXiv:1404.7473 [hep-ex]`.

[72] ATLAS Collaboration, N. Wermes and G. Hallewel, *ATLAS pixel detector: Technical Design Report*. Technical Design Report ATLAS. CERN, Geneva, 1998.

[73] SCT Collaboration, U. Y et al., *ATLAS silicon microstrip detector system (SCT)*, vol. A 511. NUCLEAR INSTRUMENTS & METHODS IN PHYSICS RESEARCH, 2003.

[74] ATLAS TRT Collaboration, E. Abat et al., *The ATLAS Transition Radiation Tracker (TRT) proportional drift tube: Design and performance*, JINST **3** (2008) P02013.

[75] ATLAS Collaboration, *ATLAS liquid-argon calorimeter: Technical Design Report*. Technical Design Report ATLAS. CERN, Geneva, 1996.

[76] ATLAS Collaboration, *ATLAS tile calorimeter: Technical Design Report*. Technical Design Report ATLAS. CERN, Geneva, 1996.

[77] ATLAS Collaboration, *The ATLAS Experiment at the CERN Large Hadron Collider*, JINST **3** (2008) S08003.

[78] *Muons in the Calorimeters: Energy Loss Corrections and Muon Tagging*, Tech. Rep. ATL-PHYS-PUB-2009-009. ATL-COM-PHYS-2009-153, CERN, Geneva, Mar, 2009. `http://cds.cern.ch/record/1169055`.

[79] ATLAS Collaboration, *ATLAS muon spectrometer: Technical Design Report*. Technical Design Report ATLAS. CERN, Geneva, 1997.

[80] ATLAS Collaboration, G. Aad et al., *Commissioning of the ATLAS Muon Spectrometer with Cosmic Rays*, Eur. Phys. J. C **70** no. CERN-PH-EP-2010-045, (2010) 875–916. 58 p, `arXiv:1006.4384 [hep-ex]`.

[81] G. Mikenberg, *The ATLAS muon spectrometer*, Mod.Phys.Lett. **A25** (2010) 649–667.

[82] A. Corso-Radu, S. Kolos, H. Hadavand, R. Kehoe, and M. Hauschild, *Data Quality Monitoring Framework for the ATLAS Experiment at the LHC*, Tech. Rep. ATL-DAQ-CONF-2008-006. ATL-COM-DAQ-2007-033, CERN, Geneva, Oct, 2007. `http://cds.cern.ch/record/1061900`.

[83] "Muon Shift Manual and Reference Guide webpage."

https://atlasop.cern.ch/twiki/bin/view/Main/MuonOperationManualShifter.

[84] ATLAS Collaboration, *ATLAS level-1 trigger: Technical Design Report*. Technical Design Report ATLAS. CERN, Geneva, 1998.

[85] ATLAS Collaboration, P. Jenni, M. Nessi, M. Nordberg, and K. Smith, *ATLAS high-level trigger, data-acquisition and controls: Technical Design Report*. Technical Design Report ATLAS. CERN, Geneva, 2003.

[86] ATLAS Collaboration, *ATLAS High-Level Triggers, DAQ and DCS Technical Proposal*,. CERN-LHCC-2000-17.

[87] ATLAS Collaboration, *ATLAS trigger performance: Status report*,. CERN-LHCC-98-15.

[88] ATLAS Collaboration, *ATLAS DAQ, EF, LVL2 and DCS: Technical progress report*,. CERN-LHCC-98-16.

[89] TOTEM Collaboration Collaboration, G. Antchev, P. Aspell, I. Atanassov, V. Avati, J. Baechler, V. Berardi, M. Berretti, E. Bossini, M. Bozzo, U. Bottigli, E. Brucken, A. Buzzo, F. S. Cafagna, M. Calicchio, M. G. Catanesi, C. Covault, M. Csanad, T. Csorgo, M. Deile, M. Doubek, K. Eggert, V. Eremin, R. Ferretti, F. Ferro, A. Fiergolski, F. Garcia, S. Giani, V. Greco, L. Grzanka, J. Heino, T. Hilden, R. A. Intonti, J. Kavspar, J. Kopal, V. Kundrat, K. Kurvinen, S. Lami, G. Latino, R. Lauhakangas, T. Leszko, E. Lippmaa, M. Lokajivcek, M. Lo Vetere, F. Lucas-Rodriguez, M. Macri, T. Maki, A. Mercadante, N. Minafra, S. Minutoli, F. Nemes, H. Niewiadomski, E. Oliveri, F. Oljemark, R. Orava, M. Oriunno, K. Osterberg, P. Palazzi, J. Prochazka, M. Quinto, E. Radermacher, E. Radicioni, F. Ravotti, E. Robutti, L. Ropelewski, G. Ruggiero, H. Saarikko, A. Santroni, A. Scribano, J. Smajek, W. Snoeys, J. Sziklai, C. Taylor, N. Turini, V. Vacek, M. Vitek, J. Welti, J. Whitmore,

and P. Wyszkowski, *Luminosity-Independent Measurement of the Proton-Proton Total Cross Section at $\sqrt{s} = 8$ TeV*, Phys. Rev. Lett. **111** no. TOTEM-2012-005. CERN-PH-EP-2012-354, (2012) 012001. 8 p.

[90] ATLAS Collaboration, G. Duckeck, D. Barberis, R. Hawkings, R. Jones, N. McCubbin, G. Poulard, D. Quarrie, T. Wenaus, and E. Obreshkov, *ATLAS computing: Technical design report*,. CERN-LHCC-2005-022, ATLAS-TRD-017.

[91] B. Acharya, J. Adelman, S. Adomeit, M. Aoki, B. Alvarez, F. Balli, W. Bell, K. Becker, K. Behr, D. Benjamin, E. Bergeaas Kuutmann, C. Bernard, K. Black, S. Calvet, R. Camacho, Y. Coadou, G. Cortiana, N. Cooper-Smith, T. Cornelissen, M. Cristinziani, V. Dao, U. De Sanctis, C. Doglioni, F. Derue, K. Finelli, K. Grahn, J. Groth-Jensen, S. Head, A. Henrichs, D. Hirschbuehl, V. Kaushik, O. Kind, H. Khandanyan, A. Krasznahorkay, T. Kuhl, E. Le Menedeu, H. Lee, A. Lister, K. Loureiro, L. Miljovic, J. Morris, R. Moles Valls, O. Nackenhorst, D. Pelikan, M. Owen, M. Pinamonti, K. Rao, K. Rosbach, M. Rudolph, G. Salamanna, J. Schwindling, J. Searcy, E. Shabalina, K. Shaw, J. Sjolin, R. Soualah, S. Stamm, D. Ta, T. Theveneaux-Pelzer, E. Thompson, K. Uchida, L. Valery, M. Vreeswijk, C. Wasicki, I. Watson, K. Yau, J. Zhong, H. Zhu, and M. zur Nedden, *Object selection and calibration, background estimations and MC samples for the Winter 2013 Top Quark analyses with 2012 data*, Tech. Rep. ATL-COM-PHYS-2013-088, CERN, Geneva, Jan, 2013.

[92] M. Wielers, R. Mantifel, A. Tricoli, and P. Bell, *Single Electron Trigger Performance Plots*, Tech. Rep. ATL-COM-DAQ-2012-146, CERN, Geneva, Jun, 2012. `https://cds.cern.ch/record/1456795`.

[93] ATLAS Collaboration, G. Aad et al., *Performance of the ATLAS muon trigger in pp collisions at $\sqrt{s} = 8$ TeV*, Eur.Phys.J. **C75** no. 3, (2015) 120, `arXiv:1408.3179 [hep-ex]`.

[94] A. D. Preparation, "Coma period runs report." https://atlas-tagservices.cern.ch/tagservices/RunBrowser/runBrowserReport/runBrowserReport.php?fnt=data12_8TeV&pn=AllYear. Accessed March 11, 2012.

[95] A. D. Preparation, "Goodrunslists for analysis." https://twiki.cern.ch/twiki/bin/view/AtlasProtected/GoodRunListsForAnalysis. Accessed March 11, 2012.

[96] S. Maettig, *Luminosity Measurements with the ATLAS Detector*,. CERN-THESIS-2012-249.

[97] A. D. Preparation, "Luminosity calculator." https://atlas-lumicalc.cern.ch. Accessed March 11, 2012.

[98] "Atlas experiment - public results: Luminositypublicresults." https://twiki.cern.ch/twiki/bin/view/AtlasPublic/LuminosityPublicResults.

[99] J. M. Butterworth, G. Dissertori, and G. P. Salam, *Hard Processes in Proton-Proton Collisions at the Large Hadron Collider*, Ann.Rev.Nucl.Part.Sci. **62** (2012) 387–405, arXiv:1202.0583 [hep-ex].

[100] A. D. Preparation, "Coma period runs report." https://atlas-tagservices.cern.ch/tagservices/RunBrowser/runBrowserReport/rBR_Period_Report.php?fnt=data12_8TeV. Accessed March 11, 2012.

[101] M. Boonekamp, F. Gianotti, R. A. McPherson, M. Nessi, and P. Nevksi, *Cosmic Ray, Beam-Halo and Beam-Gas Rate Studies for ATLAS Commissioning*, Tech. Rep. ATL-GEN-2004-001, CERN, Geneva, Feb, 2004.

[102] J. Alwall, M. Herquet, F. Maltoni, O. Mattelaer, and T. Stelzer, *MadGraph 5 : Going Beyond*, JHEP **1106** (2011) 128, arXiv:1106.0522 [hep-ph].

[103] T. Sjostrand, S. Mrenna, and P. Z. Skands, *PYTHIA 6.4 Physics and Manual*, JHEP **0605** (2006) 026, arXiv:0603175 [hep-ph].

[104] T. Sjostrand, S. Mrenna, and P. Z. Skands, *A Brief Introduction to PYTHIA 8.1*, Comput.Phys.Commun. **178** (2008) 852–867, arXiv:0710.3820 [hep-ph].

[105] T. Gleisberg, S. Hoeche, F. Krauss, M. Schonherr, S. Schumann, F. Siegert, and J. Winter, *Event generation with SHERPA 1.1*, JHEP **02** (2009) 007, arXiv:0811.4622 [hep-ph].

[106] J. Aguilar-Saavedra, *Identifying top partners at LHC*, JHEP **0911** (2009) 030, arXiv:0907.3155 [hep-ph].

[107] S. Agostinelli et al., *Geant4 A Simulation Toolkit*, Nucl. Instr. and Meth. **A506** (2003) 250.

[108] ATLAS Collaboration, *The ATLAS Simulation Infrastructure*, Eur. Phys. J. **C70** (2010) 823–874, arXiv:1005.4568 [physics.ins-det].

[109] T. Yamanaka, *The ATLAS calorimeter simulation FastCaloSim*, ATL-SOFT-PROC-2011-021 (2011).

[110] *Search for anomalous production of trilepton and same-sign dilepton events associated with b-jets in 20.3 fb^{-1} of pp collisions at $\sqrt{s} = 8$ TeV with the ATLAS detector*, Tech. Rep. ATLAS-COM-PHYS-2013-1587, CERN, Geneva, Dec, 2013.

[111] B. Acharya, J. Adelman, S. Adomeit, M. Aoki, B. Alvarez, L. Asquith, F. Balli, W. Bell, K. Becker, K. Behr, D. Benjamin, E. Bergeaas Kuutmann, C. Bernard, K. Black, S. Calvet, R. Camacho, Y. Coadou, G. Cortiana, G. Compostella, N. Cooper-Smith, T. Cornelissen, M. Cristinziani, V. Dao, U. De Sanctis, C. Doglioni, F. Derue, C. Eckardt, J. Ferrando, D. Ferreira de Lima, K. Finella, K. Grahn, J. Groth-Jensen, N. Gutierrez Ortiz,

R. Hawkings, S. Head, A. Henrichs, D. Hirschbuehl, G. Kasieczka, V. Kaushik, H. Khandanyan, O. Kind, A. Krasznahorkay, T. Kuhl, H. Lacker, E. Le Menedeu, H. Lee, A. Lister, K. Loureiro, L. Mijovic, J. Morris, R. Moles Valls, O. Nackenhorst, M. zur Nedden, M. Owen, D. Pelikan, M. Pinamonti, K. Rao, K. Rosbach, M. Rudolph, G. Salamanna, J. Schwindling, J. Searcy, E. Shabalina, K. Shaw, J. Sjolin, R. Soualah, S. Stamm, D. Ta, T. Theveneaux-Pelzer, E. Thompson, K. Uchikda, L. Valery, M. Vreeswijk, C. Wasicki, I. Watson, K. Yau, J. Zhong, and H. Zhu, *Object selection and calibration, background estimations and MC samples for top quark analyses using the full 2012 data set*, Tech. Rep. ATL-COM-PHYS-2013-1016, CERN, Geneva, Jul, 2013.

[112] M. Cacciari, G. P. Salam, and G. Soyez, *The Anti-k(t) jet clustering algorithm*, JHEP **0804** (2008) 063, `arXiv:0802.1189 [hep-ph]`.

[113] M. Cacciari and G. P. Salam, *Dispelling the N^3 myth for the k_t jet-finder*, Phys. Lett. **B641** (2006) 57–61, `arXiv:0512210 [hep-ph]`.

[114] M. Cacciari, G. P. Salam, and G. Soyez, *FastJet User Manual*, Eur.Phys.J. **C72** (2012) 1896, `arXiv:1111.6097 [hep-ph]`.

[115] ATLAS Collaboration, G. Aad et al., *Jet energy measurement with the ATLAS detector in proton-proton collisions at $\sqrt{s} = 7$ TeV*, Eur.Phys.J. **C73** (2013) 2304, `arXiv:1112.6426 [hep-ex]`.

[116] ATLAS Collaboration, *Selection of jets produced in proton-proton collisions with the ATLAS detector using 2011 data*, Tech. Rep. ATLAS-CONF-2012-020, CERN, Geneva, Mar, 2012.

[117] D. W. Miller, A. Schwartzman, and D. Su, *Pile-up jet energy scale corrections using the jet-vertex fraction method*, Tech. Rep. ATL-COM-PHYS-2009-180, CERN, Geneva, Apr, 2009.

[118] ATLAS Collaboration, *Commissioning of the ATLAS high-performance b-tagging algorithms in the 7 TeV collision data*, ATLAS-CONF-2011-102, ATLAS-COM-CONF-2011-110.

[119] A. Collaboration, *Electron efficiency measurements with the ATLAS detector using the 2012 LHC proton-proton collision data*, Tech. Rep. ATLAS-CONF-2014-032, CERN, Geneva, Jun, 2014.

[120] K. Rehermann and B. Tweedie, *Efficient Identification of Boosted Semileptonic Top Quarks at the LHC*, JHEP **1103** (2011) 059, `arXiv:1007.2221 [hep-ph]`.

[121] ATLAS Collaboration, G. Aad et al., *Electron reconstruction and identification efficiency measurements with the ATLAS detector using the 2011 LHC proton-proton collision data*, Eur.Phys.J. **C74** no. 7, (2014) 2941, `arXiv:1404.2240 [hep-ex]`.

[122] ATLAS Collaboration, G. Aad et al., *Measurement of the muon reconstruction performance of the ATLAS detector using 2011 and 2012 LHC proton-proton collision data*, Eur.Phys.J. **C74** no. 11, (2014) 3130, `arXiv:1407.3935 [hep-ex]`.

[123] A. Collaboration, *Performance of Missing Transverse Momentum Reconstruction in ATLAS studied in Proton-Proton Collisions recorded in 2012 at 8 TeV*, Tech. Rep. ATLAS-CONF-2013-082, CERN, Geneva, Aug, 2013. `https://cds.cern.ch/record/1570993`.

[124] A. Collaboration, *Search for anomalous production of events with same-sign dileptons and b jets in 14.3 fb^{-1} of pp collisions at $\sqrt{s} = 8$ TeV with the ATLAS detector*, Tech. Rep. ATLAS-CONF-2013-051, CERN, Geneva, May, 2013.

[125] A. Hocker, J. Stelzer, F. Tegenfeldt, H. Voss, K. Voss, et al., *TMVA - Toolkit for Multivariate Data Analysis*, PoS **ACAT** (2007) 040, arXiv:physics/0703039 [physics.data-an].

[126] T. Sjostrand and S. Mrenna and P.Z. Skands, *PYTHIA 6.4 Physics and Manual*, JHEP **05** (2006) 026, 0603175.

[127] J. M. Campbell and R. K. Ellis, *$t\bar{t}W^{+-}$ production and decay at NLO*, JHEP **1207** (2012) 052, arXiv:1204.5678 [hep-ph].

[128] M. Garzelli, A. Kardos, C. Papadopoulos, and Z. Trocsanyi, *$t\,\bar{t}\,W^{+-}$ and $t\,\bar{t}$ Z Hadroproduction at NLO accuracy in QCD with Parton Shower and Hadronization effects*, JHEP **1211** (2012) 056, arXiv:1208.2665 [hep-ph].

[129] S. Dittmaier, S. Dittmaier, C. Mariotti, G. Passarino, R. Tanaka, et al., *Handbook of LHC Higgs Cross Sections: 2. Differential Distributions*, arXiv:1201.3084 [hep-ph].

[130] LHC Higgs Cross Section Working Group Collaboration, S. Heinemeyer et al., *Handbook of LHC Higgs Cross Sections: 3. Higgs Properties*, arXiv:1307.1347 [hep-ph].

[131] J. M. Campbell and R. Ellis, *MCFM for the Tevatron and the LHC*, Nucl.Phys.Proc.Suppl. **205-206** (2010) 10–15, arXiv:1007.3492 [hep-ph]. http://mcfm.fnal.gov.

[132] J. R. Gaunt, C.-H. Kom, A. Kulesza, and W. J. Stirling, *Same-sign W pair production as a probe of double parton scattering at the LHC*, Eur.Phys.J. **C69** (2010) 53–65, arXiv:1003.3953 [hep-ph].

[133] A. Collaboration, *Estimation of non-prompt and fake lepton backgrounds in final states with top quarks produced in proton-proton collisions at $\sqrt{s} = 8$ TeV with the ATLAS detector*, Tech. Rep. ATLAS-CONF-2014-058, CERN, Geneva, Oct, 2014.

[134] S. Frixione and B. R. Webber, *Matching NLO QCD computations and parton shower simulations*, JHEP **06** (2002) 029, arXiv:0204244 [hep-ph].

[135] M. L. Mangano, M. Moretti, F. Piccinini, R. Pittau, and A. D. Polosa, *ALPGEN, a generator for hard multiparton processes in hadronic collisions*, JHEP **0307** (2003) 001, arXiv:0206293 [hep-ph].

[136] K. Becker, T. Cornelissen, F. Derue, A. Henrichs, D. Hirschbhl, X. Lei, O. Nackenhorst, F. O'Grady, D. Pelikan, M. Pinamonti, S. Pires, J. Sjlin, and P. Tepel, *Estimation of Fake Lepton Background for Top Analyses Using the $\sqrt{s} = 8$ TeV Dataset*, Tech. Rep. ATL-COM-PHYS-2013-1100, CERN, Geneva, Aug, 2013.

[137] D. Paredes and D. Calvet, *Estimation of the mis-identification rates of the electron charge at 8 TeV*, Tech. Rep. ATL-COM-PHYS-2013-1622, CERN, Geneva, Dec, 2013.

[138] ATLAS Collaboration, *Jet energy scale and its systematic uncertainty in proton-proton collisions at sqrt(s)=7 TeV with ATLAS 2011 data*, Tech. Rep. ATLAS-CONF-2013-004, CERN, Geneva, Jan, 2013. http://cds.cern.ch/record/1509552.

[139] ATLAS Collaboration, G. Aad et al., *Improved luminosity determination in pp collisions at $\sqrt{s} = 7$ TeV using the ATLAS detector at the LHC*, Eur.Phys.J. **C73** (2013) 2518, arXiv:1302.4393 [hep-ex].

[140] P. Anger, B. Axen, T. Dai, C. Gumpert, C. Hasterok, B. Heinemann, M. Hurwitz, N. Ilic, M. Kobel, J. Liu, L. Liu, J. Metcalfe, S. Pagan Griso, B. Zhou, S. Hou, M.-A. Pleier, U. Schnoor, J. Searcy, F. Socher, A. Sood, A. Vest, L. Xu, and J. Zhu, *Same Sign $W^{\pm}W^{\pm}$ Production and Limits on Anomalous Quartic Gauge Couplings*, Tech. Rep. ATL-COM-PHYS-2013-990, CERN, Geneva, Jul, 2013.

[141] T. Binoth, G. Ossola, C. Papadopoulos, and R. Pittau, *NLO QCD corrections to tri-boson production*, JHEP **0806** (2008) 082, arXiv:0804.0350 [hep-ph].

[142] J. Adelman, J. Erdmann, A. Hard, A. Loginov, P. Tipton, J. Vasquez, F. Wang, H. Wang, S. L. Wu, and H. Yang, *Search for* $t\bar{t}H$ *and* tH *production in the diphoton channel with* $20.3\ \mathrm{fb}^{-1}$ *of data at* $8\ \mathrm{TeV}$ *and* $4.5\ \mathrm{fb}^{-1}$ *of data at* $7\ \mathrm{TeV}$ *taken with the ATLAS detector*, Tech. Rep. ATL-COM-PHYS-2014-463, CERN, Geneva, May, 2014.

[143] J. Campbell, R. K. Ellis, and R. Rtsch, *Single top production in association with a Z boson at the LHC*, Phys.Rev. **D87** no. 11, (2013) 114006, arXiv:1302.3856 [hep-ph].

[144] M. Botje, J. Butterworth, A. Cooper-Sarkar, A. de Roeck, J. Feltesse, et al., *The PDF4LHC Working Group Interim Recommendations*, arXiv:1101.0538 [hep-ph].

[145] J.-F. Arguin, D. Cote, O. A. Ducu, M. Fiascaris, L. Gauthier, T. P. S. Gillam, G. Herten, M. Kruse, J. Maurer, T. J. Mueller, M. Pagacova, A. Paramonov, J. Pilcher, R. Povey, T. Rave, J.-E. Sundermann, and C. Zhou, *Search for strongly-produced superpartners in final states with two same-sign leptons or three leptons at sqrt(s) = 8 TeV*, Tech. Rep. ATL-COM-PHYS-2013-887, CERN, Geneva, Jun, 2013.

[146] T. Junk, *Confidence level computation for combining searches with small statistics*, Nucl.Instrum.Meth. **A434** (1999) 435–443, arXiv:hep-ex/9902006 [hep-ex].

[147] A. L. Read, *Presentation of search results: the CL s technique*, Journal of Physics G: Nuclear and Particle Physics **2810** (2002) 2693. http://stacks.iop.org/0954-3899/28/i=10/a=313.

[148] ATLAS Collaboration, *Search for same-sign top-quark production and fourth-generation down-type quarks in pp collisions at $\sqrt{s} = 7$ TeV with the ATLAS detector*, JHEP **1204** (2012) 069, arXiv:1202.5520 [hep-ex].

[149] ATLAS Collaboration, G. Aad et al., *Search for supersymmetry at $\sqrt{s}$=8 TeV in final states with jets and two same-sign leptons or three leptons with the ATLAS detector*, JHEP **06** (2014) 035, arXiv:1404.2500 [hep-ex].

[150] CMS Collaboration, S. Chatrchyan et al., *Search for new physics in events with same-sign dileptons and jets in pp collisions at $\sqrt{s} = 8$ TeV*, JHEP **1401** (2014) 163, arXiv:1311.6736.

[151] CMS Collaboration Collaboration, S. Chatrchyan et al., *Inclusive search for a vector-like T quark with charge $\frac{2}{3}$ in pp collisions at $\sqrt{s} = 8$ TeV*, Phys.Lett. **B729** (2014) 149–171, arXiv:1311.7667 [hep-ex].

[152] CMS Collaboration, S. Chatrchyan et al., *Search for top-quark partners with charge 5/3 in the same-sign dilepton final state*, Phys. Rev. Lett. **112** no. 17, (2014) 171801, arXiv:1312.2391 [hep-ex].

[153] ATLAS Collaboration, G. Aad et al., *A search for $t\bar{t}$ resonances using lepton-plus-jets events in proton-proton collisions at $\sqrt{s} = 8$ TeV with the ATLAS detector*, arXiv:1505.07018 [hep-ex].